

University of London
Imperial College of Science, Technology and Medicine
Department of Physics

**Modelling and Optimising GaAs/Al_xGa_{1-x}As
Multiple Quantum Well Solar Cells**

James P. Connolly

Submitted in part fulfilment of the requirements for the degree of
Doctor of Philosophy in Science of the University of London and
the Diploma of Imperial College, January 1997

Abstract

The quantum well solar cell (QWSC) is a p - i - n solar cell with quantum wells in the intrinsic region. Previous work has shown that QWSCs have a greater open circuit voltage (V_{oc}) than would be provided by a cell with the quantum well effective bandgap. This suggests that the fundamental efficiency limits of QWSCs are greater than those of single bandgap solar cells.

The following work investigates QWSCs in the GaAs/ $\text{Al}_x\text{Ga}_{1-x}\text{As}$ materials system. The design and optimisation of a QWSC in this system requires studies of the voltage and current dependencies on the aluminium fraction. QWSCs with different aluminium fractions have been studied and show an increasing V_{oc} with increasing barrier aluminium composition.

The QE however decreases with increasing aluminium composition. We develop a model of the QE to test novel QWSC designs with a view to minimising this problem.

This work concentrates on two design changes. The first deals with compositionally graded structures in which the bandgap varies with position. This bandgap variation introduces an quasi electric field which can be used to increase minority carrier collection in the low efficiency p and n layers. This technique also increases the light flux reaching the highly efficient depletion regions.

The second design change consists of coating the back of the cell with a mirror to exploit the portion of light which is not absorbed on the first pass.

A model of the QE of compositionally graded QWSC solar cells with back surface mirrors is developed in order to analyse the effect of these design changes. These changes are implemented separately in a number of QWSC designs and the resulting experimental data compared with the model. An optimised design is then presented.

Acknowledgements

The work in this thesis would not have happened without the support of a multitude of people. Keith Barnham has been a tireless source of encouragement and ideas over the years. Endless thanks to Jenny Nelson for always knowing what was wrong with models, for her encyclopaedic knowledge, and being there to recommend films, or have them recommended. Then there are all those who have passed through here, or are still here, including Jenny Barnes, Ian Ballard, Alex Zachariou, Paul Griffin, Ernest Tsui and Ned.

Next come the people who actually produced the solar cells in this thesis. Christine Roberts was always ready to answer constant questions about MBE machines and AlGaAs. John Roberts' produced the grade which worked first time, and was full of suggestions for new material tests. Malcolm Pate produced innumerable devices over the years, including the wafer squashed by the Royal Mail.

Then there are collaborators overseas. Antonio Marti Vega helped me take some measurements which can't be fitted in. Two hundred pages is quite enough! And Rosa Maria Fernandez Reyna in Madrid, who explained them to me and showed me around Madrid, including some very nice cafes and cinemas.

Enrique Grünbaum took TEM measurements which helped explain one of the more mystifying samples in this project, along with SIMS measurements by Federico Caccavale. The latter were enabled by Massimo Mazzer who arranged the SIMS measurements in Padua, and always had ideas for everything, including jazz concerts.

And thanks to all the people who have made daily life about the department more interesting, such as Jean Leveratt for chats on level 8 at lunchtimes and solutions to all sorts of problems, Lydia, also of Level 8, and Betty Moynihan for help with the technicalities of writing up on level 3.

As for finance, I thank the Greenpeace Trust who made the project possible, and who enabled me to go to the Solar World Congress.

Finally, there all the people I have known, or got to know over the years.

There are those who are overseas - Chris and Olenka, Marc and Malar and the Smiths, Claire and the Granjon Clan. All the Tuckmans and associates in North London apart from Jo in Guatemala, Kerry and Alberta, Karen in the East, (big) Phil, (other) Phil, Hiroe, Bruce who used to be in the West, Paul and Catherine in the centre, Vince in Cambridge, the Marchants (Pete and Jo) and Kul. Then theres Tanveer (I won, I think?), Tristan, Dorothy, Dave, Wing, thanks for the coffee Steve, and Rosa in Madrid. Thanks to everyone ... !

Finally, thanks to the family: Jim, Eva, Marie Pascal, Anne Catherine, Jeanne Chantal, Isabel and Oona for the support over the years, and for coming over now and then to visit. This thesis is dedicated to my parents.

Contents

1	Introduction	17
1.1	Current Energy Use and Alternatives	17
1.2	Reducing the Cost of Photovoltaic Power	18
1.3	Introduction to the Optimisation Program	19
2	Introduction to Solar Cells	21
2.1	Physics of Solar Cells	21
2.1.1	Intrinsic Semiconductors in Equilibrium	22
2.1.2	Doped Semiconductors	24
2.2	The Photovoltaic Effect	26
2.2.1	Light Absorption and Pair Generation	27
2.2.2	Charge Separation	29
2.2.3	Current-Voltage Characteristic of a p-n Junction in the Dark	32
2.2.4	The p-n Junction in the Light	35
2.3	The p-i-n Solar Cell	37
2.3.1	Space Charge Region of a p-i-n Diode	37
2.3.2	The Background Doping Problem in p-i-n Structures . . .	40
2.4	Limiting Efficiency of Solar Cells	42
2.4.1	Higher Efficiency Designs	44
2.5	Quantum Well Solar Cells	45
2.6	The QWSC in the AlGaAs System	46
2.7	Conclusions	48

3	Quantum efficiency and short circuit current models	49
3.1	Introduction	49
3.1.1	Review of Previous Work	49
3.2	Preliminary definitions	51
3.3	Calculation of light intensity in a QSWC	52
3.3.1	Definitions	52
3.3.2	Phase and reflectance	55
3.3.3	Generation Rate	55
3.4	Photocurrent	57
3.5	Intrinsic region photocurrent	58
3.6	p and n Region Contributions	59
3.6.1	Drift and Diffusion Currents	59
3.6.2	Current and Continuity	60
3.6.3	Transport Equations for n Layers	61
3.6.4	General Analytical Solution	62
3.6.5	Boundary Conditions	63
3.7	Constant Transport Parameters	64
3.7.1	Zero Field	64
3.7.2	Non Zero Effective Fields	65
3.8	Graded QWSCs and Numerical Solutions	67
3.8.1	Surface Boundary Condition in Compositionally Graded Cells	68
3.8.2	Numerical Accuracy	68
3.8.3	Comparisons of Analytical and Numerical Solutions	70
3.9	Conclusion	72
4	Model Parameters and Program Design	74
4.1	Program design	74
4.2	Design and Growth Parameters	76
4.3	Optical Parameters	78
4.3.1	Incident Flux	78

4.3.2	Absorption Coefficient	78
4.3.3	Reflectivity	79
4.3.4	Refractive index	80
4.4	Transport parameters	80
4.4.1	Band gap Parametrisations and the Quasi-Electric Field .	81
4.4.2	Minority carrier lifetime	82
4.4.3	Mobility and Diffusion Coefficient	83
4.4.4	Diffusion length	83
4.4.5	Recombination velocity	84
4.4.6	Discussion	86
5	QE Modelling and Optimisation	87
5.1	Ungraded Cells	88
5.1.1	Previous Work	88
5.2	Further QE Enhancements Above the Barrier Bandgap	92
5.2.1	Light Absorption and Minority Carrier Generation	92
5.2.2	Minority Carrier Transport	98
5.2.3	Minority Carrier Concentration	103
5.2.4	QE and Short Circuit Current	107
5.2.5	Windows	110
5.3	Further QE Enhancement Below the Barrier Bandgap	112
5.3.1	Generation, Flux and QE in Mirrored Cells	115
5.4	Conclusions	122
6	Device fabrication and characterisation	123
6.1	Sample Growth	123
6.1.1	Metalorganic Vapour Phase Epitaxy (MOVPE)	123
6.1.2	Molecular Beam Epitaxy (MBE)	124
6.2	Processing	125
6.2.1	Device Geometry	126
6.2.2	Mirror Backed Devices	127
6.2.3	Effects of Processing	127

6.3	Characterisation	128
6.3.1	Photoconductivity Experiment	128
6.3.2	Monochromatic current-voltage characteristics	129
6.3.3	Quantum efficiency measurements	132
6.3.4	Reflectivity measurement	132
6.3.5	External characterisation	133
6.4	Conclusion	134
7	Preliminary Characterisation	136
7.1	Monochromatic IV Measurements	136
7.1.1	Trends in QWSC and p - i - n Device MIV Data	138
7.1.2	Growth Optimisation Studies	144
7.1.3	Passivation effects	146
7.1.4	Conclusions	149
7.1.5	Reflectivity Measurements	150
7.1.6	Conclusions	152
8	Experimental and Modelled QE Spectra	154
8.1	Principles of Data Fitting	154
8.1.1	Sample geometry	155
8.1.2	Samples with efficient minority carrier transport	155
8.1.3	Samples with simplified modelling	156
8.1.4	Samples with high surface recombination parameters	157
8.1.5	Graded samples	158
8.1.6	Modelling of the quantum well QE	160
8.1.7	Mirror backed samples	160
8.2	Graded i Region Samples	161
8.2.1	Conclusions	169
8.3	Ungraded QWSC and p - i - n samples	169
8.3.1	MOVPE samples	169
8.4	MBE samples	172
8.4.1	20% samples	173

8.4.2	30% samples	175
8.4.3	40% samples	177
8.4.4	Diffusion length tabulation	177
8.4.5	Conclusion	179
8.5	Compositionally Graded p layer samples	180
8.5.1	MOVPE Samples	180
8.5.2	MBE	187
8.5.3	Conclusions	196
8.6	QE of Mirror Backed Samples	197
8.7	Optimisations	202
8.8	Conclusions to chapter 8	206
9	Conclusions	210
A	Analytical Solutions	215
A.1	General Form of the Analytical Solution	216
A.2	Ungraded p Layers	217
A.2.1	Case of Dominant Bulk Recombination	220
A.2.2	QE Near the Band Edge	220
A.2.3	High Absorption	223
A.3	Homogeneous Cells with Electric Fields	224
A.3.1	Surface Recombination Effect with Field	226
A.3.2	QE Near the Band Edge for Small Diffusion Length with Field	226
A.4	Conclusions	227
A.4.1	Ungraded Solar Cells	227
A.4.2	Solar Cells With Fields but Constant Materials Parameters	228
	References	229

List of Figures

2.1	Minority carrier photo generation, thermalisation and radiative and non radiative recombination mechanisms	28
2.2	p and n type semiconductors in equilibrium a) before contact and b) after contact. The built in voltage V_{bi} is equal to the difference between the Fermi levels in a), before contact. Also shown are ionised donor (+) and acceptor (-) atoms which give rise to V_{bi}	29
2.3	Semilog schematic of the forward bias Shockley dark current characteristic showing the generation-recombination regime (n=2) and the diffusion regime (n=1)	34
2.4	Light and dark currents of a solar cell, showing the maximum power rectangle	36
2.5	Electric field variation in an ideal p - i - n diode with zero background doping at zero and reverse biases	38
2.6	Electric field variation in a residually n doped p - i - n diode for A high reverse bias B moderate reverse bias and C an undepleted i layer	39
2.7	Light currents of solar cells with low and high bandgaps under similar illumination, showing the compromise between voltage and current. Also shown is an optimum design with a manifestly greater maximum power rectangle. . .	43
2.8	Schematic QWSC structure, absorption, recombination and escape mechanisms	47
3.1	Example generalised QWSC band diagramme, including position dependent bandgap in the p type layer and high aluminium fraction window layer . . .	53
3.2	Numerical and analytical internal QE plots for an ungraded 30% aluminium QWSC	71

3.3	Numerical and analytical QE plots for an ungraded 30% aluminium QWSC with electric field	71
5.1	Modelled a) light IV curves and b) QE spectra for a 50 well QWSC and p - i - n control pair based on a successful device.	89
5.2	Relative light intensities in a a) ungraded p - i - n cell and b) a p - i - n cell with a p layer graded from $X_{b1} = 67\%$ to $X_{b2} = 30\%$	93
5.3	Fractional increase in light intensity in a p - i - n cell with a p layer graded from $X_{b1} = 67\%$ to $X_{b2} = 30\%$ compared to an ungraded cell	94
5.4	Generation rates in an ungraded p - i - n solar cell for wavelengths above the bulk bandgap	96
5.5	Generation rates in a compositionally graded p - i - n solar for wavelengths above the bulk bandgap E_{b2}	97
5.6	Effective electric field in per micron as a function of position for a p layer graded from $X_{b1} = 67\%$ to $X_{b2} = 30\%$	100
5.7	Minority carrier concentration in an ungraded p layer for a range of wavelengths.	104
5.8	Minority carrier concentration in a p layer graded from 30% to 40% Al for a range of wavelengths.	105
5.9	Minority carrier concentration in a p layer graded from 30% to 67% Al for a range of wavelengths.	106
5.10	QE of a) a 30% p - i - n and b) a p - i - n with a p layer graded from $x_{b1} = 67\%$ to $x_{b2} = 30\%$	108
5.11	Percentage increase in QE for p, i, n layers and total enhancement for a graded p - i - n device relative to an ungraded control.	109
5.12	J_{sc} of a graded p - i - n cell as a function of the higher bandgap X_{b1}	111
5.13	Influence of window layer removal on the QE of an ungraded p layer, including surface recombination effects	113
5.14	Influence of window layer removal on the QE of a graded p layer QE , showing weak dependence on surface recombination velocity	114
5.15	Light flux in a mirror backed QWSC	115
5.16	Generation rate in a 30 quantum well QWSC	117

5.17	Generation rate in a mirror backed QWSC	118
5.18	Generation rate enhancement a) in all layers of a graded QWSC with and without a back mirror and b) percentage increase in the intrinsic region. . .	119
5.19	Quantum efficiency of a thirty well QWSC with a back mirror compared to an identical cell without a mirror.	120
5.20	Absolute QE increase in a thirty well QWSC with a back mirror compared to an identical cell without a mirror.	121
6.1	Typical MIV curves for good and moderate solar cell devices.	130
7.1	MIV data for an ungraded MOVPE grown 30 well QWSC and p - i - n control pair with $X_{b2} = 33\%$ aluminium before AR coating, showing deterioration of MIV in QWSC devices	138
7.2	MIV measurements for optimised device QT794 for NAR and AR coated devices	140
7.3	MIV data for a series of 30 well QWSC ungraded devices grown by MBE with nominal aluminium fractions $X_{B2}=20\%$, 30% and 40%	141
7.4	MIV data for a series of p - i - n ungraded devices grown by MBE with nominal aluminium fractions $X_{B2}=20\%$, 30% and 40%	141
7.5	MIV data for the 50 well graded sample U6041 and its p - i - n control U6045, indicating low net background doping	142
7.6	MIV measurements for the identical pair of QWSC devices QT468a and QT528. The latter was grown with a cleaner Ga source and shows an improved MIV characteristic.	144
7.7	MIV data for identical MOVPE single quantum well samples grown at 560C, 580C and 600C, showing little variation.	145
7.8	Degradation of MIV for a good p - i - n device QT468b	147
7.9	Improvement in MIV for poor QWSC device QT640a	147
7.10	MIV data for the 50 well QWSC sample W276 before and after exposure to a passivating hydrogen plasma	149
7.11	Reflectivities for QWSC and p - i - n devices for the U2027-U2032 MBE series	150
7.12	Reflectivities of a variety of samples with and without windows, showing that the removal of the window does not noticeably affect the reflectivity	151

8.1	QE for two linear parametrisations of L_n as a function of composition. For curve A), L_n is kept constant at $0.08\mu m$. Curve B represents the worst case scenario of $L_n(0) = 0.08\mu m$ and $L_n(x_{w_p}) = 0.01\mu m$	159
8.2	QE of 32 well QWSC Eindhoven structure W405	162
8.3	QE of p - i - n Eindhoven sample W406	163
8.4	QE of GaAs structure W407	164
8.5	Schematic compositional profile of graded i region sample W408 .	165
8.6	QE of graded i region sample W408	165
8.7	Schematic compositional profile of graded i region sample W409 .	166
8.8	QE of graded i region sample W409	167
8.9	Schematic compositional profile of GRINCH laser structure NRC1038	167
8.10	QE of GRINCH structure NRC1038	168
8.11	QE modelling and data for nominally 30% aluminium 30 well sample QT468a	170
8.12	QE modelling and data for QT468b, the p - i - n control to QT468a	170
8.13	QE modelling and data QT528, which is a repeat of QT468a with a cleaner Ga source	171
8.14	QE modelling and data for nominally 20% aluminium 30 well sample U2027 .	173
8.15	QE modelling and data for U2028, which consists of 30% p and n layers with a GaAs i region	174
8.16	QE modelling and data U4036, which is a p - i - n repeat of U2028 with a base aluminium fraction of $X_{b2} = 23\%$	174
8.17	QE modelling and data for nominally 30% aluminium 30 well sample U2029 .	176
8.18	QE modelling and data U2030, the p - i - n control to U2029	176
8.19	QE modelling and data for nominally 40% aluminium 30 well sample U2031 .	178
8.20	QE modelling and data U2032, the p - i - n control to U2031	178
8.21	Modelled minority electron diffusion length L_n for p - i - n and QWSC samples, compared with Hamaker's parametrisation for the MBE doping level doping levels	179
8.22	Experimental and modelled QE of ungraded MOVPE p - i - n QT601a . . .	181
8.23	Experimental and modelled QE of graded MOVPE p - i - n QT601c	181
8.24	QE of 30 well QWSC QT640a, with p layer grading ranging from 30% to 67%	183

8.25	QE of 50 well QWSC QT640b with p layer grading ranging from 30% to 67%	183
8.26	QE of QT641, the p - i - n control to 50 well QWSC graded 30-67%	184
8.27	Comparison of thirty well sample QT468a and similar structure QT640a which has a graded p layer	185
8.28	MOVPE version QT794a of the optimised 50 well graded QWSC design	186
8.29	SIMS measurements of C doping and aluminium composition in sample QT794a	186
8.30	Comparisons of QE for QWSC samples with and without grades, for a variety of grading schemes. Also shown is comparison of similar graded QWSC structures grown by MBE and MOVPE	188
8.31	MBE 50 well QWSC U4032, graded 20-40%	189
8.32	MBE 30 well QWSC U4033, graded 20-40%	190
8.33	MBE 30 well QWSC U4034 graded 30-67%	190
8.34	MBE 30 well QWSC U4035 graded 40-67%	191
8.35	Comparison of MOVPE and MBE versions of an optimised 50 well design QT794a and U6041 with graded p and no window	192
8.36	SIMS measurements of Be doping and aluminium composition in sample U6041	195
8.37	MBE 50 well QWSC without a window graded from $X_{b1}29\%$ to $X_{b2} = 24\%$.	196
8.38	QE of mirrored sample QT468a. Also shown for reference is the QE of an AR coated device without a mirror	197
8.39	QE of a mirrored QT468a device demonstrating non-specular reflection from the back surface and QE enhancement greater than two passes.	198
8.40	Experimental QE enhancement in two mirrored QT229 devices, compared with a AR device without a mirror	199
8.41	QE of a QT229 mirrored device showing a back surface phase change $\psi_b = 0$ radian	200
8.42	QE of a a QT229 mirrored device showing a back surface phase change $\psi_b = -3$ radian	200
8.43	QE of a mirrored device processed from the U6041 wafer	201

8.44	Theoretical prediction for optimised sample A combining the Eindhoven reflectivity, a $0.15\mu m$ grade with $X_{b1} = 67\%$ and $X_{b2} = 30\%$, a $0.02\mu m$ window with 80% aluminium, a high surface recombination and a back surface mirror.	203
8.45	Theoretical prediction for optimised sample B combining the Eindhoven reflectivity, a thin $0.10\mu m$ grade with $X_{b1} = 67\%$ and $X_{b2} = 30\%$, no window, a negligible surface recombination and a back surface mirror.	204
A.1	Components of the quantum efficiency for small diffusion length	219
A.2	Components of the quantum efficiency for large diffusion length	219
A.3	Comparison of exact and approximate solutions to the QE for low absorption and low diffusion length $L_n = 0.07\mu m$ for $x_{wp} = 0.148\mu m$	222

List of Tables

4.1	List of the main QWSC growth and design parameters.	75
4.2	Transport parameters for the p layer required by the model	76
4.3	Typical design parameter set for an anti-reflection coated 20% Al 30 well QWSC with a graded p layer and a back mirror	78
5.1	Basic QWSC growth menu	88
7.1	Predicted value of net background doping N_{BG} for a range of MIV cut-off voltages V_S , for a standard 30 well QWSC sample with $X_{b2} = 30\%$	137
8.1	Principle design parameters of MBE grown graded p QWSC samples	188

Chapter 1

Introduction

1.1 Current Energy Use and Alternatives

The sun irradiates the planet with approximately 4×10^6 EJ per year [1]. When we compare this enormous energy flux with current human consumption of around 400 EJ per year, we find that we receive somewhat more than this amount every hour in direct solar radiation.

With the exception of such sources as tidal, geothermal and nuclear energy, all the energy we consume is ultimately derived from the sun. It is largely harvested in a roundabout manner. The most important is the burning of fossil fuels, followed by nuclear and hydroelectric power.

The limited nature of the fossil fuel reserves however makes the search for alternatives important. This is exacerbated by recent concerns about global warming through the continued emission of greenhouse gasses. The recently published results of the United Nations Advisory Group on Climate Change included the conclusions of a wide range of expert opinion in this field. The conclusion was that some level of global warming is expected, and indeed, is already measurable.

Currently exploited alternatives present problems. Nuclear power, once hailed as the power source which would be too cheap to meter, has experienced well publicised difficulties related to the disposal of nuclear waste.

Hydroelectric power has been heavily exploited for decades, and in many countries is close to capacity. Moreover, the environmental impact of such schemes has, with hindsight, been found to be both significant and not always beneficial.

Solar or photovoltaic (PV) power is an attractive alternative for a number of reasons. PV installations can be designed on a small scale, point-of-use basis. Such installations have a low land requirement and little environmental impact. They do not require mechanical moving parts, and are therefore potentially robust and reliable, and subject to low maintenance costs. Photovoltaic module manufacturers already quote guaranteed lifetimes measured in decades. This compares favourably with diesel generators, for example, or even other renewable energy sources such as thermal or wind schemes which require moving parts and regular servicing.

Despite all these advantages, we see that photovoltaic power has yet to make a significant impact worldwide. The high capital cost associated with the production of the modules is a significant problem. This is partly due to inertia in the electricity generating industries and to institutional barriers resulting from the interests of established industries. Lowering the cost of alternative energy sources however clearly remains a viable route to achieving sustainable energy consumption patterns.

1.2 Reducing the Cost of Photovoltaic Power

There are three ways to reduce the cost of photovoltaic power. One is to concentrate on designing low cost PV modules, at some expense to the conversion efficiency. Larger areas will therefore be necessary, but the reduction in final cost per kilowatt may outweigh other considerations if the module cost can be brought down far enough. Examples are amorphous or poly-crystalline solar cells, and thin film solar cells made from II-VI materials such as CdTe. This strategy is currently the most successful for terrestrial PV applications. Another example of this technique is the electrochemical solar cell which has been reported by O'Regan and Grätzel [3].

The second, related method is to reduce the cost of PV systems. The cost of the solar cells in such a module may constitute less than half the cost of the finished PV module. For example the multicrystalline solar cells in Photowatt's PV modules [2] comprise about 40% of the cost of the finished module.

Another approach is improve the efficiency of the solar cells dramatically at the expense of cost. Again, the final module cost may be attractive in dollars per watt terms if the increase in output power more than compensates the increased module cost. In some cases, it may be economically viable to increase the light input to individual solar cells in a module by means of light concentrators. This approach typically involves exotic structures, complex processing, and generally requires high quality material.

To date the low cost approach has delivered marketable PV modules, whereas high efficiency cells are reserved for specialised applications in which cost is a secondary issue, such as space applications.

1.3 Introduction to the Optimisation Program

This work concerns the optimisation of a novel design of solar cell with the potential to reach high efficiencies through the use of novel physical processes. This design is the quantum well solar cell (QWSC). This is studied here particularly with regard to the efficiency with which the solar cell converts light into current, which is called the quantum efficiency or QE .

Chapter 2 will give an introduction underlying semiconductor physics before defining important solar cell parameters. A short review of some standard and high efficiency solar cell designs will be investigated, including the fundamental principles behind the quantum well solar cell.

Chapter 3 outlines the theoretical basis for QE calculations in general and describes the model we will use. This model requires knowledge of a large number of materials parameters, which are reviewed in chapter 4.

Chapter 5 describes previous work on the optimisation of the QWSC structure, and illustrates additional theoretical results from the model for a number

of designs based on the QWSC. A number of optimisations are presented.

The practical aspects of growth together with a review of experimental characterisation techniques are reviewed in chapter 6. These include preliminary characterisation techniques which allow the quality of individual growth and processing runs to be assessed. Results for these preliminary techniques are given in chapter 7.

Chapter 8 presents experimental measurements of the QE for a wide range of samples grown by two different techniques. These samples cover the optimisations suggested by the theory. The experimental data are then compared with the modelling, and conclusions drawn regarding the viability of the techniques proposed in chapter 5.

Chapter 2

Introduction to Solar Cells

In this chapter we introduce parameters such as short circuit current, open circuit voltage and fill factor, and overall conversion efficiency, which are useful for characterising and optimising solar cells. The first sections summarise the basic semiconductor physics of semiconductor p - n junctions in equilibrium and under illumination. These allows us to derive an expression for the built in potential of a p - n junction.

The behaviour of a p - n junction under different applied bias conditions is described as a basis for understanding the current voltage characteristic of a solar cell in the dark and under illumination. We describe the principles underlying the photovoltaic effect, and can then define the solar cell parameters mentioned above.

Having defined these parameters, we can identify design requirements for efficient solar cells. We review a number of high efficiency solar cell designs in a range of materials. We introduce the quantum well solar cell and explain why this design is expected to yield higher fundamental efficiencies limits than are expected from single band-gap solar cells.

2.1 Physics of Solar Cells

In this section we introduce the fundamental physics of semiconductors required to understand and optimise solar cell designs, and to define all fundamental

physical concepts and parameters which will be used in subsequent sections. The discussion is mainly based in the treatment given in Sze [4].

The crystal potential of a crystalline solid restricts the energies which can be occupied by electrons into bands of electronic states. The highest occupied band in energy in a semiconductor is the valence band, and is completely filled by the outer valence electrons of the solid at zero Kelvin.

The band immediately above it is called the conduction band, and is empty at zero Kelvin. These two bands are separated by a gap in energy where no electronic states exist. This band-gap is principal bandgap of the semiconductor E_g , and has important consequences for the electrical and optical properties of these materials.

2.1.1 Intrinsic Semiconductors in Equilibrium

The probability that an electron in a solid should occupy a given energy level is described by the Fermi-Dirac distribution function $f(E)$ of the form

$$f(E) = \frac{1}{1 + e^{(E-E_F)/k_B T}} \quad (2.1)$$

where E_F is the Fermi level. Equation 2.1 defines it as the energy at which there is a 50% chance of occupation by an electron at any temperature. k_B is Boltzmann's constant and T is the temperature.

At room temperatures thermal excitation in an undoped semiconductor generates a finite equilibrium density of electron-hole pairs known as the intrinsic carrier concentration n_i . This quantity influences the properties of semiconductor devices, and solar cells in particular.

The densities of holes p_0 and of electrons n_0 are equal in an intrinsic semiconductor because each electron leaves exactly one hole behind in the valence band. They are both equal to n_i .

$$n_0 = p_0 = n_i \quad (2.2)$$

The semiconductor in this case can conduct current through the motion under

an applied bias of the electrons in the conduction band and of hole states in the valence band.

We now consider the magnitude of this intrinsic carrier concentration by determining the number of electrons excited into the valence band at a temperature T . This can be found by integrating the product of the occupation probability $f(E)$ and the number of available states $N(E)$. We consider only direct band gap semiconductors for simplicity.

In this case, the number of available states near the band-edges may be assumed to be parabolic. The relationship between energy and electron momentum is analogous to the free-electron case, with the electron mass m_e replaced by an effective mass m_e^* , to account for the crystal potential. It can be shown [4] that the energy-momentum relationship yields the following density of states near the conduction band edge:

$$N_c(E) = \frac{8\sqrt{2}\pi m_e^{*3/2}}{h^3} (E - E_c)^{1/2} \quad (2.3)$$

A similar relationship for the density of states near the valence band edge can be found by substituting the hole effective mass m_h^* mass for m_e^* and integrating in energy from the valence band edge to minus infinity: from the valence band edge to infinity

$$N_v(E) = \frac{8\sqrt{2}\pi m_h^{*3/2}}{h^3} (E_v - E)^{1/2} \quad (2.4)$$

For energies $E - E_F > 3K_B T$, the Fermi-Dirac function can be approximated by

$$f_E \simeq e^{-(E-E_F)/k_B T} \quad (2.5)$$

Integrating the product of equations 2.3 and 2.5 over energies from the conduction band edge to infinity then gives the number of conduction electrons in the system:

$$n_0 = N_C e^{(E_F - E_c)/k_B T} \quad (2.6)$$

where N_C is known as the effective density of states in the conduction band and

is given by

$$N_C = 2 \left(\frac{2\pi m_e^* k_B T}{h^2} \right)^{3/2} \quad (2.7)$$

The number of holes is found by assuming a similar form to equation 2.5 for $E_F - E > 3K_B T$ and integrating downwards in energy from the valence band edge. This gives

$$p_0 = N_V e^{(E_v - E_F)/k_B T} \quad (2.8)$$

where N_V is the valence band effective density of states, given by

$$N_V = 2 \left(\frac{2\pi m_h^* k_B T}{h^2} \right)^{3/2} \quad (2.9)$$

Equations 2.6 and 2.8 together with equation 2.2 yield the intrinsic carrier concentration

$$n_i^2 = p_0 n_0 = N_C N_V e^{-E_g/k_B T} \quad (2.10)$$

The intrinsic carrier concentration in GaAs for example is approximately $1.79 \times 10^6 \text{ cm}^{-3}$ and a rather higher $1.45 \times 10^{10} \text{ cm}^{-3}$ in Si at room temperature because of the smaller band gap of this material.

We can now calculate the Fermi level in an intrinsic semiconductor. Equation 2.2 shows that the ratio of equations 2.6 and 2.8 is equal to one. Separating E_F gives

$$E_F = \frac{E_v + E_c}{2} + \frac{k_B T}{2} \ln \left(\frac{N_V}{N_C} \right) \quad (2.11)$$

The Fermi level is situated near the middle of the bandgap, with a small offset caused by the difference between the effective densities of states in the valence and conduction bands.

2.1.2 Doped Semiconductors

We now consider the case of a semiconductor which has been doped with impurity atoms, starting with the case of a n type semiconductor. Donor or n type impurities have valence electrons with energy levels located a few meV below the conduction band edge. At non-zero temperatures, some of these donor atoms

are ionised by lattice vibrations and contribute extra electrons to the conduction band edge. Charge neutrality is preserved, since an ionised donor exists for every extra conduction band electron. For most common semiconductor devices, the dopants are chosen so that their ionisation energy is of the order or less than $3k_B T$, where T is the operating temperature. In this case, the donors are effectively all ionised, and the extra conduction electron concentration is of the order of the doping density N_D .

The law of mass action states that the electron and hole concentrations n and p are related as follows:

$$pn = n_i^2 \quad (2.12)$$

Useful doping densities in GaAs/Al_xGa_{1-x}As are typically in the range 10^{16} - 10^{20} cm^{-3} . We have seen previously that the n_i is of the order of 10^6 cm^{-3} for GaAs at room temperature. Since $n \simeq N_D$, it can be seen from equation 2.12. that the hole concentration is typically many orders of magnitude smaller than the electron concentration, and is given approximately by

$$p_{n0} = \frac{n_i^2}{N_D} \quad (2.13)$$

The electrons in n-type material are called majority carriers, and the holes minority carriers. We use the subscript $n0$ to identify the minority hole concentration in n-type material in equilibrium.

A p-type semiconductor is one which has been doped with electron acceptors with empty electron valence states a few meV above the valence band. Electrons from the valence band are thermally excited into these states at room temperatures, ionising the acceptor and leaving a positive hole in the valence band. The majority carriers in this case are holes, and their concentration is approximately equal to the concentration N_A of acceptor atoms. The minority electron concentration is then given by

$$n_{p0} = \frac{n_i^2}{N_D} \quad (2.14)$$

where the subscript $p0$ identifies the electron minority concentration in p-type

material in equilibrium.

We can calculate the Fermi level in a n doped semiconductor from equation 2.6, noting that $n \simeq N_D$. This gives

$$E_F = E_c - k_B T \ln \left(\frac{N_C}{N_D} \right) \quad (2.15)$$

Equation 2.15 shows that as N_D approaches the effective conduction band density of states, the Fermi level increases towards the conduction band edge. This reflects the increasing probability of electronic states in the conduction band being occupied by electrons.

Similarly, the Fermi level in a p type semiconductor is

$$E_F = E_v + k_B T \ln \left(\frac{N_V}{N_A} \right) \quad (2.16)$$

The Fermi level for a p type semiconductor moves towards the valence band edge as electrons are removed by acceptors, thereby decreasing the probability of valence band states being occupied by electrons.

2.2 The Photovoltaic Effect

In the preceding sections, we looked at the static behaviour of electron and hole populations for semiconductors in equilibrium. We now examine the behaviour of these populations when the system is moved away from equilibrium under illumination, when electrical power can be extracted via the photovoltaic effect.

The photovoltaic effect converts incident light into electrical power. The process consists of two stages. The first is to create an excess minority carrier population by exciting electrons with a light flux of intensity $F(\lambda)$, in photons per second per wavelength λ . By excess minority carrier population we mean those minority carriers which exceed the minority carrier population in equilibrium. If the incident light has sufficient energy, an electron can absorb a photon and transfer from a valence band state to a conduction band state. The net effect is the creation of an electron-hole pair. The excess minority carriers form a non

equilibrium population at a higher energy than the ground state of the system.

The second stage of the photovoltaic process is to extract the potential energy of this system. It is known as charge separation, and consists of spatially separating the electron-hole pairs. This prevents them from recombining and losing their energy as heat or light, and imposes motion in opposite directions which constitutes the photocurrent. This photocurrent can then be extracted through an external circuit connected to the terminals of the solar cell.

2.2.1 Light Absorption and Pair Generation

Minority carriers are generated when an electron absorbs a photon and gains sufficient energy to be promoted to a conduction state, leaving a positively charged hole state in the valence band. This is illustrated in figure 2.1.

In p type material, electrons which absorb a photon with energy greater than the bandgap are promoted into minority carrier states high in the conduction band. They very rapidly lose this excess energy in collisions with the lattice, generating heat. This process, known as thermalisation, ceases when they reach the band edge. The minority carriers then remain in band edge states for a finite time known as the minority electron lifetime τ_n before recombining with a majority hole in the valence band. The time taken to thermalise to the band-edge is much smaller than τ_n , and the carriers therefore build up a quasi-equilibrium thermal population at the conduction band edge.

Minority holes in n type material which absorb more energy than the bandgap are promoted to holes in the valence band, and thermalise up towards the valence band edge in a similar manner, again losing the excess energy as heat. They then remain at the band edge for a minority hole recombination time τ_p before recombining with a majority electron.

Thermalisation is an important energy loss mechanism in solar cells. It ensures that the maximum amount of power delivered by a minority carrier is proportional to the bandgap of the material, irrespective of the energy of the photon providing the excitation.

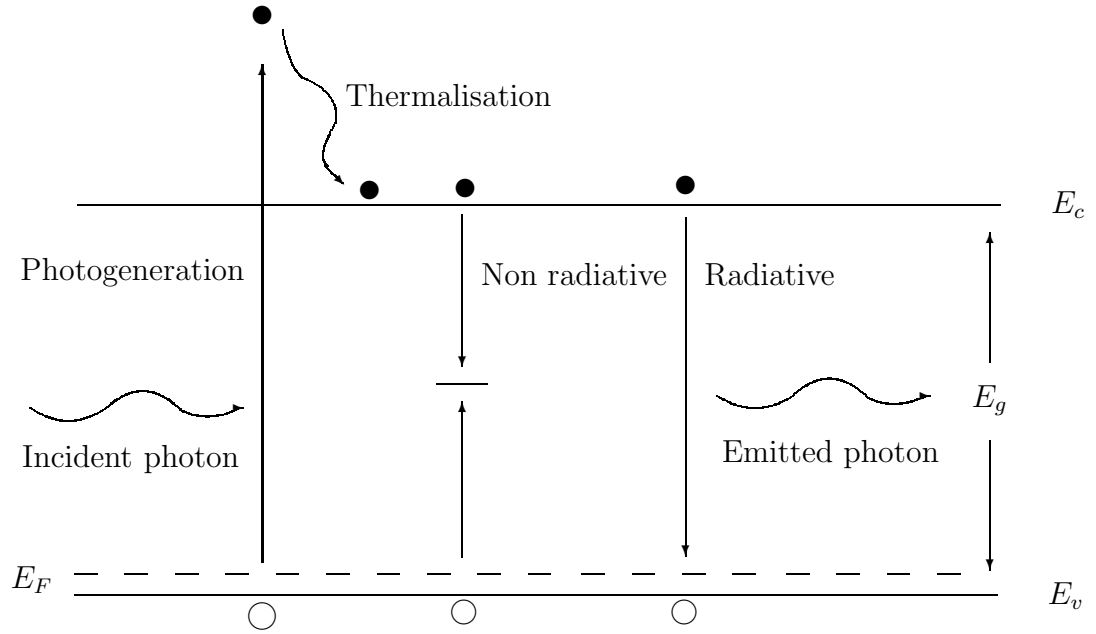


Figure 2.1: Minority carrier photo generation, thermalisation and radiative and non radiative recombination mechanisms

The generation rate G at a particular point is given by the absorption coefficient α and the light flux F

$$G = \alpha F \quad (2.17)$$

Direct and indirect semiconductors show distinctly different optical and electrical behaviour. In direct material such as GaAs the lowest electronic transition is one which does not require a change of momentum. In this case the absorption as a function of photon energy E near the band edge is approximately given [6] by

$$\alpha_{direct}(E) \sim (E - E_g)^{1/2} f(E - E_g) \quad (2.18)$$

where $f(E - E_g)$ is a step function with value 1 for $E > E_g$ and zero for $E < E_g$.

Indirect material such as silicon or $\text{Al}_x\text{Ga}_{1-x}\text{As}$ with an aluminium content greater than about 45% has an indirect bandgap. Light absorption also requires phonon absorption or emission. As a result, the absorption coefficient near the

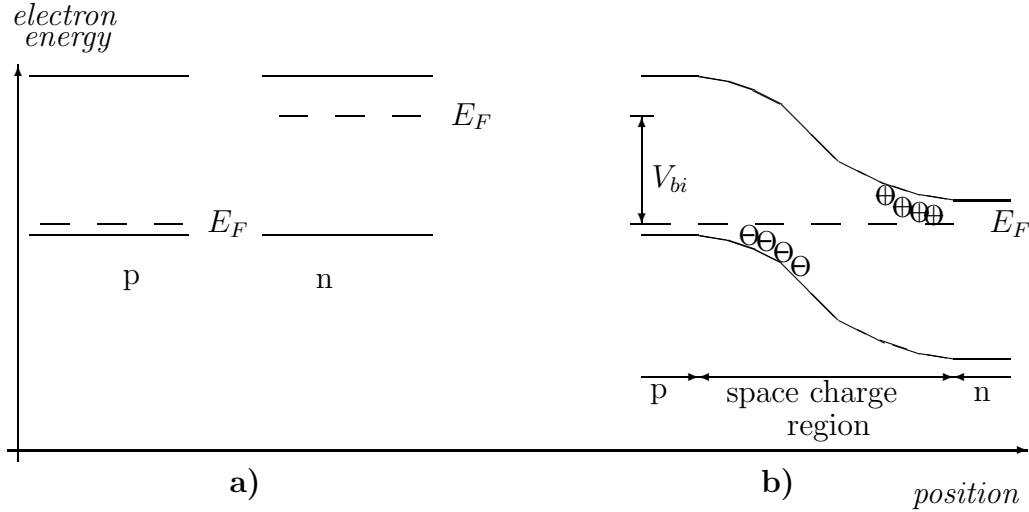


Figure 2.2: p and n type semiconductors in equilibrium a) before contact and b) after contact. The built in voltage V_{bi} is equal to the difference between the Fermi levels in a), before contact. Also shown are ionised donor (+) and acceptor (-) atoms which give rise to V_{bi} .

band-edge is significantly smaller than in direct material and takes the form

$$\alpha_{indirect} \sim (E - E_g)^2 f(E - E_g) \quad (2.19)$$

The electron hole pairs generated by light absorption are free to move through the crystal lattice until they either recombine, losing the absorbed energy as heat or light, or are collected and contribute to the photocurrent.

2.2.2 Charge Separation

Collection of photogenerated carriers requires a field to separate electrons from holes, and to impose ordered motion in the direction of the positive and negative terminals of the solar cell. This constitutes the photocurrent.

The charge separation is achieved by creating a junction region in the solar cell with p type doped material on one side, and n type dopants on the other. This results in a potential drop across the structure. Electrons drift down the potential, whereas holes drift up in the opposite direction. The precise origin of this separation potential is explained in more detail below.

The solar cell is divided into three regions. Charge separation occurs mainly

in the junction region, which we will refer to as the space-charge region. In good material, the field separates the electrons and holes with efficiencies approaching 100%.

There is no net electric field in the charge neutral sections of the p and n regions adjoining the depletion layer, which we call the p and n neutral regions.

Electrons and holes in these neutral regions move by diffusion. Spatial variations in composition of doping may contribute a small drift component. This will be investigated in chapter 3. The diffusion process is much less efficient than the drift collection which dominates in the space-charge region. Minority carriers perform a random walk with a finite average lifetime and diffusion length. A minority carrier which does not reach the interface with the space-charge region eventually recombines with a majority carrier and is lost. The collection of carriers generated in the neutral regions is described in more detail in chapter 3.

Current generation in all regions of the cell therefore depends on the presence of a built-in potential, which arises when a junction is made between p and n type material.

When p and n type semiconductors are placed in electrical contact, there is an imbalance between the large number of majority electrons on the n side and the thermal minority electron concentration on the p side. A similar but opposite concentration gradient exists for holes. These electron and hole gradients give rise to a diffusion current of electrons from the n doped side of the junction to the p, and of holes in the opposite direction.

The electron current from the n side removes the electrostatic shielding of the donor atoms, which become positively ionised. Similarly, acceptor ions on the p side of the junction are negatively ionised. The resulting distribution resembles a parallel plate capacitor with positively charged donors on one plate and negatively charged acceptors on the other. The region populated by ionised impurities is known as the space-charge region, and is made up of the p and n depletion layers.

The electric field between the ionised dopants opposes the diffusion current. In the absence of an external bias, the p - n junction in the dark reaches an equilibrium in which the electrical field cancels the diffusion potential. It can be

shown [4] that this condition is equivalent to a constant Fermi level throughout the system, as illustrated in figure 2.2b.

The thickness of these depletion layers can be found from charge neutrality and assuming that the total potential dropped is equal to the difference in Fermi levels between the two materials before electrical contact.

This difference in Fermi levels ΔE_F is equal to $-qV_{bi}$ where V_{bi} is the voltage dropped across the depleted region and is known as the built in voltage. It is conveniently expressed in terms of the intrinsic carrier concentration n_i and the dopant densities. Subtracting equation 2.15 from equation 2.16 and substituting n_i^2 for the product $N_C N_V$ from equation 2.10 gives

$$V_{bi} = -\frac{\Delta E_F}{q} = -\frac{k_B T}{q} \ln \left(\frac{N_A N_D}{n_i^2} \right) \quad (2.20)$$

The built in voltage is negative, in the sense that it is opposite to the standard terminal connection terminology, which is that the n terminal is negative and the p positive.

For heavily doped high-bandgap materials, the Fermi levels in the p and n neutral regions lie close to the conduction and valence band edges, and V_{bi} is only a few percent smaller than the bandgap of the semiconductor.

Since the space-charge region has essentially zero mobile charge density in low injection conditions, we assume that all the external bias is dropped across it, and that no net field exists in the neutral sections. The total potential drop across the space-charge region is therefore given by the sum of the applied bias V_{ext} and V_{bi}

$$V = V_{ext} + V_{bi} \quad (2.21)$$

This potential drop can also be derived by integrating Poisson's equation across the space charge region of width $W = x_{wp} + x_{wn}$.

$$V = -\int_0^W \left(\frac{\rho}{\epsilon} \right) dx \quad (2.22)$$

where ϵ is the permittivity of the material. The charge density ρ on both sides

of the junction is given by N_A and N_D .

Since there is no electrical field in the neutral sections of the p and n layers, the sum of fixed positively and negatively charges must cancel. The charge density in the p depletion layer is negative and equal to $-qN_A$, where q is the magnitude of the electronic charge. It is exactly opposite to $+qN_D$ in the n depletion layer. If x_{w_p} and x_{w_n} are the p and n layer depletion widths, this charge neutrality condition can be written

$$x_{w_p}N_A = x_{w_n}N_D \quad (2.23)$$

By solving equation 2.22 subject to 2.23 and 2.21 we find that the depletion widths (with $V_{bi} < 0$) are

$$x_{w_p} = \frac{1}{N_A} \sqrt{\frac{2\epsilon(-V_{bi} - V_{ext})}{q(\frac{1}{N_A} + \frac{1}{N_D})}} \quad (2.24)$$

$$x_{w_n} = \frac{1}{N_D} \sqrt{\frac{2\epsilon(-V_{bi} - V_{ext})}{q(\frac{1}{N_A} + \frac{1}{N_D})}} \quad (2.25)$$

where ϵ is the permittivity of the material. We note that the depletion widths increase as the applied bias becomes large and negative, and tend to zero as the positive applied bias cancels the built in potential.

2.2.3 Current-Voltage Characteristic of a p-n Junction in the Dark

The current flowing through a solar cell is the sum of the photocurrent and of a diode characteristic, known as the dark current. The dark current component is important in determining the open circuit voltage of the cell. A good understanding of the dark current is therefore important in optimising the overall efficiency of the solar cell design.

Studies of dark current in p - n diodes were pioneered by Shockley et al. [7]. They established that an exponentially increasing current flows if the diode is driven into forward bias by making the p contact positive with respect to the n. This is because the applied bias reduces the electric field in the space charge

region away from its equilibrium value. The drift current no longer cancels the diffusion current, and a net current flows.

A negative applied bias on the other hand increases the field in the space charge region, inhibiting the diffusion of majority carriers from the p and n sides of the junction. The diffusion current therefore decreases and no longer cancels the drift current due to generation-recombination effects in the neutral regions. A small, voltage independent saturation current J_0 is seen to flow until the external applied bias exceeds a critical break-down voltage, at which the structure cannot sustain potential difference across the terminals and a sudden increase in reverse current is observed.

Shockley *et al.* [7] initially modelled the dark current of an ideal diode in terms of semiconductor majority and minority carrier transport equations. This considers only the diffusion currents of holes and electrons from the neutral sections of the diode and neglects the generation-recombination current in the space charge region. This approach yields the Shockley ideal diode equation

$$J_{ideal}(V) = J_{01}(e^{qV/k_BT} - 1) \quad (2.26)$$

where the saturation current J_{01} is the ideal saturation current. It can be expressed in terms of the electron and hole transport parameters. It is proportional to n_i^2 and is therefore given in Sze [4] as

$$J_{01} \simeq e^{E_g/k_BT} \quad (2.27)$$

A more advanced analysis takes the generation-recombination current in the space charge region into account. The discussion in Sze [4] based on analysis by Sah, Noyce and Shockley [5] shows that the electron and hole emission is dominated by recombination centres situated at energies in the middle of the bandgap. The generation-recombination current J_{gr} can then be expressed in terms of a recom-

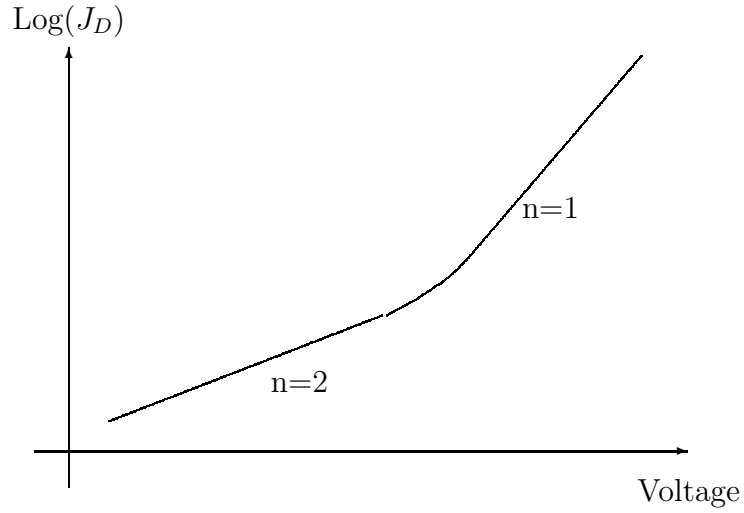


Figure 2.3: Semilog schematic of the forward bias Shockley dark current characteristic showing the generation-recombination regime ($n=2$) and the diffusion regime ($n=1$)

bination lifetime τ_r , the total space-charge region width W and n_i :

$$J_{gr} = \frac{qWn_i}{2\tau_r} \left(e^{qV/2k_BT} - 1 \right) \quad (2.28)$$

The sum of equations 2.26 and 2.28 gives the Shockley-Read-Hall diode dark current J_D

$$J_D = J_{01}(e^{qV/k_BT} - 1) + J_{02}(e^{qV/2k_BT} - 1) \quad (2.29)$$

Equation 2.29 neglects the thermal contribution to the dark current, which has a bandgap dependence of $\simeq e^{-E_g/k_BT}$ but is negligibly small in semiconductor structures suitable for solar cell applications. The expression is frequently simplified as follows when modelling data:

$$J_D \simeq J_0(e^{qV/nk_BT} - 1) \quad (2.30)$$

where n is called the ideality factor. It can be seen from equations 2.26 and 2.28 that $n = 1$ for an ideal diode, and $n = 2$ for p - n junctions with strong generation-recombination currents. Figure 2.3 shows a schematic of a diode dark current in forward bias.

Diodes made from materials with small, direct band gaps tend to follow the ideal diode equation adequately, because the relatively large value of n_i ensures that the diffusion currents from the neutral regions dominate the dark current.

Diodes made from high bandgap materials on the other hand frequently show two regimes. At high forward bias, the diffusion current dominates and a factor $n = 1$ is seen. For low forward bias, the reverse is true and n tends to 2.

2.2.4 The p-n Junction in the Light

We have mentioned before that the photocurrent from a solar cell is made up of two components which flow in the opposite way to a conventional current. Minority carriers in the space-charge region are rapidly separated by the built in field, and swept to the interface with the neutral regions where they become majority carriers.

Minority carriers generated in the neutral regions must reach the space-charge region before they can contribute to the photocurrent, because no field exists in these regions. Transport is dominated by carrier diffusion.

Both these cases are examined in detail in section 3. The photocurrent J_L is expressed as the sum of diffusion components from the p and n regions J_p and J_n , and a drift component from the space charge region J_i

$$J_L = J_p + J_i + J_n \quad (2.31)$$

A significant decrease in the photocurrent is observed if the solar cell is forced into forward bias of the order of the built in potential, because charge separation in the space-charge region is impaired. A small increase is seen in reverse bias as the space charge region broadens because of the enhanced internal field. However, in the operating range of high quality solar cells, the photocurrent J_L may be assumed to be constant with bias and equal to the short circuit value J_{sc} .

The current-voltage characteristic of an illuminated solar cell $J(V)$ is then approximately given by sum of J_L and the dark current J_D of equation 2.30,

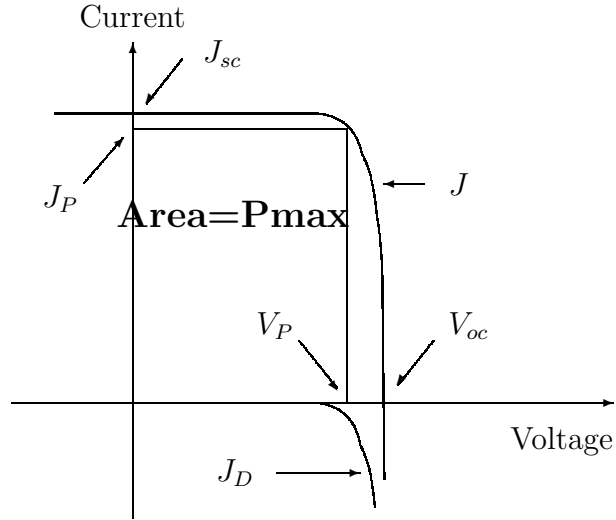


Figure 2.4: Light and dark currents of a solar cell, showing the maximum power rectangle

noting that the photocurrent is negative

$$J = J_0(e^{qV/nk_BT} - 1) - J_L \quad (2.32)$$

A typical light current characteristic is given in figure 2.4.

We now define some of the more useful quantities for solar cell characterisation and optimisation. The open circuit voltage V_{oc} is the forward bias at which the dark current exactly cancels the photocurrent, and no net current flows. Setting $J = 0$ in equation 2.32 and assuming that J_D is dominated by diffusion currents at such voltages such that $J_{gr} \ll J_{ideal}$, we obtain

$$V_{oc} = \frac{k_BT}{q} \ln \left(\frac{J_{sc}}{J_{01}} \right) \quad (2.33)$$

The maximum power which can be extracted from the solar cell is given by the largest rectangle which can be fitted under the curve, as shown in the schematic figure 2.4. This rectangle defines the maximum power point, and the associated optimum operational current and voltage J_P and V_P . The maximum power is then

$$P_{max} = J_P V_P \quad (2.34)$$

It is useful to define a fill factor FF as follows

$$FF = \frac{P_{max}}{V_{oc}J_{sc}} \quad (2.35)$$

The overall efficiency of the cell η is given by the ratio of the the maximum power P_{max} and incident power P_{inc} . It is usually expressed as follows

$$\eta = \frac{V_{oc}J_{sc}FF}{P_{inc}} \quad (2.36)$$

2.3 The p-i-n Solar Cell

In the last sections we have defined the principal characteristics of p - n junction solar cells. We saw in section 2.2.2 that carriers photogenerated in the space-charge region are collected with efficiencies approaching 100%. It is therefore clearly desirable to extend the width of this layer. Although equations 2.24 and 2.25 show that this can be achieved by reducing the p and n doping densities, this technique has two unfortunate consequences. The first is the reduction of the V_{oc} according to equation 2.33. The second is an increased resistivity in the neutral regions due to lower doping.

We now introduce a structure which circumvents these problems. This is the p - i - n diode, which is commonly used for high efficiency photodetectors because the spectral response of the cell can be optimised as a function of the response time. It serves as a useful starting point for the design of an efficient quantum well solar cell, as we shall see below.

2.3.1 Space Charge Region of a p-i-n Diode

The p - i - n solar cell consists of an ordinary p - n diode, with a layer of nominally undoped material inserted between the p and n regions. This layer is known as the intrinsic region, of thickness x_i . The total space-charge region thickness is then given by

$$W_i = x_{wp} + x_i + x_{wn} \quad (2.37)$$

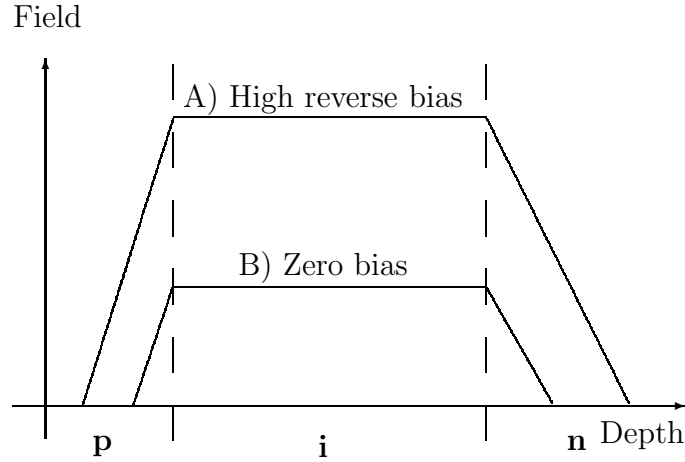


Figure 2.5: Electric field variation in an ideal p - i - n diode with zero background doping at zero and reverse biases

Figure 2.5 shows the electric field variation in such a structure at reverse bias and at zero bias. The p and n depletion regions decrease in size as the field drops. The field in the i region will only drop to zero when the V_{ext} is equal and opposite to V_{bi} .

Although the intrinsic layer is nominally undoped, we always find a residual or background doping density N_{BG} , which may be either n or p type depending on the growth machine and growth conditions. It is of the order $N_{BG} \sim 10^{14}\text{cm}^{-3}$ in good material, but may be as high as 10^{16} or even 10^{17}cm^{-3} .

The calculation of W_i is similar to the calculation outlined in section 2.2.2. The built-in potential is given by equation 2.20 and by Poisson's equation 2.22 as before. The main difference is that the double integral is over the new space charge region thickness W_i , and must include any residual space-charge due to the background doping N_{BG} . Figure 2.6 shows the variation of field as a function of position in a p - i - n structure where the background doping is p type. Curve A shows the field for a large negative applied bias. In the case of curve B, the magnitude of the negative applied bias is lower, and the depletion regions are smaller. Curve C shows a case where the i layer is not completely depleted.

For the p - i - n cell with a n type background doping shown in figure 2.6, the potential V dropped across W_i is again the sum of external and built in

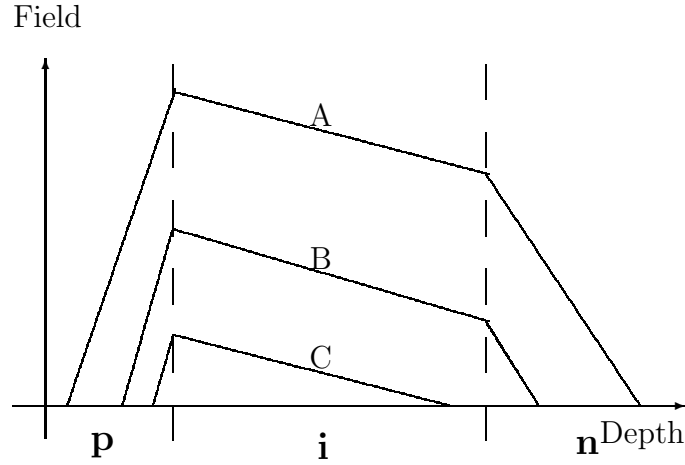


Figure 2.6: Electric field variation in a residually n doped p - i - n diode for A high reverse bias B moderate reverse bias and C an undepleted i layer

potentials, and is defined as before by equations 2.20 and 2.21. It can also be calculated by integrating Poissons equation across W_i ,

$$V = -\frac{qN_A x_{wp}^2}{2\epsilon} - \frac{qN_A x_{wp} x_i}{\epsilon} + \frac{qN_{BG} x_i^2}{2\epsilon} - \frac{qN_D x_{wn}^2}{2\epsilon} \quad (2.38)$$

The charge neutrality condition of equation 2.23 must be re-written to take the background doping into account:

$$-x_{wp} N_A + x_i N_{BG} + x_{wn} N_D = 0 \quad (2.39)$$

Equations 2.38 and 2.39 define the depletion widths in terms a quadratic equation. For the p side depletion layer of the n type background doped cell we have been discussing, this quadratic equation takes the form

$$\begin{aligned} x_{wp}^2 \left[\frac{N_A^2}{2\epsilon} \left(\frac{1}{N_A} + \frac{1}{N_D} \right) \right] + x_{wp} \left[\frac{N_A N_{BG} x_i}{\epsilon} \left(\frac{1}{N_{BG}} - \frac{1}{N_D} \right) \right] \\ + x_i^2 \left[\frac{N_{BG}^2}{2\epsilon} \left(\frac{1}{N_D} - \frac{1}{N_{BG}} \right) \right] + \frac{V}{q} = 0 \end{aligned} \quad (2.40)$$

Similar expressions describe the n depletion width x_{wn} . If the intrinsic doping is n type, the sign of the term in N_{BG} of equation 2.38 must be reversed.

2.3.2 The Background Doping Problem in p-i-n Structures

In this section we consider the influence of the intrinsic region thickness x_i and the background doping N_{BG} on the performance of a p - i - n solar cell, according to theory described by Paxman [8]. We then introduce a method of calculating N_{BG} from the dependence of the photocurrent J_L on voltage.

A calculation of depletion widths as a function of intrinsic region width x_i and N_{BG} raises a number of potential problems with this type of structure. The n and p depletion layer thicknesses decrease as x_i is made larger, thereby decreasing the overall space charge region width. Calculations however show that the decrease in n and p depletion layer thicknesses is negligible compared to the increase due to the intrinsic layer.

Another consequence of increasing the intrinsic region width is a lower electric field in the space charge region, which simply results from the fact that the constant built in potential is dropped across a wider thickness. This sets a practical limit on the amount of intrinsic material which can be inserted between the doped layers. This is not usually a serious limitation in practical solar cells.

Studies of the space charge region thickness dependence on background doping reveal more challenging technological problems, as we shall see in the next section. In this case, the ionised background charge may cause the electric field to drop to zero in the intrinsic region. Since N_{BG} is always much smaller than N_A and N_D , Poisson's equation shows that the rate of reduction of the space charge region thickness with increasingly positive voltage becomes much greater. Furthermore, cell resistance may increase because of the presence of an undepleted and low doped thickness adjoining either the n or the p region. Both these effects will reduce the solar cell efficiency.

We now consider the variation of photocurrent J_L for p - i - n cells with high and low values of N_{BG} . In the case of low N_{BG} , a nearly constant photocurrent is seen into forward bias. A residual voltage dependence does in principle exist, and is due to the change in depletion widths as a function of applied bias. The

photocurrent in forward bias may drop because of experimental considerations which will be considered in chapters 6 and 7. In theory, however, it drops at the point where the applied bias is equal and opposite to V_{bi} . This removes the charge separating potential, and the device no longer operates as a solar cell.

In the case of a cell with a high background doping, the higher space charge density in the intrinsic region imposes a significant electric field gradient, as illustrated by the curves of figure 2.6. In this case, the width of the space charge region decreases slowly while the p and n depletion widths are greater than zero, and J_L is only weakly dependent on the applied bias.

As the applied bias is increased, either the p or the n depletion layer vanishes. At this point, there is still a field in the space charge region, and charge separation still occurs. However, the space charge region diminishes much more quickly with increasing bias because of the lower doping density in the space charge region. A significant decrease in J_L with increasing voltage is suddenly seen.

The corresponding shoulder in the curve of J_L versus applied bias provides us with a useful tool for estimating N_{BG} in poor quality samples. At the shoulder, the p - i - n cell is effectively behaving like a p⁻ncell with the p type depletion layer given simply by the intrinsic region width, and an effective p doping $N_A^- = N_{BG}^p$. We can therefore substitute x_i for x_{wp} and N_{BG}^p for N_A in equation 2.24, giving

$$N_{BG}^p = \frac{N_D}{2} \left[\sqrt{1 + \frac{8\epsilon(-V_{bi} - V_{sh})}{qx_i^2 N_D}} - 1 \right] \quad (2.41)$$

where V_{sh} is the measured voltage at the shoulder. The equivalent relation for a n type $N_{BG}^n = N_D^-$ is given by equation 2.25

$$N_{BG}^n = \frac{N_A}{2} \left[\sqrt{1 + \frac{8\epsilon(-V_{bi} - V_{sh})}{qx_i^2 N_A}} - 1 \right] \quad (2.42)$$

Equations 2.42 and 2.41 can be used to estimate the maximum tolerable background doping for a given p - i - n solar cell design. For a typical structure with a p type background doping, $N_D \simeq 10^{17} \text{cm}^{-3}$ and an intrinsic layer thickness $x_i \simeq 0.8 \mu\text{m}$ we find that the highest background doping density permitting the

cell to operate adequately to voltages of about a volt is $N_{BG}^p \sim 5 \times 10^{14} \text{cm}^{-3}$

2.4 Limiting Efficiency of Solar Cells

In the previous sections we have introduced the quantities describing the efficiency of a solar cell. Equation 2.36 provides a starting point for designing a high efficiency solar cell.

High efficiencies require large values of J_{sc} , V_{oc} and FF. The series resistance of the cell is important in determining FF and is ideally small. Although this can be achieved by high doping levels, practical limits are set by the degradation of transport parameters in heavily doped samples.

A high J_{sc} clearly depends on absorption of as much light as possible. Equations 2.18 and 2.19 show that a low bandgap increases absorption by reducing the cut-off energy below which no photons are absorbed.

The requirements for a high V_{oc} can be found from equation 2.33. A fundamental requirement for a low J_D and hence a high V_{oc} is a low recombination. Recombination can be reduced to some extent by improved cell fabrication techniques and passivation which reduce the concentration and activity of non-radiative recombination centres. The fundamental and unavoidable radiative limit however guarantees a lower limit to the dark current. We shall see in subsequent sections that GaAs/Al_xGa_{1-x}As solar cells are dominated by Shockley-Hall-Read non-radiative recombination mentioned in section 2.2.3.

We have seen that the the saturation current contains an exponential bandgap dependence of the form $J_{01} \sim e^{-E_g/k_B T}$ for the ideal diode.

The dependence of J_{sc} on E_g is more complex. Experimental and theoretical studies (see chapters 3 and 8) however show that it decreases with increasing bandgap. This can be partly explained by the change in absorption. An increase in bandgap moves the absorption edge to higher energies and decreases the absorption coefficient above that threshold (see equations 2.18 and 2.19). The direct result is a reduction in minority carrier generation and therefore a smaller light current. This decrease however is weaker in character and magnitude than the

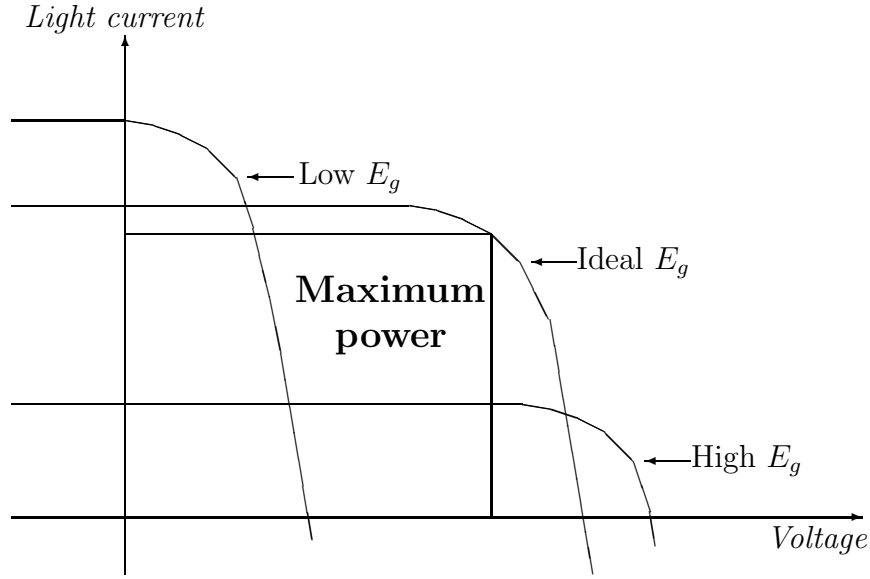


Figure 2.7: Light currents of solar cells with low and high bandgaps under similar illumination, showing the compromise between voltage and current. Also shown is an optimum design with a manifestly greater maximum power rectangle.

exponential dependence of the saturation current. The form of the V_{oc} therefore reduces to

$$V_{oc} \sim E_g \ln(J_{sc}) \quad (2.43)$$

A compromise therefore exists between the high bandgap requirement for a high V_{oc} and the low bandgap for a high J_{sc} , as illustrated in figure 2.7.

Limiting efficiencies for solar cells as a function of bandgap have been calculated by Henry [9]. The figures quoted are for the AM1.5d standard solar spectrum. This spectrum corresponds to direct sunlight at noon at a latitude of 48° . Other standards include the AM0 spectrum, which is sunlight without any atmospheric absorption.

An optimum of 30.6% reported by Henry for materials with bandgaps in the region of 1.35eV, which is near to the GaAs bandgap (1.424eV) for direct semiconductors, and to Si (1.12eV) for indirect materials. Higher efficiencies can be achieved by concentrating the incident light, which increases both the short circuit current and the open circuit voltage and increases the maximum efficiency to about 37.2%. The concentrator approach is limited by cell heating under the concentrated light. The increased operating temperature increases the

dark current, thereby reducing the open circuit voltage. Cells for concentration must therefore be designed with this effect in mind, or cooled.

Cells for concentrator applications must also be designed with a much lower series resistance, because of the higher current densities. Although cell resistances can be reduced by increasing the doping, this leads to a reduced minority carrier mobility because of the increased number of scattering centres.

Cells with efficiencies in the high 20's have been achieved in practice. Standard tabulations of world record solar cell efficiencies under AM1.5 illumination published by Green [11] quote the best GaAs solar cell as having an efficiency of $\sim 25\%$, and $\sim 24\%$ for Si. Laboratory cells are therefore close to achieving the fundamental efficiency limits, and increasingly complex designs are necessary to achieve higher efficiencies in single bandgap systems.

Higher efficiency designs however, which are not subject to the same efficiency limits as single band-gap solar cells, have been suggested. These are reviewed in the next section.

2.4.1 Higher Efficiency Designs

We have seen that the two fundamental factors limiting the maximum efficiency of single bandgap solar cells are the trade-off between V_{oc} and J_{sc} , and the related problem of thermalisation losses.

A solution to this trade-off is to combine several band gaps in a single solar cell. Different parts of the incident spectrum are absorbed in solar cell components with appropriate bandgaps. The component with the highest bandgap absorbs short wavelength light and delivers current at a high voltage. The cell with the lowest bandgap absorbs long wavelength light and operates at a lower voltage. The operational principles of the component cells remain those of single bandgap cells. The combination of the different bandgaps however reduces thermalisation losses, resulting in higher efficiency limits. This concept is known as the rainbow or cascade cell. Henry [9] predicts a maximum theoretical efficiency of around 75%.

Unfortunately, this design suffers from serious technological problems. If the cells are not connected in series, the output voltage is that of the cell with the lowest bandgap. On the other hand, connection in series requires that the current output of all the components be equal, because the output current of the cell will be that of the worst component.

Finally, series connection of cells is technologically difficult. It can be achieved at high cost in complex electrical connections, or during growth by the incorporation of tunnel junctions.

A simplified approach is the tandem cell. This exploits the same principle as the rainbow cell but restricts the design to two materials, thereby simplifying the current matching and electrical connection problems. Henry [9] predicts a fundamental efficiency for this system of 50%. A recent indium-gallium-phosphide/gallium arsenide tandem cell reported by Bertness [10] has achieved a record efficiency of 29.5% in AM1.5g (global) illumination.

2.5 Quantum Well Solar Cells

In previous sections we have described the operating principle of the photovoltaic effect and given an overview of fundamental loss mechanisms. We have reviewed a number of higher efficiency designs which can minimise these losses and lead to higher efficiencies.

We now present the main design studied in this thesis, which is the quantum well solar cell (QWSC), first suggested by Barnham [12]. The QWSC is a p - i - n cell with quantum wells grown in the intrinsic region. This cell is similar to tandem cells because it contains material with two different bandgaps.

Figure 2.8 shows a schematic of the QWSC. The structure contains two bandgaps E_g and E_a which are the barrier bandgap and quantum well bandgap respectively. The material behaves like bulk material for electron and hole energies greater than E_g and like a quantum well or superlattice states for energies below E_g .

For incident photons with energies greater than E_g , the QWSC operates like

a conventional single bandgap p - i - n cell.

Photons with energies between E_g and E_a however are absorbed in the quantum well states. Once excited into well states, they can recombine radiatively or non radiatively or escape from the well. The escape mechanisms are thermionic emission into a bulk state, tunnelling, or a combination of the two. Experimental and theoretical studies of this system by Nelson [13] have shown that the escape probability from GaAs quantum wells embedded in $\text{Al}_x\text{Ga}_{1-x}\text{As}$ with a composition of 34% is about 100% at room temperatures. This very high escape probability is seen even when the field across the quantum well is low. Thermionic emission therefore is sufficient to ensure high carrier escape probabilities from the wells at room temperatures.

Further work by Barnham *et al.* [14] has shown that the output voltage is greater than would be expected from a single junction cell with the quantum well bandgap E_a . This has been observed in three different materials systems. In the $\text{Al}_x\text{Ga}_{1-x}\text{As}$ system, this work showed that increasing barrier bandgaps E_g give increased voltage enhancements over the V_{oc} expected from a single bandgap cell with the quantum well effective bandgap E_a .

The QWSC design therefore departs from the analysis used by Henry [9] in his analysis of the fundamental efficiency limit. Unlike the separate components of a single bandgap cell, the QWSC operates in a physically different way to single bandgap cells because of the minority carrier escape from the quantum wells. Since it is in principle capable of generating the same photocurrent as a single bandgap cell with a higher voltage, the design has a higher fundamental efficiency limit than a single bandgap cell.

The fundamental efficiency limits of QWSCs are not yet clearly understood. The review article by Nelson [15] gives an overview of the subject.

2.6 The QWSC in the AlGaAs System

Work by Paxman [8] has demonstrated efficient carrier escape from QWSC structures in $\text{Al}_x\text{Ga}_{1-x}\text{As}$ with $x \simeq 30\%$. This resulted in a sample grown by Tom

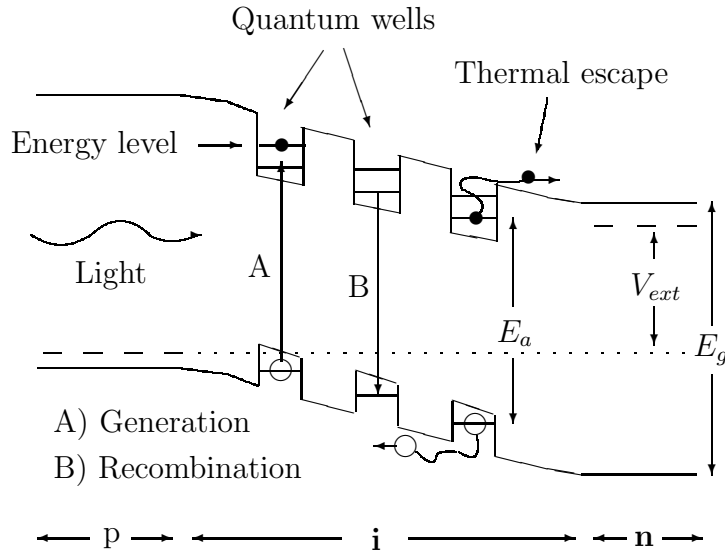


Figure 2.8: Schematic QWSC structure, absorption, recombination and escape mechanisms

Foxon at Phillips Laboratories, Redhill, which was 14.2% efficient in AM1.5. This sample showed a good V_{oc} of 1.07V, and a fill factor $FF = 77\%$. More detail concerning optimisations carried out in this work will be given in chapter 5.

The work by Paxman however showed scope for improvement in the J_{sc} of QWSCs in $Al_xGa_{1-x}As$. The advantages of this material include extensive characterisation and a material which is lattice matched for compositions ranging from GaAs to AlAs. The lattice spacing in GaAs and AlAs is only different by about 0.14% according to Adachi [16].

The material however suffers from poor transport characteristics. As we shall see in chapter 4, minority carrier transport is poor, and the J_{sc} of single bandgap $Al_xGa_{1-x}As$ cells decreases rapidly with increasing aluminium composition x .

We conclude that QWSCs in the $Al_xGa_{1-x}As$ system mainly suffer from poor minority carrier characteristics, which result in a low J_{sc} . Work presented in further chapters will address this problem with theoretical and experimental analysis of design changes made to the basic QWSC design.

2.7 Conclusions

This chapter has reviewed the operating principles of solar cells and defined the main parameters allowing characterisation of their performance.

We have seen that single bandgap solar cells are limited to efficiencies in unconcentrated sunlight of about 30% by fundamental loss mechanisms. Although designs such as the cascade cell and variations on this design are capable of reaching higher efficiencies, they are subject to complex technological problems because they combine two or more component solar cells in one design. Moreover, the approach represents a technological solution rather than one which introduces fundamental changes to solar cell operation.

The QWSC solar cell however is governed by physically different efficiency limits, because it has a V_{oc} which is higher than that of a single bandgap cell with the quantum well effective bandgap. This principle has been demonstrated in three different materials systems.

The $\text{Al}_x\text{Ga}_{1-x}\text{As}$ system shows a number of advantages for quantum well applications. Unfortunately, it suffers from poor minority carrier transport properties, which degrade with increasing aluminium fraction. This results in a poor short circuit current, and poor efficiencies for solar cells fabricated from this material.

We conclude that the voltage enhancement aspect of designing an efficient QWSC in the $\text{Al}_x\text{Ga}_{1-x}\text{As}$ cell has been demonstrated, but that the J_{sc} must be increased. The following chapters will present a theoretical and experimental analysis of this problem.

Chapter 3

Quantum efficiency and short circuit current models

3.1 Introduction

Optimisation of the short circuit current (J_{sc}) requires an understanding of the spectral response of the cell at zero applied bias. In this chapter we give a brief survey of previous theoretical work on such models, before going on to describe a model of the J_{sc} for GaAs/Al_xGa_{1-x}As QWSCs with position dependent transport and optical properties. Values of the materials parameters are discussed in chapter 4.

3.1.1 Review of Previous Work

Modelling of Al_xGa_{1-x}As solar cells has largely been confined to theoretical studies of cases which can be solved analytically. Hovel [69] gives a good review of solar cell physics, including discussions of a range of analytical and numerical models.

The theoretical model by Konagai [20] considers a p Al_xGa_{1-x}As - p GaAs n GaAs compositionally graded p layers grown epitaxially on GaAs. He does not consider the position dependence of the transport parameters, and uses an analytical expression for the absorption coefficient. The effect of the grade is

expressed via the quasi-electric minority carrier field it produces in the graded region. The field is taken as the gradient of the bandgap due to the compositional change, and is discussed in more detail in chapter 4. This work suggests that the grade is especially useful in reducing the minority carrier recombination at the surface of the cell. Efficiencies of the order of 20% are predicted under air mass zero (AM0).

Hutchby [21] has studied a similar design, but for an $n \text{ Al}_x\text{Ga}_{1-x}\text{As} - n \text{ GaAs} - p \text{ GaAs}$ design. This work is again purely theoretical, and makes similar assumptions by assuming that the minority carrier transport is constant. The absorption coefficient is a semi-empirical fit to data. The quasi-electric field in this model is again taken as proportional to the band-gap gradient, and the minority carrier transport parameters are assumed to be essentially independent of the aluminium composition. The theoretical efficiency in this case is 17.7% for an AM0 spectrum.

Sutherland [22] has presented a theoretical study which uses semi-empirical parameterisations to model the position dependence of the materials parameters. He finds good agreement with the earlier studies, predicting a peak efficiency of about 20% for a $n \text{ Al}_x\text{Ga}_{1-x}\text{As} - n \text{ GaAs} - p \text{ GaAs}$ design.

Hamaker [24] has presented a theoretical model of a $n - p$ and $p - n \text{ Al}_x\text{Ga}_{1-x}\text{As}$ cell with graded emitter layers. This is the most accurate model published to date, and uses semi-empirical parametrisations combined with data for the materials parameters. An optimisation in terms of doping and compositional profiles is included. The predicted efficiencies are similar to those predicted by the previous studies. Very little difference however is reported between the different designs studied.

Of the work mentioned above, the Hamaker [24] model is closest to the one we shall present in this chapter. We note however that the models, with the exception of Hamaker [24] have used analytical approximations for the materials parameters and generally only consider the position dependence of the optical parameters.

The models mentioned here are not compared with experimental data. In

the following sections we will present a model similar to that of Hamaker [24] but which is equipped to deal with quantum wells and compositional grading throughout the structure. The model furthermore will be designed to reproduce experimental data, and the relevant fitting parameters identified. The main methodology has been described by Connolly [25].

3.2 Preliminary definitions

We start by introducing the external quantum efficiency or QE. It describes the spectral efficiency of the cell independently of the particular incident spectrum and is defined as the probability of an incident photon of wavelength λ generating an electron-hole pair which contributes to the J_{sc} . It can be expressed as the ratio of the number of steady state current carriers J_{sc}/q collected under an illumination of wavelength λ to the number of photons incident on the top surface of the cell $F(\lambda)$ where q is the magnitude of the electronic charge.

$$QE(\lambda) = \frac{J_{sc}(\lambda)}{qF(\lambda)} \quad (3.1)$$

We also define the internal QE_{int} , which is defined in the same way, but where the flux F is replaced by the flux actually transmitted into the solar cell. The two differ only by a factor dependent on the surface reflectivity.

The model calculates the QE , which can then be used to predict the J_{sc} for a given cell design and illumination by multiplying the QE by the appropriate spectrum.

The wide range of QWSC and p - i - n solar cell designs considered in the characterisation and optimisation program requires a general approach to each part of the calculation. These designs include cells with compositionally graded neutral and space charge regions. These will be referred to as graded cells. Cells without these compositional changes are referred to as ungraded cells. We also consider cells which operate as Fabry-Perot cavities because they feature a mirror which is deposited on the back surface of the cell. These will be referred to as

mirror backed cells.

The first problem we consider in this chapter is the variation of the light intensity in the solar cell as a function of position, wavelength, and front and back surface reflectivities. The generation rate can then be calculated from the absorption coefficient and the light intensity at any particular position and wavelength.

We then describe the photocurrent calculation in the two cases of depleted space-charge regions and neutral regions. In a general p - i - n cell, the space-charge region is made up of the p depletion region, the nominally undoped i region, and the n region depletion layer. Under the depletion approximation described below, the photocurrent calculation reduces to an integral of the generation rate over the depletion region and wavelength.

The second case deals with the photocurrent from the electrostatically neutral sections of the n and p layers. Solutions to the resulting transport equations are first discussed for ungraded cells where materials parameters are constant, and an analytical solution can be found.

In the case of graded cells however an analytical solution cannot in general be found and the transport equations must be solved numerically. A standard difference method for this case is presented in the final part of the chapter.

3.3 Calculation of light intensity in a QSWC

3.3.1 Definitions

In this section we derive the light intensity in a solar cell of total thickness d and in which the optical parameters may be position dependent. We define the optical parameters required to calculate the light intensity for cells where interference effects may be significant. We consider only the normal incidence case. A comprehensive discussion is given in Macleod [35].

The first phenomenon experienced by a beam of light of intensity \mathcal{I}_i which is incident on a solar cell is reflection. We quantify this by the front surface

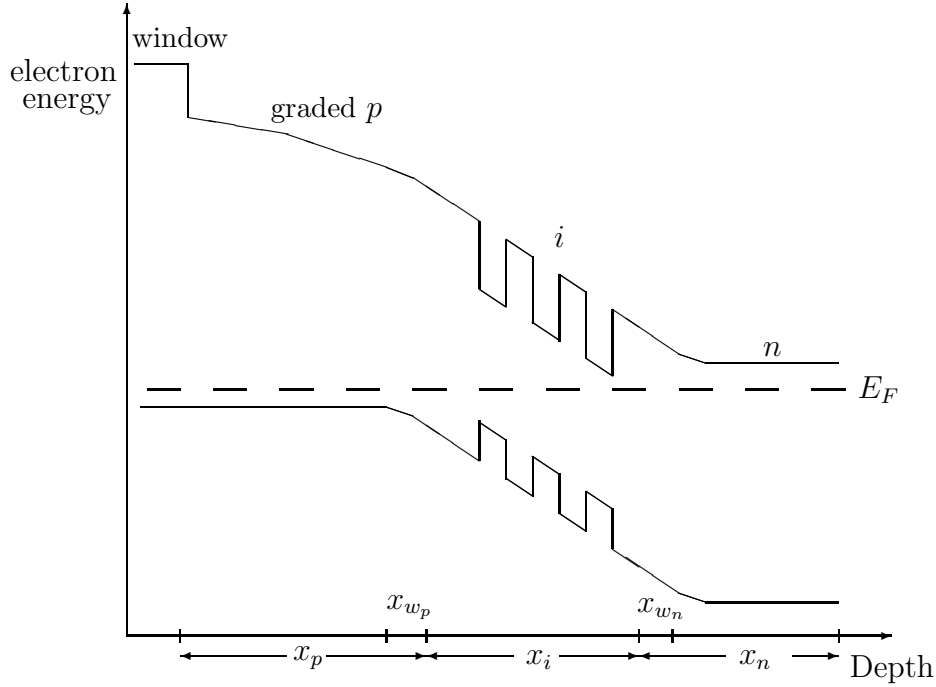


Figure 3.1: Example generalised QWSC band diagramme, including position dependent bandgap in the p type layer and high aluminium fraction window layer

reflectivity R which is the fraction of light intensity of wavelength λ reflected by that surface.

For graded material the absorption coefficient varies with distance. In this case the intensity at a particular point depends on the integral of the absorption which the light has suffered up to that point, minus the fraction of light reflected at the front surface.

$$\mathcal{I}(x, \lambda) = \mathcal{I}_i(\lambda)(1 - R(\lambda))e^{\int_0^x \alpha(x', \lambda) dx'} \quad (3.2)$$

This expression allows us to calculate the light intensity for cases where light only makes one pass. By this we mean that the amount of light internally reflected from the back surface of the cell is negligible.

This is not the case for cells which are coated on the back surface with a mirror and which leave a significant amount of light unabsorbed on the first pass. In this case, successive reflected beams suffer phase changes with distance and upon reflection at the front and back surfaces. The superposition of beams of light with different phases leads to interference phenomena. To take these effects into account, we must derive the intensity from the complex amplitude of the

light. The electric field component of the light \mathcal{E} is a convenient quantity to use and we refer to it as the amplitude for brevity. It is of the same form as \mathcal{I} and is characterised by a complex decay constant k . The real part of k characterises the exponential decrease in electric field strength due to light absorption, and the imaginary part reflects the change in phase of the electric field with distance. \mathcal{E} is then

$$\mathcal{E}(x, \lambda) = \mathcal{E}_0(\lambda) e^{-\int_0^x k(x', \lambda) dx'} \quad (3.3)$$

where \mathcal{E}_0 is the amplitude at position zero.

The light intensity \mathcal{I} is proportional the product of the electric field amplitude and its complex conjugate [35]:

$$\mathcal{I}(x, \lambda) = \epsilon v \mathcal{E} \mathcal{E}^* \quad (3.4)$$

where \mathcal{E}^* denotes complex conjugate of \mathcal{E} , and ϵ and v are respectively the permittivity and the speed of light at position x .

\mathcal{E}_0 is related to the incident flux \mathcal{I}_i by substituting the value of $\mathcal{I}(0, \lambda)$ from equation 3.2 into equation 3.4. Since the phase changes in the cell are all relative to the phase of the incident light, we choose to set this incident phase to zero. \mathcal{E}_0 is then real and of the form

$$\mathcal{E}_0 = \sqrt{\frac{(1 - R)\mathcal{I}_i}{\epsilon v}} \quad (3.5)$$

The total amplitude \mathcal{E} is found by summing the amplitude contributions from successive reflections \mathcal{E}_j , where i is the order of reflection.

$$\mathcal{E}(x, \lambda) = \mathcal{E}_0 \sum_{j=1}^{\infty} \mathcal{E}_j(x, \lambda) \quad (3.6)$$

The dimensionless components \mathcal{E}_j are a measure of the amplitude of the j^{th} amplitude component relative to the amplitude \mathcal{E}_0 transmitted through the front surface of the cell, and are calculated below.

Equations 3.6 and 3.4 together define the intensity as a function of distance

and wavelength in terms of the amplitude components \mathcal{E}_0 .

3.3.2 Phase and reflectance

Before calculating the components \mathcal{E}_j we must relate the reflectivity and absorption coefficient to the corresponding quantities for the amplitude. Both of these can be derived from inspection of equation 3.4.

When a normally incident beam of light of intensity \mathcal{I} is internally reflected, the intensity is reduced by a factor R . Consistency with equation 3.4 demands that the corresponding amplitude should be modified by a factor \sqrt{R} . A factor $e^{i\psi}$ describes the phase change upon reflection at the back surface, where $i = \sqrt{-1}$ and ψ is the phase change. The complex reflectance is therefore the square root of the R multiplied by the ψ .

$$r = e^{i\psi} \sqrt{R} \quad (3.7)$$

The relationship between amplitude and intensity in equation 3.4 together with equations 3.2 and 3.3 shows us that the real part of k is simply half the absorption coefficient α . However, it is a complex quantity and may have an associated phase.

The phase of an electromagnetic wave changes by a factor 2π over a distance of one wavelength. Furthermore, the wavelength of light in a medium with refractive index n is λ/n . The phase change is therefore simply the ratio $2\pi in/\lambda$. The phase change over a distance x will be the integral of this phase over distance.

The complex decay constant is then the sum of $\alpha/2$ and the phase

$$k(x, \lambda) = \frac{\alpha}{2} - \frac{2\pi in}{\lambda} \quad (3.8)$$

3.3.3 Generation Rate

We can now explicitly write down the successive terms in the sum of amplitudes as a function of position x . The first is the simply the transmitted beam and

starts with the relative amplitude of 1.

$$\mathcal{E}_1(x) = e^{-\int_0^x k dx'} \quad (3.9)$$

The initial amplitude of the second beam is equal to the limit of \mathcal{E}_1 at the back mirror, but with a reflectance factor. We introduce the back surface reflectance r_b and it's associated phase change ψ_b which is related to the back surface internal reflectivity R_b as outlined above. The amplitude of the second beam is then dependent on an integral over $-dx$ from the back surface d to the position x . This is the same as integrating forwards from x to d over $+dx$. Component \mathcal{E}_2 is then

$$\mathcal{E}_2(x) = e^{-\int_0^d k dx'} r_b e^{-\int_x^d k(x') dx'} \quad (3.10)$$

If r_f is the front surface internal reflectance, with associated phase ψ_f and reflectivity R_f , subsequent reflections take the form

$$\begin{aligned} \mathcal{E}_3(x) &= e^{-2\int_0^d k dx'} r_f r_b e^{-\int_0^x k(x') dx'} \\ \mathcal{E}_4(x) &= e^{-3\int_0^d k dx'} r_f r_b^2 e^{-\int_x^d k(x') dx'} \\ \mathcal{E}_5(x) &= \dots \end{aligned} \quad (3.11)$$

Rewriting the even reflections in terms of an integral from 0 to d minus an integral from 0 to x and factorising by the extra term in r_b , we obtain two geometric series which differ only by a factor relating to the amplitude attenuation over one pass and the back surface reflectance. It has the limit

$$\mathcal{E} = \mathcal{E}_0 \left[e^{-\int_0^x k dx'} + \frac{r_b e^{-2\int_0^d k dx'}}{e^{-\int_0^x k dx'}} \right] \times \left[\frac{1}{1 - r_f r_b e^{-2\int_0^d k dx'}} \right] \quad (3.12)$$

The intensity in the solar cell can be written independently of the factor ϵv as follows

$$\mathcal{I}(x, \lambda) = \mathcal{I}_i (1 - R) \left(\frac{\mathcal{E} \mathcal{E}^*}{\mathcal{E}_0 \mathcal{E}_0^*} \right) \quad (3.13)$$

We emphasize here that this treatment consitutes a first approximation to the problem, since it does not consider the internal reflections taking place at the

quantum well interfaces. The reflectivity at these surfaces, however, is not great, since the change in refractive index between GaAs and $\text{Al}_x\text{Ga}_{1-x}\text{As}$ is not large for the barrier compositions considered. A brief calculation using optical parameters reviewed in chapter 4 indicates that the reflectivity in the worst case of a 45% aluminium barrier is only 0.2%. On the other hand, a large number of wells may make this effect significant. Further discussion of this point is given with respect to experimental data in chapter 8.

The generation rate G is then readily given by the product of α and I as follows

$$G(x, \lambda) = \alpha(x, \lambda)\mathcal{I}(x, \lambda) \quad (3.14)$$

3.4 Photocurrent

Having derived an expression for the generation rate we now investigate the mechanisms which transform these photo-generated carriers into a useful electric current.

In general, the depleted or space-charge region of the QWSC includes the p depletion region of width x_{w_p} (see figure 3.1), the intrinsically doped i region (width x_i), and the n region depletion layer (width x_{w_n}). We have seen in section 2.3 that the i region may not be fully depleted either if the forward applied bias is larger than the magnitude of V_{bi} , or if the background doping level is high. In this case, the electric field drops to zero within the intrinsic region.

If, however, the background doping level is low, a field is maintained across the i region in the moderate forward bias regime and carrier transport is drift dominated. Under the depletion approximation described below, carrier recombination in the space-charge region is negligible and charge collection efficiencies are 100%.

In the neutral window, p and n regions, transport is dominated by diffusion and recombination is not negligible. The photocurrent from these layers is found by solving minority carrier transport equations. Previous work by Braun [48] has shown that the high band-gap window layer does not contribute a measurable

photocurrent and may be treated simply as a non-contributing surface absorber.

In the following sections the photocurrent calculations for space charge and neutral regions are discussed for the general case of a p - i - n structure with position dependent parameters. We then examine the simplified case of an ungraded structure and the manner in which certain parameters can be determined from this simplified case. We then develop a numerical method to solve the more general graded case.

3.5 Intrinsic region photocurrent

Calculation of the photocurrent J_i from depletion layer is based on the depletion approximation. This assumes that minority carriers generated or injected into the i region are swept across it to the boundary with the depletion edge where they become majority carriers. That is, electrons are swept towards the n interface, whilst holes are swept to the p interface with no loss. This is a good approximation for cells in which a field is maintained across the i region. For cells with either compensated or low background doping, this condition is maintained into moderate forward bias. J_i can then be found from the generation rate.

The photocurrent contribution from the quantum wells is calculated assuming an escape efficiency of 100%. Once the carriers have escaped from the wells, they behave like other minority carriers. Previous work by Nelson [13] has shown this to be true for GaAs wells in $\text{Al}_x\text{Ga}_{1-x}\text{As}$ with an aluminium fraction of 30%.

The photocurrent density J_i from the space charge region is then simply given by the integral of the generation rate

$$J_i(\lambda) = \int_{x_p - x_{wp}}^{x_p + x_i + x_{wn}} G(x, \lambda) dx \quad (3.15)$$

Although in general an analytical form for J_i can only be found for ungraded solar cells, the calculation is identical for the graded case. The quantum well absorption coefficient is described by Paxman [49].

3.6 *p* and *n* Region Contributions

The photocurrent from neutral *p* and *n* regions is found from current and continuity relations outlined below. Since the method in both cases is identical, the following discussion concentrates on the *p* for clarity.

3.6.1 Drift and Diffusion Currents

Minority carrier currents can be caused by drift or diffusion. The former results from the acceleration of carriers in an electric field, whereas the latter is the consequence of a carrier concentration gradient. In the low injection limit and for moderate electric fields, the net current flowing at depth x in the *p* layer $j_p(x)$ is the sum of these two currents [4].

$$j_p(x) = q\mu_n(x)E(x)n_p(x) + qD_n(x)\frac{dn_p}{dx} \quad (3.16)$$

where μ_n is the minority electron mobility, D_n the electron diffusivity and E the quasi-electric field. These parameters are position dependent in the general case. We note here that some workers use the terminology j_p as the minority hole current in the *n* layer. We choose to define it in this way in order to keep the same subscript between the excess minority carrier concentration n_p and the corresponding current j_p .

The total minority electron carrier concentration n_p is defined as the sum of the equilibrium carrier concentration n_{p0} and the excess minority carrier concentration n as follows:

$$n_p = n_{p0} + n \quad (3.17)$$

No net current flows in equilibrium, and equation 3.16 gives

$$q\mu_n(x)E(x)n_{p0}(x) + qD_n(x)\frac{dn_{p0}}{dx} = 0 \quad (3.18)$$

Subtracting 3.18 from 3.16, we obtain

$$j_p(x) = q^2 \frac{D_n(x)E(x)}{k_B T} n(x) + qD_n(x) \frac{dn}{dx} \quad (3.19)$$

where we have used the Einstein relation $\mu_n = qD_n/k_B T$. This is valid for equilibrium [17] where the diffusion current due to the electron and hole carrier concentration gradients can be equated with the drift current flowing in the opposite direction. We assume that in the low field diffusion dominated regime the mobility and diffusion coefficient are equal to their equilibrium values. This is confirmed by low field mobility measurements by Walukiewicz [18]

Equation 3.19 allows us to calculate the photocurrent in terms of the excess minority carrier concentration n only, because the intrinsic carrier concentration gives no net current.

The total current contribution of the p layer is the current injected from the p layer into the i region. In the depletion approximation, n is zero at the edge of the space charge. In this case this is at the junction between the electrostatically neutral section of the p region and the p depletion layer. Equation 3.19 then becomes

$$J_p = \left(qD_n \frac{dn}{dx} \right)_{x=x_{wp}} \quad (3.20)$$

Calculating J_p therefore reduces to the problem of determining the gradient dn/dx at the depletion edge from the current and continuity equations.

3.6.2 Current and Continuity

A minority electron in the p layer can be generated, drift, diffuse or recombine with a hole. The rate of change of current as a function of position is given by the difference between generation and recombination rates:

$$\frac{dJ_p}{dx} = -qG(x, \lambda) + q \frac{n}{\tau} \quad (3.21)$$

In $\text{Al}_x\text{Ga}_{1-x}\text{As}$ the recombination time τ is dominated by non-radiative Shockley-Read-Hall recombination mentioned earlier in section 2.2.3. If we differentiate equation 3.19 and substitute for τ using $L_n = \sqrt{\tau D_n}$, we obtain the following differential equation after dividing throughout by D_n

$$\frac{d^2 n}{dx^2} + \left(\frac{qE}{k_B T} + \frac{D'_n}{D_n} \right) \frac{dn}{dx} + \left(\frac{qE D'_n}{D_n k_B T} + \frac{qE'}{k_B T} - L_n^{-2} \right) n + \frac{G}{D_n} = 0 \quad (3.22)$$

where $D'_n = dD_n/dx$. In order to clarify subsequent discussions, we re-write equation 3.22 as follows

$$\frac{d^2 n}{dx^2} + b(x) \frac{dn}{dx} + c(x)n + g = 0 \quad (3.23)$$

where functions b and c and the generation function g are defined by comparison with equation 3.22. Given suitable boundary conditions, equation 3.23 defines the minority carrier density as a function of position.

3.6.3 Transport Equations for n Layers

For completeness we briefly indicate the differences between the transport equations for p layer and n layers. For an n type semiconductor, the minority carriers are holes with a positive charge of q . The drift current takes the same form, but the diffusion current changes sign. Equation 3.16 becomes

$$j_n(x) = q\mu_n(x)E(x)p_n(x) - qD_p(x)\frac{dp_n}{dx} \quad (3.24)$$

The differential equation 3.22 however does not change except the the hole diffusion length L_p substituted for L_n , and D_p and p_n are substituted for D_n and n_p respectively.

Since the solution to the problem is identical in both cases, we shall not consider the n layer contribution explicitly in the following sections in order to avoid unnecessary repetition.

3.6.4 General Analytical Solution

Equation 3.23 is an inhomogeneous differential equation which has a standard solution described for example by Boas [26]. A study of this method however increases our understanding of the influence of the parameters governing the behaviour of the solution. In the dark, equation 3.23 reduces to

$$\frac{d^2 n}{dx^2} + b(x)\frac{dn}{dx} + c(x)n = 0 \quad (3.25)$$

A general solution to this homogeneous second order linear differential equation exists of the form

$$n_{dark} = a_1 U_1(x) + a_2 U_2(x) \quad (3.26)$$

where a_1 and a_2 are constants fixed by two boundary conditions and U_1, U_2 are functions of position.

Following the methods outlined in Boas [26], we postulate that the solution to the inhomogeneous case 3.23 is of the form

$$U_3 = A(x)U_1 + B(x)U_2 \quad (3.27)$$

where A and B are two arbitrary functions which can be found with standard solution methods, and take the form

$$\begin{aligned} A(x) &= \int^x \frac{gU_2}{U_1U_2' - U_1'U_2} dx' \\ B(x) &= - \int^x \frac{gU_1}{U_1U_2' - U_1'U_2} dx' \end{aligned} \quad (3.28)$$

These two functions together with the dark solution form the particular integral solution

$$U_3 = U_1 \int^x \frac{gU_2}{U_1U_2' - U_1'U_2} dx' - U_2 \int^x \frac{gU_1}{U_1U_2' - U_1'U_2} dx' \quad (3.29)$$

The general solution is then

$$n(x) = a_1 U_1 + a_2 U_2 + U_3 \quad (3.30)$$

The constants a_1 and a_2 are found as described in the next section. In general, analytical solutions cannot be found and we resort to numerical methods of solving equation 3.23 described below.

3.6.5 Boundary Conditions

The first boundary condition is that the surface current flow is equal to a recombination current characterised by a recombination velocity S_n

$$J_p(0) = qS_n n(0) \quad (3.31)$$

The surface recombination may be either due to interface recombination centres at an abrupt junction between layers with different aluminium compositions or may be a surface recombination associated with defects present at the interface between the semiconductor and the air (Hovel [69]).

Real devices may depart from this behaviour because of increased recombination at the front contacts [19] or damage to the front surface. Both these effects may lead to very high recombination velocities, and a possible reduction of the p layer thickness. This is discussed further in section 4.4.5.

Substituting equation 3.19 for the current and the general solution 3.30 for n into the previous expression we obtain

$$\begin{aligned} & a_1 \left(D_n U_1'(0) + \left(\frac{qD_n E}{k_B T} - S_n \right) U_1(0) \right) \\ & + a_2 \left(D_n U_2'(0) + \left(\frac{qD_n E}{k_B T} - S_n \right) U_2(0) \right) \\ & = U_3(0) \left(S_n - \frac{qD_n E}{k_B T} - D_n U_3'(0) \right) \end{aligned} \quad (3.32)$$

The second boundary condition states that the minority carrier concentration at the boundary with the depletion region is zero, according to the depletion approximation

$$n_{x_{wp}} = 0 \quad (3.33)$$

Substituting for n from equation 3.30 we obtain

$$a_1 U_1(x_{w_p}) + a_2 U_2(x_{w_p}) = -U_3(x_{w_p}) \quad (3.34)$$

The constants a_1 and a_2 are then obtained from the two coupled equations 3.32 and 3.34.

Two different cases requiring two methods of solving equation 3.23 are presented in the following sections. The first covers the case of an ungraded solar cell, for which there is no electric field in the neutral regions and materials parameters can be assumed to be constant. A hypothetical cell with constant materials parameters but with an effective electric field applying only to minority carriers is examined as a preliminary to the general compositionally varying case.

The second case is that of compositionally graded QWSCs, for which all the parameters in equation 3.23 are position dependent. The same boundary conditions are applicable in both cases.

3.7 Constant Transport Parameters

In this section we consider the p layer QE of ungraded cells with and without effective fields. In this case, the parameters L_n and D_n are constant. The original work is described in the recent review by Nelson [15].

3.7.1 Zero Field

For a layer with a zero field, a trial solution e^{kx} yields the functions

$$U_1 = e^{x/L_n} \quad (3.35)$$

$$U_1 = e^{-x/L_n} \quad (3.36)$$

Constants a_1 and a_2 are obtained from equations 3.32 and 3.34, thereby defining the minority carrier profile. The photocurrent from the p layer is then found from equation 3.20.

Appendix A gives more detail, and shows that the photocurrent for these ungraded structures is only weakly dependent on the diffusion coefficient and the recombination velocity if

$$\frac{1}{L_n} \gg \frac{S_n}{D_n} \quad (3.37)$$

The appendix further shows that the QE in the limit of $L_n < x_{wp}$ near the band edge is well approximated by

$$QE \simeq L_n \alpha e^{-\alpha x_{wp}} \quad (3.38)$$

This result agrees with a brief treatment given by Ludowise [27], and reviewed in more detail by Hovel [69]. The $\text{Al}_x\text{Ga}_{1-x}\text{As}$ structures we will study generally obey this limit for acceptable p layer thicknesses. The photocurrent near the band edge is dominated by p and i contributions. Since, as we have seen, the i region photocurrent is well understood, L_n can be estimated by modelling the QE in this wavelength range.

Appendix A further shows that the QE at short wavelengths remains sensitive to the recombination velocity, and tends to a limit determined primarily by the surface recombination velocity and the absorption coefficient. For diffusion lengths which are of the order or greater than the p layer thickness, a simple limit is found, depending solely on absorption coefficient and recombination velocity. Since the absorption coefficient varies slowly at such wavelengths, the overall QE becomes weakly dependent on wavelength. This behaviour is primarily observed in solar cells made from materials with high absorption coefficients at short wavelengths, such as GaAs.

3.7.2 Non Zero Effective Fields

A brief examination of the hypothetical case of an ungraded cell with electric fields present in the neutral regions is useful here. Detail is again provided in appendix A. We now define the effective field \mathcal{E}_f due to the compositional grade,

in units of per metre, as follows:

$$\mathcal{E}_f = \frac{qE}{k_B T} \quad (3.39)$$

A trial solution for cells with $\mathcal{E}_f \neq 0$ yields the solutions

$$U_1 = e^{k_1 x} \quad (3.40)$$

$$U_2 = e^{k_2 x} \quad (3.41)$$

with

$$k_1 = +\sqrt{\mathcal{E}_f^2 + L^{-2}} - \mathcal{E}_f \quad (3.42)$$

$$k_2 = -\sqrt{\mathcal{E}_f^2 + L^{-2}} - \mathcal{E}_f \quad (3.43)$$

Since $\mathcal{E}_f < 0$, parameter k_1 tends to $2|\mathcal{E}_f|$ for large fields, whereas k_2 tends to zero. The exponentially growing solution is therefore favoured, and the resulting minority carrier distribution shifted in a positive direction towards the depletion layer, increasing minority carrier collection.

We now examine the effect of the field on the surface boundary condition. Appendix A shows that the condition of 3.37 is replaced by

$$|\mathcal{E}_f| \gg \frac{S_n}{D_n} \quad (3.44)$$

In this limit, the QE is insensitive to the surface boundary condition and the surface recombination velocity in particular. This limit is readily achieved even for high surface recombination velocities. We shall see in section 4 that it may fail however if the recombination velocity is unusually high. This may occur if recombination at the contacts is large, or if the surface quality is poor.

We conclude however that the presence of a field renders the QE relatively insensitive to the surface recombination.

We shall see in subsequent sections that the real picture is somewhat less clear in the case of a full numerical solution to equation 3.22. We shall see however in

the modelling section that cells with electric fields are much less sensitive to the magnitude of the surface recombination velocity, as carriers in a well designed cell tend to diffuse in the direction of the greater effective diffusion length.

3.8 Graded QWSCs and Numerical Solutions

Analytical solutions to equation 3.30 generally cannot be found if the parameters b and c are position dependent. We now develop a numerical scheme to solve equation 3.23 in this case.

We express the first and second differentials of n using standard centred differencing described by Potter [30] as follows:

$$\begin{aligned} n'_k &= \frac{1}{2\Delta}(n_{k+1} - n_{k-1}) \\ n''_k &= \frac{1}{\Delta^2}(n_{k+1} - 2n_k + n_{k-1}) \end{aligned} \quad (3.45)$$

where k is the position index and Δ the grid spacing of a one dimensional grid of length N . Substituting these expressions into equation 3.23 we obtain

$$n_{k-1}\left(\frac{1}{\Delta^2} - \frac{b_k}{2\Delta}\right) + n_k\left(c_k - \frac{2}{\Delta^2}\right) + n_{k+1}\left(\frac{1}{\Delta^2} + \frac{b_k}{2\Delta}\right) = -g_k \quad (3.46)$$

The surface boundary condition equation 3.31 can be written as

$$n_1\left(\frac{qE}{k_B T} - \frac{S_n}{D_n} - \frac{1}{\Delta}\right) + \left(\frac{n_2}{\Delta}\right) = 0 \quad (3.47)$$

The second boundary condition equation 3.33 becomes

$$n_N = 0 \quad (3.48)$$

Equations 3.46, 3.47 and 3.48 can be expressed as the following matrix equation

$$MN = G \quad (3.49)$$

This equation is then solved by standard Gaussian elimination with backsubsti-

tution. A good review of this technique is given in Press [29]

Although more complex methods were investigated, this simple method was chosen because trials with a number of different numerical schemes shows that this method is preferable to methods which are nominally quicker and avoid explicitly calculating the inverse matrix. This is mainly because the matrix M need only be inverted once, but is typically used about six hundred times to cover the wavelength range we are considering. For the matrices we consider, which may have a dimension of a few hundreds, we observe that the calculations involved in solving equation 3.49 are the most time consuming.

3.8.1 Surface Boundary Condition in Compositionally Graded Cells

The surface boundary condition is expressed by the topmost row of matrix M , and is identical to the boundary condition in the analytical case. We conclude that compositionally graded designs remain insensitive to the surface recombination velocity.

More detailed conclusions regarding the general behaviour of the QE of such cells are best illustrated by numerical calculation, and are investigated further in chapter 5.

3.8.2 Numerical Accuracy

To determine the numerical accuracy of the scheme we express the minority carrier concentration as a Fourier series

$$n = \sum_{j=0}^{\infty} a_j e^{ik_j x} \quad (3.50)$$

where k_j is the wavevector of the j^{th} mode. The exact differential of an arbitrary mode e^{ikx} is

$$n' = aikn \quad (3.51)$$

When we use our difference expression of 3.45 for the same differential we obtain

$$\begin{aligned} n' &= \frac{a}{2\Delta}(e^{ik(x+\Delta)} - e^{ik(x-\Delta)}) \\ &= \frac{an}{2\Delta}(2i \sin(k\Delta)) \end{aligned} \quad (3.52)$$

If we substitute the Taylor series expansion for the sine term this gives

$$\begin{aligned} n' &= \frac{ain}{2\Delta}(2k\Delta - \frac{(k\Delta)^3}{3} + O(k\Delta)^5) \\ &= aikn(1 - \frac{(k\Delta)^2}{6} + O(k\Delta)^4) \end{aligned} \quad (3.53)$$

where $O(k\Delta)^4$ refers to fourth order terms. A similar treatment for the second differential gives the analytical result

$$n'' = -ak^2n \quad (3.54)$$

whereas the numerical expression is

$$n'' = -ak^2n(1 - \frac{(k\Delta)^2}{24} + O(k\Delta)^5) \quad (3.55)$$

The error is given by the difference between the analytical expressions and the numerical result in both cases and depends on Δ^2 . This scheme is therefore second order accurate.

We further note that the error also depends on the square of the wavevector k and will increase rapidly as k becomes comparable with Δ . A large value of k is equivalent to a minority carrier density which is varying rapidly in space. We must therefore be careful of trusting the results if the composition changes very rapidly over a small distance, and this design is not suitable for neutral regions with sharp discontinuities in any of the material parameters. This is unlikely to cause problems since sharp interfaces are generally avoided in the neutral regions because of the increased interface recombination they cause.

3.8.3 Comparisons of Analytical and Numerical Solutions

In this section we briefly consider the stability of the numerical solution. We then continue to compare numerical and analytical calculation methods in order to test the numerical method.

Stability of Boundary Value Problems

Unlike initial value problems, boundary value calculations are not prone to numerical instability. This is because the solution is constrained at the two end points.

However, rounding errors in the manipulation of large matrices can grow and swamp the real solution. However, this is rarely a problem in sparse matrices such as ours where the number of operations is relatively low. Furthermore, Potter [30] states that the use of double precision can circumvent this problem for medium size matrices where N is of the order of some hundreds.

Furthermore, Gaussian elimination with back-substitution is more stable than many more complex methods [29].

Zero Field

In this section the results of the numerical model are compared to those of the analytical model in two cases where this is possible.

Figure 3.2 shows a comparison of the internal p layer QE spectra predicted by analytical and numerical methods for an typical highly doped p layer which is $0.15\mu m$ thick and has a composition of 30% aluminium. The calculation uses a grid spacing of 400 points for the p layer.

We note that the numerical method slightly underestimates the QE at short wavelengths. This is a result of increased numerical inaccuracy due to increased position dependence of both generation rate and minority carrier concentration.

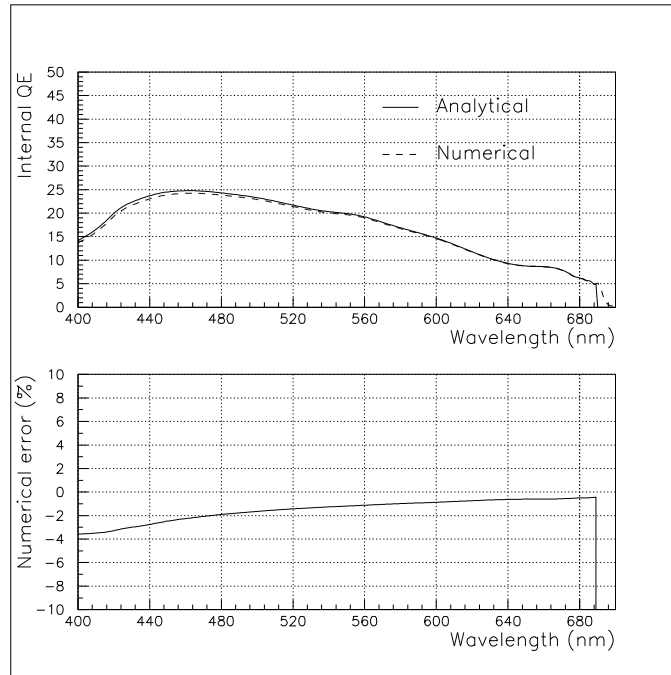


Figure 3.2: Numerical and analytical internal QE plots for an ungraded 30% aluminium QWSC

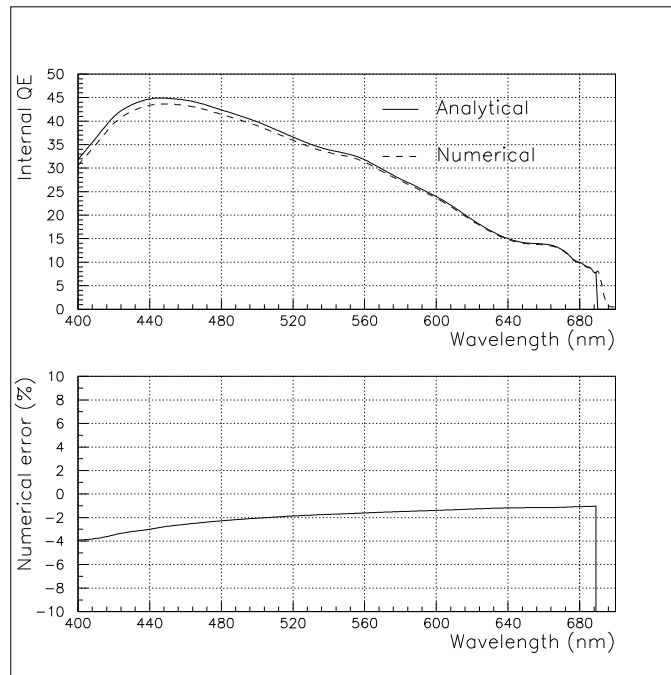


Figure 3.3: Numerical and analytical QE plots for an ungraded 30% aluminium QWSC with electric field

Cells With Fields

No analytical method exists for a graded p layer, making precise evaluation of the performance of the numerical model difficult. As a first approximation, we compare results for the hypothetical case of ungraded cells with an effective field in the neutral regions.

Figure 3.3 compares the analytical and numerical results for a QWSC identical to that of the previous subsection, but with an effective field of -10^6Vm^{-1} in the p layer. The results are again very similar, with the numerical model again underestimating the QE slightly at short wavelengths.

The error in the numerical case is marginally greater than in the ungraded case, but still amounts only about one percent in the predicted QE at short wavelengths. It is again weakly sensitive to the grid spacing.

Conclusions

For the general case of an graded structure, we have no analytical model model for comparison. Analysis of the closest approximation however shows an error which is about a fifth of the experimental uncertainty at short wavelengths. The model furthermore is relatively insensitive to the number of grid-points used.

We conclude that the principal source of modelling error lies in the physical assumptions underlying the model and in the values of physical parameters, rather than in the numerical method. This is investigated further by comparison with experimental data in chapter 8.

3.9 Conclusion

In this chapter we have described a method of calculating the light intensity for a solar cell with varying optical parameters and with or without multiple internal reflections for a normally incident spectrum.

Having calculated the generation rate from the light intensity, we have looked at methods of calculating the resulting photocurrent. These methods fall into

two broad categories. The first deals with ungraded cells where we find that an analytical solution to the minority carrier concentration exists. The QE in this case is only weakly dependent on the diffusion coefficient for low recombination velocity. We have found that it is possible to estimate the diffusion length by modelling the QE in cells subject to this limit.

Brief examination of the abstract case of an ungraded solar cell with effective fields in the neutral layers shows that such cells are significantly less sensitive to surface recombination.

This useful property is also true for compositionally varying cells. We have described a numerical scheme for calculating the QE of such structures. The second case, which deals with graded cells, requires a numerical solution method and a good understanding of the dependence of transport parameters on aluminium content.

Chapter 4

Model Parameters and Program Design

In this chapter we describe the way a QWSC is represented by the model. We then identify the main adjustable parameters used to fit experimental data. We give a review of the current state of knowledge of these and non-adjustable parameters used by the model.

4.1 Program design

The FORTRAN program SOLAL closely follows the progression outlined in section 3. The program design is modular and menu driven, and interfaces with the PAW graphics program. It calculates both analytical and numerical QE spectra.

The main design parameters are summarised in table 4.1. The anti-reflection (AR) coat is represented by a wavelength dependent reflectivity, which may be arbitrarily specified by the user. Three standard reflectivities are provided. These are a free GaAs surface, and two standard reflectivities based on data from Eindhoven and Sheffield. The latter two will be discussed in chapter 7.

Surface	GaAs reflectivity or SiN reflectivity or MgF:ZnS reflectivity or Measured reflectivity data
Non-contributing surface layers	Layer thicknesses
	Linear compositional profiles of the layers
	Number of layers
p and n layers	Layer thicknesses
	Arbitrary composition profile
	Constant doping
Bulk i region	Number of strips
	Thickness of strips
	Linear compositional profiles of strips
MQW i region	Total i region width
	Well width
	Barrier composition
	Number of wells

Table 4.1: List of the main QWSC growth and design parameters.

Sample structure

The solar cells are represented as a series of $\text{Al}_x\text{Ga}_{1-x}\text{As}$ layers which may have linearly varying aluminium composition. These are split into surface layers which do not contribute to the QE , and contributing p, n, and i layers. Most of our designs have a single surface layer, which is the $\text{Al}_x\text{Ga}_{1-x}\text{As}$ window.

The p layer can be subdivided into several strips, each with a linearly varying composition. The only recombination velocity included in the calculation is that between the AR coat or GaAs surface and the p layer. The doping however is assumed constant. Depletion widths are included in the calculation, and the effective aluminium fraction at the edge of the depletion width is readjusted in graded structures to match that at the edge of the calculated depletion width. The treatment for the n layer is identical, with the difference that the surface or interface recombination velocity is replaced by a back surface recombination velocity.

The i layer may be of two types. The first is a conventional i layer, which may be composed of a number of linearly graded strips. A constant background doping

Ungraded p	$\left. \begin{matrix} S_n \\ D_n \end{matrix} \right\}$	Recombination parameter $\mathcal{S} = S_n/D_n$
	Diffusion length L_n	
Graded p	$\left. \begin{matrix} S_n \\ D_n(x=0) \end{matrix} \right\}$	Recombination parameter $\mathcal{S} = S_n/D_n(x=0)$
	Diffusion length $L_n(x)$	
	Diffusivity $D_n(x)$	

Table 4.2: Transport parameters for the p layer required by the model

level is assumed throughout. The second type of i layer is one which contains quantum wells. This layer may not be compositionally graded except for the sharp interfaces between quantum wells and barriers. Details of the quantum well modelling parameters have been supplied by Paxman [49]. The parameters in this case are the total i region width, the barrier composition, the number of wells and the well thickness.

Minority carrier transport in neutral layers

The minority carrier transport parameters required to calculate the QE of the neutral p and n sections vary according to the type of structure being considered. They are summarised for graded and ungraded structures in table 4.2.

For ungraded structures, the ratio of surface recombination velocity and diffusivity are specified for each layer, together with the minority carrier diffusion length.

Graded structures require a parametrisation of diffusion length and diffusivity as a function of position x .

These parameters are reviewed in the following sections. The parametrisations used are reviewed in chapter 5.

4.2 Design and Growth Parameters

In this section we review the parameters summarised in tables 4.1 and 4.2. These parameters fall into two categories, the first of which are functions of cell design

and growth. Examples are the dimensions of the cell layers, their composition and doping levels. Knowledge of these parameters is usually good because the QWSC fabrication process uses highly accurate epitaxial methods.

The second category contains parameters which are a function of growth method, growth run and processing. Examples include surface recombination, transport parameters and optical properties. These parameters are largely taken from existing data in the literature.

Tables 4.1 and 4.2 show the most important modelling parameters for a graded QWSC with an anti reflection (AR) coat. Dimensions such p,i and n layer thicknesses, and doping levels are generally well known.

The quantum well width is frequently found to depart from the design specification by a few percent. However, this does not affect the overall electrical characteristics of the QWSC and simply restricts or extends the QW absorption edge in the infrared. Such deviations from the specifications are discussed further with respect to modelling in chapter 8.

The background doping level N_{BG} in the intrinsic region, however, is frequently subject to large uncertainty. This is largely because residual impurity levels in the solid or gas sources are poorly known. In addition, the net background doping level is a function of reciprocal compensation by donor and acceptor impurities. The final background doping level may also be affected by unpredictable passivation effects during processing.

As detailed in chapter 2, a large value of N_{BG} degrades the performance of the QWSC because the built-in electric field drops to zero in the intrinsic region.

The QE measurements however are taken when the photocurrent is maximised. In this case, the only effect of N_{BG} on the photocurrent is to influence the width of the depletion layers. A more detailed discussion is given with experimental data in chapter 7.

AR coat	$\sim 70\text{\AA}$ SiN, measured reflectivity
Window layer	300\AA $\text{Al}_{0.67}\text{Ga}_{0.33}\text{As}$
p layer	$0.15\mu\text{m}$ $\text{Al}_{0.4}\text{Ga}_{0.6}\text{As}$ <i>graded to</i> $\text{Al}_{0.2}\text{Ga}_{0.8}\text{As}$ Carbon doping $1.34 \times 10^{18}\text{cm}^{-3}$
i region	30 GaAs wells of width 87\AA 60\AA barriers, composition $\text{Al}_{0.2}\text{Ga}_{0.8}\text{As}$ Well absorption $\sim 1\%$ per level per well
n region	$0.6\mu\text{m}$ $\text{Al}_{0.2}\text{Ga}_{0.8}\text{As}$ Si doping $6 \times 10^{17}\text{cm}^{-3}$
Metallic back mirror	Reflectivity $\sim 95\%$ across entire wavelength range

Table 4.3: Typical design parameter set for an anti-reflection coated 20% Al 30 well QWSC with a graded p layer and a back mirror

4.3 Optical Parameters

4.3.1 Incident Flux

The QE calculation is independent of the incident flux. Estimated values of the short circuit current given in subsequent chapters are given for the AM1.5 solar flux which was described in section 2.4.

4.3.2 Absorption Coefficient

Connolly [31] has shown that the QE is very sensitive to the absorption coefficient α , and has proposed an absorption model based on accurate GaAs tabulations published by Aspnes [32]. The absorption model uses a non linear wavelength dependent energy shift which depends on the aluminium composition x to fit the GaAs absorption to data for $\text{Al}_x\text{Ga}_{1-x}\text{As}$ published in [33]. This approach only gives the absorption of $\text{Al}_x\text{Ga}_{1-x}\text{As}$ for direct aluminium compositions.

Subsequent work in [49] fits an exponential tail below the direct absorption threshold for indirect aluminium fractions to account for the weaker indirect absorption. Since the indirect and direct absorption routines were initially slightly ill matched, this work introduces a further continuous transition between the two

parametrisations.

Connolly [31] has also indicated that the absorption coefficient near the band edge is subject to significant uncertainty for aluminium fractions in the region of 30%. This is seen both in the experimental data tabulations and in a range of models which are reviewed in the reference.

We conclude that the absorption coefficient remains a source of systematic error near the band edge. Since, however, the absorption model uses the most recent tabulated absorption data available, it is difficult to reduce this source of uncertainty.

4.3.3 Reflectivity

Given the very small size of typical QWSC mesa-photodiode test devices, direct reflectivity measurements are difficult. In order to make such measurements possible, pieces of wafer were exposed to all processing steps at the same time as the material which was used to fabricate devices, with the exception of mesa-etching and metallisation. This is discussed in more detail in section 7

These pieces of AR coated wafer are not available for devices processed before 1995. For such samples, an average over previous processing runs is used in the modelling.

The GaAs reflectivity was obtained from published data [32]. Measurements on GaAs wafers has produced close agreement.

Further reflectivity for the double-layer MgF:SiN coating deposited and characterised in Eindhoven Technical University was available for devices processed in Eindhoven.

The reflectivity of the metallic back-mirror is given by Hass [34]. It is found to be very nearly constant across the wavelength range of interest for gold and aluminium. The front surface reflectivity was modelled as a fraction of the measured surface reflectivity. The corresponding fraction is the prime parameter used in modelling the amplitude of Fabry-Perot peaks in mirror-backed devices, and varies from about 70% to 100% of the measured reflectivity. This factor is

described in more detail in chapter 8.

The front surface phase change ψ_f for internal reflection in a dielectric material at an interface with air is given by Macleod [35] as zero. The phase change is π if the interface is with a material with a higher refractive index. Work by Whitehead [36] on multiple quantum well optical modulators indicates that the phase change ψ_b at the metallic back mirror is variable and device dependent. We shall see in chapter 8 that different devices processed from the same wafer may have different modelled values of ψ_b . More recent discussions with the author [37] have suggested that this quantity can be used as a fitting parameter to adjust the frequency of the Fabry-Perot oscillations seen in the QE of mirror backed devices.

4.3.4 Refractive index

Reliable ellipsometric measurements of the refractive index of $\text{Al}_x\text{Ga}_{1-x}\text{As}$ as a function of energy have been tabulated by Aspnes [32] for eleven aluminium compositions for aluminium mole fractions ranging from 0 to 1. For intermediate energies and compositions, a linear interpolation is used.

4.4 Transport parameters

We have seen that good agreement exists on the optical materials parameters of $\text{Al}_x\text{Ga}_{1-x}\text{As}$, and that consistent values are available in the literature

Most of the minority transport parameters however are sensitive to device history. Growth conditions between different runs on the same machine may differ significantly due to relatively small variations in the composition of the gas or solid sources used in the epitaxial growth. Furthermore, post-growth processing, involving device exposure to etches, plasmas and heat treatments, may also affect transport. Examples include accidental passivation, diffusion of impurities and a modification of the recombination velocity. Finally, a number of these parameters are dependent on the device structure. The following section explores current knowledge of these parameters in the literature.

4.4.1 Band gap Parametrisations and the Quasi-Electric Field

We saw in chapter 2 that an externally applied bias in a p - i - n structure is entirely dropped across the intrinsic region for moderate applied bias where the majority carrier profile is not significantly affected by the external voltage. That is, no externally applied bias is dropped across the neutral sections of the n and p layers.

The effective electric field acting on minority carriers in n and p type graded structures is examined by Sutherland [22], Hutchby [21] and is reviewed by Hamaker [24]. It is generally referred to as the quasi field. This electric field is sometimes taken to be proportional to the gradient of the electron affinity as in Sutherland [22]. Other workers however express it as the gradient of the bandgap. The review by Hamaker [24] explains the origin of the field and expresses it in terms of doping, bandgap and Fermi level gradients. In samples designed in the present work, the nominal doping is constant. We will not therefore consider fields due to doping gradients.

Sassi [23] has estimated the field due to the Fermi level gradient as less than 2% of the field due to the bandgap gradient. Sassi therefore neglects the gradient of the Fermi level. Taking the example of the minority electron quasi field E_e in p type material, this gives

$$E_e = -\frac{dE_g}{dx} \quad (4.1)$$

where E_g is in electronvolts and x the position. This assumption of low Fermi level gradient is especially true in heavily doped material such as we use in our solar cell designs. It is the most commonly found parametrisation for the quasi-field acting on minority carriers, and is used for example in work by Konagai [20], Hutchby [21] and Sassi [23]. We shall therefore use this method in this study.

The corresponding hole quasi field in electronvolts for n type material is

$$E_h = +\frac{dE_g}{dx} \quad (4.2)$$

We shall not consider graded n layers in the $\text{Al}_x\text{Ga}_{1-x}\text{As}$ system, and will revert to the nomenclature of chapter 3, which refers to E_e as E .

An added complication is the transition from direct to indirect material in $\text{Al}_x\text{Ga}_{1-x}\text{As}$. The review article by Pollack [39] put this transition at a composition in the region of 45% aluminium.

Two expressions are given for E_g in the literature. We write these in terms of a composition dependent step function Θ for convenience, which has value 1 below the direct-indirect transition, and 0 above. The bandgap is derived from expressions by Casey and Panish [44] for the direct regime, and Hutchby [21] for the indirect material.

$$E_g = \Theta(1.424 + 1.247X) + (1 - \Theta)(1.92 + 0.17X + 0.07X^2) \quad (4.3)$$

4.4.2 Minority carrier lifetime

Although the model outlined in section 3.4 does not explicitly require knowledge of the minority carrier lifetime τ , this parameter is mentioned here for completeness. It is related to the minority carrier diffusivity and the diffusion length by

$$\tau_n = \frac{L_n^2}{D_n} \quad (4.4)$$

for electrons. A similar expression holds for holes. Minority carrier lifetimes in $\text{GaAs}/\text{Al}_x\text{Ga}_{1-x}\text{As}$ have been measured for a range of aluminium compositions. The most common methods are time resolved photo-luminescence (TRPL) (Ahrenkiel [41]) and zero-field time-of-flight (ZFTOF) (Zarem [42]) techniques. This data is summarised and discussed in the review article by Ahrenkiel [45]. Unfortunately, little data is available for compositions above about 40% aluminium. The large scatter observed in experimental data indicates that the lifetime is dominated by defect-related Shockley-Hall-Read recombination processes. It is therefore sensitive to material quality and according to Ahrenkiel may vary by orders of magnitude compared with the published values in the review article.

4.4.3 Mobility and Diffusion Coefficient

We have seen that the model does now explicitly depend on the magnitude of the diffusivity. The functional form of this parameter however is important in determining the QE of graded structures.

Values of the diffusion coefficients D_p and D_n for minority holes and electrons are not available in the literature, and, like the diffusion length values, must be obtained indirectly.

The review article by Ahrenkiel [45] states that the diffusivity is most conveniently found by extrapolation from the electron and hole majority Hall mobilities μ_e and μ_h in the low field, low injection limit where the Einstein relationship is valid. The two quantities are then approximately related as follows

$$\begin{aligned} D_p &\simeq \frac{k_B T \mu_h}{q} \quad (\text{holes}) \\ D_n &\simeq \frac{k_B T \mu_e}{q} \quad (\text{electrons}) \end{aligned} \tag{4.5}$$

Low field hole and electron mobilities are supplied in the review by Walukiewicz [18]. A wide spread is observed, indicating that the mobility is material dependent. Both electron and hole mobilities decrease sharply from GaAs to $\text{Al}_{0.5}\text{Ga}_{0.5}\text{As}$. For aluminium compositions greater than about 50%, both mobilities appear essentially constant.

This behaviour is essentially reproduced by a parametrisation of the diffusivity as a function of composition and doping presented by Hamaker [24]. The Hamaker paper does not give details, but states that the parametrisation is based on experimental data. We use this as a guide to diffusivity values. More detail concerning this point is provided in chapter 5.

4.4.4 Diffusion length

The diffusion lengths L_n and L_p in $\text{GaAs}/\text{Al}_x\text{Ga}_{1-x}\text{As}$ are sensitive to growth method, device structure and aluminium composition. As we shall see in chapter 5, they are significant QE fitting parameters. We review here some of the expected values in $\text{Al}_x\text{Ga}_{1-x}\text{As}$. Specific values of this parameter will be referred to with

respect to modelling in chapter 8.

Ahrenkiel [45] recommends extracting L for both minority holes and electrons from the minority carrier lifetime and the diffusion coefficient discussed above through the relation

$$L_n = \sqrt{D_n \tau_n} \quad (4.6)$$

for minority electrons. A similar expression holds for minority holes. These values can only provide a rough starting point for modelling, since the diffusion length is strongly device dependent.

Ahrenkiel reports that the diffusion length dependence on aluminium fraction is similar to that of the mobility. It generally decreases with increasing aluminium fraction over the direct region, but is found to increase near the direct/indirect transition region at about 40% aluminium. It remains approximately constant for indirect material, at a value which is however only a fraction of the GaAs diffusion length.

Hamaker [24] gives a parametrisation similar to that which was discussed for the diffusivity in the previous section. We shall compare values predicted by Hamaker with values estimated from the modelling of QE spectra in chapter 8.

Grünbaum [46] has measured minority hole diffusion lengths in some of our $\text{Al}_x\text{Ga}_{1-x}\text{As}$ material using Electron Beam Induced Current techniques. This technique however was only applied to one sample relevant to this study. It is unfortunately currently incapable of the resolution required to measure the more significant minority electron diffusion length L_n . Moreover, the predicted L_p values are rather large.

4.4.5 Recombination velocity

Chapter 3 showed that surface or interface recombination velocities in our material cannot be separated from the diffusivity, which was reviewed earlier in this chapter. Modelled values of the surface recombination parameter \mathcal{S} however indicate whether or not our values are in qualitative agreement with those reported in the literature.

An unfortunate result of any heterojunction in a semiconductor structure is the presence of interface recombination centres. These may result for a variety of reasons. For heterojunctions these include lattice mismatch and abrupt changes in growth conditions.

Two more cases occur. The first is the junction between a semiconductor and air. Recombination velocities in this case are particularly high. Measurements presented by Fonash [19] quote values up to three orders of magnitude greater than for heterojunctions. The third case is that of a semiconductor and an anti-reflection coating, such as deposited SiN.

Measurements are carried out by time resolved photoluminescence (TRPL) studies of double heterojunction devices. The active region is grown with a lower bandgap, and its thickness varied. The variation of the PL signal decay time as a function of active layer thickness can then give an indirect measurement of the interface recombination velocity. This method has been used by 'tHooft and Van Opdorp [47]. Results are included in the review article by Timmons [40].

Devices which have suffered surface damage as a result of handling or processing may however deviate from this picture. Furthermore, Fonash [19] has indicated that recombination at the contacts increases the effective surface recombination. This effect can be reduced by the use of appropriate contacts. Selective ohmic contacts, for example, present a potential barrier to minority carriers, and inhibit minority carrier recombination at the contacts. They are, however, ohmic to majority carriers [19].

Theoretical studies however such as those reviewed in chapter 3 usually use values which are one to two orders of magnitude greater than these. The largest reported value for interface recombination in $\text{Al}_x\text{Ga}_{1-x}\text{As}$ is quoted by Timmons [40] as $3 \times 10^4 \text{cm/s}$. Surface recombination velocities of $4 \times 10^5 \text{cm/s}$ have been observed in $\text{Al}_{0.08}\text{Ga}_{0.92}\text{As}$ material exposed to the air.

Details concerning the recombination velocity and the way this parameter is combined with the diffusivity are given in chapter 5 which deals with modelling techniques.

4.4.6 Discussion

In this chapter we have briefly described the method used to design the modelling program, before discussing the parameters required to model the QE of real solar cells. We have seen that these parameters can be divided into two broad categories. The first are optical, compositional and geometrical parameters and are reasonably well known.

The second category involves the transport parameters. These are generally dependent on sample growth and device processing, and are poorly defined. Values quoted in the literature are variable and show a large spread. However, experimental and parametrised values quoted in the literature provide bounds within which we can expect our values to lie.

The treatment of the modelling techniques associated with using mutually consistent values requires simultaneous examination of the modelling results. These considerations are described in chapters 5 and 8.

Chapter 5

QE Modelling and Optimisation

The reliability of the analytical method has been established in previous work by modelling published data by Bernd Braun [48]. The first section of this chapter summarises the main results of this work.

We go on to investigate a number of theoretical predictions made by the model for a number of promising structures. All results apply to the QWSC design shown in table 5.1 and to p - i - n control samples which are identical except for the lack of wells in the intrinsic region.

The optimisation is broadly separated into two cases according to incident photon energy. The first is the case of photons with energies above the bulk bandgap E_{b2} , which corresponds to aluminium fraction X_{b2} (see table 5.1).

The QE in this range is mainly determined by the minority carrier transport efficiency of the p layer. Graded structures are further characterised by the aluminium fraction X_{b1} at the top of the grade, and its associated bandgap E_{b1} .

The separate optimisation of the quantum well QE applies to incident photons with energies between the quantum well bandgap E_a and the lower bulk bandgap E_{b2} and its associated aluminium composition X_{b2} . This optimisation is mainly dependent on the absorptivity of the quantum wells and the light levels in the i region.

Layer type	Thickness	Doping	$\text{Al}_x\text{Ga}_{1-x}\text{As}$ composition x (%)
cap	400Å	p^+	$x = 0$
window	300Å	p^+	$x = 67$
p layer	$0.15\mu m$	p	grade $\begin{cases} x = X_{b1} \\ x = X_{b2} \end{cases}$
i buffer	400Å	i	$x = X_{b1}$
i layer	$30 \times \begin{cases} 60\text{Å barrier} \\ 87\text{Å well} \end{cases}$	i	Wells: $x = 0$ Barriers: $x = 30$
i buffer	400Å	i	$x = X_{b1}$
n layer	$0.6\mu m$	n	$x = X_{b1}$
GaAs substrate		n^+	$x = 0$

Table 5.1: Basic QWSC growth menu

5.1 Ungraded Cells

5.1.1 Previous Work

Photocurrent and Voltage Enhancement

Early work presented by Mark Paxman *et al.* in reference [49] showed that the short circuit current of a QWSC is greatly enhanced over that of a control structure which is identical, but with the well material replaced by an equal thickness of barrier material.

Further work showed that the V_{oc} for the QWSC drops relative to that of the control sample, but remains greater than the V_{oc} which would be expected from a cell with the quantum well effective bandgap E_a .

One of the samples with fifty wells showed a V_{oc} of 1.07V, which is greater than that of the worlds' best GaAs cell (reference [11]). The modelled light IV curves and QE spectra for this sample are illustrated in figure 5.1. The large increase in J_{sc} more than compensates for the decrease in V_{oc} leading to an overall efficiency enhancement in the QWSC relative to the p - i - n control.

A set of identical ungraded samples were designed with the help of the opti-

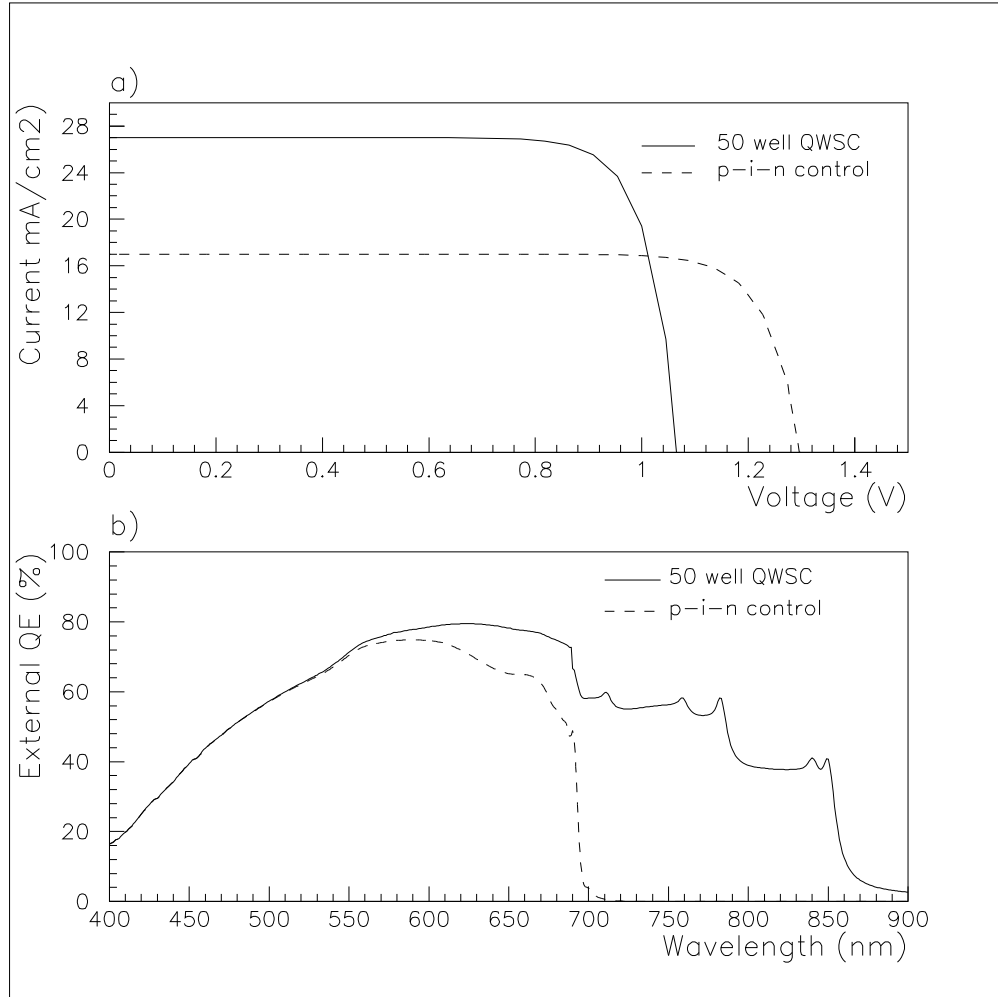


Figure 5.1: Modelled a) light IV curves and b) QE spectra for a 50 well QWSC and p - i - n control pair based on a successful device.

misation program we described in chapter 3 and grown by MBE. They feature different values of X_{b2} but identical geometries. We concluded that the V_{oc} increases with X_{b2} . Unfortunately, the material quality and QE decrease with increasing X_{b2} . We concluded that a value of X_{b2} in the region of 30% is a reasonable compromise between the requirements of good material quality and high V_{oc} .

Anti Reflection (AR) Coating

The reflectivity of the standard single layer SiN AR coat has been optimised in reference [49]. Further reductions in reflectivity across the wavelength range of interest are possible with more sophisticated multilayer AR coats.

This work, however, is concerned mainly with the internal QE of QWSC structures, and has used the recommended SiN AR coat of thickness $\sim 70nm$ throughout.

Short Wavelength Optimisation

Previous work has recommended a number of optimisations which may be carried out. This work concluded that thinning the p layer increases the minority carrier collection efficiency, particularly at short wavelengths. It also transmits more light to the i layer. Both effects enhance the QE . This method, however, is limited by the increase in series resistance as the p layer is thinned. This is particularly damaging for concentrator applications.

The addition of a window layer has been found to reduce recombination at the front of the p layer. This is due both to the replacement of a surface recombination velocity by a lower interface recombination between the p layer and the window, and the reflection of minority carriers away from the surface by the bandgap discontinuity at the interface.

Although this method successfully reduces the recombination velocity, some of this advantage is lost because even thin window layers absorb a significant fraction of incident light at short wavelengths. The previous work has shown

that the window layer is very inefficient at converting this absorbed radiation to photocurrent, and essentially contributes no photocurrent.

Use of a very high aluminium fraction for the window layer can reduce the window absorptivity, but introduces new difficulties. This is due to an increased recombination velocity for high window aluminium fraction, caused both by an increased lattice mis-match at the interface and lower window material quality.

The techniques above have been successfully demonstrated in reference [49]. However, we conclude that there is still much room for improvement at short wavelengths, which requires more complex structures.

Long Wavelength Optimisation

As shown indicated by Paxman [49], the long wavelength QE can be increased simply by introducing more wells in the i region. This can be done by reducing the barrier thickness. This approach however is expected to reduce the V_{oc} of the cell.

Increasing the width of the i layer is an alternative route. We saw however in section 2.3.2 that this leads to a reduced QE in forward bias and a degradation of the fill factor FF . Furthermore, a more fundamental limit is imposed by the increase in dark current for wider i layers.

Previous work resulted in a QWSC with fifty wells, which nevertheless failed to absorb approximately half the incident light at energies below E_{b2} . Failing material with lower background doping, more complex techniques are required to increase the QE in the long wavelength range.

Conclusions

We have seen that the short circuit current enhancement techniques presented by Paxman [49] are limited by a range of physical and materials considerations.

Short wavelength efficiency enhancements in ungraded GaAs/Al_xGa_{1-x}As solar cells are limited by series resistance, window absorptivity and poor material quality at high aluminium fractions.

At longer wavelengths, the background doping sets a limit on the number of wells which may be inserted in the structure, and hence the total absorptivity of the wells.

In both wavelength ranges therefore, there is potential for optimisation by improving p layer transport and by increasing the absorptivity of the i layer.

5.2 Further QE Enhancements Above the Barrier Bandgap

Chapter 3 shows that a variation of material composition with position can significantly alter the optical and transport properties of the QWSC. This section investigates the effect of such changes on light intensity and generation rate as a function of position and incident light wavelength. The consequences for minority transport are covered before reviewing the minority carrier density and *QE* optimisation of graded structures.

5.2.1 Light Absorption and Minority Carrier Generation

Light Intensity

In chapters 3 and 4 we saw that $\text{Al}_x\text{Ga}_{1-x}\text{As}$ is direct for aluminium fractions up to approximately 45%. Direct materials are characterised by high absorption coefficients. Unlike indirect materials such as silicon, direct materials can absorb most of the incident light spectrum in a relatively short depth. However, given the poor materials characteristics of $\text{Al}_x\text{Ga}_{1-x}\text{As}$, it is desirable to increase light levels deeper in the cell so that minority carriers are generated preferentially near or in the depleted layers where they may be collected by the built in potential. This may be achieved by compositional grading.

The relative light intensity for typical ungraded and graded p - i - n cells is shown for a range of wavelengths in figure 5.2. The intensity immediately starts to decrease in the ungraded cell for all wavelengths above the bandgap. At very short wavelengths, no light reaches the i region.

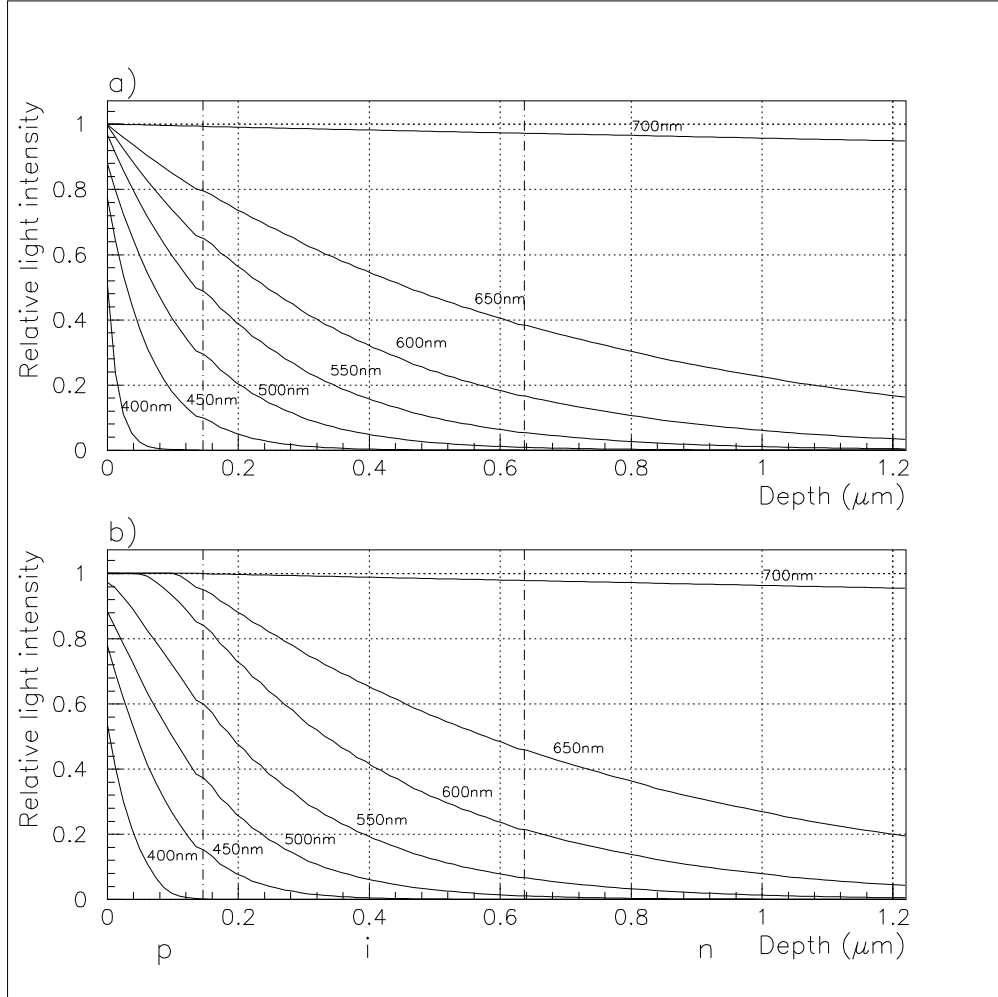


Figure 5.2: Relative light intensities in a) ungraded p - i - n cell and b) a p - i - n cell with a p layer graded from $X_{b1} = 67\%$ to $X_{b2} = 30\%$

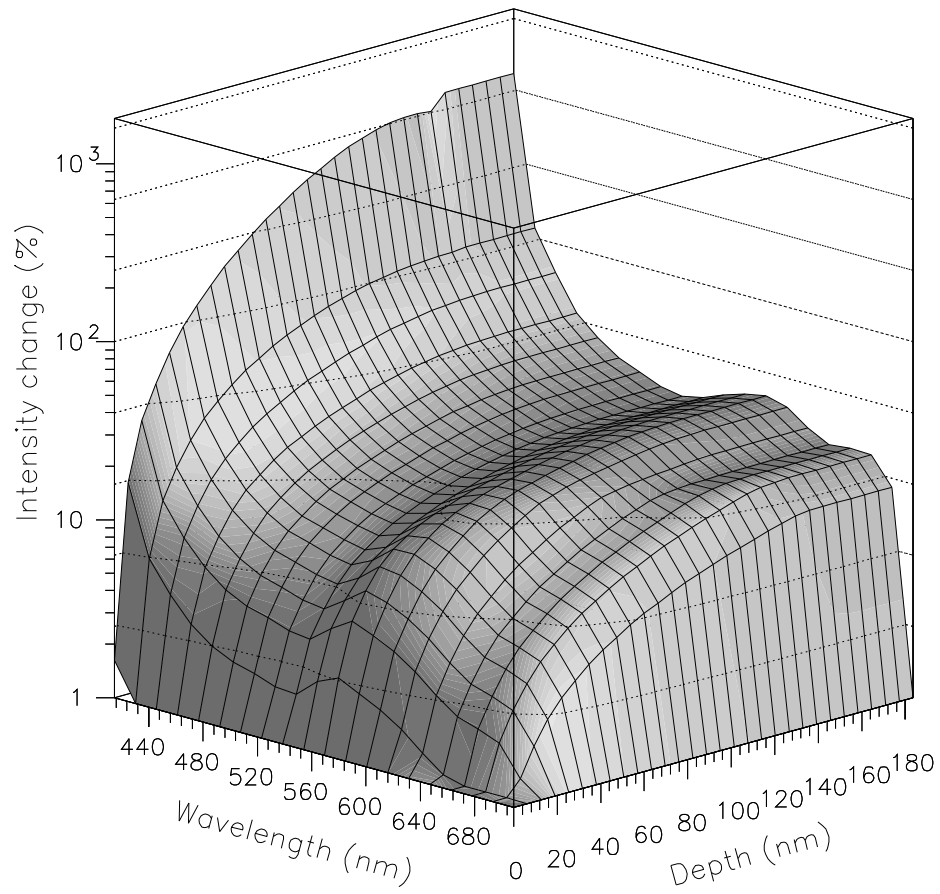


Figure 5.3: Fractional increase in light intensity in a p - i - n cell with a p layer graded from $X_{b1} = 67\%$ to $X_{b2} = 30\%$ compared to an ungraded cell

In the graded sample for long wavelengths such as 600nm, absorption in the p layer only becomes significant at a depth of about 70nm, at which point the bandgap decreases below the corresponding absorption threshold. A constant plateau in light intensity is seen from zero to 70nm because of the lack of absorption.

Figure 5.3 gives the difference in light levels between ungraded and graded cells, expressed as a percentage of the light level in the ungraded cell. Higher light levels are seen for all wavelengths in the graded design. The gain in intensity increases with depth until the junction with the i layer at a depth of 150nm. For greater depths, no further increase is seen since the absorption coefficients of the i and n layer are identical for the two cell designs used in this example.

The gain in light level is strongest at short wavelengths because the difference in the absorptivities of the graded and ungraded p layers is greatest for high energies. The calculations of intensity at 400nm represented in figure 5.2 show that $\sim 95\%$ of the incident light is absorbed in the first 40nm of an ungraded cell, whereas $\sim 85\%$ is absorbed in the same depth for the graded structure. Whilst the light intensity in the i and n layers appears much higher in the graded structure relative to the ungraded cell, the absolute light level remains very low. The absolute light intensity in the i and n layers in the short wavelength range therefore remains very low.

Improvement in the short wavelength range will be due to an improved p layer response due to a better distribution of light, as we shall see in subsequent sections.

For wavelengths between approximately 450nm and the bandedge, increases of between 10% and 40% are seen throughout the cell. This is particularly significant for the i layer, which converts absorbed light into photocurrent with nearly 100% efficiency. For energies very close to E_{b2} , the intensity enhancement tends to zero since neither cell absorbs strongly.

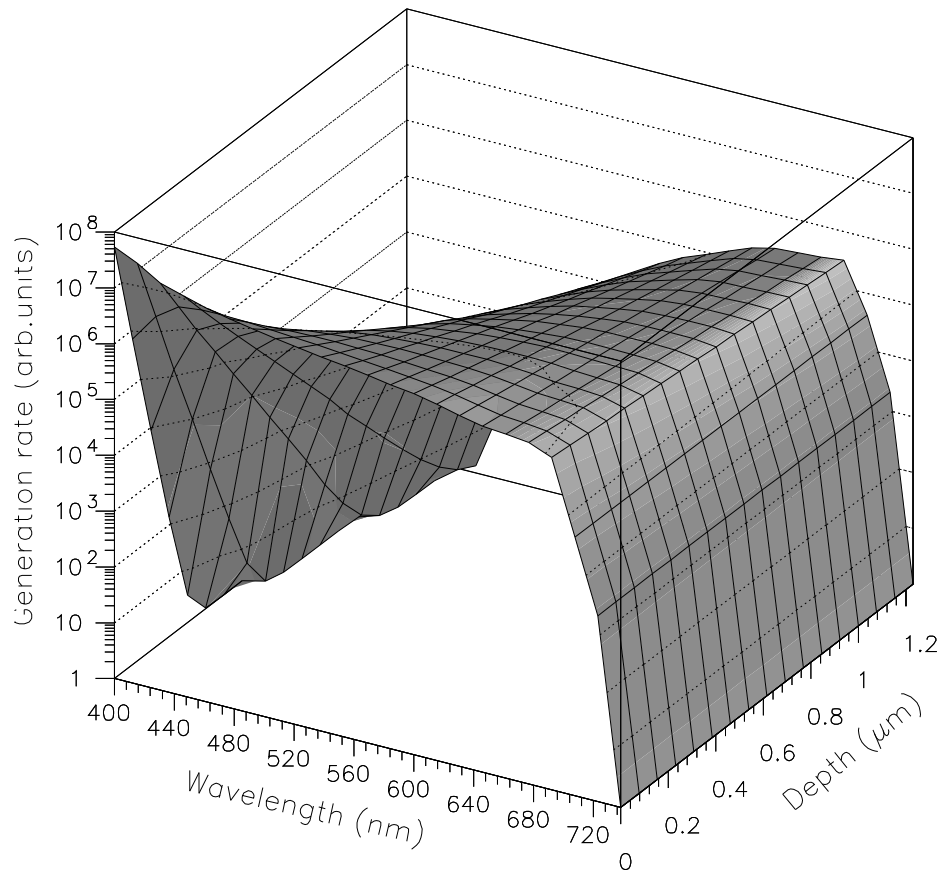


Figure 5.4: Generation rates in an ungraded p - i - n solar cell for wavelengths above the bulk bandgap

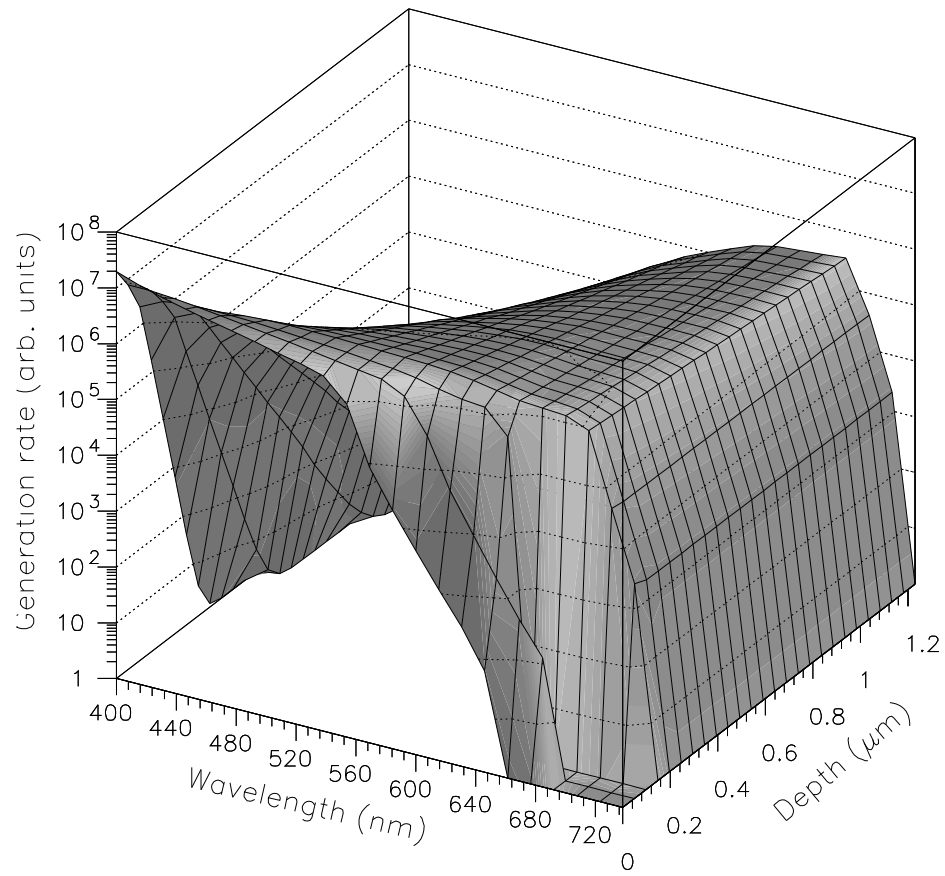


Figure 5.5: Generation rates in a compositionally graded p - i - n solar for wavelengths above the bulk bandgap E_{b2}

Generation Rate

Figures 5.4 and 5.5 show the generation rates for the structures of figure 5.3 as a function of depth and position. In the homogeneous cell, the generation at each wavelength decreases exponentially with increasing depth. The exponential decay however very nearly approximates a constant for wavelengths within about 50nm of the bandedge.

The graded case is considerably different. Considering the p layer first, we see that the generation rate at short wavelengths is decreased because of the lower absorptivity near the surface.

At lower photon energies, the generation rate falls to zero as the high Al fraction material towards the front of the cell ceases to absorb light. The generation rate at 650nm for example only becomes significant at a depth of about $0.1\mu m$, which is over two thirds of the total p layer width.

We conclude that the grade improves the generation profile both by shifting minority carrier generation rate in the p towards the i layer, and by increasing the generation rate in the latter. An increase in generation rate in the n region is also visible but is not expected to modify the n region QE considerably because the light levels in this layer remain low. The magnitude of the subsequent QE enhancements in all three regions of the solar cell is discussed below.

5.2.2 Minority Carrier Transport

In chapter 3 we saw that the QE of graded structures depends on the diffusion length and diffusivity of the neutral layers. Both of these parameters are composition dependent functions.

Neither quantity can directly be measured in the QWSC structures. We are therefore obliged to make a number of assumptions regarding the functional form of both the diffusion length and the diffusivity.

n Layer Minority Carrier Transport

In the structures we are considering, the n layer remains ungraded, and only constant values of L_p and D_p are required. Since the n region contribution in our case is small, we cannot estimate values of these parameters from QE measurements. We rely instead on the values reviewed in chapter 4. Although this approach is inaccurate, the effect on the absolute QE is small because of the very low n region QE contribution in p - i - n $\text{Al}_x\text{Ga}_{1-x}\text{As}$ devices.

p Layer Minority Carrier Diffusion Lengths

The spatial variation of L_n and D_n is an important factor in determining the overall p layer QE . A number of assumptions must be made to compensate for the lack of direct measurement.

Appendix A shows that the QE of ungraded p layers is directly proportional to L_n for low absorption and low L_n . Experimental measurements of the QE of ungraded devices with different values of X_{b2} can therefore be used to build up a picture of the functional dependence of L_n on aluminium composition. In turn, this gives the spatial variation of L_n in compositionally graded structures.

We make the further assumption that growth conditions are reproducible and the resulting table of L_n as a function of X_{b2} can be generalised to graded structures.

p Layer Diffusivity

Chapter 3 showed that the QE of ungraded p layers depends on the ratio S_n/D_n . Since the recombination velocity S_n is device dependent and cannot be measured directly in our structures, we cannot extract the functional form of D_n from QE spectra. We must therefore make a further assumption allowing us to parametrise the effect of the diffusivity in terms of a single parameter.

Chapter 3 further showed that D_n affects the QE of graded structures in two ways. The first is similar to the ungraded case and involves the recombination velocity parameter \mathcal{S} . It was also demonstrated however that \mathcal{S} has a weaker

effect in graded structures because of the bandgap gradient effective field \mathcal{E}_f .

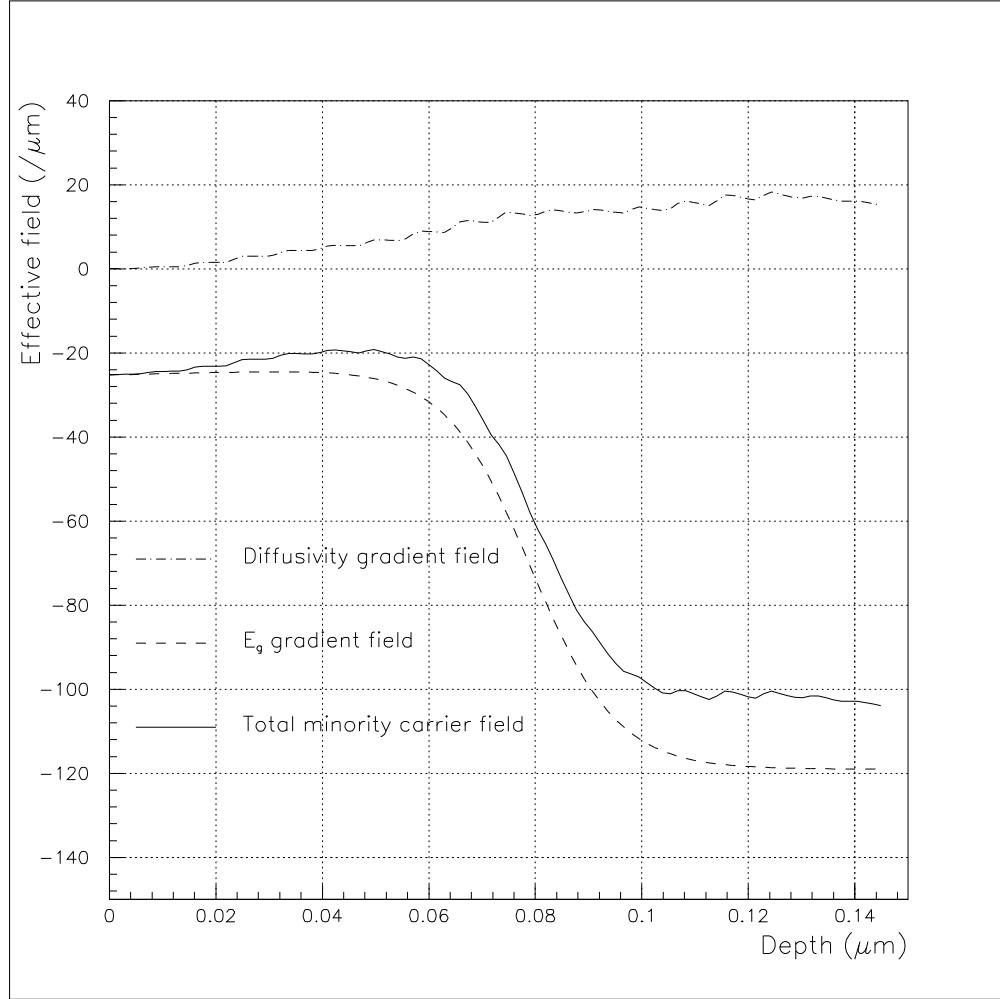


Figure 5.6: Effective electric field in per micron as a function of position for a p layer graded from $X_{b1} = 67\%$ to $X_{b2} = 30\%$

D_n also appears as a term D'_n/D_n which we define as the diffusivity field \mathcal{D}_f in units of per metre:

$$\mathcal{D}_f = \frac{\nabla_x D_n}{D_n} \quad (5.1)$$

This term expresses the current flow caused by minority carriers in regions of high mobility moving towards regions where minority carriers are less mobile. Although it is expressed here in terms of the differential with respect to distance $\nabla_x D_n$, it can be re-expressed in terms of the aluminium compositional gradient

$$\mathcal{D}_x = \frac{\nabla_x}{D_n} \quad (5.2)$$

This form, which we will call the diffusivity field, has the advantage of being independent of the device geometry, and is dimensionless. The diffusivity in terms of these two forms is

$$\begin{aligned} D_n(x) &= D_n(0) \exp(\mathcal{D}_f x) \\ &= D_n(0) \exp(\mathcal{D}_{\mathcal{X}}(X(x) - X_{b1})) \end{aligned} \quad (5.3)$$

where $X(x)$ is the aluminium composition at position x . The diffusivity field is related to \mathcal{D}_f via the relation

$$\mathcal{D}_{\mathcal{X}} = \mathcal{D}_f \left(\frac{x_{w_p}}{X_{b2} - X_{b1}} \right) \quad (5.4)$$

The diffusivity field defined this way has a value of about -4 if we use the Hamaker parametrisation of chapter 4, for p type $\text{Al}_x\text{Ga}_{1-x}\text{As}$ doped at about $2 \times 10^{18} \text{cm}^{-3}$.

Since comparisons between samples with different geometries are more clearly apparent with this form, we shall use it in the modelling section. We continue to use the device dependent form \mathcal{D}_f here, however, because it has the same units as the effective field \mathcal{E}_f and is therefore better suited to this discussion. In terms of \mathcal{D}_f , then, the total field \mathcal{E}_t acting on the electron minority carriers is

$$\mathcal{E}_t = \mathcal{E}_f + \mathcal{D}_f \quad (5.5)$$

According to experimental data presented in reference [18] (reviewed in chapter 4), D_n decreases rapidly with increasing aluminium fraction, before levelling off for indirect material. Figure 5.6 shows the resulting fields \mathcal{D}_f , \mathcal{E}_f and \mathcal{E}_t where \mathcal{E}_f is calculated as in chapter 4 and \mathcal{D}_f is found from the experimental data of reference [18].

Since the diffusivity is higher in $\text{Al}_x\text{Ga}_{1-x}\text{As}$ with a low aluminium fraction, \mathcal{D}_f is positive and, unfortunately, opposes the drift field \mathcal{E}_f due to the bandgap gradient. The figure shows that a significant decrease in \mathcal{E}_t may be expected.

The functional form of D_n therefore may have important consequences for the overall effect of a compositional grade on minority carrier transport efficiency.

Since we cannot experimentally determine the compositional dependence of \mathcal{D}_f , we must find a parametrisation which can reduce this poorly defined function to a single fitting parameter.

An exponential parametrisation for D_n suggested by Hamaker [24] was reviewed in chapter 4. The Hamaker parametrisation reproduces the functional form of the experimental data given in reference [18]. For the example shown in figure 5.6, the Hamaker value is $\mathcal{D}_f \sim 10\mu m^{-1}$, which agrees qualitatively with the published experimental data. Because of material variability, however, we do not expect the Hamaker parametrisation to yield accurate values of \mathcal{D}_f for our material.

In the general case of an exponential parametrisation for D_n , \mathcal{D}_f is a position independent constant for linear compositional gradients. Moreover, it is independent of the magnitude of D_n . This means that the magnitude of the diffusivity influences the *QE* of a graded structure only through the surface boundary parameter \mathcal{S} . Since, as we have mentioned earlier in this section, \mathcal{S} has a weak effect in graded structures, we are left with a single principal fitting parameter which is the diffusivity field D_f .

We will therefore assume an exponential form for D_n along the lines suggested by Hamaker but will treat the diffusivity field \mathcal{D}_f as a position independent fitting parameter.

Summary of the Transport Model

Modelling of the *QE* from the neutral regions is therefore subject to a number of assumptions which we will review here.

The first is that the n region contribution is small. We only treat ungraded n layers, and rely on published data for transport parameters in this case.

For ungraded p layers, we have seen that parameters are well known except for L_d , D_n and S_n . Because the diffusion length in our structures is smaller than the p layer width x_p , L_n can be estimated from the *QE* close to the bulk bandedge at energy E_{b2} .

The parameters S_n and D_n in ungraded structures can be separated as a

single surface recombination parameter \mathcal{S} (see chapter 3) which is used as the sole fitting parameter in the short wavelength regime.

For compositionally graded structures, we make the assumption that the epitaxial material is of reproducible quality. The values of L_n derived from modelling the QE of ungraded structures with different values of X_{b2} are used to build up a table of the compositional dependence of L_n . Under the aforementioned assumption, this provides the position dependence of L_n for the graded structures.

We finally make the assumption that the functional dependence of D_n on aluminium fraction is exponential. The diffusivity field \mathcal{D}_f is therefore a constant, which is independent of the magnitude of the parametrisation $D_n(x)$. Since chapter 3 has shown that the QE of graded structures is only weakly dependent on the surface recombination parameter \mathcal{S} , we are left with a single dominant fitting parameter which is \mathcal{D}_f .

The number of assumptions involved in this modelling prevents us from expecting quantitative predictions of the QE of graded structures. We expect, however, to qualitatively describe the dependence QE enhancement factors due on the one hand to better light distribution and on the other, to improved minority carrier transport in graded solar cell structures.

5.2.3 Minority Carrier Concentration

Figures 5.7 and 5.8 show the minority carrier concentrations for an ungraded p layer and a cell graded from 30% to 40%. The concentrations are given in arbitrary units but are subject to the same normalisation factor.

We see that the minority carrier concentration in the graded case decreases in magnitude by a factor of about two, and is shifted towards the depletion region. The decrease in concentration is due partly to decreased absorption and partly to the modifications in minority carrier transport efficiency caused by the grade. The effective field in particular sweeps carriers to the junction. Increased bulk recombination due to the higher aluminium fraction also plays a role.

Figure 5.9 shows the case of a p layer graded from 30% to 67%. In this

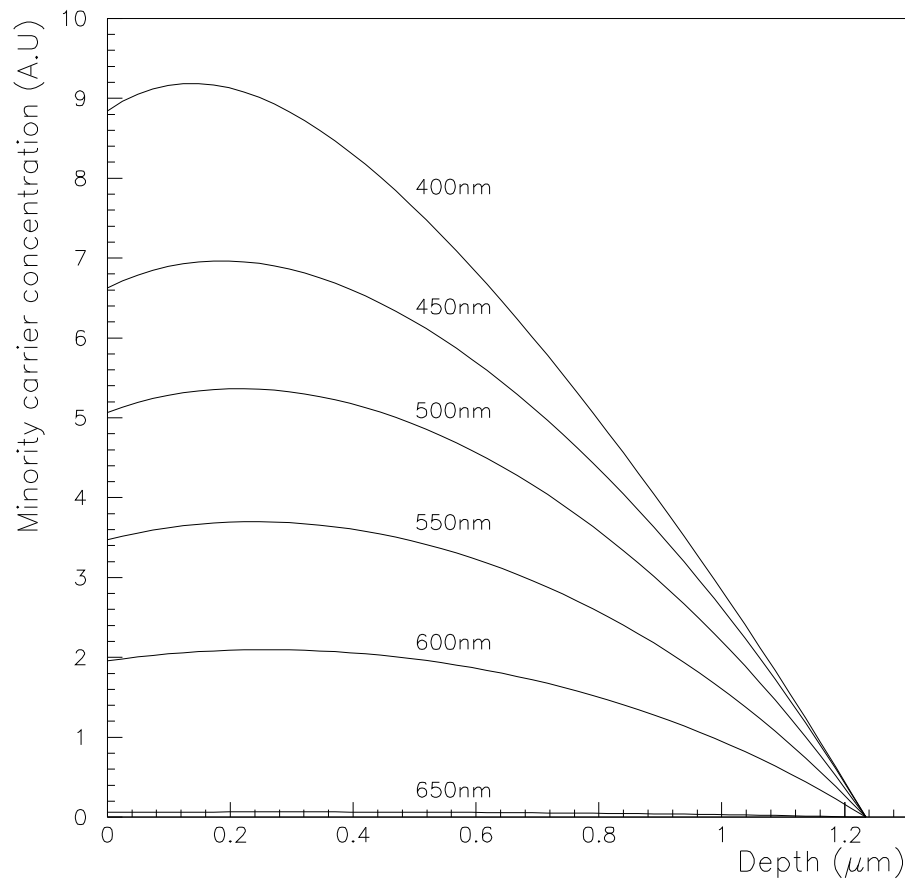


Figure 5.7: Minority carrier concentration in an ungraded p layer for a range of wavelengths.

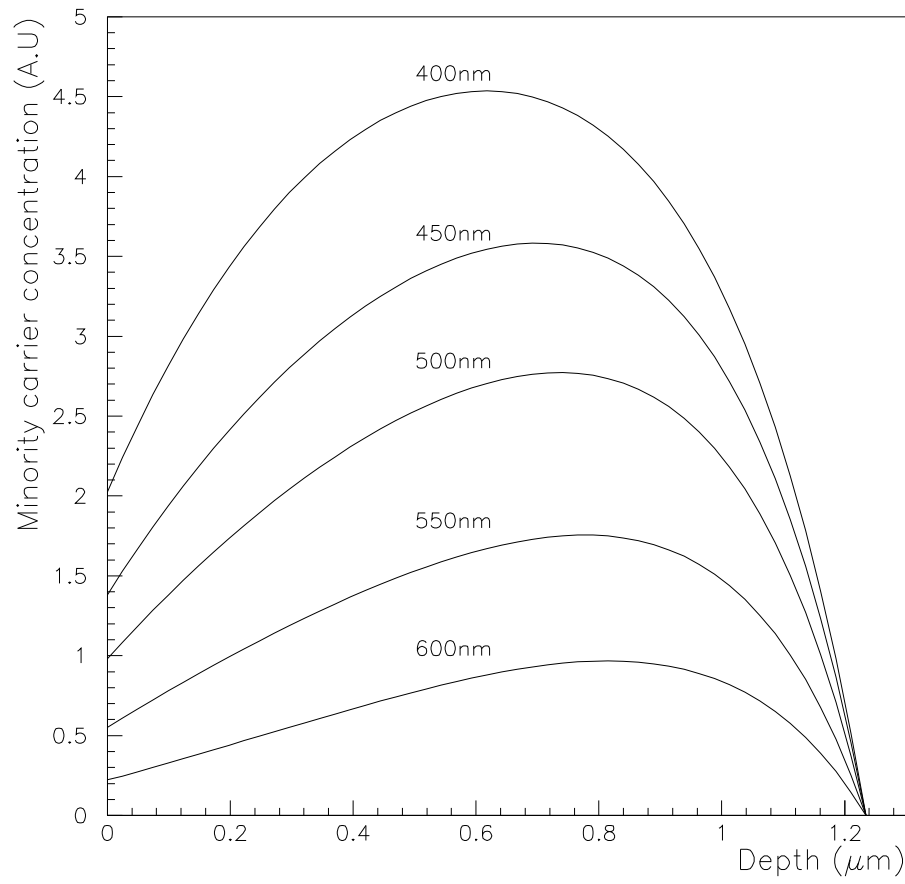


Figure 5.8: Minority carrier concentration in a p layer graded from 30% to 40% Al for a range of wavelengths.

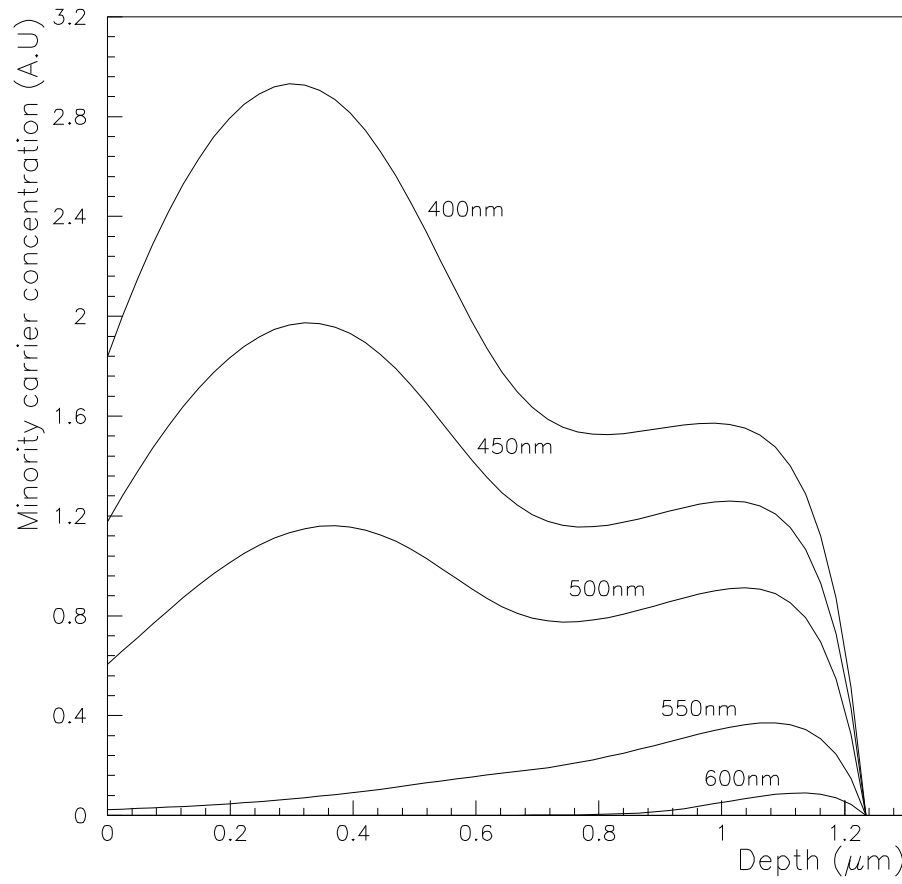


Figure 5.9: Minority carrier concentration in a p layer graded from 30% to 67% Al for a range of wavelengths.

case, the two separate field regions are clearly reflected in the minority carrier concentration. The lower direct transition region near the depletion layer has a lower minority carrier concentration in this case because the higher field sweeps carriers towards the depletion layer more efficiently than the lower field in the indirect region near the surface.

The overall minority carrier concentration is again lower than the previous two cases we have looked at for the same reasons. The change is greater in this case because of the increased compositional gradient.

5.2.4 QE and Short Circuit Current

The quantum efficiency for the ungraded and graded cells described in the previous sections is shown in figure 5.10. The breakdown of percentage increase in p, i, n and total QE is given in figure 5.11. We note that the p layer contribution is increased at short wavelengths but decreased near the bulk band edge.

The improvement at very short wavelengths is the result of increased carrier collection efficiency in the p layer. This is due to improved minority carrier transport and the shifting of the minority carrier generation profile towards the i region. The deterioration near the band edge however is due to reduced light absorption in the p layer at low photon energies.

Figure 5.12a shows a prediction of short circuit current as a function of the topmost aluminium fraction in the p layer. Such calculations are subject to large uncertainty however, particularly given the large distribution of possible diffusivity gradients. The calculation of figure 5.12a uses a gradient which is about half that of the published data of chapter 4 which as we shall see in chapter 8 is consistent with experimental QE spectra. Although the model cannot indicate the magnitude of the diffusivity, this deviation of a factor of two in gradient is well within the margins expected.

With the uncertainties due to \mathcal{D}_f in mind, we note that J_{sc} initially rises sharply as the effects of surface recombination become less important. For higher grades, the gain in i region contribution is increasingly balanced by a reduction of

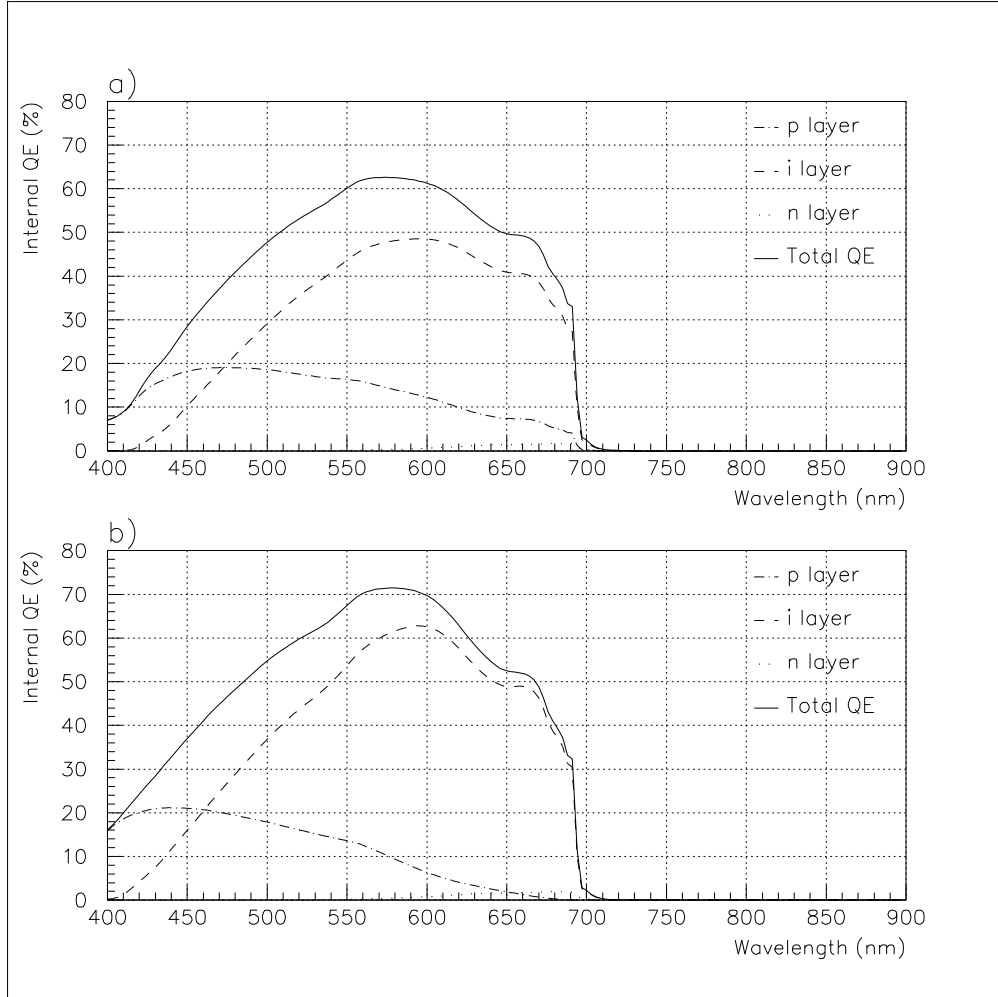


Figure 5.10: QE of a) a 30% p - i - n and b) a p - i - n with a p layer graded from $x_{b1} = 67\%$ to $x_{b2} = 30\%$

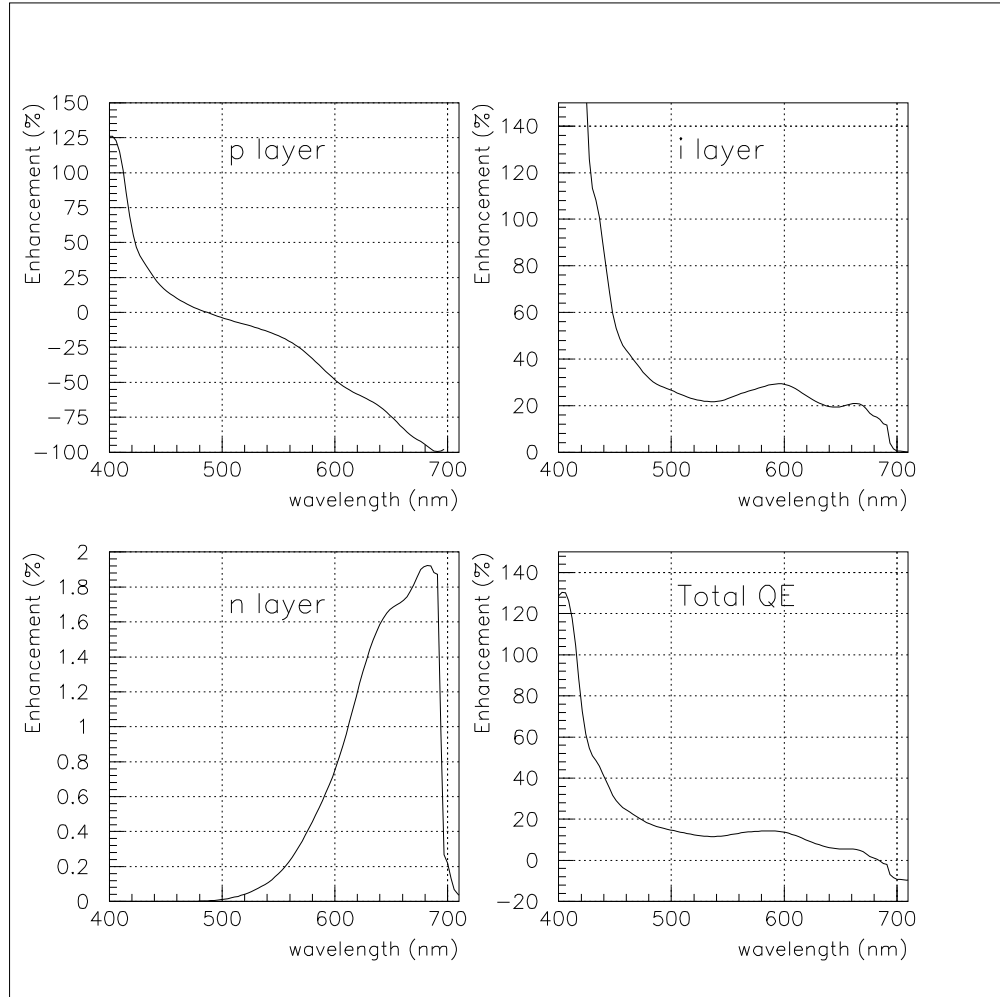


Figure 5.11: Percentage increase in QE for p, i, n layers and total enhancement for a graded p - i - n device relative to an ungraded control.

the p layer current. In this example the QE reaches a clear optimum. Relatively small changes to the diffusivity can have significant effects on the behaviour of the QE at high aluminium fractions.

The common feature of such theoretical studies is the increase of QE up to $X_{b1} \sim 50\% \pm 5\%$. Thereafter, more optimistic parametrisations of \mathcal{D} than that used in the figure show a QE which continues to increase monotonically as a function of X_{b1} , albeit at a slower rate.

We conclude that a successful grade in a cell with $X_{b2} \sim 30\%$ requires a grade of approximately $X_{b1} \geq 40\%$. A higher grade is not expected to significantly affect the overall short circuit current, and may in fact improve it, depending on the depth dependence of the diffusivity. This is partly due to the fact that two enhancement mechanisms are present, and that even devices with disappointing transport parameter profiles will benefit from enhanced i region QE because light intensity QE enhancement mechanism is independent of transport and is greater for higher grades.

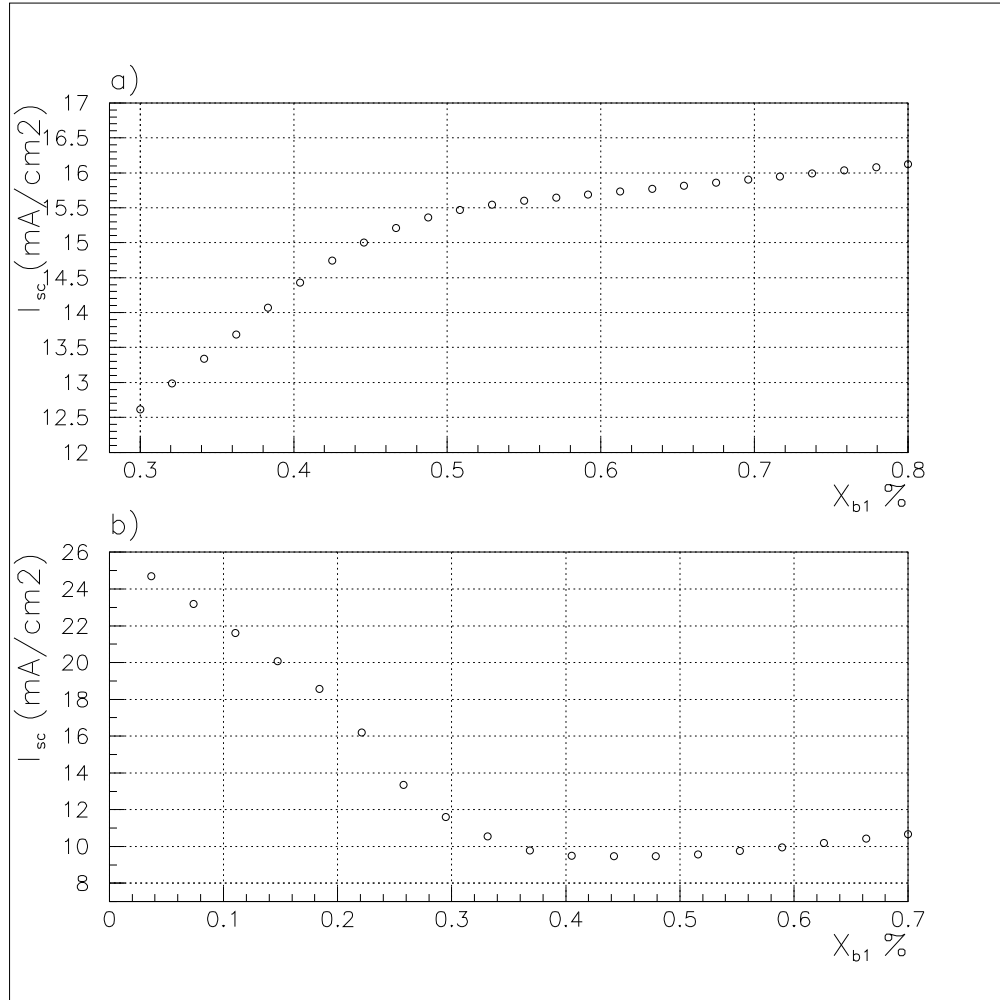
The choice of the higher aluminium fraction is not therefore critical from a modelling point of view. It is possible to favour one enhancement mechanism over another without seriously affecting the overall short circuit current.

In real devices, however, this must be offset against the technological problems involved in growing and processing $\text{Al}_x\text{Ga}_{1-x}\text{As}$ layers which are graded to high aluminium fractions over the short distances involved.

We note finally that in good material, a grade may in fact reduce the overall J_{sc} . Figure 5.12 b) shows the extreme example of a series of J_{sc} predictions starting with a good GaAs cell. In this case the QE of the cell is rapidly degraded as the efficient GaAs material at the front of the cell is replaced with $\text{Al}_x\text{Ga}_{1-x}\text{As}$ with increasing aluminium fraction.

5.2.5 Windows

Figure 5.13 shows the QE of an ungraded p layer with and without a window for a recombination velocity of 500m/s , which is frequently observed in our samples.

Figure 5.12: J_{sc} of a graded p - i - n cell as a function of the higher bandgap X_{b1}

If we assume the recombination velocity is unchanged, we see a significant increase in QE because less light is lost before the incident spectrum reaches the p layer. However, removal of the window layer is expected to increase surface recombination. The lowest curve on the graph shows the worst case scenario of a recombination which is large enough to force the minority carrier concentration to negligible levels at the front of the cell. We note that increased light transmission in this case cannot compensate the loss of carriers at the surface.

The behaviour in graded structures however is different. Appendix A shows that the effect of surface recombination is reduced by the effective field. In good material with appropriate contacts (see chapter 6), the surface recombination velocity is expected to be very small compared to the effective field term.

Figure 5.14 shows calculations analogous to those of figure 5.13 but for a structure graded from 30% to 67% aluminium. In this case, both calculations assuming an unchanged surface recombination and a worst case infinite surface recombination after removal of the window predict an enhanced QE .

Although the predicted gain in QE is not large, we conclude that window removal may be beneficial because the graded p layer fulfills the function which the window is designed to perform.

5.3 Further QE Enhancement Below the Barrier Bandgap

The quantum wells in a standard QWSC design typically absorb less than half the incident light. The remaining fraction is absorbed in the substrate and does not contribute to the photocurrent.

The quantum well photocurrent can be increased by ensuring that the light is reflected back through the cell after the first pass. This is achieved by removing the GaAs substrate and coating the back of the n layer with a metallic back surface mirror, as described in chapter 6

This technique has consequences for all optical functions associated with the

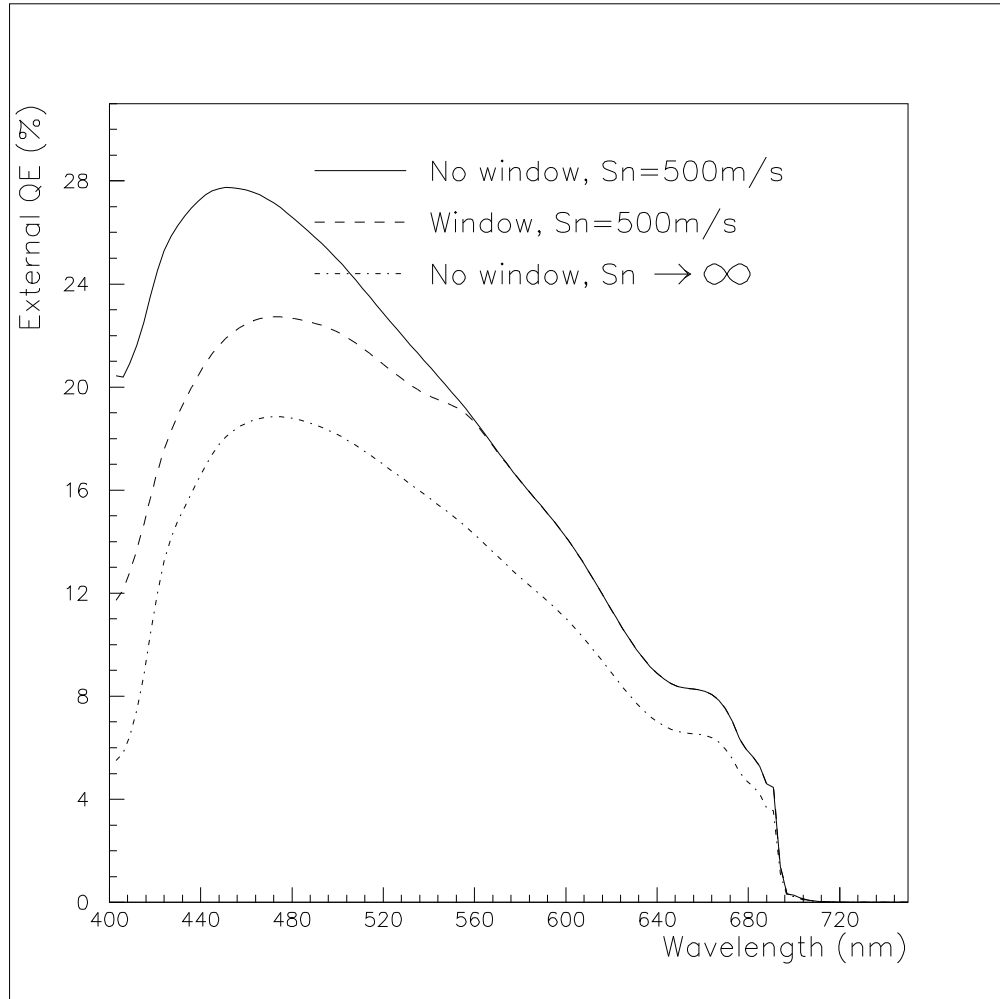


Figure 5.13: Influence of window layer removal on the QE of an ungraded p layer, including surface recombination effects

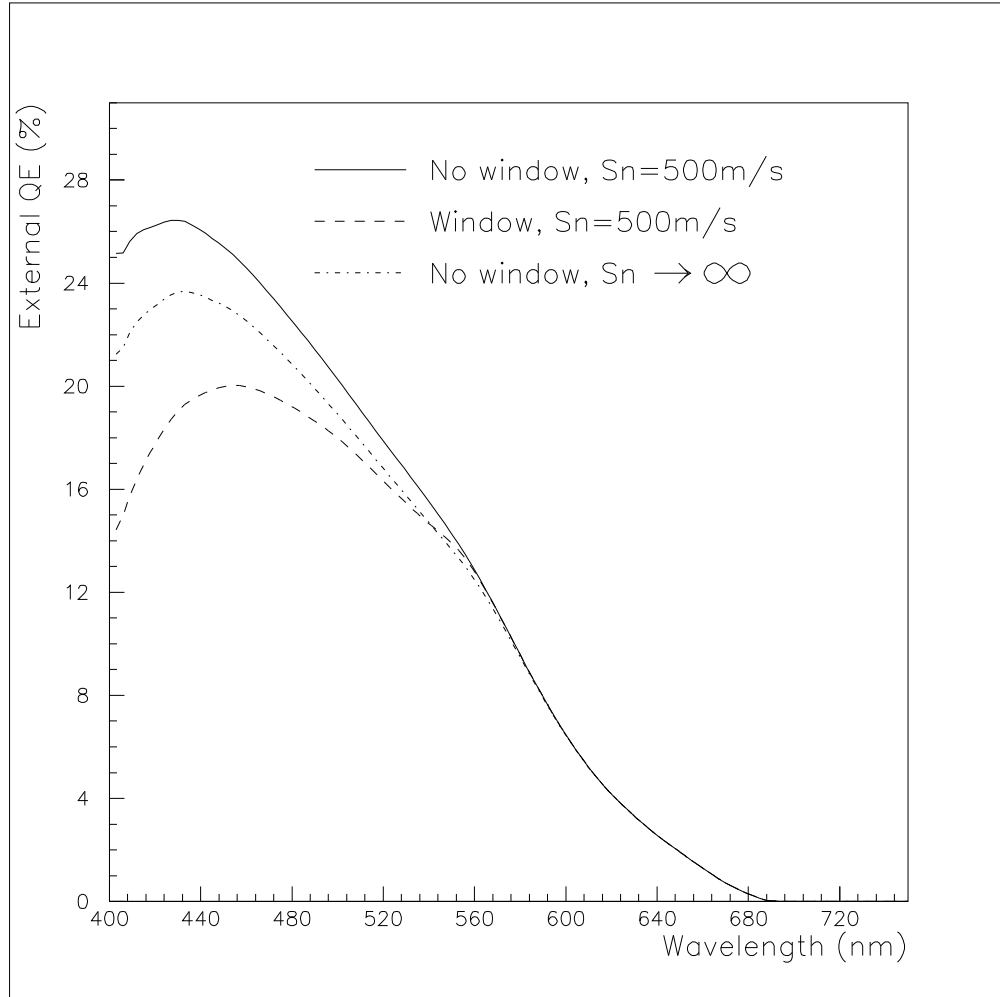


Figure 5.14: Influence of window layer removal on the QE of a graded p layer QE , showing weak dependence on surface recombination velocity

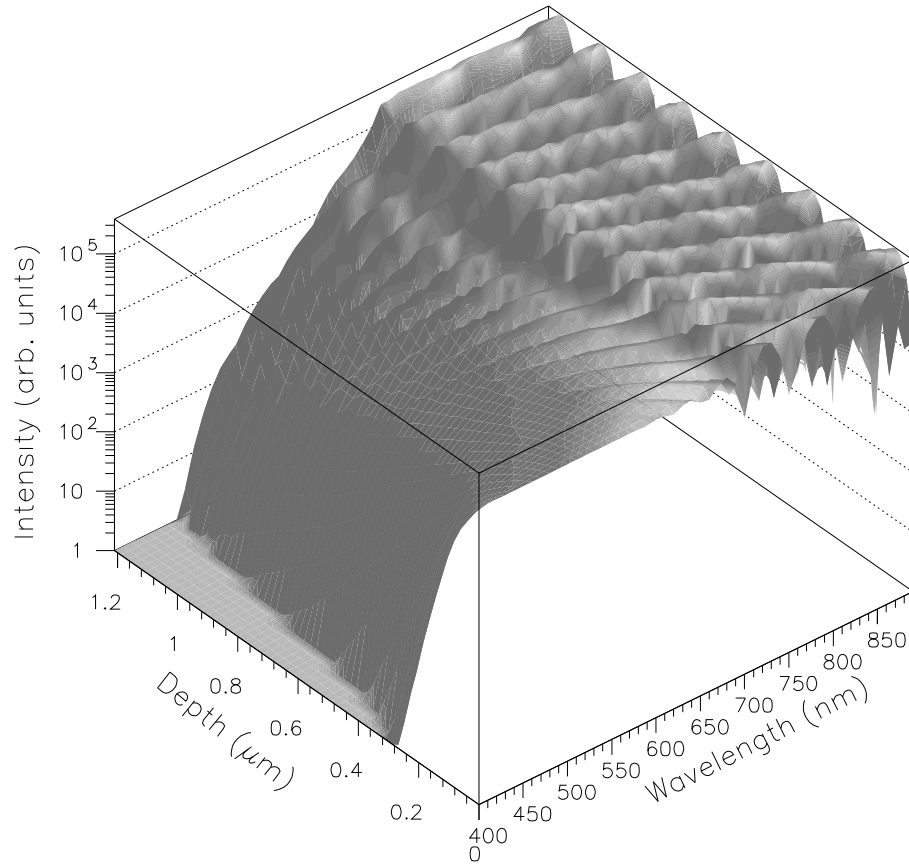


Figure 5.15: Light flux in a mirror backed QWSC

cell, which are examined in the following sections.

The modelling results presented assume a measured wavelength dependent front surface reflectivity and a back surface reflectivity of 95%.

5.3.1 Generation, Flux and QE in Mirrored Cells

Figure 5.15 shows how the addition of a back mirror alters the light intensity as a function of position in a QWSC. The light levels at long wavelengths are significantly increased. The main overall consequence is a more uniform light intensity throughout the solar cell. The position and wavelength dependent Fabry-Perot oscillations in light intensity are due to interference phenomena.

Figure 5.16 shows the generation rate of a 30 well graded QWSC as a function

of position and wavelength. The extended quantum well generation is clearly visible for wavelengths between 700nm and 870nm. The detail of the generation in individual wells is not visible since, as we saw in section 3, the model considers the i region as a weighted average of quantum well and bulk material.

Figure 5.17 gives the generation rate for an identical cell with a back surface mirror, again as a function of wavelength and position. Interference effects impose a strong position dependent oscillation in the quantum well generation which is absent in the non mirrored device.

The magnitude of the generation enhancement is visible in figure 5.18a, which shows the generation rates in both cases, integrated over wavelengths from 400nm to 900nm. Significant enhancements are seen for the i and n regions. In the design used for this example, insufficient light makes a second pass through the light to significantly affect the generation rate in the p layer.

Figure 5.18b shows the enhancement in the i layer, expressed as a percentage of the generation rate in the cell without a mirror. Since the QE of the i layer is proportional to the i layer generation rate, an enhancement of approximately 30% in QE is expected for this example.

Finally, figure 5.19 shows the QE enhancement expected in a 30 well ungraded QWSC with a back mirror, assuming 95% specular reflection from the back mirror and an internal front surface reflectivity given by the mean 70nm SiN AR coat. The breakdown in QE enhancement layer by layer is shown in figure 5.20. Contributions to the QE increase from the neutral p and n regions are expected to be negligible.

Enhancement for photon energies above E_{b2} is minimal since most of the light at these energies is absorbed during the first light pass.

The wavelength at which the Fabry-Perot oscillations in the QE spectrum appear are critically determined by the bulk bandgap E_{b2} . This provides a very useful characterisation tool for determining the exact value of E_{b2} in QWSC samples

The overall predicted i region enhancement in the quantum well absorption range is of the order of 25% for such a device. This enhancement ratio decreases

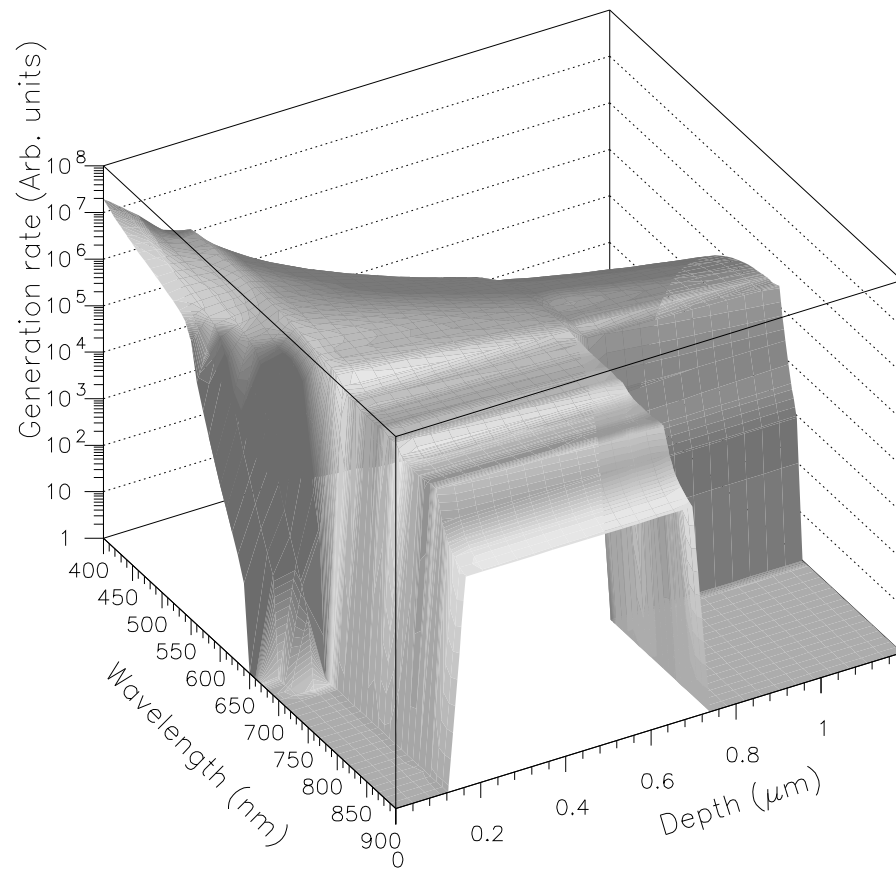


Figure 5.16: Generation rate in a 30 quantum well QWSC

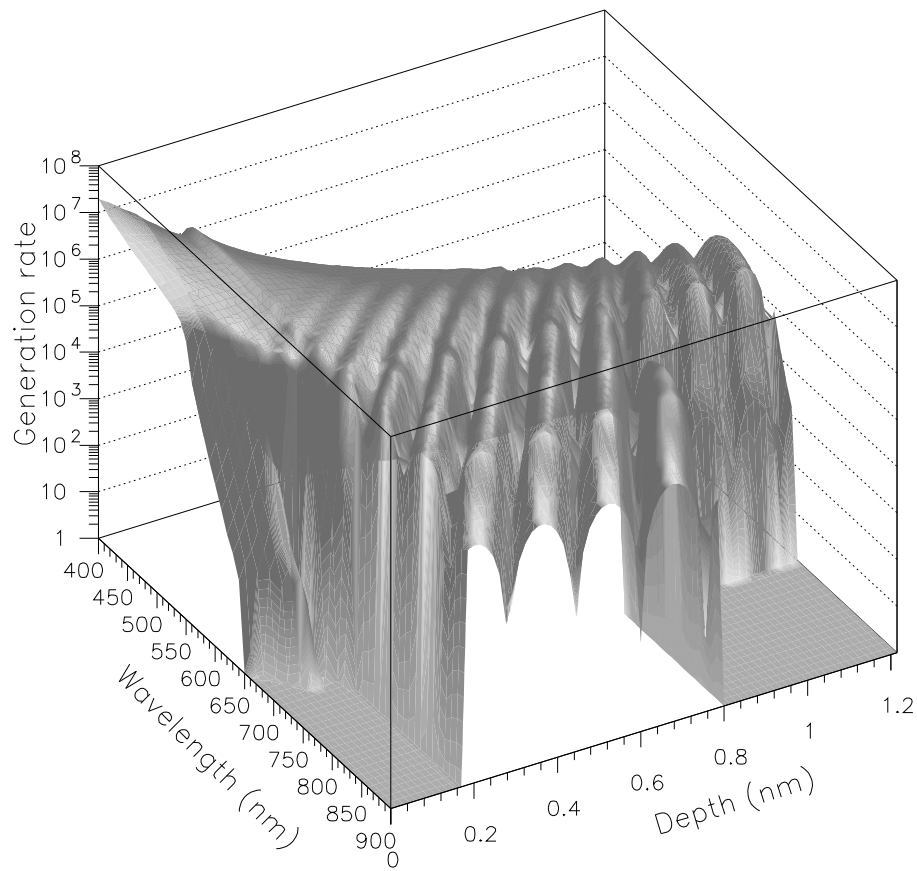


Figure 5.17: Generation rate in a mirror backed QWSC

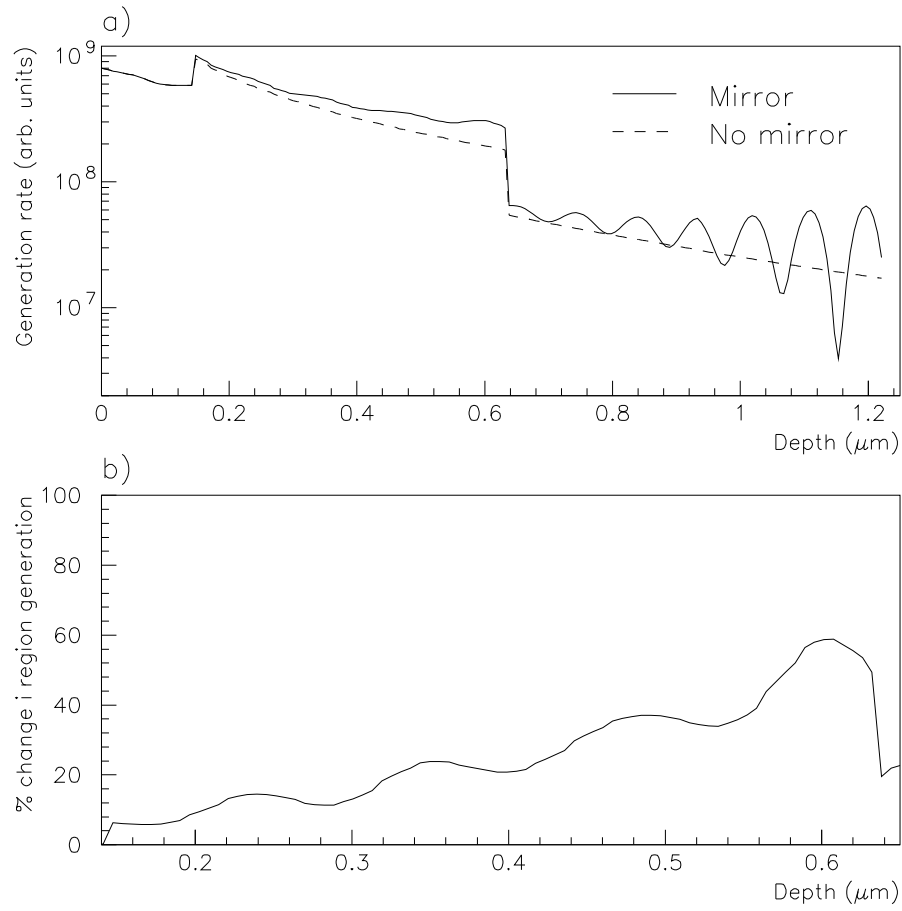


Figure 5.18: Generation rate enhancement a) in all layers of a graded QWSC with and without a back mirror and b) percentage increase in the intrinsic region.

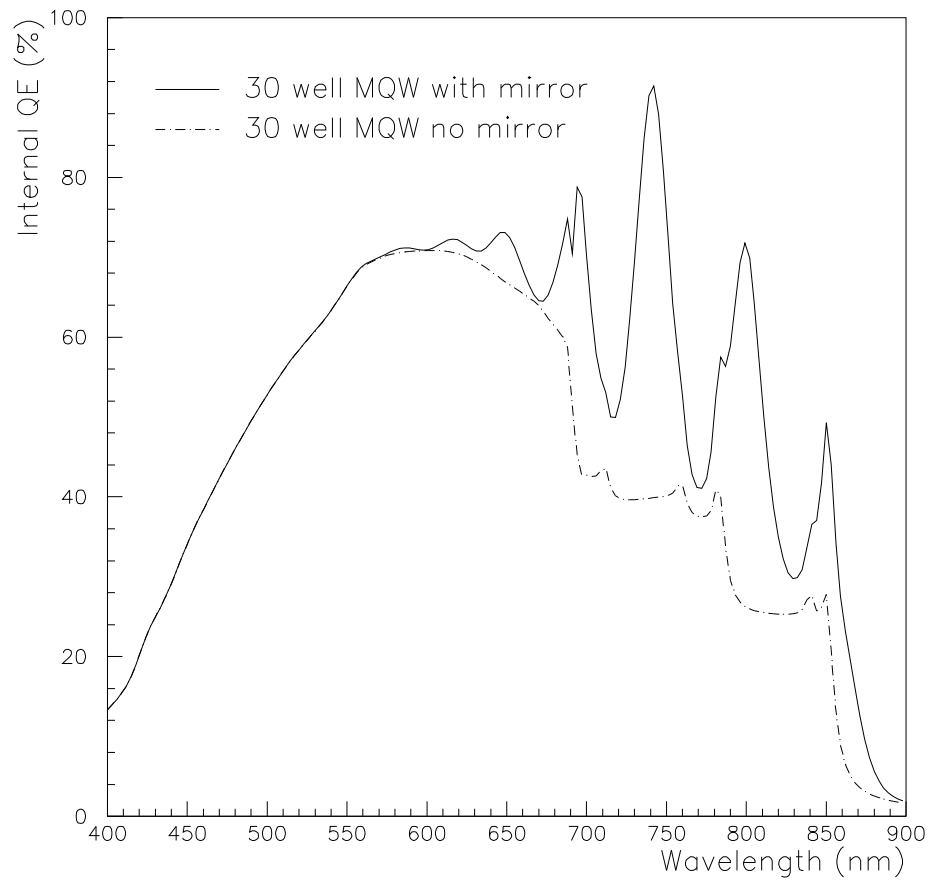


Figure 5.19: Quantum efficiency of a thirty well QWSC with a back mirror compared to an identical cell without a mirror.

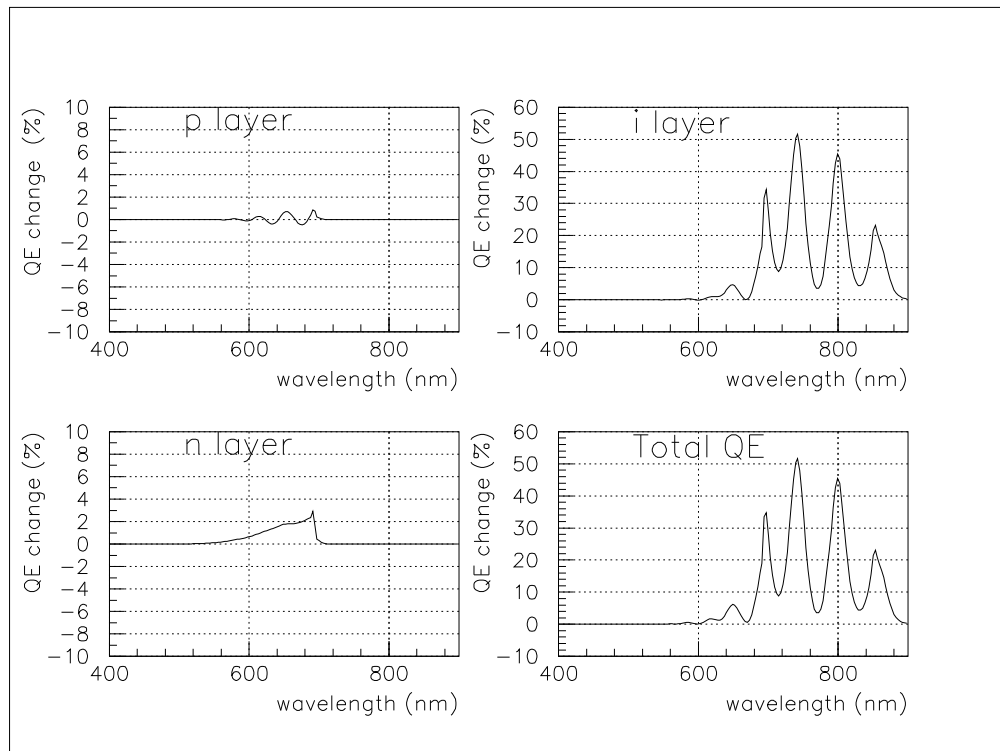


Figure 5.20: Absolute QE increase in a thirty well QWSC with a back mirror compared to an identical cell without a mirror.

to about 20% for fifty well samples because of the greater light absorption on the first pass.

5.4 Conclusions

In the preceding sections we have reviewed previous work on QE and J_{sc} enhancement in ungraded cells and explained the limitations of the optimisation in ungraded QWSCs.

We have separately considered further enhancements above the barrier bandgap for graded QWSCs and below the barrier bandgap for any QWSC cell.

Above the barrier bandgap we have seen that the spatial variation of optical and transport parameters increases the QE by reducing minority carrier generation near the surface of the solar cell and by increasing light transmission to the highly efficient i region.

The compositional grade results in improved carrier collection in a graded p layer because of the presence of an effective field. The consequent improvement in QE due to this mechanism is difficult to predict quantitatively because of the added complexity introduced by the spatial variation of materials parameters, and the assumptions made necessary by the lack of knowledge regarding the position dependence of transport parameters in particular. We have presented a modelling scheme which uses previously derived theoretical results in conjunction with published and measured experimental data to permit modelling of the QE of graded layers with a minimum set of free parameters.

The model in this case can only be used as a qualitative guide to suggest optimal parameters for graded p layers, but may be improved by comparison with experimental data.

Below the barrier bandgap the J_{sc} from the quantum wells can be greatly enhanced by coating the back of the QWSC with a mirror. The large fraction of light which is not absorbed upon a first pass is reflected back and forth in the cell, increasing light absorption in the quantum wells and hence the J_{sc} .

Chapter 6

Device fabrication and characterisation

The QWSC design is based on a MQW photodiode detector described by Whitehead [36]. Each successive generation of QWSC design passes through design, growth, processing and characterisation stages.

6.1 Sample Growth

Successive growth runs are determined by a combination of the characterisation of earlier samples and optimisations carried out using the short circuit current model. Sample growth was carried out using two epitaxial growth techniques, which are briefly described below.

6.1.1 Metalorganic Vapour Phase Epitaxy (MOVPE)

MOVPE growth was carried out by John Roberts at the EPSRC III-V Semiconductor Facility at Sheffield University using a Quantax MOVPE reactor. Details are given in reference [70].

MOVPE growth consists in passing reagent chemicals in vapour form over a heated substrate. The precursor gases dissociate at the surface of the substrate, depositing atoms at the rate of about one monolayer per second.

Substrate temperatures in our case varied between 560C and 600C. For the $\text{Al}_x\text{Ga}_{1-x}\text{As}$ system, the reagents were trimethyl gallium (TMG, $\text{Ga}(\text{CH}_3)_3$), trimethyl aluminium (TMA, $\text{Al}(\text{CH}_3)_3$) and arsine (AsH_3).

The p-type dopant in early studies was zinc in the form of dimethyl zinc (DMZ, $\text{Zn}(\text{CH}_3)_2$). This was later switched to carbon doping in the form of CCl_4 to reduce p-type dopant diffusion. n-type doping was achieved using disilane (Si_2H_6). These reagents are transported to the growth chamber in a hydrogen carrier gas at atmospheric pressure.

The MOVPE growth technique has a number of attractive features. The most interesting from the perspective of solar cell production is the high productivity, given that commercial MOVPE reactors are currently capable of growth on many wafers at the same time. Moreover, the gas sources used in growth can be replenished without shutting down the reactor. MOVPE growth is therefore significantly cheaper than some other epitaxial growth methods.

Compositional control is, in principle, lower in MOVPE than in MBE and suffers from a lack of in-situ measurement techniques such as reflection high energy electron diffraction. Accordingly, growth mechanisms in MOVPE are less well understood than in MBE in particular. Nevertheless, near monolayer control is routinely achieved in good MOVPE material.

However, most of the MOVPE material we have characterised suffers from electrical problems due to high background doping levels. As we saw in chapter 2, a high background doping adversely affects the open circuit voltage of the QWSC. Early material showed tolerable net dopant densities. We shall see in subsequent sections that a lower silicon background doping density, for example, may in fact lead to a higher background doping density due to the loss of a compensation effect for the carbon background.

6.1.2 Molecular Beam Epitaxy (MBE)

Molecular beam epitaxy was performed by Christine Roberts in the III-V Interdisciplinary Centre for Semiconductor Materials in Imperial College.

MBE growth consists in firing collimated beams of molecules at a substrate heated to between 480C and 630C, which is situated in an ultra high vacuum growth chamber. Collimated molecular beams are generated in heated crucibles, which contain the precursors in solid or liquid form. Evaporation produces the molecular beam. The molecules dissociate at the surface of the substrate, depositing the metal atoms.

Compositional control is achieved by changing the temperature of the solid sources. Very sharp compositional changes of the order of a monolayer are possible simply by placing a shutter in front of any given source. The sample is generally rotated during growth to ensure uniform growth across the wafer.

Dopants in this study are Be for p-type and Si for n-type $\text{Al}_x\text{Ga}_{1-x}\text{As}$. As we shall see in subsequent sections, the Be dopant is prone to significant diffusion at the doping levels and growth temperatures used in this study.

This growth method is relatively well understood, since an array of characterisation tools may be placed in the growth chamber. A review of these characterisation tools has been written by Foxon [38].

The method is complementary to the MOVPE technique. It is inherently more costly, but can achieve higher purity due partly to the use of UHV techniques, cryogenic paneling, the wide range of in-situ characterisation techniques available, and the relatively well understood growth mechanisms.

Although the background doping levels in MBE material were generally low, decreasing material quality with increasing aluminium fraction has consistently been observed.

6.2 Processing

Processing was carried out by Malcolm Pate at the III-V Semiconductor facility at Sheffield. This last stage before obtaining finished devices is critical, since the devices are exposed to potentially damaging environments.

The most common device configuration is the mesa photodiode. The early studies described in reference [8] used both anti-reflection coated (AR) and non

AR coated (NAR) versions of this structure in order to save processing time on poor material. This study concentrates on the AR coated devices.

The principal stages of the processing routine are tried and tested, and involve relatively few processing steps. Reference [61] gives a summary. The principle innovation is the addition of a back surface mirror. We now outline the main steps involved in turning a piece of QWSC wafer into the finished device.

6.2.1 Device Geometry

The photodiode devices are $1000\mu m$ circular mesa structures defined by photolithography followed by an etch. Gold ring contacts are then laid down on the mesa, defining the $600\mu m$ diameter optical window.

NAR devices retain the protective $\sim 40nm$ thick GaAs capping layer which is grown on the front surface of the cell to prevent $Al_xGa_{1-x}As$ oxidation and surface damage in handling. AR devices are subjected to two further steps. The first of these is the removal of the GaAs capping layer with a selective etch which stops short at the $Al_xGa_{1-x}As$ window, which acts as an etch-stop. A reliable etch stop requires an aluminium fraction of at least 30% Al.

Following the removal of the cap, a SiN AR coat of thickness $\sim 70\text{\AA}$ is deposited onto the optical window. This step involves a brief exposure of the unprotected device to air, followed by device exposure to a silane/nitrogen plasma deposition machine at about 300C. SiN is deposited at a rate of approximately 50nm per minute.

Where possible, a piece of unprocessed QWSC wafer is AR coated at the same time as the devices, since these are too small to allow accurate measurement of the reflectivity. Such pieces of wafer were received for about half the samples processed.

Design and processing of large area devices follows similar steps and is described in [66].

6.2.2 Mirror Backed Devices

The addition of a back mirror to the QWSC devices was first tried with mesa photodiode devices. The initial steps are identical to those listed in the previous section. In addition to these, however, the light absorbing GaAs substrate is removed only under the optical window with a selective etch which uses the n layer as an etch-stop.

This leaves a $\sim 300\mu m$ hole of diameter $\sim 600\mu m$. The gold metal constituting the mirror is then deposited in this hole, in direct contact with the back surface of the n layer.

6.2.3 Effects of Processing

Exposure of QWSC wafers to processing leads to unavoidable consequences in device performance. Effects which are directly related to processing include the wavelength optimisation of the AR coat and the electrical characteristics of the solar cells. The former may be improved by tuning the thickness of the AR coat to suit a particular cell, whereas the electrical characteristics such as series and parallel resistance may be optimised by the choice of appropriate alloys and mask sets at the contacting stage.

Other processing effects are accidental and relate to the internal quantum efficiency of the devices. The removal of the cap has been known to cause problems in some MBE material for reasons as yet unknown, leading to a poor window surface. Malcolm Pate has reported difficulties with the etch stop in some cases. This may be due to poor material quality at the surface, or an unexpectedly low aluminium mole fraction at the front surface.

Another source of damage is oxidation following the removal of the protective cap and subsequent exposure of the topmost $Al_xGa_{1-x}As$ layers of the cell to air. Since these $Al_xGa_{1-x}As$ layers are particularly susceptible to oxidation, this exposure must be as brief as possible to avoid oxygen diffusion through the thin $Al_xGa_{1-x}As$ window to the p layer beneath.

A general decrease in device quality is generally seen as the number of pro-

cessing steps is increased. This is particularly visible in mirrored samples which show variable device quality. Surface contamination is frequently observed in these samples.

On the other hand, we shall see in subsequent sections that there is evidence to suggest that the AR coating stage has a passivating effect, leading to improved electrical characteristics in forward bias for initially poor devices. High quality samples on the other hand are generally degraded by the AR coating process.

We conclude that the processing stage unfortunately introduces a variability in the characteristics of the finished QWSC devices. This variability is difficult to ascribe to any given cause, even with the limited number of steps involved.

6.3 Characterisation

Experimental data were obtained using equipment designed and built by Mark Paxman and described in reference [8]. The two routine characterisation tools are photocurrent (PC) spectroscopy, monochromatic current-voltage (MIV), and measurements of the anti-reflection coating (AR measurements).

Other characterisation techniques carried out by collaborators include transmission electron microscopy (TEM) and secondary ion mass spectroscopy (SIMS).

6.3.1 Photoconductivity Experiment

QE, MIV and AR measurements were all carried out on the photoconductivity rig which has been extensively covered in references [8], [67] and [62].

Illumination is provided by a tungsten-halogen lamp. The light is passed through a grating monochromator which is capable of wavelength resolution of the order of $0.3nm$ (reference [8]). Two power supply units (PSUs) enable the device to be driven to reverse or forward bias.

A pinhole placed at the exit slit of the monochromator transmits light to a collimator. The image of the pinhole is then projected on to the surface of the device. The diameter of the pinhole must be made smaller than that of the optical

window in order to ensure that no light is lost by reflection from the contacts. The light power incident on the device is usually of the order of 100nW.

The light beam is modulated by a chopper wheel at $\sim 180\text{Hz}$. A lock-in amplifier is then used to measure the resulting photocurrent. The use of lock-in techniques ensures that the DC background due to ambient light and the dark current is removed from the measurement.

The incident power is measured by a calibrated silicon photodiode placed at the same position as the QWSC. This additional calibration measurement can then be used to compute the QE as a function of wavelength.

The experiment is controlled by a computer running a Turbo Pascal program written by Mark Paxman. It should be noted that measurements at short wavelengths are prone to large errors because of the low reponse of the Si photodiode in this wavelength range. The error over most of the wavelength range has been quoted as $\sim \pm 5\%$ in reference [8].

Measurements performed on this rig are AC and are designed to eliminate DC signals due to the dark currents of both the solar cell devices and the detector. The resulting measurement gives the photocurrent, as opposed to the DC light current which includes a dark current component.

6.3.2 Monochromatic current-voltage characteristics

Monochromatic IV (MIV) measurements consist of measuring photocurrent as a function of applied bias at a fixed wavelength. The measurement is normalised to 100% at the voltage independent saturation level reached in reverse bias. This technique provides information on the quality of both growth and processing.

Measurements are normally carried out above the bulk band-edge in order to prevent distortion of the MIV with voltage because of the modification of quantum well absorption with Stark shift. Below the bulk band-edge, full QE measurements (see section 6.3.3 below) as a function of bias must be taken in order to identify a wavelength range in which the QE is relatively insensitive to the Stark shift.

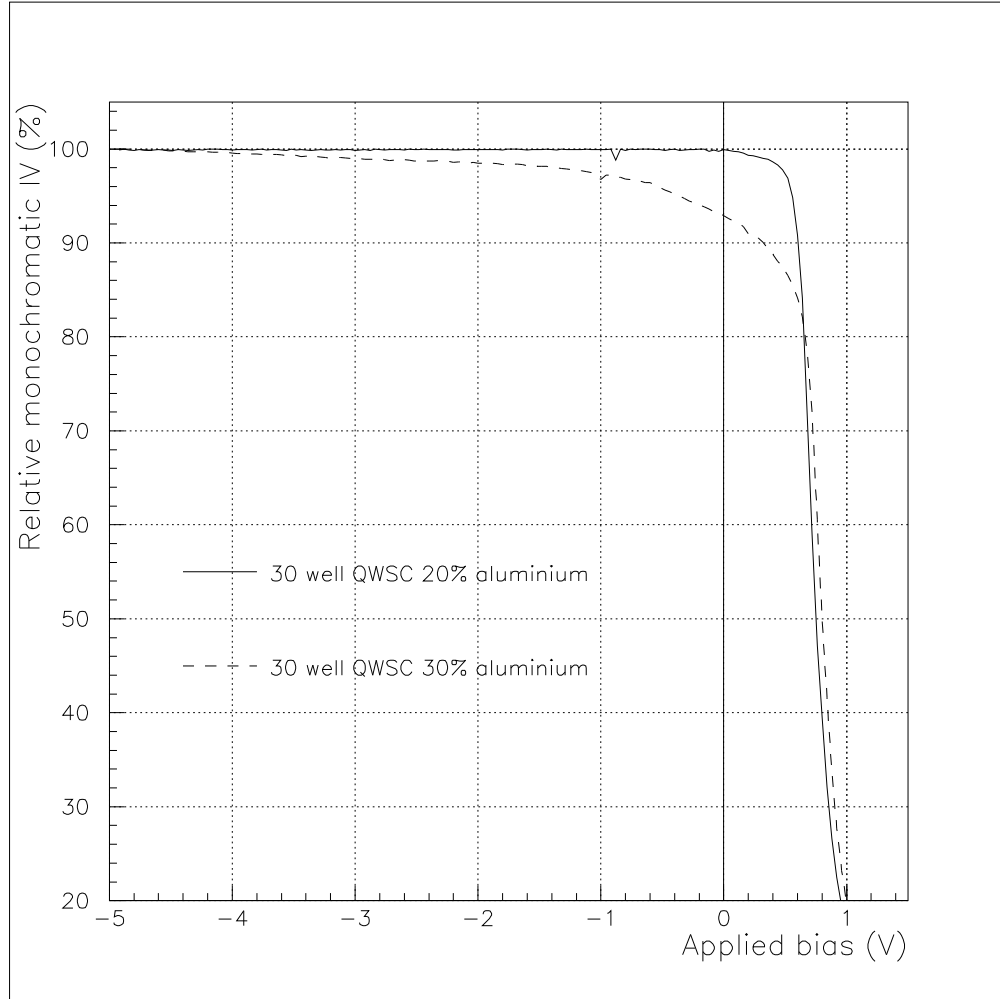


Figure 6.1: Typical MIV curves for good and moderate solar cell devices.

Typical MIV curves for good and moderate devices are shown in figure 6.1. The "square" curve, showing a MIV which starts to fall off at zero bias was measured for a 30 well MBE grown ungraded QWSC with $X_{b2} \simeq 20\%$. The second curve showing a MIV which starts to decrease at -4V represents data for an identical sample grown in the same series with $X_{b2} \simeq 30\%$.

Good devices such as the 20% sample maintain a constant photocurrent into forward bias. At a moderate forward bias, the signal falls abruptly. A cut-off occurring in forward bias may be due to the failure of the experimental technique, since the lock-in amplifier begins to detect the increasingly large AC variation in the dark current caused by the chopped light. Details of these problems have been given by Paxman [8] and Barnes [67]. In reverse bias, the MIV remains constant

until the breakdown voltage, not shown here because the MIV measurement does not measure the dark current. At this point, the dark current increases very rapidly. Detection of the photocurrent against this background becomes difficult, and the resulting data noisy.

Devices with significant background doping levels such as the 30% device show a photocurrent which falls off at voltages well below the V_{oc} . This current drop is due not to the increasing influence of the dark current, but to the decrease in field across the intrinsic region, and subsequent failure of the p - i - n structure to operate as a solar cell.

With increasing reverse bias, the PC of such cells reaches a maximum. We saw in section 2.3.2 that the voltage at which the drop in photocurrent occurs can be used to estimate the background doping. The method however becomes inaccurate for devices with doping levels in excess of $\sim 10^{16}\text{cm}^{-3}$ and in samples which do not conform to the abrupt p - i - n doping profile assumed in the model.

Device quality

Many devices of lower quality depart significantly from the picture described. This may be due either to growth or processing problems.

Samples with doping profiles which do not conform to the sharp p - i - n doping profile assumed in the previous discussion will behave in a more complex manner. If for example the voltage is varied from negative to positive bias, the p and n side depletion widths will vary in a manner which reflects the doping profiles on both sides. An estimate of this profile may only be obtained if the one is much greater than the other.

In practice, this method cannot be exploited further because such variations may also result from device history. Difficulties in processing in particular may lead to electrical problems. This may be manifest as a very noisy MIV measurement or as the absence of a plateau in reverse bias allowing the curve to be normalised to 100%.

We conclude that the MIV measurement is useful in identifying promising devices and furthermore indicates whether the devices conform to the idealised

structure assumed by the modelling programs.

6.3.3 Quantum efficiency measurements

Measurements quoted in chapter 7 are always taken at voltages for which the i region of the cell is fully depleted, in order to maintain the field across the i region and fulfill the assumptions in the model. Although the PC spectrum in the wells moves with applied bias due to the Stark shift, this dependence is quoted by reference [60] as being of the order of meV for typical biases of up to a few volts and shifts the quantum well absorption edge by only a few nm for the moderate biases used in the measurements.

The MIV technique of the previous subsection provides a useful guide to the voltage at which the QE measurement should be taken.

6.3.4 Reflectivity measurement

The last routine characterisation tool is the reflectivity experiment. A slight modification of the experimental setup described above is required. As mentioned in section 6.2, pieces of wafer are generally AR coated at the same time as the photodiode devices. Direct reflectivity measurements are possible on large area devices.

The reflectivity measurement consists of placing the AR coated sample at the position normally occupied by a device. Light reflected from the surface is collected and measured by the Si photodiode at as low an angle as possible. The sample is then removed, and the incident power measured directly by the Si photodiode, the optical path length being kept constant. The reflectivity is then given by the ratio of the two signals. Beam angles are typically below 5 degrees. Measurements were repeated on different dates and a maximum error of about 5% in reflectivity at long wavelengths was found.

A good knowledge of the reflectivity is required for accurate modelling of QE spectra. For some photodiode devices however, pieces of AR coated wafer were unavailable. In this case, we are forced to use an average of previous measure-

ments for the AR coating method used. A significant error is introduced in this case, which may be qualitatively reduced by examining the devices under a light. Typical AR coats are a characteristic blue colour.

Reflectivity measurements give additional indications of processing or growth problems. This is typified by a large variation in reflectivity over the AR coated sample.

6.3.5 External characterisation

In addition to the experiments described above, more sophisticated characterisation techniques were applied to a selection of structures by collaborators.

Transmission electron microscopy (TEM)

TEM measurements were carried out by Professor Grunbaum in the Materials Department of Oxford University.

Transmission electron microscopy consists of firing a collimated electron beam through a thinned cross section of a sample. The electron beam is diffracted by the crystal lattice, and the diffraction pattern recorded on a fluorescent screen or on photographic film. Details of this technique are given in the review articles by Holt [63] and Hutchinson [64].

Resolution of the order of 0.15nm is possible on state of the art microscopes. Compositional contrast is possible because of the different electron beam scattering factors for $\text{Al}_x\text{Ga}_{1-x}\text{As}$ with different values of x . TEM micrographs can therefore give unprecedented direct measurement of the physical dimensions of QWSC samples. Measurements were carried out on selected samples to verify the dimensions of the quantum wells in particular, and of the larger scale p layer thickness.

Secondary ion mass spectroscopy (SIMS)

SIMS measurements were carried out by Federico Caccavale of Padua University.

The technique is described in detail by Clegg [65]. This measurement involves

firing a collimated beam of ions at the sample. The high energy incident beam removes atoms from the first few monolayers of the sample. The flux of these sputtered atoms is then measured by a mass spectrometer.

The incident beam progressively digs a pit in the surface of the sample, providing compositional information as a function of depth. The technique must be tuned by choice of incident atomic beam and mass spectrometer setting to detect the spatial variation of different elements. The focus in the two measurements carried out for this project was the variation of doping density and aluminium composition with depth.

Depth resolution is dependent on factors including the type of atom used in the incident beam and the beam energy. Use of oblique incident atomic beams and non-normal incidence to prevent mixing at the surface of the sample can achieve resolutions of the order of a few nm.

6.4 Conclusion

In this chapter we have described growth, fabrication and characterisation of QWSC devices. We have seen that the behaviour of the finished devices may depart significantly from the theoretical picture given in previous chapters. Both growth and processing may contribute to this deviation.

The most readily identifiable problem is that of background doping. This is revealed by MIV measurements, which are also used to suggest an appropriate bias at which to measure the QE.

Although QE measurements may be taken at zero bias in good material, it is frequently necessary to force the device into reverse bias to ensure that the approximations in the model are consistent with the experiment.

Reflectivity measurements are essential to a correct analysis of the QE of a device. In some cases such measurements had to be extrapolated from an average over previous AR coating runs.

Apart from these routine experimental tools, we have reviewed the SIMS and TEM characterisation techniques which were carried out by collaborators. These

additional characterisation methods may be used to verify or adjust the geometry and composition of QWSC samples.

Chapter 7

Preliminary Characterisation

In this chapter we present results of the MIV and reflectivity techniques reviewed in chapter 6. These are the preliminary characterisation tools used to make an estimate of the device quality. The reflectivity furthermore is required for subsequent analysis of quantum efficiency data.

The samples in this chapter are referred to by their growth name, and relevant design characteristics are given in the text.

7.1 Monochromatic IV Measurements

A good device is characterised by a MIV curve which remains constant into forward bias, before showing an abrupt cut-off for reasons given in chapter 6. If this cut-off occurs at forward biases greater than about 0.6V, attribution is difficult because of experimental considerations.

If the cut-off occurs at reverse bias and the acceptor, net background and donor doping levels N_A , N_{BG} and N_D layers are abrupt, the drop in photocurrent can be related to the net background doping level N_{BG} , as described in chapter 2.

Calculations of N_{BG} for a range of cut-off voltages are shown in table 7.1. The variation of predicted N_{BG} is only weakly dependent on the cut-off voltage V_S . The technique can therefore only provide a rough estimate of N_{BG} , because the values of V_S generally vary only within a few volts. A further limitation is

V_s (V)	0	-2	-4	-6	-8	-10
N_{BG} ($10^{16}cm^{-3}$)	1.0	2.0	3.0	4.0	5.8	5.9

Table 7.1: Predicted value of net background doping N_{BG} for a range of MIV cut-off voltages V_s , for a standard 30 well QWSC sample with $X_{b2} = 30\%$

introduced by the poorly understood electrical influences on the MIV characteristic, and by the fact that the abrupt doping assumption is frequently erroneous, as shown by SIMS measurements in chapter 8. The position dependence of the p layer doping in particular has been investigated by SIMS in both MOVPE and MBE samples. This position dependence introduces a further voltage dependence which makes the precise attribution of the MIV voltage shoulder difficult. Furthermore, the shoulder is generally imperfectly defined in poor samples, and may be subject to errors of several volts.

Jenny Nelson has developed a model, in collaboration with Alex Zachariou, which estimates the background doping by modelling the QE at zero volts, and using N_{BG} as the main fitting parameter. Varying N_{BG} in this model alters the effective p, i and n layer thicknesses. The p layer in this case is modelled as two undepleted layers with doping levels N_A and N_{BG} respectively. This approach allows a more quantitative estimation of N_{BG} , but nevertheless still assumes square doping profiles.

The model presented in this thesis does not use this approach. The MIV data in the following discussion is principally used as an indication of material quality. In particular, we will use it to qualitatively assess those samples in which N_{BG} is large enough to degrade device operation. We further use the MIV data as indicative of the reverse bias at which to take QE measurements.

MIV data for QWSC devices grown for this project is generally poorer than the corresponding data for the p - i - n controls. We now examine this trend as a function of growth method and describe the effect of changing growth conditions on this problem.

In the final part of this section we look at the effect of the AR coating process on the MIV characteristics of the samples, and compare these results with data

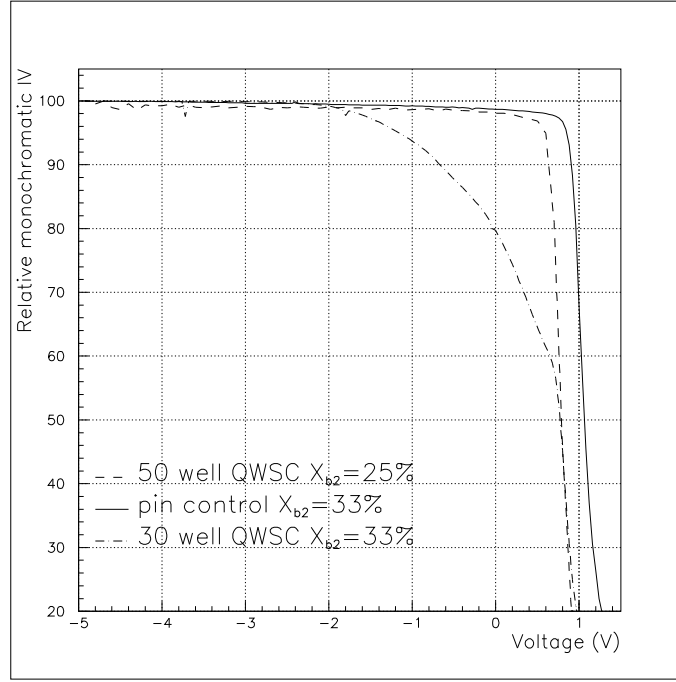


Figure 7.1: MIV data for an ungraded MOVPE grown 30 well QWSC and p - i - n control pair with $X_{b2} = 33\%$ aluminium before AR coating, showing deterioration of MIV in QWSC devices

from a passivation study carried out at Eindhoven University of Technology as a result of these observations.

7.1.1 Trends in QWSC and p - i - n Device MIV Data

MOVPE Devices

Figure 7.1 shows MIV data for the MOVPE grown 30 well QWSC and p - i - n control pair QT468a and QT468b. The nominal aluminium composition is $X_{b2} = 33\%$. Neither device in this example is AR coated in order to minimize the variability introduced by processing. Also shown is data for a 50 well QWSC grown previously on a different MOVPE reactor.

The MIV data for the 30 well QWSC device shows a voltage independent plateau in reverse bias. A cut-off is seen at about -2V. Assuming that this current decrease is due to a loss of field in the i region as explained in chapter 2, we can estimate the net background doping as $N_{BG} \simeq 2 \times 10^{16} \text{cm}^{-3}$. The net background doping for our MOVPE material is p type residual carbon [56].

The curve for the p - i - n device is constant up to the point at which the measurement becomes unreliable for reasons given in chapter 6. The MIV cut-off in this case cannot therefore reliably be attributed to a loss of field in the i region. The cut-off point at about 0.8V however allows us to estimate the upper limit of the net background doping as $N_{BG} \leq 5 \times 10^{15} \text{cm}^{-3}$.

The 50 well device MV370 of figure 7.1 was grown on the Sheffield MR100 machine, which was subsequently removed from the $\text{Al}_x\text{Ga}_{1-x}\text{As}$ growth program. The high quality MIV of this 50 well sample shows that QWSC devices with a large number of wells and a low net background doping can be grown by MOVPE. Data for other high quality MOVPE grown QWSC samples of this type have been published [49]. The data in this case again only allows us to set an upper limit estimate on the net background doping, which is $N_{BG} \leq 2 \times 10^{15} \text{cm}^{-3}$.

John Roberts [56] has suggested that the systematic difference in MIV seen between p - i - n and MQW samples may be caused by a lack of self compensation between oxygen and carbon impurities in samples with multiple quantum wells due to reduced oxygen impurity levels in the quantum wells. This leads to a higher than expected p type carbon background. Moreover, the difference in net background doping levels on either side of a quantum well barrier interface is expected to lead to poor interface quality and high interface recombination velocities.

John Roberts has further suggested that $\text{Al}_x\text{Ga}_{1-x}\text{As}$ material will have poor minority carrier transport properties despite the low net background doping levels, because of the high impurity levels. We shall see in subsequent sections that the $\text{Al}_x\text{Ga}_{1-x}\text{As}$ minority carrier transport properties decrease with increasing aluminium content, even though the net background doping levels observed in p - i - n structures such as that of figure 7.1 appear low.

Very poor MIV characteristics have been recorded for some MOVPE samples. Figure 7.2 shows the MIV data for optimised sample QT794a. This 50 well sample has no window, and a thin p layer nominally graded from $X_{b1} = 40\%$ to $X_{b2} = 30\%$. The MIV data in this case begins to drop off at -9.5V, suggesting $N_{BG} \simeq 3 \times 10^{16} \text{cm}^{-3}$. SIMS data taken by Federico Caccavale were aimed at

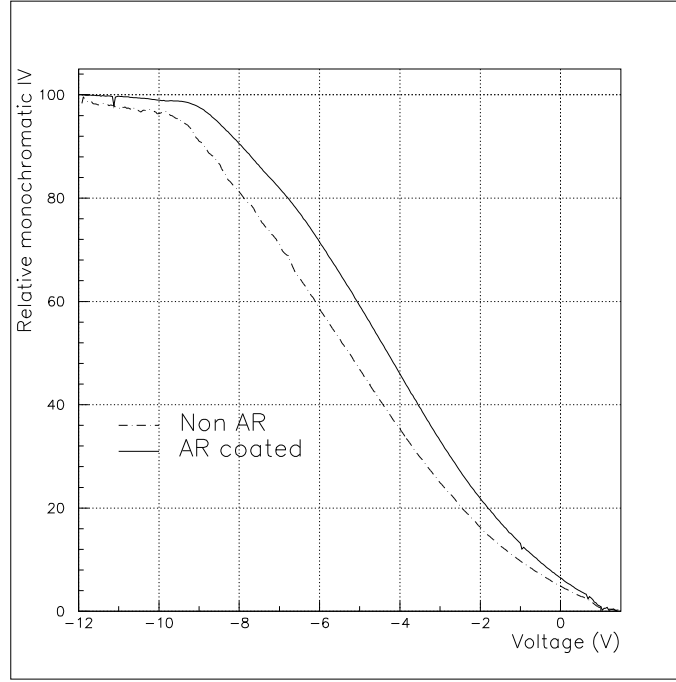


Figure 7.2: MIV measurements for optimised device QT794 for NAR and AR coated devices

verifying sample geometry, composition and intentional doping profiles. The p type carbon background doping sensitivity was $\sim 10^{17}\text{cm}^{-3}$ and was unfortunately too insensitive to verify this value of N_{BG} .

Further discussions concerning this sample in the QE modelling section of this chapter show that the minority carrier efficiency in this sample is severely reduced, as suggested by John Roberts.

MBE Devices

QWSC and p - i - n samples grown by MBE show a similar trend to MOVPE samples discussed in the previous section. Figure 7.3 shows the MIV data for three ungraded 30 well QWSC samples grown and processed in the same run. The nominal composition of these samples was $X_{b2} = 20\%$ for U2027, $X_{b2} = 30\%$ for U2029 and $X_{b2} = 40\%$ for U2031. Similar data for their respective controls U2028, U2030 and U2032 which have matching composition but no wells is shown in figure 7.4.

The data for the 20% p - i - n U2028 has been smoothed to eliminate noise

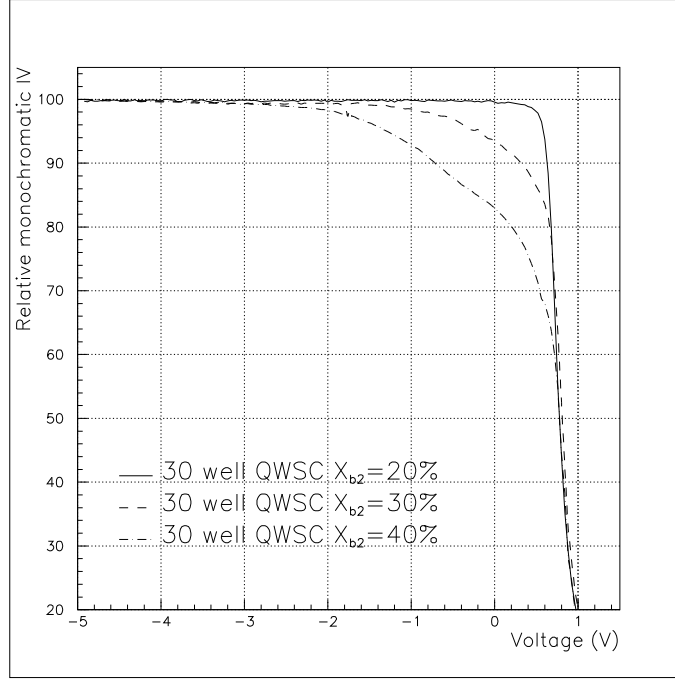


Figure 7.3: MIV data for a series of 30 well QWSC ungraded devices grown by MBE with nominal aluminium fractions $X_{B2}=20\%$, 30% and 40%

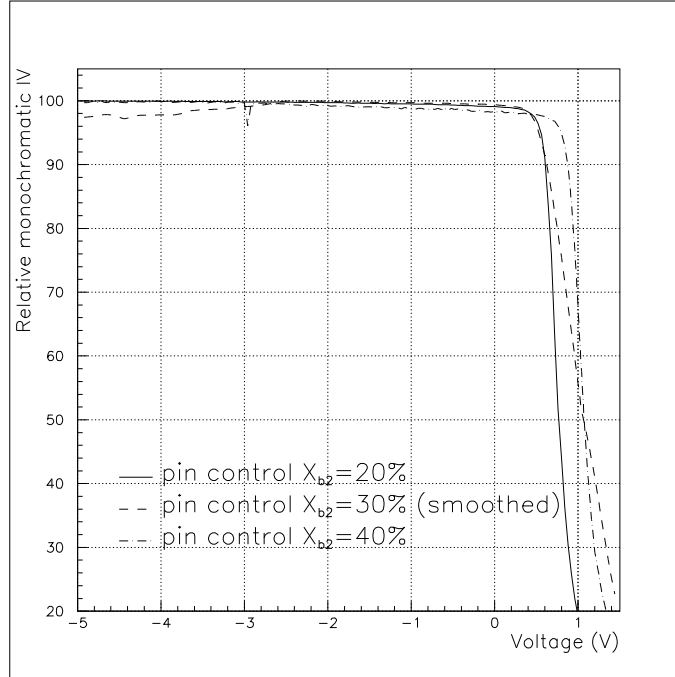


Figure 7.4: MIV data for a series of p - i - n ungraded devices grown by MBE with nominal aluminium fractions $X_{B2}=20\%$, 30% and 40%

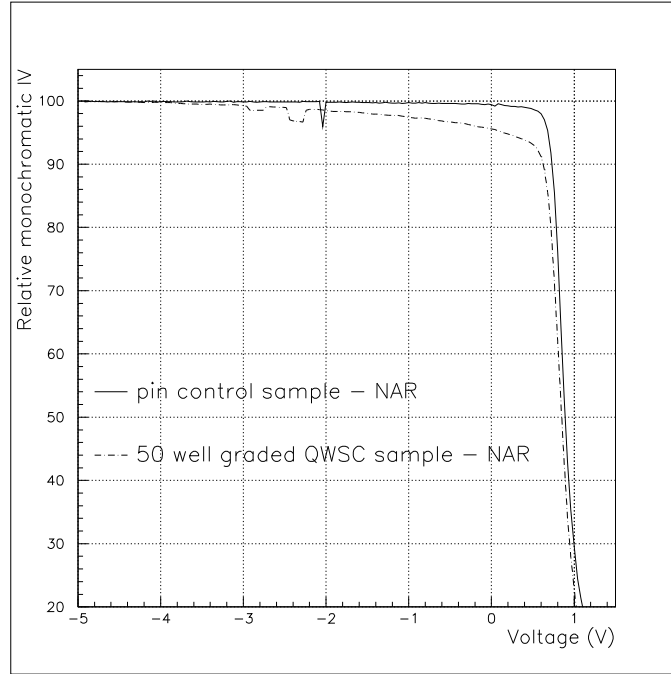


Figure 7.5: MIV data for the 50 well graded sample U6041 and its p - i - n control U6045, indicating low net background doping

spikes. We note that the MIV data at 20% are nearly ideal in both QWSC and p - i - n cases with estimated limits on the net background doping of $N_{BG} \leq 7 \times 10^{15} \text{cm}^{-3}$. The same limit is found for the 30% and 40% aluminium p - i - n samples.

The QWSC MIV data however become increasingly poor as the aluminium content is increased, whereas the p - i - n control MIV data remain good. Estimates of the net background doping yield values of $N_{BG} \simeq 2 \times 10^{16} \text{cm}^{-3}$ for the 30% and 40% QWSC structures. Although the two curves are significantly different, the MIV cut-off method of determining N_{BG} is not sufficiently sensitive to differentiate between the net background doping levels in the two samples. A model such as Jenny Nelson's model which was mentioned in the introduction to this section would however be more sensitive to N_{BG} in this case.

Finally, figure 7.5 shows MIV data for NAR devices processed from p - i - n and 50 well QWSC structures grown in the latter part of this project. Although the nominal lower aluminium fraction X_{b2} for these samples was 30%, modelling in both cases indicates a much lower $X_{b2} \simeq 24\%$. Similar behaviour is again

apparent, with the p - i - n sample performing better than the QWSC.

In this case, however, a phenomenological difference with the 30 well samples of figure 7.3 can be seen. Instead of a steady decrease from the cut-off voltage seen in reverse bias for the 30 well samples, the current for the 50 well device of figure 7.5 decreases slowly from about -3V, but is still at about 95% of the reverse bias maximum at zero bias. Furthermore, SIMS data presented in chapter 8 indicates diffusion of the Be p type dopant from the p layer into the i layer. This leads to an exponentially decreasing Be doping profile in the i layer. This means that the depletion width in the p layer will begin to decrease more rapidly with an applied bias varying in the positive direction, as the depletion edge scans through regions of the p layer with exponentially decreasing doping.

We therefore ascribe the slow decrease in MIV from 100% at -3V to about 95% at 0V to the inhomogeneity in the doping profile, and the fact that it does not match our assumptions regarding square doping profiles.

The voltage cut-off at about 0.6V is then too low to allow us to reliably suggest an absolute value of N_{BG} . However, we can again set an upper limit which is $N_{BG} \leq 2 \times 10^{15}$. This agrees with the upper limit set by the SIMS measurements. Net background doping levels of this magnitude are sufficiently low to allow efficient solar cell operation for 50 well QWSC designs.

Previous studies presented in Mark Paxman's thesis [8] include measurements of MBE material grown by Tom Foxon at Phillips Research Laboratories in 1990. This is sample G951, which was a 50 well QWSC with an aluminium fraction of $X_{b2} = 33\%$, and was shown to have a net background doping level of $N_{BG} \simeq 3 \times 10^{14} \text{cm}^{-3}$.

As in the case of MOVPE material, we conclude that the background doping problem is not unsurmountable.

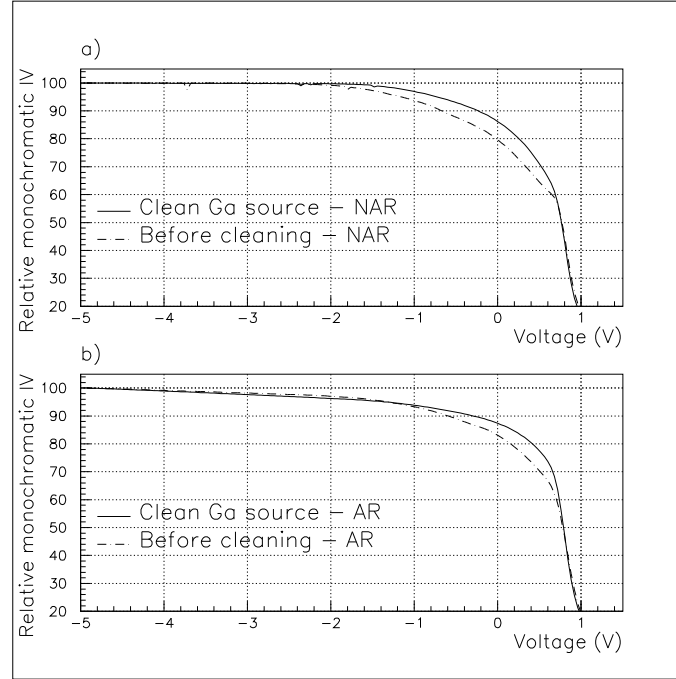


Figure 7.6: MIV measurements for the identical pair of QWSC devices QT468a and QT528. The latter was grown with a cleaner Ga source and shows an improved MIV characteristic.

7.1.2 Growth Optimisation Studies

MOVPE Ga Precursor Optimisation

An attempt was made to reduce the background impurity concentration in MOVPE samples in collaboration with John Roberts of the III-V Semiconductor Growth Facility in Sheffield. This involved comparing device quality before and after an improved TMG source was used for the MOVPE growth.

Figure 7.6 shows MIV measurements for QT468a and the repeat structure QT528. The latter is identical to QT468a but was grown with the cleaner TMG source. The MIV data for both NAR and AR devices is better for the material grown with the cleaner TMG source. This supports the principle that poor MIV data is indicative of high impurity levels in the growth precursors.

We note however that the voltage at which the MIV drops is very similar in both cases. The simple theory outlined in chapter 2 would therefore predict the same net background doping level in both cases of $N_{BG} \simeq 2 \times 10^{16} \text{cm}^{-3}$. This further indicates that the main source of background impurities is the TMA source.

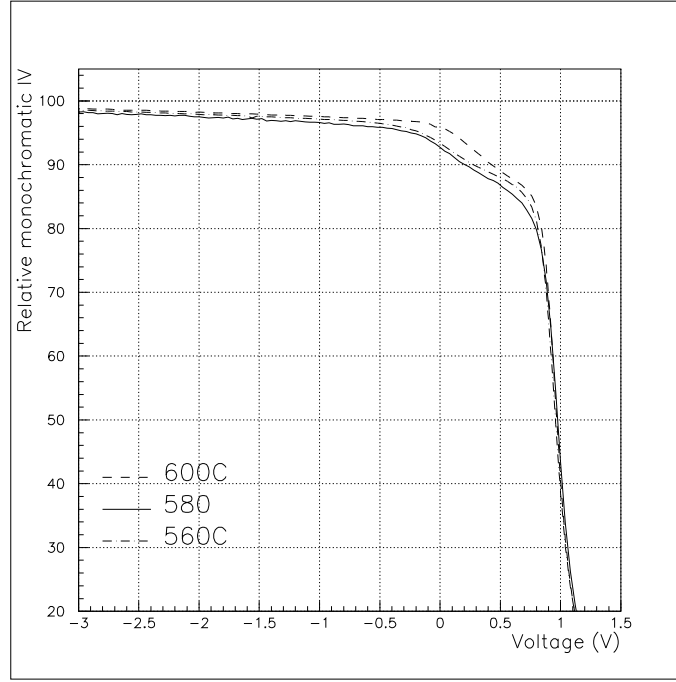


Figure 7.7: MIV data for identical MOVPE single quantum well samples grown at 560C, 580C and 600C, showing little variation.

MOVPE Growth Temperature Optimisation

MOVPE growth temperature may significantly affect growth morphology and impurity incorporation during growth. In particular, carbon incorporation decreases at lower temperatures. This is offset by an increased defect density [56].

A series of identical single quantum well (SQW) samples were grown at three different growth temperatures in order to identify an optimum growth temperature. The temperatures were 560C for QT574b, 580C for QT874a and 600C for QT874c. The MIV characteristics for these samples are given in figure 7.7. We again consider NAR devices in order to minimize the device variability introduced by the AR coating process. The p layer in all samples was grown at 700C.

Although the data for 600C appears higher than the other two at 0V, the difference is only of the order of 3%, which is comparable or smaller than the experimental uncertainty. The MIV measurement in this case cannot distinguish between the three samples. Clearer conclusions can be drawn from PL spectra taken by J.S. Roberts [56]. The relative strengths of PL signals measured from the wafers relative to the 560C sample were 3.5 for 580C and 1.35 for 600C. A

temperature of 580C was therefore proposed as the optimum by John Roberts. He suggests that this temperature represents a good compromise between increased background carbon incorporation at higher growth temperatures and greater defect densities at lower temperatures.

7.1.3 Passivation effects

Comparison of MIV Data of AR Coated and As-Grown Devices

Figure 7.8 shows MIV data for the p - i - n sample QT468b for samples with and without an AR coat. The initially good MIV characteristic is degraded by the AR coat deposition. The decrease in MIV in reverse bias however shows a constant gradient. Linear behaviour of this type may be due to a change in the effective doping profile brought about by the AR coating process. Other influences such as electrical problems related to the extra processing step cannot however be ruled out.

Figure 7.9 shows similar data for QT640a, which is a QWSC sample with the same dimensions as QT468b but which has a graded p layer. The initially poor MIV characteristic is improved by the AR coating process. The improvement however does not significantly change the voltage point at which the MIV starts to fall. The net background for both NAR and AR devices is therefore estimated at $N_{BG} \sim 2 \times 10^{16} \text{cm}^{-3}$.

The degradation of good samples and improvement of poor ones upon the deposition of the AR coat has frequently been observed in the devices processed for this project.

Such behaviour was also observed in samples grown at Eindhoven Technical University. Peter Ragay *et al.* [53] of the III-V Solar Cell group at Eindhoven have carried out passivation studies which show similar behaviour in QWSC samples.

MIV data for the 50 well QWSC sample W276 is given in figure 7.10. The wafer was grown by MBE at Eindhoven Technical University. The two curves in the graph show the device characteristic before and after exposure to a hydrogen

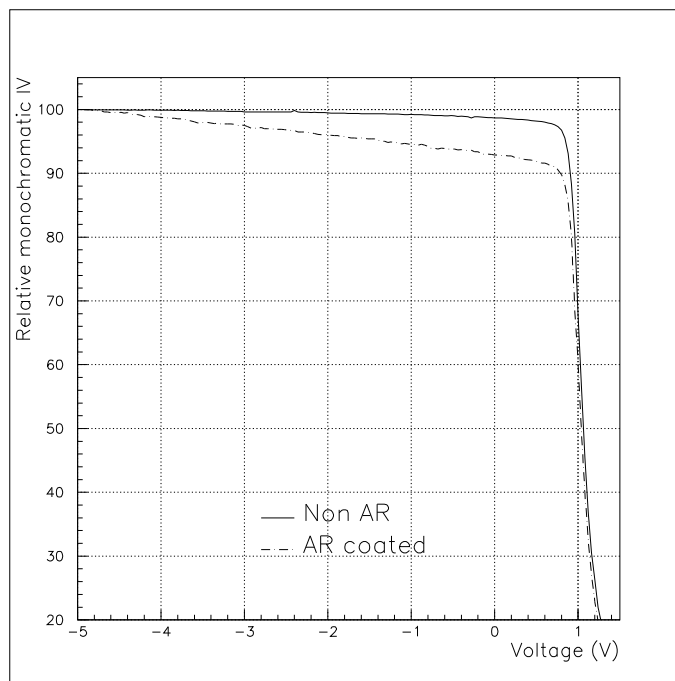


Figure 7.8: Degradation of MIV for a good p - i - n device QT468b

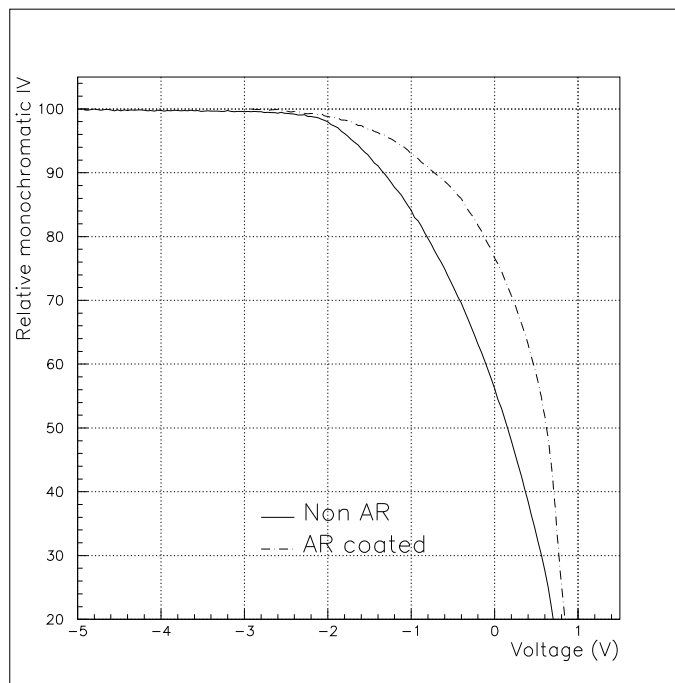


Figure 7.9: Improvement in MIV for poor QWSC device QT640a

passivating plasma. Hydrogen ions diffuse through the crystal lattice and bond to impurities and defects. These may include materials defects, minority carrier traps, and ionised donor and acceptor impurities in the crystal. The mechanisms are reviewed for GaAs in [51] and for $\text{Al}_x\text{Ga}_{1-x}\text{As}$ in [52].

Although the MIV data for the passivated device is much improved, electrical characterisation by Guido Haarpainter indicated that the treatment significantly increased the series resistance of the device. This is ascribed to the degradation of the intentional p and n layer doping due to unintentional passivation of the donor and acceptor dopant atoms.

The analogies between passivated and AR devices suggest that the hydrogen present in the silane plasma may have a passivating effect on AR devices. The exposure time of one to two minutes is however very much smaller than the typical times of 30 minutes quoted by Ragay [53], and does not benefit from the driving field which is usually employed to assist ionic diffusion. This however must be set against the fact that the samples we are considering are very thin. The i layer in the samples quoted above is approximately $0.15\mu\text{m}$ from the surface of the sample, which is smaller than the thicknesses of several microns usually studied in the literature. Furthermore, our samples show a weaker change in MIV than the Eindhoven samples. Confirmation of this hypothesis would require further characterisation.

Passivation effects in indium phosphide solar cells have been reported by Chatterjee and Ringel [54]. This study observed an increased V_{oc} in passivated $p^+ - n$ samples. Deep level transient spectroscopy confirmed that deep levels were passivated. Consequences for the series resistance and overall efficiency of the cells are not given in this reference.

We conclude that passivation may be of use in improving the dark currents of solar cells by passivating deep levels, and may also decrease the N_{BG} . The expected degradation of the intentional doping however presents a significant problem. It is expected to increase the series resistance and hence reduce the efficiency of the solar cell.

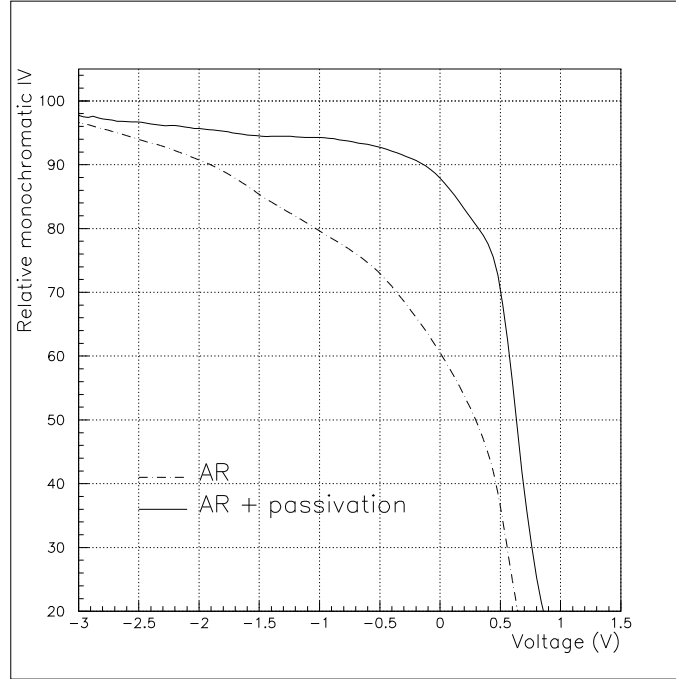


Figure 7.10: MIV data for the 50 well QWSC sample W276 before and after exposure to a passivating hydrogen plasma

7.1.4 Conclusions

High net background doping levels have proved to be a significant problem in both MOVPE and MBE material with values of N_{BG} qualitatively estimated as greater than 10^{16}cm^{-3} observed in both systems. The systematic difference between QWSC and p - i - n devices has been ascribed to improved compensation properties in p - i - n structures. The background doping problem is more systematic in MOVPE grown material.

Efforts to reduce the background doping levels in MOVPE material have so far met with little success and the high levels of N_{BG} estimated for this growth method for QWSC devices continue to pose problems.

Previous MOVPE and more recent MBE material has shown that both systems are capable of net background doping densities of the order of 10^{15}cm^{-3} .

The AR coating process has been shown to significantly alter the MIV characteristics of solar cell devices. In general, the AR coat degrades the MIV data of good devices but improves that of poor devices. Samples which fall into the latter category show similarities with a passivated sample from Eindhoven University

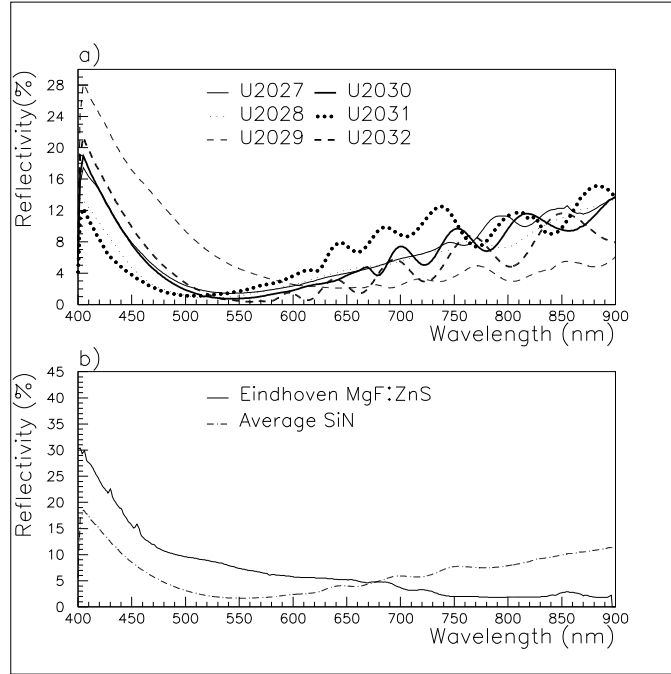


Figure 7.11: Reflectivities for QWSC and p - i - n devices for the U2027-U2032 MBE series

of Technology. This is likely to be due to unintentional passivation of intentional and unintentional impurities in our samples by the hydrogen in the silane plasma used for the AR coating processing step. It is difficult to make use of this effect in practice since the passivation process unavoidably alters the intentional doping levels. This has been indirectly observed as an increased series resistance in the passivated Eindhoven device which degrades solar cell efficiency.

7.1.5 Reflectivity Measurements

We now briefly consider spread and reproducibility of reflectivity measurements. These are important in determining the internal QE of devices, and cannot always be measured directly.

Figure 7.11a shows the spread in reflectivity for a range of samples processed in the same AR coating run. Of the six samples shown in the figure, only sample U2029 deviates significantly.

These data form the basis of the average SiN reflectivity curve which was discussed in chapter 6. This mean reflectivity is shown figure 7.11b, and is used to model the reflectivity of those samples for which a dedicated reflectivity mea-

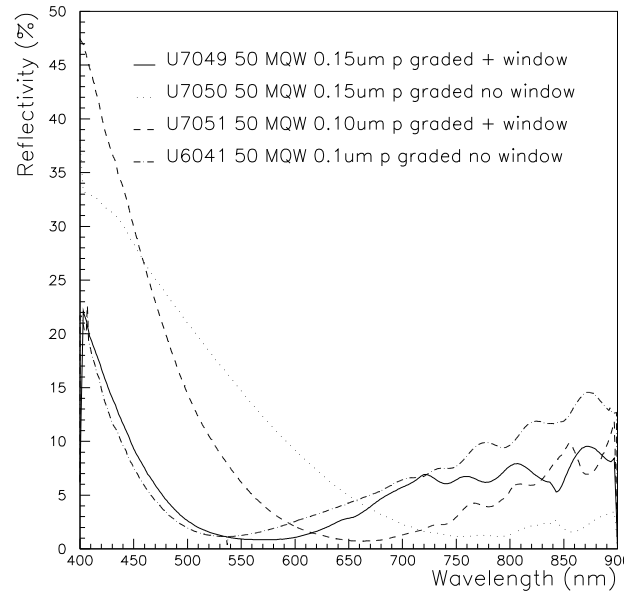


Figure 7.12: Reflectivities of a variety of samples with and without windows, showing that the removal of the window does not noticeably affect the reflectivity

surement sample is not provided.

Also shown in figure 7.11a is a standard reflectivity for the Eindhoven MgF:ZnS double layer AR coat deposited at Eindhoven. We note that it is optimised at longer wavelengths, but is small over a wider wavelength range than the SiN single layer coat.

The curves in figure 7.12 however show reflectivity data for samples grown towards the end of the project, just before the AR coating kit was upgraded. A large spread is seen for the samples AR coated at this time. This is consistent with discussions with Malcolm Pate of the III-V Semiconductor Facility at Sheffield University regarding the problems experienced with the original deposition equipment prior to the upgrade.

It has been suggested [49] that the thin window may be used in conjunction with the SiN layer to produce a double layer AR coat. The optimum suggested window thickness was 30nm for the 70nm SiN AR coat.

The data of 7.12 includes two samples with and without windows, but with a nominally indentical SiN AR coat. The window thickness in this case was 20nm

instead of 30nm. Both samples were coated in the same processing run. We note that the data for the large area device processed from the U6041 wafer, which has no window, is very similar to the mean reflectivity of figure 7.11.

The reflectivity of the fifty well sample U7049 is again very similar in magnitude and wavelength dependence, despite the fact that it has a window. The two other reflectivity curves shown in figure 7.12 are very high at short wavelength, indicating that the SiN coat is thicker than expected. The reflectivity for these samples is effectively optimised at longer wavelengths.

We note furthermore than if we were to normalize the reflectivities of these four samples to the same wavelength, the windowless sample U7050 would have the lowest reflectivity.

The window thickness in this example is 50% different from the optimum. The large differences observed in these data however lead us to conclude that the reflectivity of our samples is primarily determined by factors other than the presence or absence of a window. The reflectivity overall is reasonably reproducible, with the exception of samples processed towards the end of the project, just before the AR coating kit was overhauled by Malcolm Pate.

7.1.6 Conclusions

In this chapter we have considered results and implications of the MIV and reflectivity characterisation techniques. The first section demonstrated the use of the MIV measurement to estimate sample quality in MOVPE and MBE samples. The technique has been shown to qualitatively demonstrate the magnitude of the background doping N_{BG} . Quantitative analysis however requires further analysis of the kind developed by Jenny Nelson and Alexander Zachariou [62].

We established that QWSC structures generally suffer from higher levels of N_{BG} than their p - i - n controls. This has been assigned to the loss of a compensation mechanism in QWSC structures by discussion with John Roberts. We further saw that previously grown QWSC samples have demonstrated that this problem is not insurmountable. Some recently grown MBE samples have con-

firmed this, although they have not reached the standard laid down by a sample (G951) grown at Phillips Research Laboratories in 1991. Overall, we conclude that MOVPE material is more variable than MBE material, and is subject to higher values of N_{BG} and a wider departure from nominal design parameters.

Consequences of the AR coating process for device performance have been considered. An interesting observation is that the MIV characteristics of poor NAR samples tend to improve in corresponding AR devices. This has shown interesting correlation with work by Peter Ragay [53] on hydrogen passivation.

Reflectivity measurements were considered and shown to be reasonably consistent. Samples processed towards the end of the project however showed more variability. An average reflectivity was presented in order to enable modelling of samples for which the reflectivity was not directly measurable.

Chapter 8

Experimental and Modelled QE Spectra

The first section of this chapter gives an overview of the techniques used to model selected types of devices and outlines the information which may be extracted from the modelling, together with limitations in each case.

We then present experimental and modelled QE spectra for a set of samples with unusual i region compositional profiles. We then examine a set of ungraded samples grown by MOVPE and MBE, in order to estimate the dependence of the minority carrier transport on aluminium fraction. A set of graded devices are characterised, using the information derived from the previous sections. The final section presents QE spectra for QWSC devices equipped with back surface mirrors.

The samples are referred to by their growth name, and relevant design characteristics are given in the text. Supplementary information is included in the graphical output of the modelling program.

8.1 Principles of Data Fitting

In this section we present experimental QE data and the corresponding modelling results for a range of ungraded samples grown by MBE. We start by reviewing theoretical results from chapter 3 relevant to modelling experimental data, and

establishing the modelling techniques which will be used throughout this section.

8.1.1 Sample geometry

Sample descriptions are generally accurate, because of the epitaxial methods used in sample growth. Compositions however frequently need to be adjusted. This is usually possible only if a sharp cut-off in QE is present, for example in p - i - n devices. Aluminium fractions in QWSC samples can be estimated by fitting the shape of the QE above the base aluminium fraction X_{b2} and by looking at the position of the excitonic peaks in the quantum well QE .

Adjustments are occasionally necessary to the window thickness, and are justified by the presence or absence of a characteristic dip in the QE for photon energies greater than the window bandgap.

An additional problem in MBE material is dopant diffusion. The sample U6041 which will be described in some detail below was characterised by SIMS. This revealed that the effective p thickness was approximately 40nm larger than expected, which for this sample represents an increase of nearly 50%. This casts some doubt over modelling other MBE samples with nominal layer thicknesses. In practice, modelling has shown that the extra thickness is not important in most MBE samples because they have p layers which are thicker than U6041. Furthermore, these samples do not show the symptoms of this problem. These are an overestimated i region QE at wavelengths of about 600nm, or an overestimation of the quantum well QE resulting from unintentional doping of wells near the p layer.

8.1.2 Samples with efficient minority carrier transport

Chapter 3 shows that the QE is dominated by different parameters in different wavelength ranges. In particular, the QE at photon wavelengths corresponding to the band edge energy E_{b2} is dominated by the i region contribution, and by the absorption and diffusion lengths in the p and n electrostatically neutral layers.

Section 8.2 will show that the i region QE of even quite complex samples

may be modelled accurately, as long as the i region geometry and composition are close to specifications. We will further establish that the model is useful as a diagnostic tool. It can be used to adjust compositions, in the cases where the latter determine a sharp cut-off in QE at a certain wavelength.

In the most general case, fitting of the model to the experimental QE is subject to three main parameters, which are the recombination velocity parameter for the front of the p layer $\mathcal{S} = S_n/D_n$, and the p and n diffusion lengths L_n and L_p . The recombination velocity at the back of the n layer is not a significant parameter. This is because the n layer is negligible at short wavelengths, and small overall. Furthermore, the n layer thickness of $\sim 0.6\mu m$ is much greater than L_p .

Appendix A shows that it is impossible to draw any clear analytical conclusions without making assumptions about the relative magnitudes of one or the other of these parameters. Experience with modelling however shows that different parameters dominate in different wavelength ranges. The diffusion lengths L_n and L_p are most significant near the band edge energy E_{b2} , whereas \mathcal{S} is important at short wavelengths. Fitting the theory to the data in this case is an iterative process involving repeated adjustment of the three parameters until a best fit is found for all wavelength ranges. Samples falling into this category are generally those with good material quality and thin i layers, such as the low aluminium fraction 30 well samples.

We will present results from samples grown at Eindhoven Technical University which also conform to this picture. In this case, however, the QE at short wavelengths is good, suggesting a very low value of \mathcal{S} . The fitting then reduces to a two parameter fit, with the short wavelength QE being exclusively determined by L_n , and L_p being estimated subsequently by fitting the band edge QE .

8.1.3 Samples with simplified modelling

More exact modelling is possible in samples conforming to the simplified analytical expressions for the QE derived in Appendix A.

Samples with small n region contributions in particular allow the QE near the band edge to be fitted mainly in terms of L_n . A further coincidental simplification arises from the fact that the n region contribution is generally small in samples where L_n is less than the effective p layer thickness x_{w_p} . This is due to the fact that both p and n contributions to the QE are decreased in poor material. In this case, results from chapter 3 and Appendix A have shown that the QE for photon energies near E_{g2} is very weakly dependent on \mathcal{S} . The overall QE in this case can essentially be modelled independently at short and long wavelengths, in terms of \mathcal{S} and L_n only. Samples falling into this category include those with base aluminium fractions X_{b2} greater than about 30% and samples with thick i regions.

8.1.4 Samples with high surface recombination parameters

At short wavelengths, the QE generally depends on both the recombination parameter \mathcal{S} and the electron minority diffusion length L_n . As we saw above, the discussion need only consider the value of \mathcal{S} in the p layer. As mentioned in chapter 5 we cannot separately estimate S_n and D_n .

A consequence of the analytical model of chapter 3 is that values of \mathcal{S} comparable to the term $1/L_n$ are required to affect the QE significantly at short wavelengths. Since diffusion lengths in the majority of our samples are only a fraction of a micron, it follows that surface recombination only becomes significant if $\mathcal{S} > 10^7 \text{m}^{-1}$. Values quoted in chapter 4 however set an upper limit on \mathcal{S} of about 10^6m^{-1} . The larger values required to fit some samples indicate either unusually low mobilities together with high recombination velocities, or with a p layer width which is greater than the specifications. More fundamentally, this behaviour may be due to a failure of the recombination velocity to adequately represent minority carrier transport at the front of the cell.

The recombination velocity represents the high defect concentration near the surface as a sheet of charge, which acts as a carrier sink. In reality, these defects

are distributed over a finite depth, and may be caused not only by crystal defects such as dangling bonds, but by surface oxidation which may extend some distance into the sample. If this damage is extended over a depth which is not negligible compared to the thickness of the p layer, the latter will be effectively shortened, and very high surface recombination velocities required to reproduce experimental QE data.

The following discussion attempts to model samples with recombination velocities and diffusivities which are consistent with published data. For samples with thin p layers and low diffusion lengths, this in practice means values of \mathcal{S} which are too low to have a significant effect.

When such an approach is not possible, we shall assume that the surface recombination picture does not accurately describe the minority transport at the front of the cell, and substitute a recombination parameter which is large enough to saturate this mechanism. In practice, this means values such that $\mathcal{S} > 1/L_n$, which are effectively infinite insofar as they are large enough to reduce the minority carrier concentration at the front of the cell to negligible levels.

8.1.5 Graded samples

A number of important differences appear when modelling graded samples. The first is that the p region QE for wavelengths corresponding to energy E_{b2} is generally small, particularly for grades with a large compositional gradient. The QE near the band edge in graded samples is therefore principally determined by the i and n region contributions. Since we will not consider samples with compositionally graded n layers, this simplifies the fit near band edge E_{b2} .

Fitting the overall QE of graded p samples is necessarily limited by the assumptions we are forced to make regarding minority carrier transport in compositionally graded material. In particular, the assumption that the estimated dependence of L_n on aluminium fraction and position can be extrapolated from the values used to model samples with different X_{b2} is clearly liable to lead to large errors. Figure 8.1 shows two QE calculations. Curve A has no diffusion

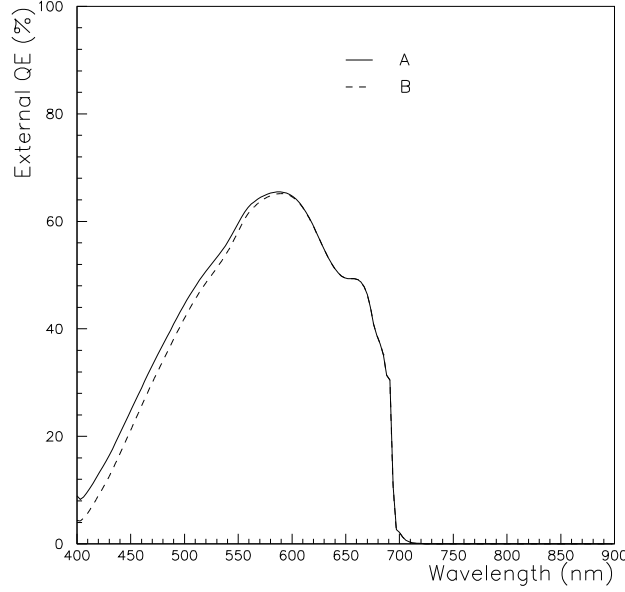


Figure 8.1: QE for two linear parametrisations of L_n as a function of composition. For curve A), L_n is kept constant at $0.08\mu m$. Curve B represents the worst case scenario of $L_n(0) = 0.08\mu m$ and $L_n(x_{w_p}) = 0.01\mu m$

length gradient, and curve B has a higher than expected L_n gradient. The calculation is for a value of $\mathcal{D}_\chi = -4$. We note that even in this extreme case, the QE is relatively insensitive to the variation in L_n . The QE in this case is therefore determined primarily by the diffusivity field \mathcal{D}_χ defined in section 5.2.2.

The theoretical considerations in chapter 3 and empirical tests using the model have shown that the recombination parameter \mathcal{S} has little effect on the QE of the p layer at short wavelengths. Fitting the model to experimental QE data for graded samples is greatly simplified, since \mathcal{D}_χ is the determining parameter at short wavelengths.

Although the diffusivity field \mathcal{D}_χ is in principle determined solely by the diffusivity D_n , it will in practice be influenced by other parameters. This is a consequence of reducing the modelling to a two parameter fit which is dominated by \mathcal{D}_χ . Inaccuracies in the assumptions we have made regarding the diffusion length, for example, are subsumed into the modelled value of \mathcal{D}_χ .

Modelling graded structures therefore follows similar guidelines to modelling the QE of ungraded structures, with the difference that the L_n is eliminated as

a parameter and the band edge response is determined by the i and n region contributions. The short wavelength QE will be modelled in terms of $\mathcal{D}_\mathcal{X}$ and to a lesser extent the recombination parameter \mathcal{S} . This simplified approach is made necessary by the lack of detailed knowledge of the position dependence of the minority carrier transport parameters.

8.1.6 Modelling of the quantum well QE

The quantum well QE has been modelled in previous work by Jenny Nelson, which has been reviewed in [49]. For photon energies corresponding to electronic levels near the top of the well, the model for this wavelength range underestimates the QE to some extent because of superlattice states which are not included, and because of the change from a two dimensional to a three dimension density of states, which the model assumes is abrupt.

With the exception of this correction, the model has been shown to reliably reproduce the quantum well QE , including excitonic features, and is sufficiently accurate for our purposes. The model is expected to be accurate for the first quantum well continuum, which is deep enough in energy to approximate the theoretical model accurately.

The parameters for the quantum well QE are kept fixed, since they are well understood and have been reviewed extensively [49].

8.1.7 Mirror backed samples

Modelling of mirror backed samples introduces two new parameters. The first is the phase change ψ_b experienced by light internally reflected from the back surface mirror. This is a variable quantity which is poorly known [37].

The parameter ψ_b can however be accurately determined from the position of the wavelength dependent Fabry-Perot oscillations which are observed in mirrored samples.

In principle, no other parameters are required, since the phase change ψ_f upon internal reflection at the front surface semiconductor-air interface is 0 radians [35],

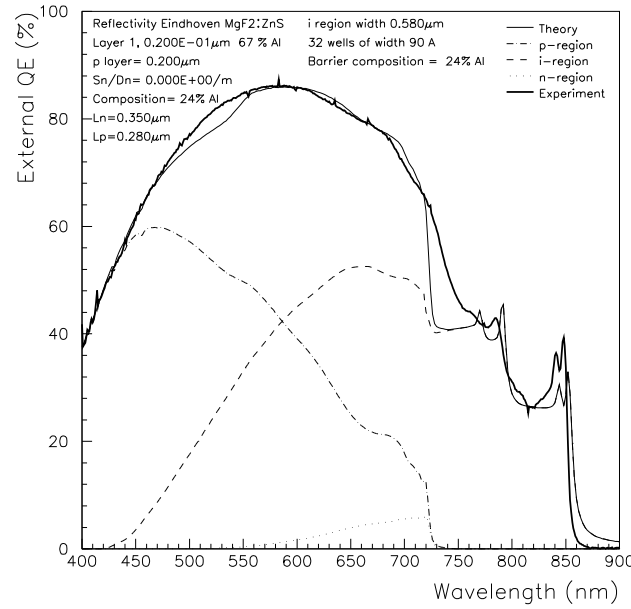
the back surface reflectivity is well known from the reflectivity of the relevant metal, and the front reflectivity is generally measured.

In practice, we shall see that some samples show clear signs of non specular reflections from the back surface, and show an enhancement in QE which is greater than that expected for light reflected normally from the back surface. This case is further characterised by lower Fabry-Perot amplitudes than expected. In some samples, they may be absent altogether.

Finally, although the front surface reflectivity is measured, the model frequently predicts larger Fabry-Perot peaks than are in practice observed. The modelling in this case can be improved by the introduction of a front reflectivity factor \mathcal{F} . This reduces the modelled amount of light reflected back into the cell upon the third pass, and is a factor of the front surface reflectivity R_f of section 3.3.3. A value of \mathcal{F} smaller than 1 reduces the amount of light reflected back into the cell from the front surface. This reduces the amplitude of the Fabry Perot peaks, but has little or no effect on the overall enhancement factor. The origin of this factor is not clear, but may be due to the fact that the light is not incident normally, or to an unintentional roughening at the back surface mirror. Furthermore, we saw in section 3.3.3 that the internal reflections occurring at the interfaces between the quantum wells and the barriers are not included in the model. A brief calculation showed however that the effect is expected to be small. More discussion of this point is given in section 8.6. Finally, the uncertainty in reflectivity also plays a role, since measured reflectivities were not available for the mirrored samples.

8.2 Graded *i* Region Samples

A series of samples grown by MBE in Eindhoven University of Technology was studied. All structures have identical, ungraded window, p and n layers but have different *i* region specifications. These samples were initially grown to compare the efficiency of QWSC structures, p - *i* - n controls and p - *i* - n heterostructures with graded *i* layers, as reported by Ragay [53]. These samples are also useful

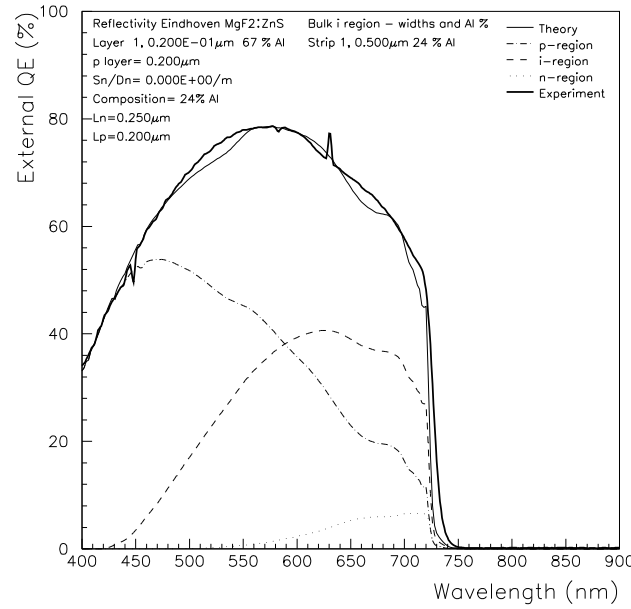
Figure 8.2: *QE* of 32 well QWSC Eindhoven structure W405

because they allow us to test the accuracy of the *QE* model in reproducing experimental data for devices with complex *i* region designs.

MIV data for these samples were uniform and reproducible, indicating good device quality and a low value of $N_{BG} \leq 5 \times 10^{15} \text{cm}^{-3}$.

The samples consist of a QWSC device, its p - i - n control, a GaAs cell and two samples with linearly graded sections in the *i* layer. Although the nominal p layer thickness was $0.5 \mu\text{m}$, Peter Ragay has confirmed that the real thickness is $0.2 \mu\text{m}$ for all devices. Furthermore, the nominal window layer of $0.04 \mu\text{m}$ was estimated as at most $0.02 \mu\text{m}$ by the modelling, on the basis of the high *QE* value at short wavelengths. A thicker window would produce a characteristic sharp decrease in *QE* for energies above the window bandgap. The *QE* measurements for these Eindhoven samples were taken by Ernest Tsui.

Figures 8.2 and 8.3 show the experimental data and best fit from the model for a QWSC structure W405 and its $\text{Al}_x\text{Ga}_{1-x}\text{As}$ control p - i - n W406. The *i* layer of W405 contains 32 wells of width 90\AA separated by 60\AA barriers. The *i* layer of the control W406 consists of $0.5 \mu\text{m}$ of $\text{Al}_x\text{Ga}_{1-x}\text{As}$ with a nominal aluminium fraction of $X_{b2} = 20\%$. The model however indicates that the true aluminium

Figure 8.3: QE of p - i - n Eindhoven sample W406

content is about $X_{b2} \simeq 24\%$ because of the sharp cut-off in QE observed at about 730nm.

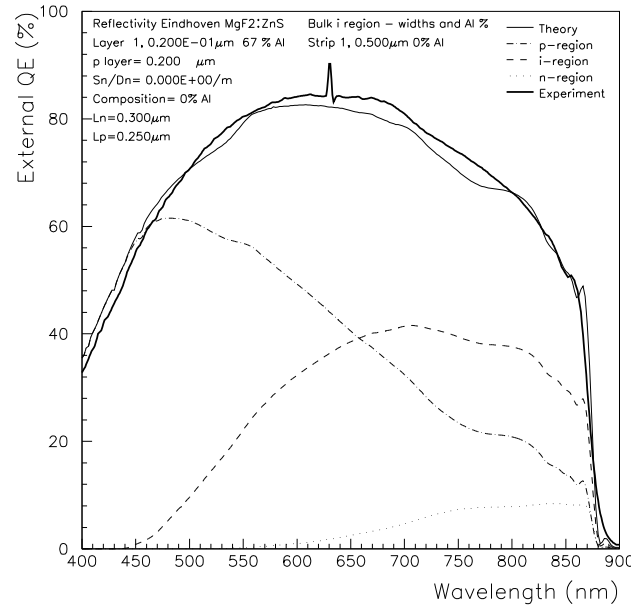
We first consider the QE for photon energies above the neutral layer bandgap E_{b2} . The interface recombination parameter \mathcal{S} is estimated as too small to have any effect on the QE at short wavelengths, and is set to zero.

In this case of negligible recombination parameter \mathcal{S} , the QE of the neutral layers depends only on L_n , L_p and the reflectivity. The modelling assumes a standard reflectivity supplied by Peter Ragay, and assumes that the layer specifications are correct, with the exception of the window layer thickness as mentioned above.

Modelled diffusion lengths are of the order or greater than the neutral layer widths at about $0.3 \mu\text{m}$. The hole diffusion length L_p is slightly smaller than the electron diffusion length L_n as expected. These are close to Hamaker's values, which are $L_n \simeq 0.39 \mu\text{m}$ and $L_p = 0.20 \mu\text{m}$ respectively.

We conclude that the minority carrier transport in the neutral layers of these devices is efficient, and the MBE material of high quality.

Below bandgap E_{b2} , the quantum well QE in sample W405 is accurately re-

Figure 8.4: *QE* of GaAs structure W407

produced. The main source of error in this case is the reflectivity. The accuracy of the fit in this wavelength range suggests that the Eindhoven AR coating process is reproducible. Furthermore, it serves to confirm the assumption of carrier collection efficiencies close to 100% in the space charge region.

Figure 8.4 shows similar data for sample W407. The device specification is identical to W406 except that the $\text{Al}_x\text{Ga}_{1-x}\text{As}$ is replaced by GaAs leading to an ungraded GaAs cell. The modelling in this case indicates minority carrier transport which does not differ significantly from the previous two samples. In general, significantly higher diffusion lengths are expected in GaAs.

The schematic of figure 8.5 shows compositional profile of graded *i* region sample W408. In the depletion approximation, the *QE* below the bandgap X_{b2} is dependent only on the reflectivity and the integrated absorption. Figure 8.6 shows the experimental and modelled *QE* for this sample. We note that the short wavelength response for photon energies above E_{b2} requires slightly smaller diffusion lengths than samples W405-W407. The aluminium fraction X_{b2} is again estimated at about 24%.

The model predicts the *i* region contribution remarkably accurately, confirm-

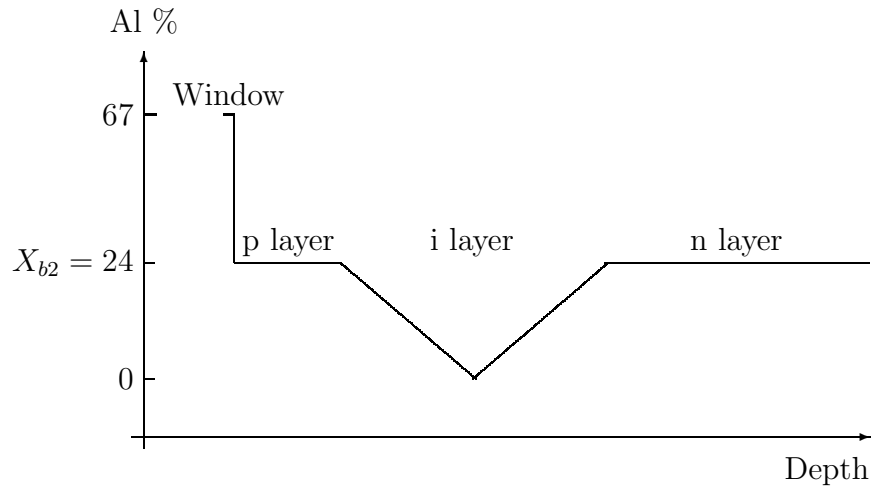


Figure 8.5: Schematic compositional profile of graded i region sample W408

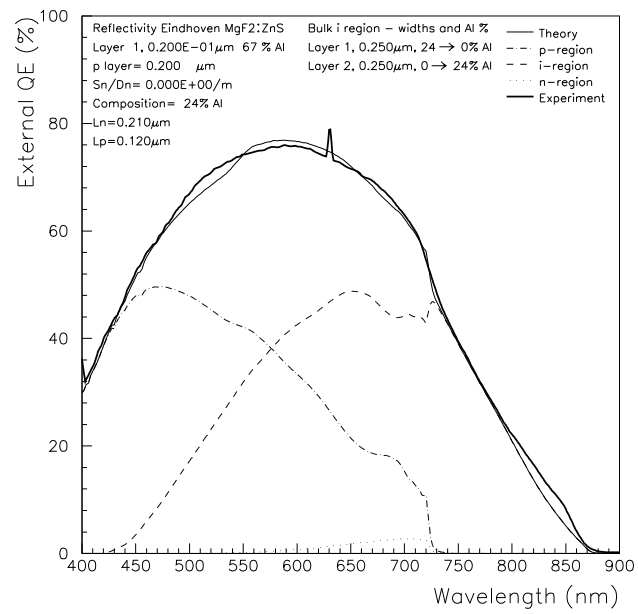


Figure 8.6: QE of graded i region sample W408

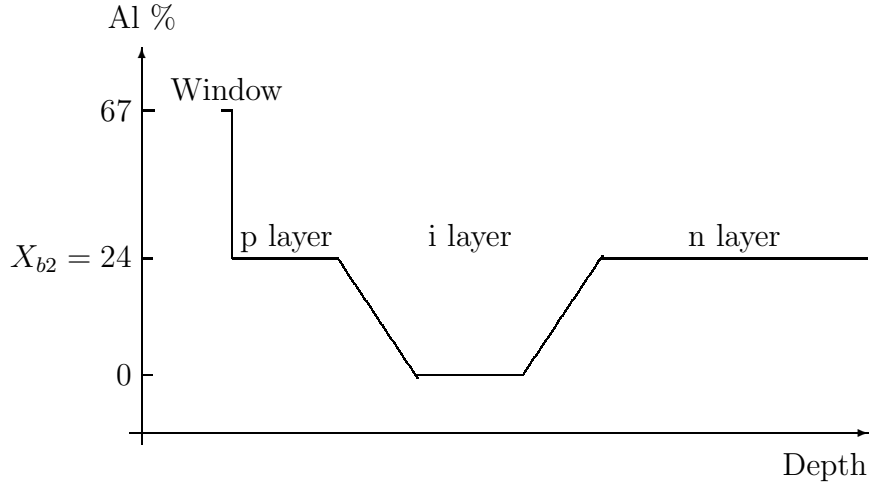


Figure 8.7: Schematic compositional profile of graded *i* region sample W409

ing the reliability of the absorption coefficient parametrisation reviewed in chapter 4 for aluminium fractions between 0 and, in this case, 24%.

Figure 8.7 shows the schematic compositional profile of the last Eindhoven sample W409. This sample is similar to W408 except that the *i* region grades are sharper, and a $0.2\mu\text{m}$ GaAs layer is grown in the centre of the *i* region. Modelled minority carrier transport in the neutral layers is similar to W408. The *i* region QE , for photon energies below E_{b2} , is again satisfactorily reproduced.

Figure 8.9 shows a schematic compositional profile of the GRINCH laser structure NRC1038. This structure has been investigated by colleagues as a promising structure for a high V_{oc} QWSC structure since studies have shown that the dark current in such structures is very low. The measured and modelled QE data for this structure are given in figure 8.10.

The *p* layer of this structure is very thick. It consists of a heavily doped graded layer starting at $X_{b1} = 25\%$ at the surface and rising to a nominal $X_{b2} = 70\%$ at a depth of 120nm . This is followed by $1.484\mu\text{m}$ of $\text{Al}_x\text{Ga}_{1-x}\text{As}$ of nominal composition X_{b2} . Only a negligible amount of photons with energy greater than the higher *p* layer bandgap X_{b2} reach the intrinsic region. The *p* layer QE is negligible because of the very high aluminium fraction in this layer. The associated low minority electron diffusion length in this case prevents photogenerated minority electrons from reaching the depletion layer. A sharp cutoff is therefore

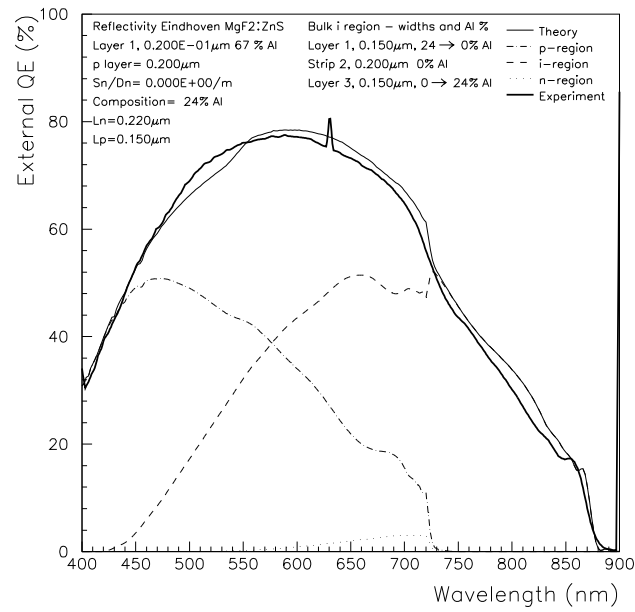
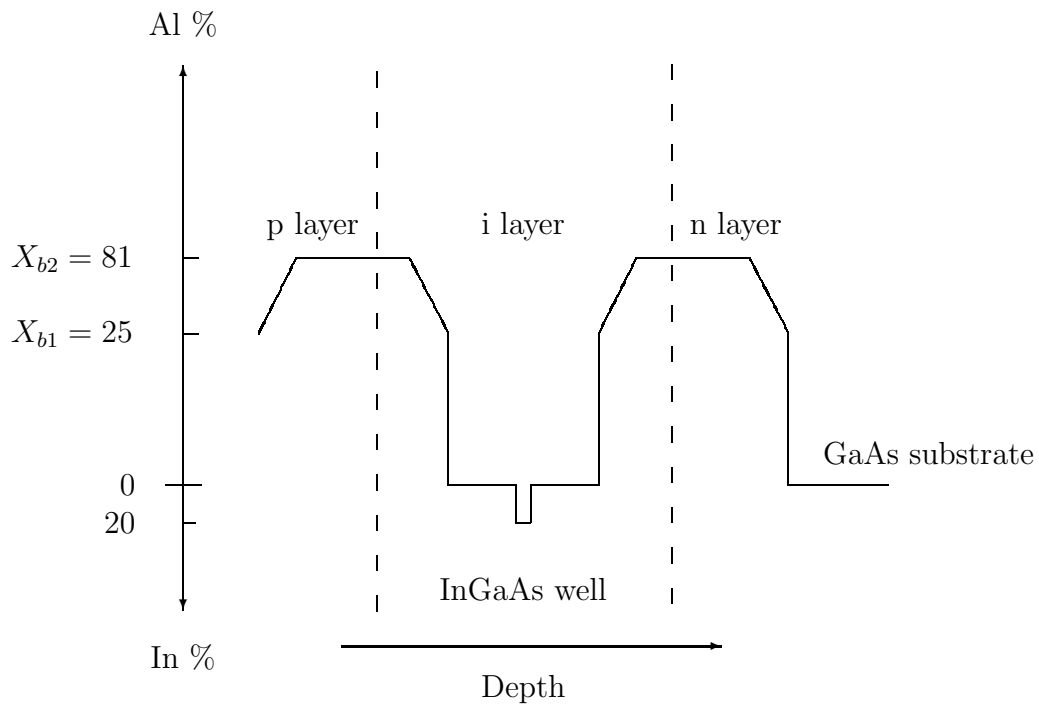
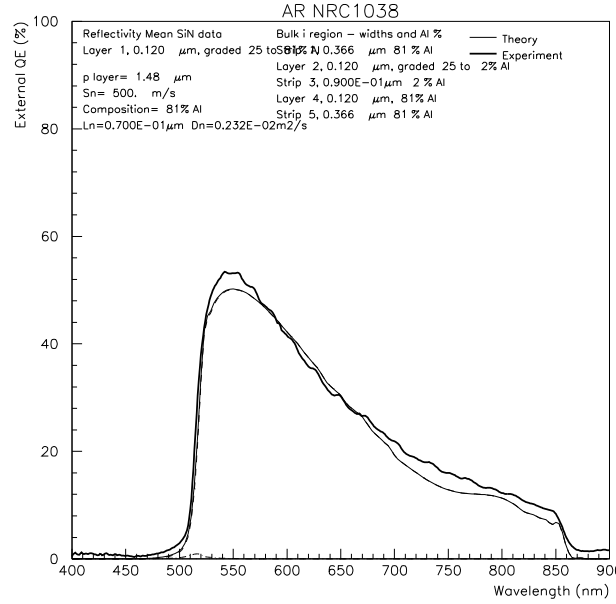
Figure 8.8: *QE* of graded *i* region sample W409

Figure 8.9: Schematic compositional profile of GRINCH laser structure NRC1038

Figure 8.10: QE of GRINCH structure NRC1038

observed in the QE at energy E_{b2} corresponding to a photon wavelength of about 500nm. The main p layer composition can be estimated from this cutoff, and is of the order of $X_{b2} \simeq 81\%$.

The *i* region consists of seven different sections, as illustrated in the schematic. These include both ungraded sections with composition X_{b2} and grades from X_{b2} to X_{b1} . The centre of the *i* layer is GaAs. The $\text{In}_{0.2}\text{Ga}_{0.8}\text{As}$ well at the centre of the *i* layer is modelled as an equivalent thickness of GaAs since the model is not equipped with an InGaAs quantum well absorption routine. The aluminium fraction $X_{b1} \simeq 25\%$ is assumed accurate, since we have no sharp threshold from which to make a reliable estimate. The QE cutoff at the nominal GaAs band edge occurs at a slightly higher photon wavelength than expected, and corresponds to $\text{Al}_x\text{Ga}_{1-x}\text{As}$ with a composition of 2% Al.

Overall, the QE of this GRINCH laser structure is well reproduced by the model. Since the QE of the *i* layer is critically determined by the amount of light transmitted through the p layer, this fit confirms that the absorption of the graded section at the front of the p layer has been accurately modelled, with the proviso that the lower aluminium fraction X_{b1} is assumed to be 25% as specified

in the growth menu.

8.2.1 Conclusions

The series of Eindhoven samples presents a number of design features which have allowed us to test the reliability of the theoretical model for complex structures grown on a different MBE system. In particular, the graded i region samples allow us to test the accuracy of the depletion approximation and of the integrated absorption. The QE in both long and short wavelength ranges has been accurately modelled with typical values of the transport parameters.

These structures also demonstrate high diffusion lengths for both electrons and holes, albeit at relatively low aluminium fractions. Finally, the interface recombination parameter \mathcal{S} is negligibly small for these samples, despite the rather large compositional change from $\sim 20\%$ to $\sim 67\%$ between the p layer and the window.

The GRINCH laser structure NRC1038 has been used to test the model in the case of a complex structure where the composition changes rapidly and where the QE is essentially determined solely by the integral of the absorption coefficient over the cell.

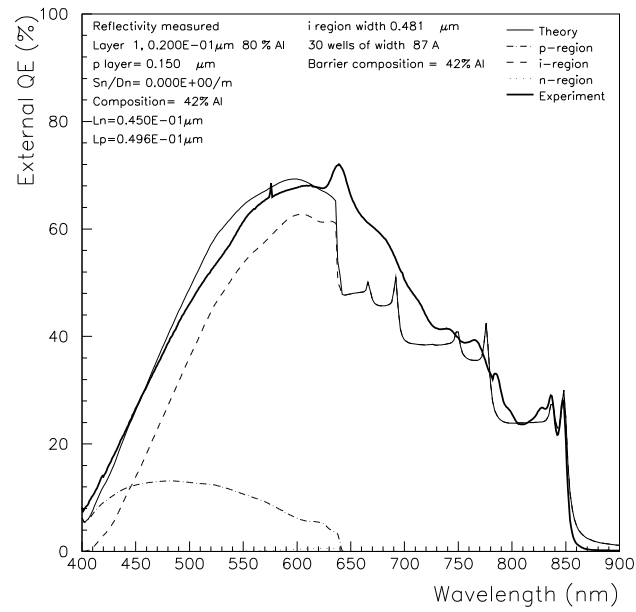
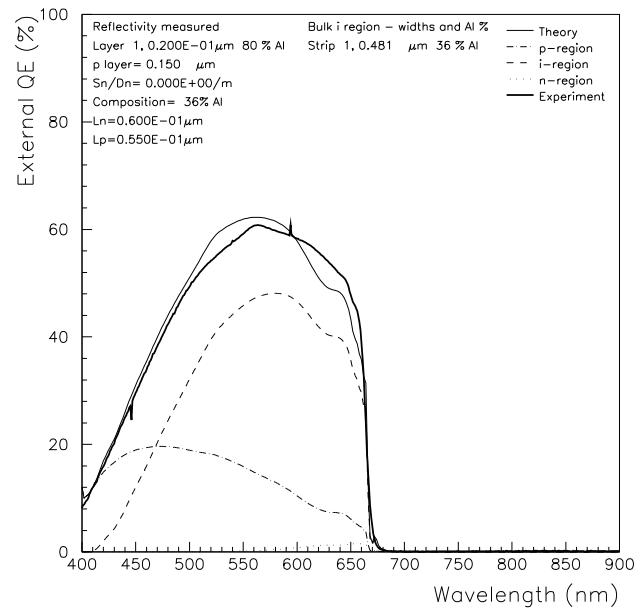
8.3 Ungraded QWSC and p - i - n samples

8.3.1 MOVPE samples

All MOVPE samples were grown with nominal aluminium fractions of about $X_{b2} = 30\%$. They conform to the same basic design, which consists of an 80% aluminium window layer of thickness $0.02\mu m$, a $0.15\mu m$ p layer, carbon doped at $1.34 \times 10^{18} \text{cm}^{-3}$. The n layer consists of $0.6\mu m$ Si doped at $6 \times 10^{17} \text{cm}^{-3}$.

No direct reflectivity measurements were available for the samples presented in this section. We therefore use the mean SiN data mentioned earlier in section 7.1.5.

The composition of samples frequently departs from the specifications by a

Figure 8.11: *QE* modelling and data for nominally 30% aluminium 30 well sample QT468aFigure 8.12: *QE* modelling and data for QT468b, the p - i - n control to QT468a

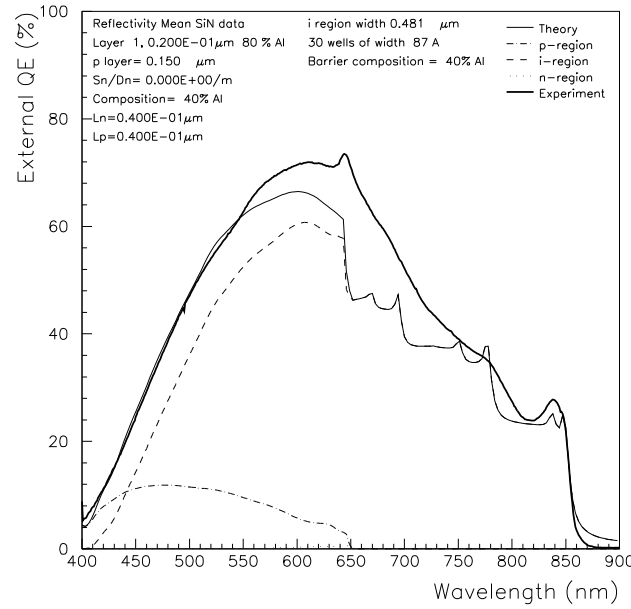


Figure 8.13: QE modelling and data QT528, which is a repeat of QT468a with a cleaner Ga source

few percent. Experimental QE and modelling for the 30 well QWSC QT468a and its control sample QT468b are shown in figures 8.11 and 8.12. The nominal aluminium fraction in both cases is $X_{b2} = 33\%$. Modelling however suggests the rather high value 42% for QT468a and 36% for QT468b. The value of 42% for QT468a is, as we shall see in section 8.6 supported by modelling the Fabry-Perot peaks of mirrored samples.

The fitting for QT468a suggests a p layer diffusion length of $L_n = 0.075 \mu\text{m}$. The n layer QE is negligible. The modelling uses a negligible surface recombination parameter, which is set to 0.

Sample QT468b shows a shortfall in QE near the band edge. This is not ascribed to a large n layer QE , given that a value of L_p much larger than L_n would be required to raise the theoretical QE in this wavelength range to the experimental level. The shortfall may be due either to an increased effective i region thickness or to the error introduced by the use of the mean SiN reflectivity. Finally, it may be due to the uncertainty in the absorption coefficient which was mentioned in chapter 4. The error in modelling however is not serious, in view of the $\pm 5\%$ error on the experimental data.

Finally, figure 8.13 shows modelled and measured QE for sample QT528, which is a repeat of QT468a but with a cleaner Ga source. The composition is modelled as $X_{b2} = 40\%$. The modelled diffusion length is significantly shorter than QT468a, at $L_n = 0.04\mu m$. For material with these very low diffusion lengths, minority carrier loss at the front of the cell is dominated by bulk recombination. The modelling becomes insensitive to the surface recombination parameter \mathcal{S} , which cannot therefore be ascertained with any degree of confidence. It is therefore set to zero.

The model significantly underestimates the experimental QE at wavelengths between about 550nm and 650nm. This may again be due to the assumption of a mean SiN reflectivity. Possible departures from sample specification might also account for the shortfall in theoretical QE but cannot be established without further characterisation, for example SIMS.

The modelling however suggests that minority carrier transport is much lower than that observed in the Eindhoven samples. The diffusion lengths are slightly lower than the values suggested by Hamaker, and vary significantly between growth runs. The surface recombination parameter in all three samples was negligible.

8.4 MBE samples

The samples U2027 to U2032 and U4036 mentioned in section 7.1.1 were modelled with a view to establishing how the minority carrier transport depends on the base aluminium fraction X_{b2} for MBE material. The samples all consist of a 67% aluminium window of width $0.02\mu m$, a $0.15\mu m$ p layer Be doped at $2 \times 10^{18}\text{cm}^{-3}$, a $0.481\mu m$ i layer, and finally a $0.6\mu m$ n layer Si doped at $6 \times 10^{17}\text{cm}^{-3}$.

The samples took the form of ungraded QWSC devices and their p - i - n controls. All samples were grown in the same growth run with the exception of the 20% p - i - n sample U2028 which was initially grown with a GaAs i region instead of the intended $\text{Al}_x\text{Ga}_{1-x}\text{As}$. This device was repeated in a subsequent growth run as sample U4036.

Experimental QE and modelling data for the AR coated devices processed

from these samples are presented in graphs 8.14 to 8.20.

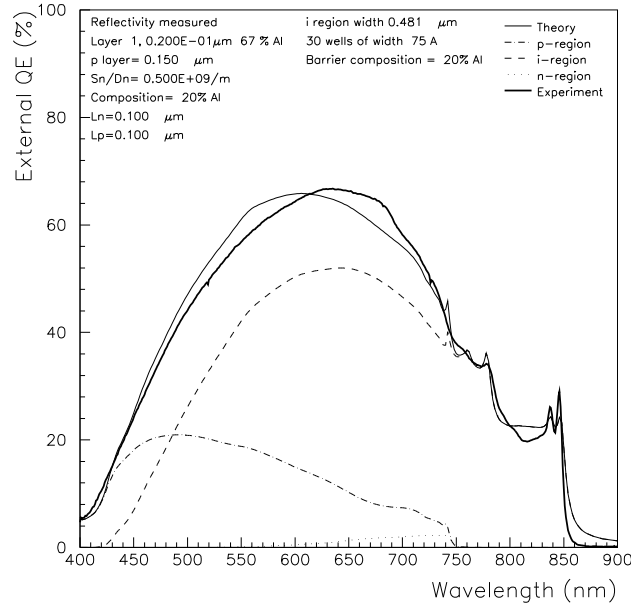


Figure 8.14: QE modelling and data for nominally 20% aluminium 30 well sample U2027

8.4.1 20% samples

Samples U2027 and U2028 are accurately modelled with aluminium fractions of $X_{b2} = 20\%$. U4036 however has a composition close to 23%.

Although the modelling inaccuracies for these samples are of the order of the experimental error, the fitting procedure for these samples presents some problems concerning choice of parameters. The modelled QE peaks at a shorter wavelength than the data. This could in principle be modelled more closely by increasing L_p to boost the n layer near the band edge, at about 750nm, and reducing L_n . The short wavelength response is poor, and sets a limit on the maximum value of L_n . Since, in general, holes are less mobile than electrons, the electron diffusion length should be greater than the hole diffusion length. The Hamaker parametrisation for example suggests that L_n is about twice as large as L_p for all aluminium fractions.

We cannot in principle rule out that L_p may be greater than L_n , for example due to particular growth or geometrical considerations. In the absence of more

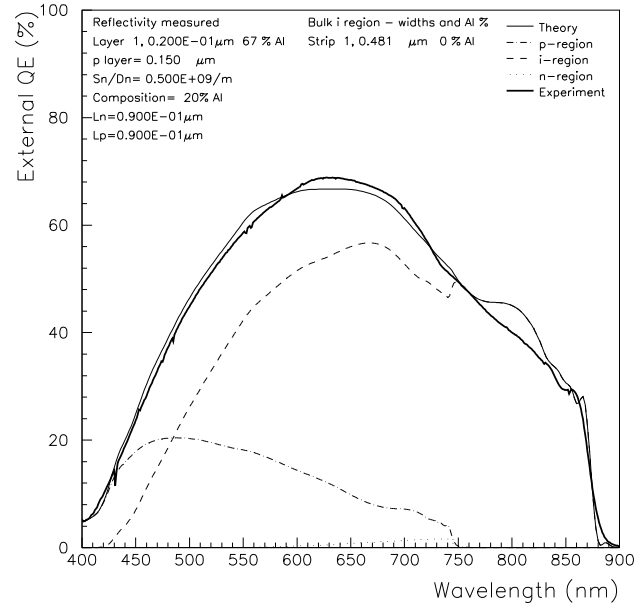


Figure 8.15: *QE* modelling and data for U2028, which consists of 30% p and n layers with a GaAs i region

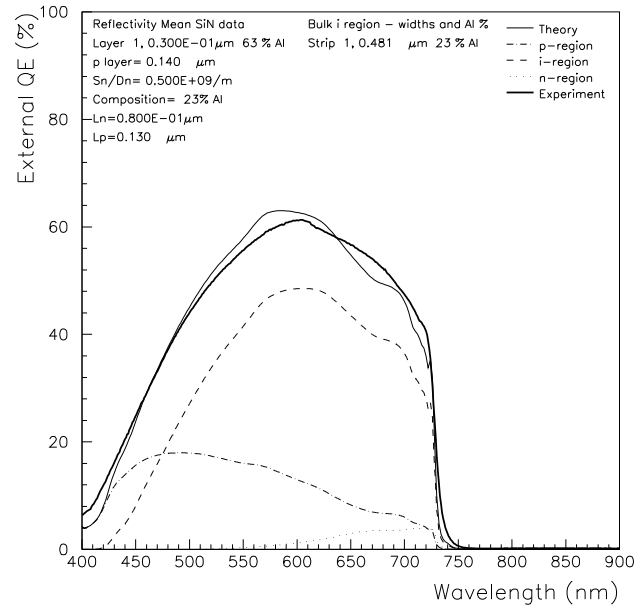


Figure 8.16: *QE* modelling and data U4036, which is a p - i - n repeat of U2028 with a base aluminium fraction of $X_{b2} = 23\%$

detailed information, however, we choose to set a limit on the maximum value of L_p , which is that it should be less than or equal to L_n

The short wavelength response then poses a problem because a value of L_n high enough to fit the band edge causes the model to overestimate the QE at short wavelengths, even though we use a quasi-infinite recombination parameter.

The fits presented in figures 8.14 to 8.16 are the result of a compromise between these two constraints. The resulting diffusion lengths of L_p and $L_n \sim 0.10\mu m$ are smaller than those given by the Hamakers parametrisation, which predicts $L_n \sim 0.39\mu m$ and $L_p \sim 0.20\mu m$.

Finally, the quantum wells in the QWSC sample are modelled as 70\AA , which is significantly smaller than the nominal 87\AA . Furthermore, we note that the model overestimates the QE contribution in the first quantum well continuum, at about 800nm . The misfit in this wavelength range is not serious, however, and is of the order of the experimental error of $\pm 5\%$ in QE .

This may be interpreted as indicating a loss mechanism in the quantum wells, possibly due to the increased recombination at the interface between quantum wells and the barriers. Alternatively, dopant diffusion, combined with a diffusion length which is closer to the Hamaker value would reduce the QE at short wavelengths and increase it near the band edge E_{b2} . More characterisation is required to establish whether or not this is the case.

8.4.2 30% samples

Figures 8.17 and 8.18 show QE data and modelling for U2029 and U2030. The true aluminium fractions are estimated at $X_{b2} = 33\%$ and $X_{b2} = 36\%$ respectively. The n layer contribution of the QWSC device appears negligible, and no reliable estimate of L_p is possible. The recombination parameter \mathcal{S} is modelled as small but finite. L_n is then the single significant fitting parameter, and is modelled as about $L_n \sim 0.07\mu m$. This compares favourably with the Hamaker value of $0.053\mu m$.

The quantum well QE is again overestimated by the model. This may be

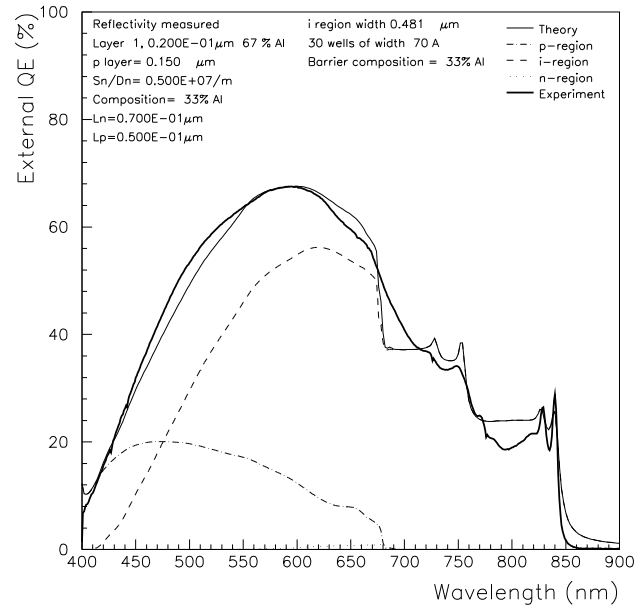


Figure 8.17: *QE* modelling and data for nominally 30% aluminium 30 well sample U2029

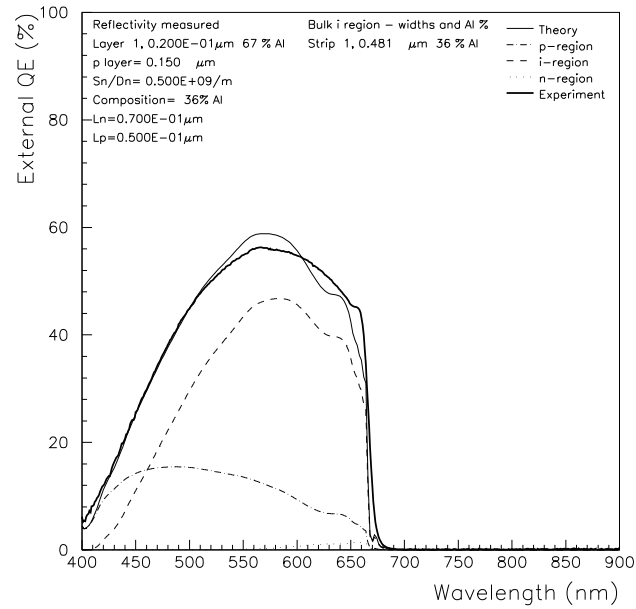


Figure 8.18: *QE* modelling and data U2030, the p - i - n control to U2029

ascribed to the same reasons as were given for U2027 in the previous section.

For the p - i - n samples U2030, the n layer QE is again negligible. The surface recombination parameter in this case appears effectively infinite, although the predicted diffusion length is identical to the QWSC sample. Problems in the fit are similar to those seen for sample U4036, but are again comparable to the experimental error.

The estimate of L_n in this case is more reliable than in the case of the 20% samples because the fitting procedure is simpler and the resulting match between theory and experiment better.

8.4.3 40% samples

The 40% samples U2031 and U2032 are mutually more consistent, and are shown in figures 8.19 and 8.20. Both have a modelled aluminium fraction of 47% instead of the nominal 40%. The n region QE is again vanishingly small. \mathcal{S} in both cases appears too low to model, and is set to zero.

The diffusion lengths in this case are modelled as $L_n \sim 0.040\mu m$ for the QWSC and $L_n \sim 0.055\mu m$ for the p - i - n sample. Hamaker in this case suggests $0.02\mu m$.

The quantum wells in this case fit very closely in the first continuum. This however contradicts the possible explanation for an overestimated well QE in the 20% and 30%, since the interface recombination in a 40% sample should in principle be higher.

8.4.4 Diffusion length tabulation

Figure 8.21 shows the modelled value of L_n as a function of aluminium fraction X_{b2} for QWSC and p - i - n MBE grown ungraded structures of the previous section. Also shown is the Hamaker parametrisation [24] for the relevant doping level.

The modelled values show a weaker dependence on aluminium fraction than the Hamaker parametrisation. The modelled values decline slowly with increasing

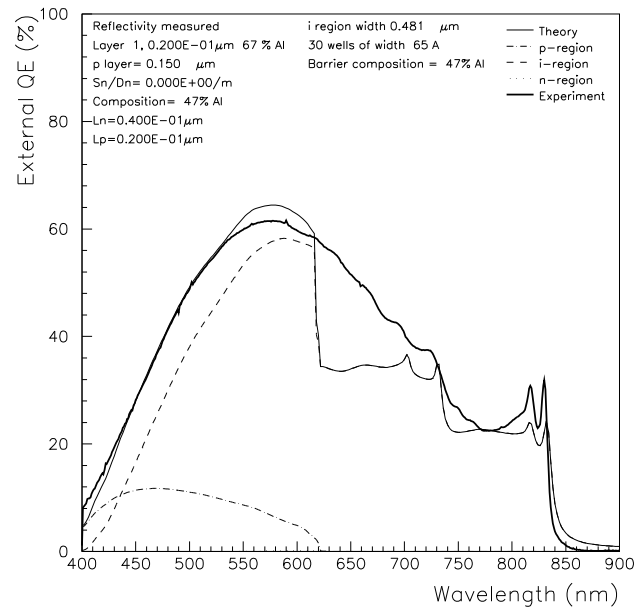


Figure 8.19: *QE* modelling and data for nominally 40% aluminium 30 well sample U2031

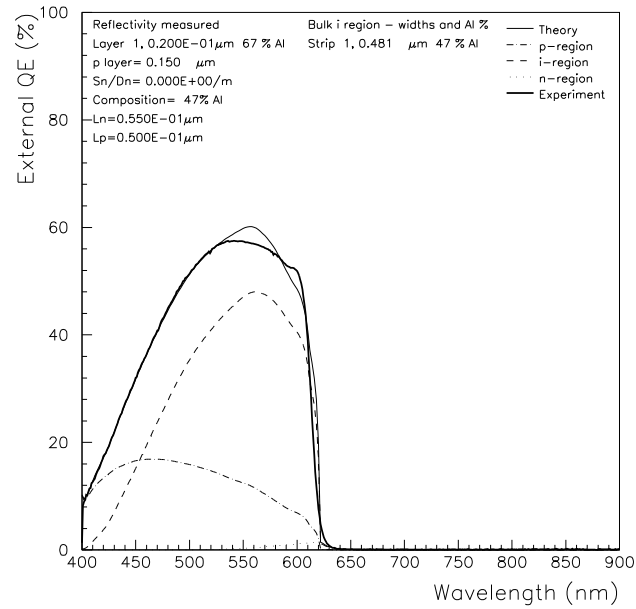


Figure 8.20: *QE* modelling and data U2032, the p - i - n control to U2031

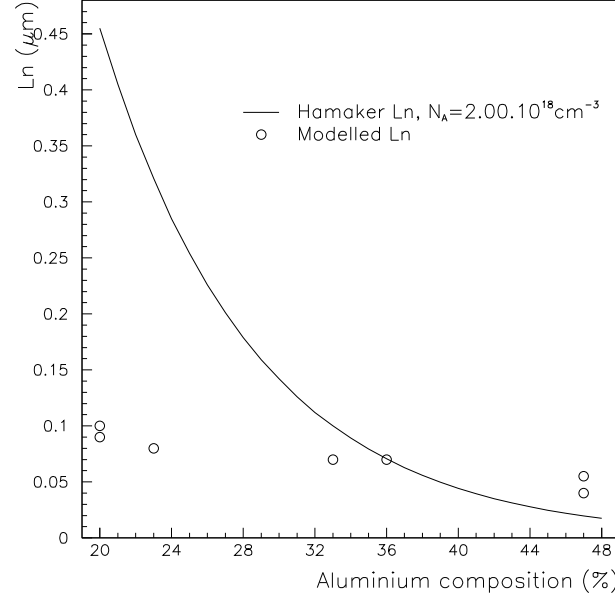


Figure 8.21: Modelled minority electron diffusion length L_n for p - i - n and QWSC samples, compared with Hamaker's parametrisation for the MBE doping level doping levels

X_{b2} . These values define the piecewise linear parametrisation which is used to define the position dependence of L_n in the graded structures of the section 8.5.

We conclude however that the transport parameters derived from the QE spectra systematically indicate poorer minority carrier transport efficiency than has been reported in the highest quality $\text{Al}_x\text{Ga}_{1-x}\text{As}$. Bachrach[43], for example, has reported diffusion lengths of the order of $2.3\mu\text{m}$ in p doped $\text{Al}_x\text{Ga}_{1-x}\text{As}$ with a composition of $x = 36\%$, although at a lower doping level of $N_A \sim 10^{17}\text{cm}^{-3}$. The review by Ahrenkiel [45] shows that diffusion lengths greater than those given by the Hamaker parametrisation are possible.

8.4.5 Conclusion

In this section we have modelled a selection of samples from the two available growth systems. The resulting p layer diffusion length has in all cases proved smaller than the p layer width. Although the MOVPE material seems to have more variable minority carrier transport properties, the values obtained are close to those of the MBE material. A small mismatch between theory and experiment

has been observed in a number of samples. This may be due the uncertainty in the absorption coefficient mentioned in chapter 4, although other influences such as the reflectivity, depletion widths and i region width cannot be ruled out.

The resulting tabulation of the electron minority carrier diffusion length L_n is more weakly dependent on the aluminium fraction than suggested by the parametrisation due to Hamaker [24]. The results further indicate that the minority carrier transport efficiency in both MOVPE and MBE material is relatively poor compared to values in the literature.

The surface recombination parameter \mathcal{S} is low in most of the samples we have studied. Notable exceptions are the MBE grown samples with low aluminium composition and one p - i - n sample from the same growth system. These samples used a quasi-infinite \mathcal{S} . Supplementary characterisation is required to establish whether this is due to inaccurate modelling of the minority carrier transport near the surface of the cell, or to geometrical and compositional factors.

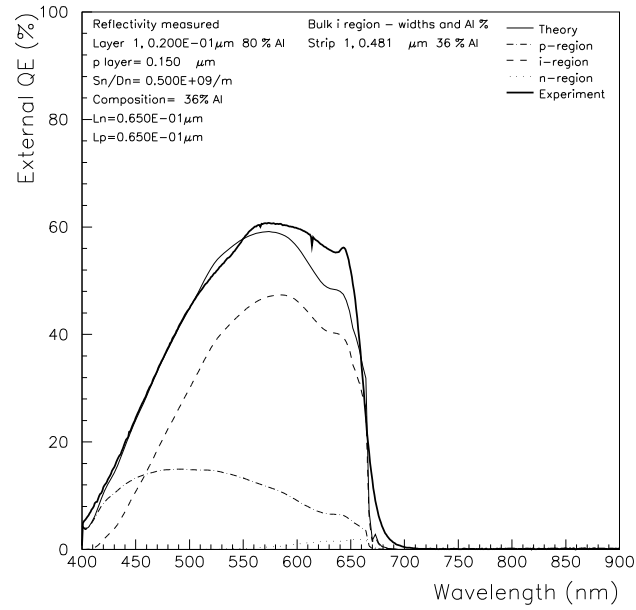
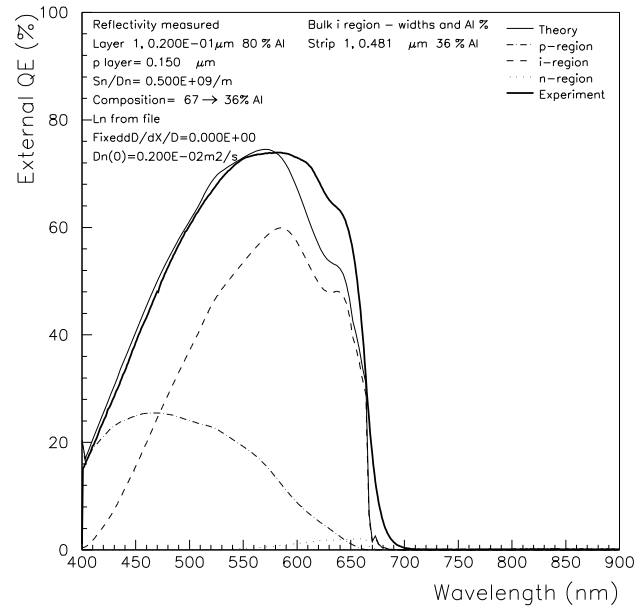
8.5 Compositionally Graded p layer samples

In this section we present data and theoretical modelling of the QE of graded p layer samples grown by MOVPE and MBE. We will quote estimates of the short circuit current density J_{sc} calculated from the experimental QE data for an illumination of AM1.5. These figures do not include contact shading.

In the case of MBE samples, we will use the diffusion length parametrisation based on the modelling of ungraded samples. In the case of MOVPE samples, we do not have as wide a range of samples with different aluminium fractions. The previous section however has demonstrated that the diffusion length in both growth systems is similar. We shall therefore use the same table of L_n as a function of aluminium fraction for MOVPE material.

8.5.1 MOVPE Samples

The graded p design was initially tested by graded p - i - n device QT601c and its control structure QT601a, which is identical but has no grade. The graded p

Figure 8.22: Experimental and modelled QE of ungraded MOVPE p - i - n QT601aFigure 8.23: Experimental and modelled QE of graded MOVPE p - i - n QT601c

in sample QT601c is $0.15\mu\text{m}$ thick and is graded from $X_{b1} = 67\%$ to $X_{b2} = 33\%$, and has a window of thickness $0.02\mu\text{m}$ with a composition of 80% aluminium. John Roberts however has indicated that growth problems cast some doubt over the real value of the aluminium fraction X_{b1} at the top of the grade. The QE data and modelling for these samples is shown in graphs 8.22 and 8.23.

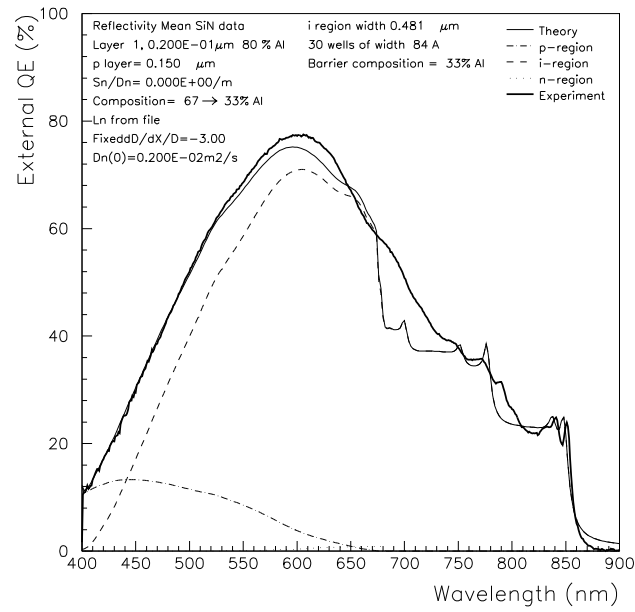
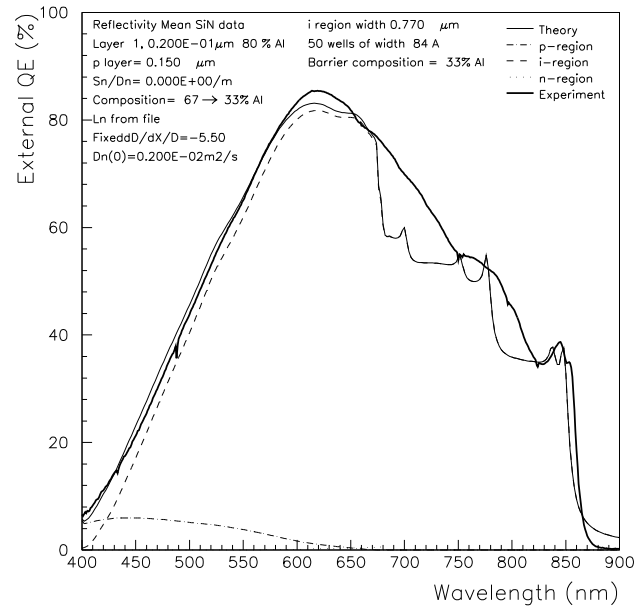
The fit for both samples requires a quasi-infinite recombination parameter and L_n and $L_p \sim 0.06\mu\text{m}$. The fitting problems here are again reminiscent of samples such as the 20% ungraded devices of the previous section, but are more significant. A larger value of L_p would again improve the QE fit, but cannot be justified without more information.

The QE of graded sample QT601c suffers from a similar problem near the band edge. The short wavelength QE however is accurately modelled with $\mathcal{D}_\mathcal{X} = -1.5$, versus the Hamaker value of -4.2. The grade in this case enhances the short circuit current in AM1.5 from $J_{sc} = 8.06\text{mA}/\text{cm}^{-2}$ for QT601a to $J_{sc} = 10.35\text{mA}/\text{cm}^{-2}$. This represents an overall increase in projected J_{sc} of 28%.

A set of three samples was subsequently grown to investigate the performance of a grade in MOVPE QWSC designs. The first of these is QT640a, which is similar to QT468a but for a grade in the p layer with nominal composition $X_{b1} = 67\%$ and $X_{b2} = 33\%$. Sample QT640b is identical to QT640a and has the same grading scheme, but has a wider i region of $0.78\mu\text{m}$ containing 50 wells. Finally, QT641 is a p - i - n control to QT640b but does not contain a grade. This last p - i - n sample was grown to compare material quality between the two growth runs.

The experimental QE and modelling for QT641 is shown in figure 8.26. The experimental QE is very poor at short wavelengths, indicating poor minority carrier transport. The modelled p layer QE is dominated by bulk recombination losses, and the parameter \mathcal{S} is not significant in the fitting. It is therefore set to zero. Finally, the n layer QE is negligible.

The two QWSC samples bear out the conclusion that minority carrier transport efficiency for these samples was lower than for the previously grown samples QT601a and QT601c. Although the grades in both QWSC samples are of iden-

Figure 8.24: *QE* of 30 well QWSC QT640a, with p layer grading ranging from 30% to 67%Figure 8.25: *QE* of 50 well QWSC QT640b with p layer grading ranging from 30% to 67%

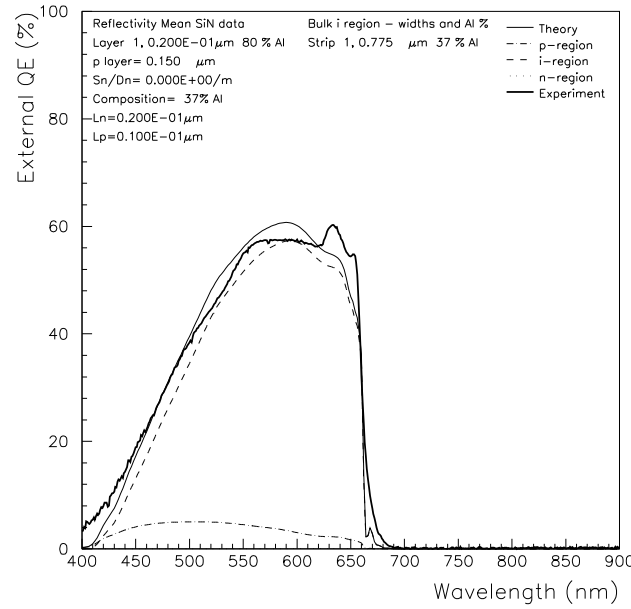


Figure 8.26: QE of QT641, the p - i - n control to 50 well QWSC graded 30-67%

tical design to that of QT601c, they perform more poorly.

The modelling and data for these samples is shown in figures 8.24 and 8.25. The modelling assumes a mean SiN reflectivity. The diffusivity field for QT640a was $\mathcal{D}_\chi = -3$. The p layer QE of sample QT640b in particular is seriously degraded, and is modelled with $\mathcal{D}_\chi = -5.5$. The rather large value of \mathcal{D}_χ for QT640b is expected to be at least partly due to the assumption that the L_n tabulation based on the MBE samples of the previous section is over-optimistic for these samples.

Figure 8.27 compares the QE of QT640a with QT468a, which has the same design but for the absence of the grade. The QE enhancement at short wavelengths is too small to be significant. We can state however that the grade has at the very least maintained the p layer QE in poorer material. This does not take into account the different reflectivities in the two samples however, which was better in the ungraded sample.

At intermediate wavelengths, a significant QE enhancement is observed because of increased light transmission to the i layer.

Comparison of short circuit current densities gives $J_{sc} = 14.94 \text{ mA/cm}^{-2}$ and

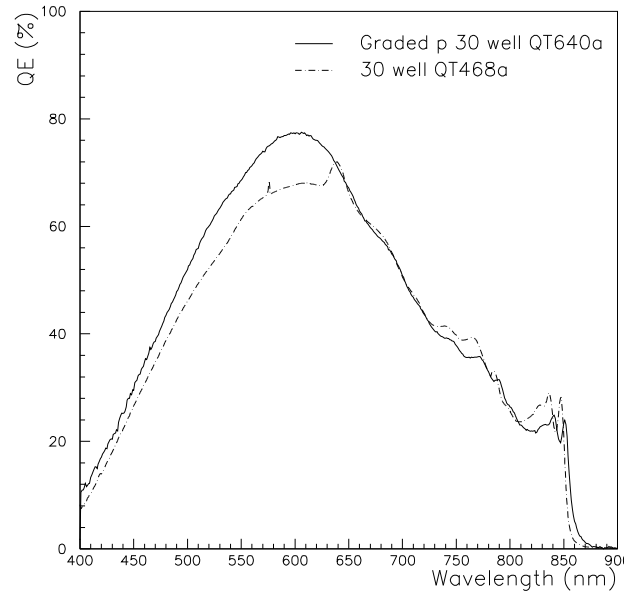


Figure 8.27: Comparison of thirty well sample QT468a and similar structure QT640a which has a graded p layer

$J_{sc} = 14.02 \text{ mA/cm}^{-2}$ respectively. This represents an enhancement of 7% in J_{sc} for the graded sample, despite the inferior material carrier transport in sample QT640a. We conclude that these samples illustrate the principle of a grade in QWSC samples, despite the fact that the ungraded benchmark sample benefits from superior minority transport properties.

Finally, we present experimental and theoretical data for sample QT794a which cannot be explained by the model. This sample has been mentioned in section 7.1 and was shown to have an high N_{BG} .

This sample was designed with a reduced p layer thickness of $0.1 \mu\text{m}$. The grading scheme was aimed at maximising the p layer response by choosing a moderate grade ranging in composition from $X_{b1} = 40\%$ to $X_{b2} = 30\%$. This is at the lower end of the optimised theoretical grading predictions presented in section 5.2.4, and is intended to ensure good minority carrier transport by reducing the amount of aluminium towards the front of the p layer. We shall present results in the MBE section below which demonstrate successful grades over this compositional range. Furthermore, the results of section 5.2.5 were

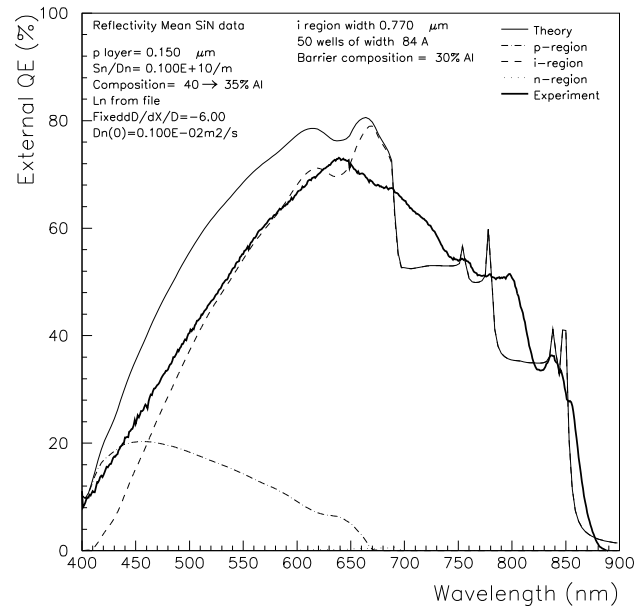


Figure 8.28: MOVPE version QT794a of the optimised 50 well graded QWSC design

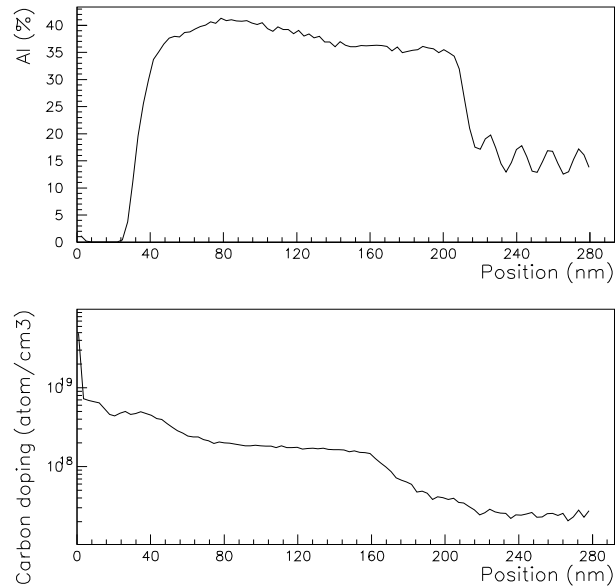


Figure 8.29: SIMS measurements of C doping and aluminium composition in sample QT794a

exploited and the window in this sample removed.

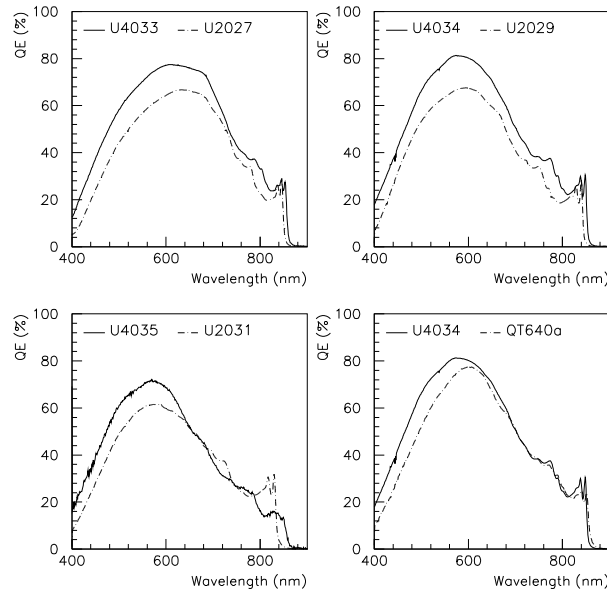
The results are shown in figure 8.28. The modelling benefits from a measured reflectivity. The MIV data indicated that the QE measurement had to be performed at at least -10V in order to ensure full depletion of the device. We note that the experimental QE between about 500nm and 620nm is approximately equal to the i region QE alone, suggesting the the p layer QE is essentially zero in this range. It is impossible to model the p layer contribution consistently under this constraint, particularly since the short wavelength response is not negligible, indicating that at least some minority carriers from the front of the cell are collected.

SIMS and TEM measurements were performed on this sample and its MBE grown companion U6041, which will be presented in the following section. The TEM measurements confirmed that the dimensions of this sample were correct. The compositional SIMS measurements had to be calibrated by inferring the aluminium content from QE spectra. The resulting aluminium profile is shown in figure 8.29. The depth calibration used by Federico Caccavale in the SIMS results was independently verified by the TEM measurements. The mean sum of the well and barrier thickness was estimated as $(15.3nm \pm 0.5nm)$, which is experimentally indistinguishable from the nominal value of $14.7nm$ set down in the sample description.

8.5.2 MBE

For MBE material, it was decided to continue the study of QE as a function of base aluminium fraction X_{b2} for QWSC graded structures. The samples are, in the first instance, based on those studied in section 8.4. They are all Be doped at a level of $N_A = 1.34 \times 10^{18} \text{cm}^{-3}$ in the p layer and Si doped with $N_D = 6.00 \times 10^{17} \text{cm}^{-3}$ for the n layer. The main design characteristics of the samples studied here are summarised in table 8.1. No reflectivity measurements could be performed on the samples U4034-U4035 due to the absence of reflectivity measurement samples in the processing run.

Sample	U4032	U4033	U4034	U4035	U6041
Window (μm)	0.03	0.03	0.035	0.035	0
X_{b1} (%)	40	40	67	67	40
X_{b2} (%)	20	20	30	40	30
x_i (μm)	0.81	0.481	0.481	0.481	0.81
Wells	50	30	30	30	50

Table 8.1: Principle design parameters of MBE grown graded *p* QWSC samplesFigure 8.30: Comparisons of *QE* for QWSC samples with and without grades, for a variety of grading schemes. Also shown is comparison of similar graded QWSC structures grown by MBE and MOVPE

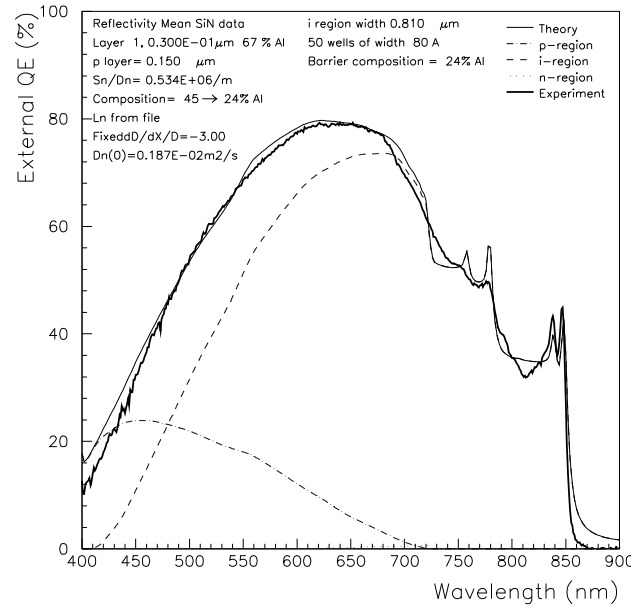


Figure 8.31: MBE 50 well QWSC U4032, graded 20-40%

The four graphs of figure 8.30 compare the experimental QE of ungraded QWSC structures U2027, U2029 and U2031 with their graded counterparts. Enhancements in QE are observed in all cases. The increases in predicted J_{sc} are 21%, 24% and 11% for the samples with $X_{b2} = 20\%$, 30% and 40% respectively. The last figure is lower because of the degraded QE in the wells.

Figure 8.30 also shows a comparison between the MOVPE sample QT640a reviewed in the previous section and U4034, which has similar specifications. Although U4034 has a thicker window than QT640a, it nevertheless has a significantly better short wavelength QE . Comparison of modelling results for these two samples indicates a p layer QE about three times better for the MBE sample. This confirms the conclusion reached in the previous section regarding the poor material quality in the graded MOVPE samples.

Experimental and modelled QE results for these samples are given in graphs 8.33 to 8.34. Modelling is accurate for U4032 and U4034, but shows significant deviations for U4033 and U4035.

Sample U4032 requires a diffusivity field $\mathcal{D}_X = -3$ and shows a slight shortfall in the wells, although this is not significantly greater than the experimental error.

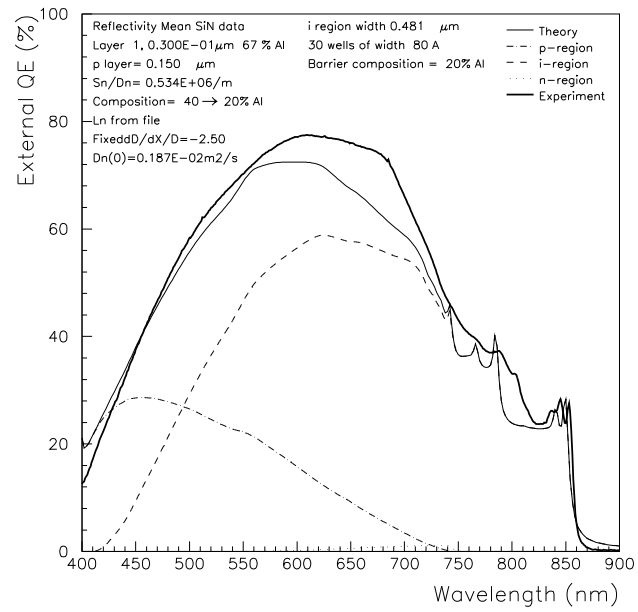


Figure 8.32: MBE 30 well QWSC U4033, graded 20-40%

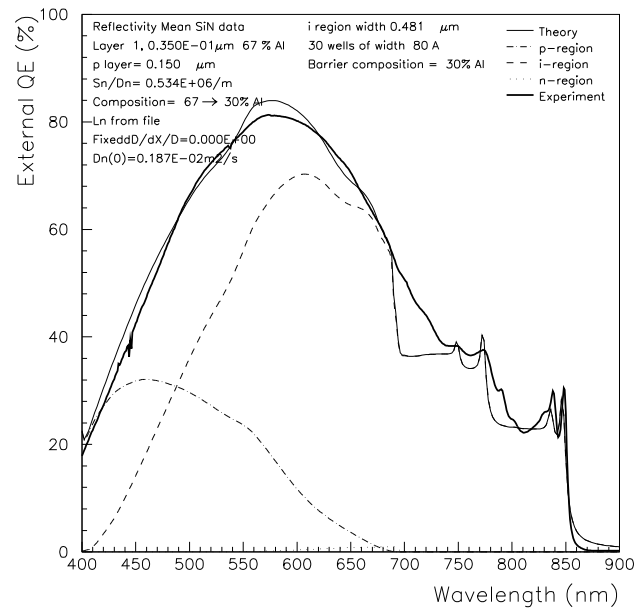


Figure 8.33: MBE 30 well QWSC U4034 graded 30-67%

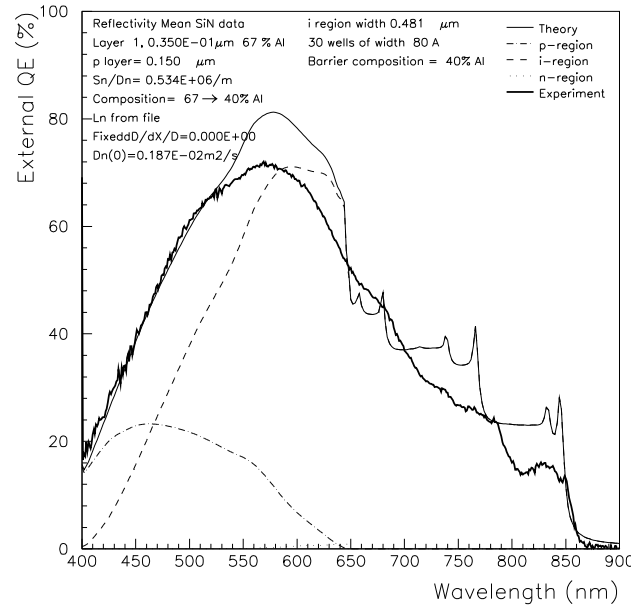


Figure 8.34: MBE 30 well QWSC U4035 graded 40-67%

Sample U4033 presents a serious shortfall in modelled QE near band edge E_{b2} . This has previously been observed in several MBE and MOVPE samples such as U2027, U4036 and QT601c. As in the fitting carried out for these samples, the value of L_p required to fit the QE more accurately in this wavelength range is too great to provide a realistic explanation without direct measurement of this parameter. We have therefore used the value of L_p found to fit previous MBE samples with aluminium fractions of 20%, which is $L_p \sim 0.1\mu m$. The diffusivity field in this case is $\mathcal{D}_{\mathcal{X}}=-2.5$.

Sample U4034 (figure 8.33) is modelled accurately with a diffusivity field $\mathcal{D}_{\mathcal{X}}=0$. In theory, this indicates a constant diffusivity in the p layer. In practice, however, this is probably due to the assumptions we have made regarding the dependence of L_n on aluminium fraction and a reflectivity which is given by the average SiN data.

Sample U4035 (figure 8.34) is accurately modelled in the short wavelength regime with $\mathcal{D}_{\mathcal{X}}=0$. This is ascribed to the same reasons given for U4034. For this sample, however, there is a clear misfit in i region contribution. Devices for this sample were generally poor, and the QE data noisy. The correct attribution of the

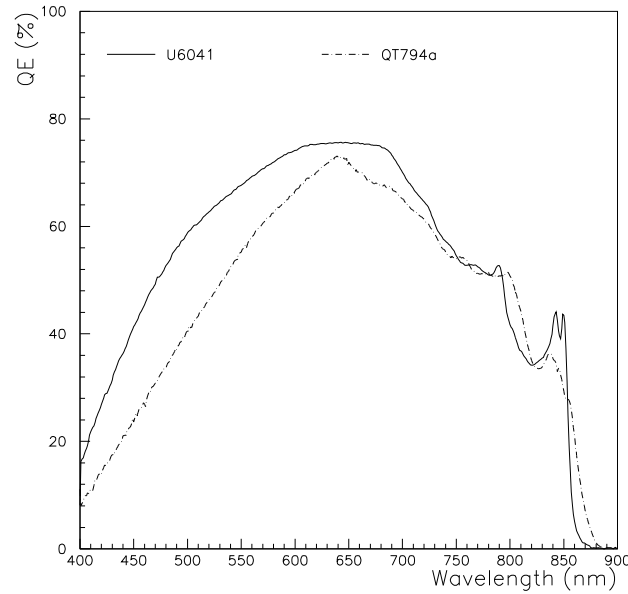


Figure 8.35: Comparison of MOVPE and MBE versions of an optimised 50 well design QT794a and U6041 with graded p and no window

i region shortfall requires reprocessing, and could be assisted by supplementary characterisation such as SIMS measurements. The short wavelength response however suggests that the p layer contribution is being accurately modelled.

Finally, figure 8.35 shows optimised sample U6041. The concepts underlying the design of this sample are identical to MOVPE grown QT794a and were outlined in section 8.5.1. The figure also shows the QE of the MOVPE device. As in the case of QT640a and U2029, the MBE device again performs better.

Initial modelling of the experimental data with nominal parameter values showed similar problems to those experienced for QT794a. In particular, the modelled i region QE was greater than the experimental QE between about 550nm and 600nm. This suggests departure from design characteristics. Furthermore, the model significantly overestimates the QE at short wavelengths, indicating an impaired p layer QE .

Extensive characterisation was carried out on this sample. Calibration of the SIMS depth scale was verified by TEM, as for sample QT794a in previous section 8.5.1. TEM data indicated that mean sum thickness of barrier and well

was $(14.1\text{nm} \pm 0.5\text{nm})$, with the error estimated from the resolution of the micrograph. The specification was 14.7nm , which is not significantly greater. The total thickness of the multiple quantum well system confirmed the depth calibration of the SIMS data presented in figure 8.36. The graphs show only the most relevant data, which are the aluminium fraction and Be doping for the first $0.6\mu\text{m}$ of the sample, including the $0.04\mu\text{m}$ GaAs capping layer. Lower resolution measurements covering the entire sample were also supplied.

Federico Caccavale has confirmed that the aluminium SIMS signal in counts per second will be linearly dependent on the aluminium composition for the range of aluminium fractions in these samples. Modelling of a mirrored device processed from the U6041 wafer will be presented in section 8.6. This has allowed us to fix the lower aluminium fraction at $X_{b2} = 24\%$. The linear relationship between SIMS signal and aluminium fraction, together with the value of X_{b2} , enable us to calibrate the SIMS mass spectrometer signal.

The resulting aluminium compositional profile is shown in the lower part of the figure. We note first that the aluminium composition peaks at only 29%. Christine Roberts who grew this sample has confirmed [55] that grades over thin layers are technologically difficult. This is a consequence of the growth scheme for graded structures, which treats the grade as a series of ungraded strips grown close together. In practice, a smooth grade is obtained by ensuring that the aluminium source is never in equilibrium, and has a constantly increasing output flux.

If however the nominally ungraded strips are too thin, the aluminium source has too little time to ramp up to the higher temperature required for the material with a higher aluminium fraction. The result is a lower final aluminium composition than expected, as seen in this sample. The grading technique can be improved by characterisation such as the SIMS data presented here, which can help in determining an optimum strip width resulting in both a smooth grade and an accurate target aluminium fraction X_{b1} .

Furthermore, the unexpectedly slow decrease in aluminium at the front of the p layer has resulted in a positive bandgap gradient with increasing distance at

the front of the p layer. The origin of this feature is not clearly understood.

This rounding off of the aluminium profile towards the top of the sample results in a thin layer with a bandgap gradient pointing towards the front of the cell. The resulting field will tend to drive minority carriers generated towards the front of the cell away from the depletion region, thereby degrading the short wavelength QE . This unforeseen effect is a result of removing the window layer. A similar effect in a sample with a window would not cause this problem, because the step in the conduction band at the interface between the window and the p layer acts as a minority carrier reflector.

Finally, we note that the Be dopant profile extends significantly further than the nominal $0.1\mu m$. Illegems [58] studied Be diffusion in MBE GaAs and $Al_xGa_{1-x}As$. He concluded that this dopant was promising insofar as it allows high doping levels ($\sim 10^{19}cm^{-3}$) whilst maintaining good surface morphology in the MBE material. Be diffusion coefficients are quoted in this work. Be diffusion has more recently been reported as a problem. Lee [59] has studied this problem more recently in $Al_xGa_{1-x}As$ as a function of aluminium composition and anneal temperature.

Using the correlated TEM and SIMS data, we predict an effective p layer thickness of $0.14\mu m$. This fairly conservative value, is based on the fact that the quantum well signal fits theory accurately, suggesting that the first wells on the p side of the i layer are not significantly doped. We note finally that the residual background doping in this sample is n type silicon, and were estimated in chapter 7 as being below $10^{15}cm^{-3}$ by both SIMS and the MIV technique.

The resulting QE modelling is shown in figure 8.37. Theory reproduces the experiment closely with a diffusivity field of -4.5. The surface recombination parameter is set to an effectively infinite value to account for the drop in aluminium fraction over the first few nm of the sample. The aluminium composition used in this case is based on the SIMS scan, and includes the ungraded $0.04\mu m$ unintentionally doped layer between the p and i layers.

The SIMS and TEM data also indicated that the n layer thickness is $0.72\mu m$ thick instead of the nominal $0.6\mu m$.

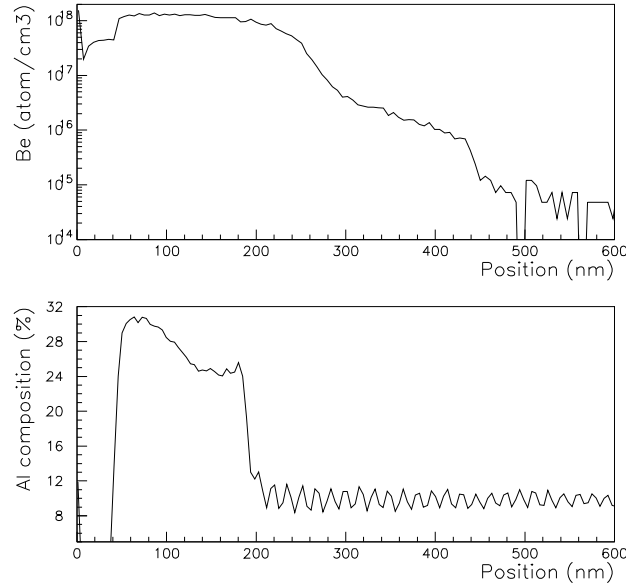


Figure 8.36: SIMS measurements of Be doping and aluminium composition in sample U6041

The dopant diffusion has proved crucial in understanding the QE of this sample. The extension of the p layer and consequential reduction in i layer thickness explains why modelling using nominal sample specifications overestimated the i region QE . Similarly, the extra thickness in the p layer and lack of grade over nearly a third of this layer explains the reduced p layer QE .

The final efficiency of this sample was estimated by Paul Griffin at $(14.2\% \pm 0.5\%)$ under tungsten illumination corrected to AM1.5 light levels. This is comparable with the efficiency reached by the previous best $Al_xGa_{1-x}As$ sample G951, which was mentioned in section 7.1.1. There is no control sample to compare the estimated short circuit current enhancement for this sample.

Despite the departure from device specifications, we have shown that the model has adequately reproduced data given corrected device specifications. This increases confidence in the ability of the model as a diagnostic tool.

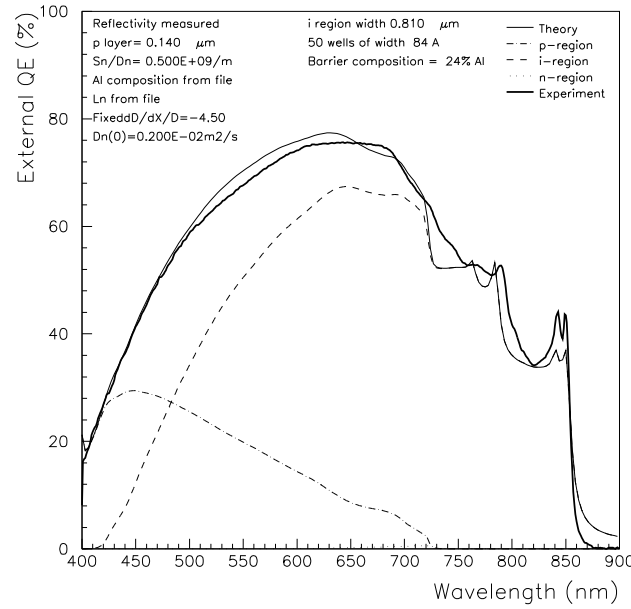


Figure 8.37: MBE 50 well QWSC without a window graded from $X_{b1}29\%$ to $X_{b2} = 24\%$.

8.5.3 Conclusions

The study of a wide range of grades has demonstrated their capacity to increase the QE of p - i - n and QWSC samples grown both by MBE and by MOVPE.

The case of sample U6041 has served to increase our confidence in the model both as a diagnostic tool and as a basis for further optimisations.

A large amount of detailed information about each sample is required. Since the advanced experimental characterisation cannot be carried out as a matter of course, we are frequently forced to make assumptions about composition. The modelling has furthermore had to use transport data extrapolated from ungraded samples. Finally, reflectivities are not always available.

As a result, theoretically well defined parameters such as the the diffusivity field and the recombination parameter which are used in the modelling are in practice ill-defined, since modelled values contain systematic errors due to the assumptions we have mentioned.

Despite these difficulties, the accuracy of the compositionally graded $Al_x-Ga_{1-x}As$ model has been demonstrated for a wide range of samples. In addition, the model can reproduce changes in QE due to a number of design changes to

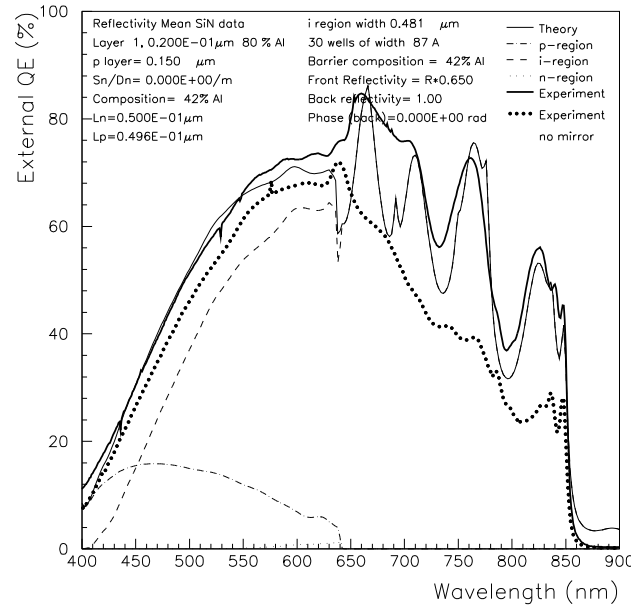


Figure 8.38: QE of mirrored sample QT468a. Also shown for reference is the QE of an AR coated device without a mirror

the original structure. These include compositional grades in neutral layers and depleted layers from three different growth systems. Enhancements in QE for samples with graded p layers have been shown in a wide range of samples.

The diagnostic capabilities of the model have furthermore been confirmed by comparison with quantitative characterisation techniques. To our knowledge, this is the first model of compositionally graded $\text{Al}_x\text{Ga}_{1-x}\text{As}$ cells to be used to model experimental data.

8.6 QE of Mirror Backed Samples

In this section we investigate the QE enhancement in the quantum well wavelength range. The technique was tested on the 30 well sample QT468a. Theoretical modelling and experiment for this sample is shown in figure 8.38, together with the QE of an AR coated device without a mirror for comparison. The increase in predicted J_{sc} for this device is 27%. Main fitting parameters are given on the graphs.

The wavelength dependence of the Fabry-Perot peaks is accurately modelled.

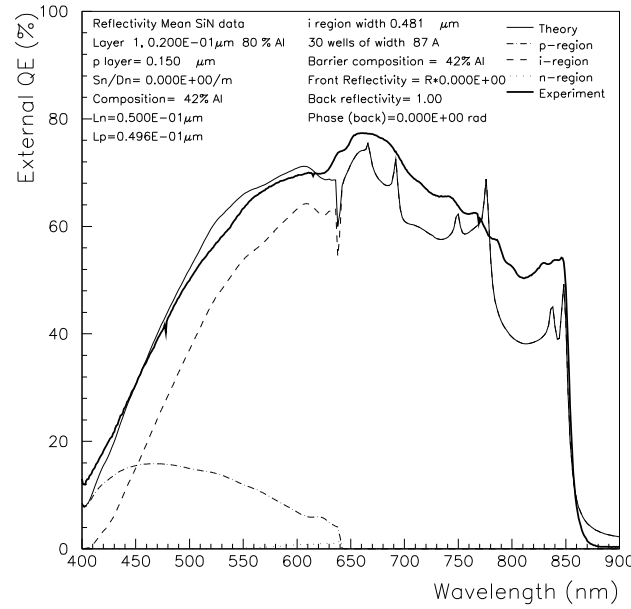


Figure 8.39: QE of a mirrored QT468a device demonstrating non-specular reflection from the back surface and QE enhancement greater than two passes.

Variations in model accuracy over the quantum well wavelength range are visible, and are due to the underlying inaccuracy of the quantum well absorption model.

Amplitudes of Fabry-Perot peaks in the experiment are variable, and generally lower than those predicted by the model. The broadening mechanism responsible for this is not well understood, but may be partly due to roughness at the surface of the mirror.

Figure 8.39 illustrates a mirrored device processed from the QT468a wafer at the same time as that of figure 8.38. We note a complete absence of interference peaks in this case. Moreover, the QE enhancement is more than can be explained by a double pass. We interpret this as indicating that the light is not being specularly reflected from the back surface. The randomising effect of reflection from a rough mirror causes the relative phases of internally reflected light beams to be randomized. Since the mean path length is also increased, this results in both increased light trapping in the cell and the disappearance of the Fabry-Perot peaks. Both devices processed from the QT468a wafer are modelled with a zero back surface phase change.

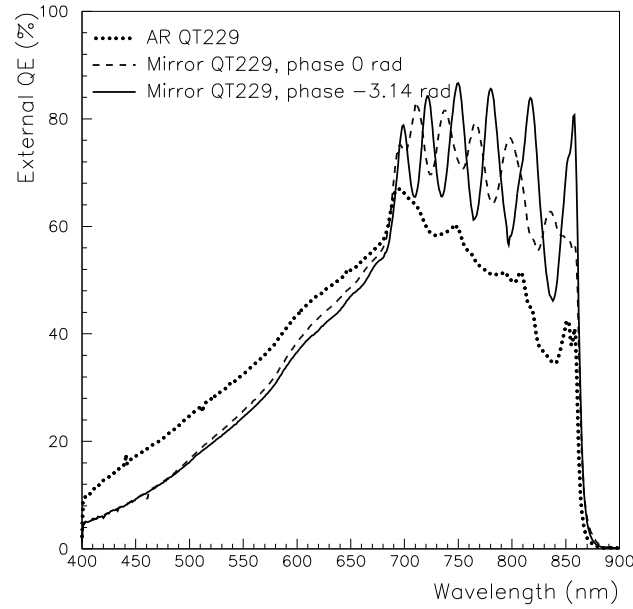


Figure 8.40: Experimental QE enhancement in two mirrored QT229 devices, compared with a AR device without a mirror

Figure 8.40 shows experimental data for QT229, which is a 50 well QWSC with a very thick p layer of nominal thickness $0.5\mu m$. The three QE curves relate to an AR coated device and two AR coated and mirrored devices. We note that the positions of the Fabry-Perot peaks for the two mirrored samples are significantly out of phase. The modelling for these two samples is given in graphs 8.41 and 8.42. The modelled phase change differs by a factor of nearly π . This result is not unexpected in the light of discussions with Mark Whitehead [37] which indicated that the phase change is device dependent at metal- semiconductor interfaces.

We note that the frequency of the theoretical peaks in wavelength is smaller than that of the experiment. This suggests that the model is underestimating the width of the optical cavity defined by the mirror and the front surface. The accurate fits obtained in other samples support the conclusion that the cell is wider than expected.

Experimental and theoretical QE for a mirrored device processed from the U6041 wafer is shown in figure 8.43. Only two devices of this type were processed, one of which was not successful.

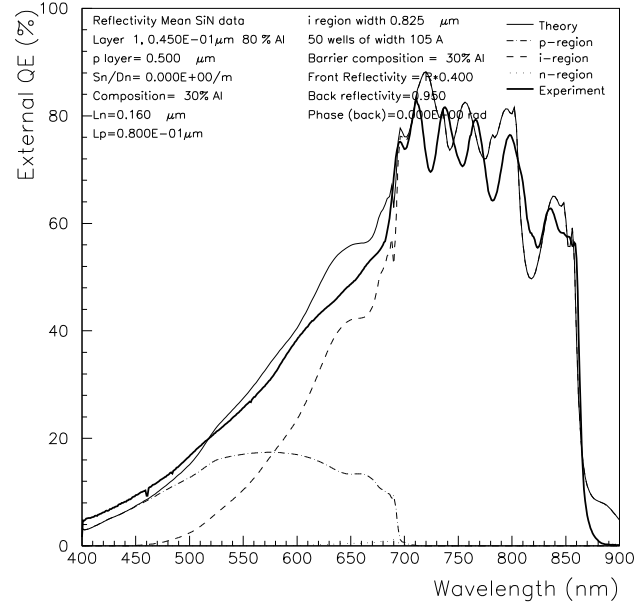


Figure 8.41: QE of a QT229 mirrored device showing a back surface phase change $\psi_b = 0$ radian

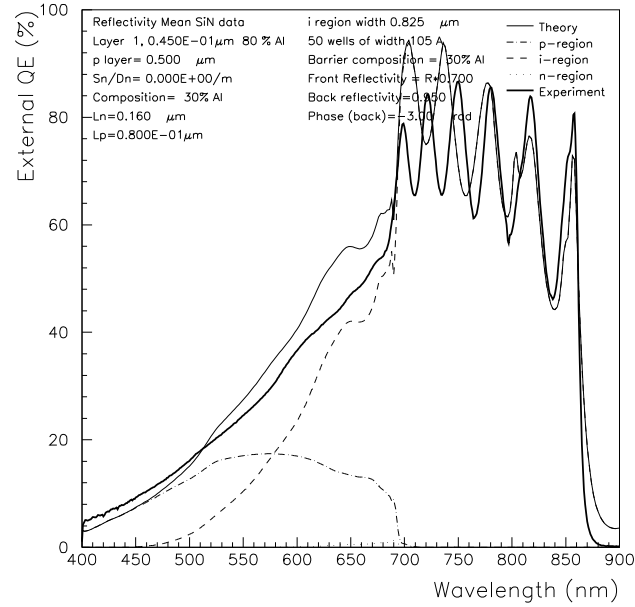


Figure 8.42: QE of a a QT229 mirrored device showing a back surface phase change $\psi_b = -3$ radian

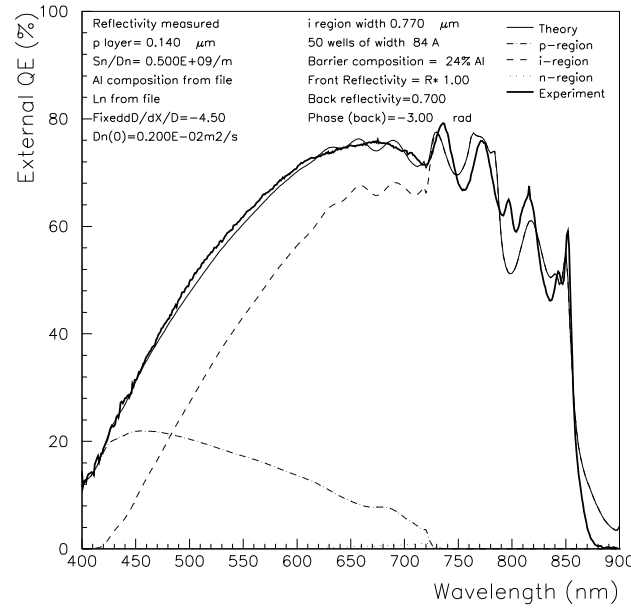


Figure 8.43: QE of a mirrored device processed from the U6041 wafer

Despite this, an accurate fit is obtained using the same parameters as in section 8.5.2 together with a back surface phase change of -2.8 radians and a front reflectivity factor $\mathcal{F} = 0.4$, such as was estimated for the QT229 modelling of figure 8.41.

No measured reflectivity was available for this sample. We have assumed a poor reflectivity, basing this on the fact that the mirrored device has a significantly poorer response at short wavelength than the device without a mirror discussed in section 8.5.2. This was clearly visible on the devices, which showed a green tint characteristic of high reflectivity at short wavelengths. This device was processed at the time as the sample whose reflectivity was used in the modelling.

As we explained earlier, this sample was studied by SIMS and TEM. The wavelength dependence of the Fabry-Perot oscillations is reproduced.

This sample again illustrates the diagnostic capacities of the model, by showing that accurate modelling of the experimental data is possible if the structure is of good quality and the composition and geometry is well known.

8.7 Optimisations

Optimisation of Available Material

The model can now be used to optimise the QWSC design we have been considering. Two approaches to this exist. The first of these is to identify design changes made separately to samples that have been characterised, and to combine these in a single optimised sample.

This relatively conservative approach is illustrated in figure 8.44. This design, which we will call sample A, is based on a combination of the Eindhoven AR coat, an 80% window layer, and the grade demonstrated in sample U2029 together with the back surface mirror seen in 50 well QWSC devices processed from QT229 and U6041. Also shown is a prediction for the corresponding control without a grade or a mirror.

The modelled short circuit currents in this case are 22.3mAcm^{-2} for A and 17.0mAcm^{-2} for the control. This corresponds to an enhancement of 31% with the new design modifications when compared to the control shown in the figure.

The second and less reliable approach is an extrapolation to design parameters which have not been observed. Figure 8.45 shows a similar comparison between an optimised sample B and its control. The design in this case has an Eindhoven AR coat, no window, and a thinner $0.1\mu\text{m}$ p layer. In the case of the optimised sample, this p layer is again graded between $X_{b1} = 67\%$ and $X_{b2} = 30\%$.

The modelled short circuit current for these predictions are $J_{sc} = 23.6\text{mAcm}^{-2}$ for the optimised design and $J_{sc} = 19.7\text{mAcm}^{-2}$ for the control, or an enhancement of 20% overall compared to the control without a grade or mirror.

These results indicate that the more conservative approach can nearly match the current output of the more adventurous design. Both samples compare favourably with the previous best MBE sample G951 which was mentioned in sections 7.1.1 and 8.5.2, and which has a theoretical $J_{sc} = 18.2\text{mAcm}^{-2}$, compared to the experimental value of $(17.5 \pm 0.5)\text{mAcm}^{-2}$ quoted in Barnham *et al.* [50]. This estimate is an independent measurement carried out at the Fraunhofer

institute in Germany.

A prediction of the efficiency requires a model of the dark current of the cell. This is the subject of ongoing work by collaborators. However, we can make a rough estimate by assuming that the new samples have the same $\mathcal{FF} = 78\%$ and $V_{oc} = 1.07V$ which were observed experimentally in G951. This sets a lower limit to the projected efficiency of optimisation A since the higher current levels in this cell will increase the V_{oc} , and the similarity between G951 and design A should produce the same \mathcal{FF} . With these assumptions, the final estimated efficiency for this sample is then 18.6%.

The corresponding efficiency for sample B under the same assumptions is 19.7%. These results compare well with a good conventional ungraded p - n cell reported by Amano *et al.* [73], which had an aluminium composition of 30% and was 14.6% efficient under AM1.5 illumination. This cell was the result of extensive growth optimisation and had large diffusion lengths L_p and L_n , a high $V_{oc} = 1.28V$, a fill factor $FF = 70.7\%$ and a short circuit current $J_{sc} = 16.2mA/cm^{-2}$.

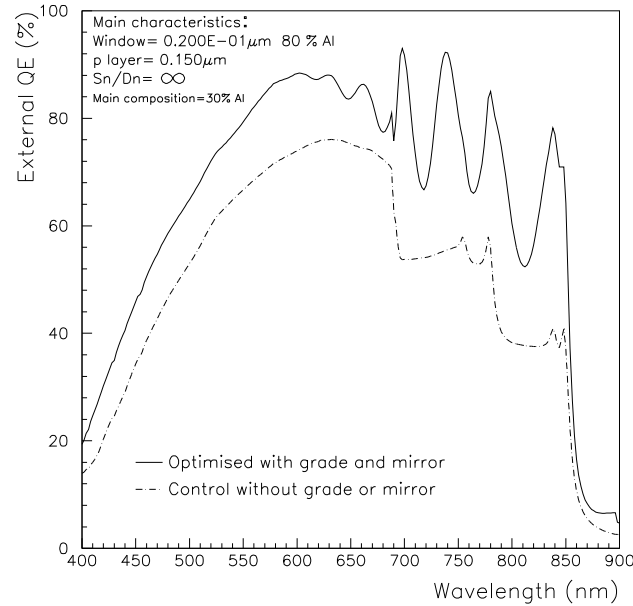


Figure 8.44: Theoretical prediction for optimised sample A combining the Eindhoven reflectivity, a $0.15\mu m$ grade with $X_{b1} = 67\%$ and $X_{b2} = 30\%$, a $0.02\mu m$ window with 80% aluminium, a high surface recombination and a back surface mirror.

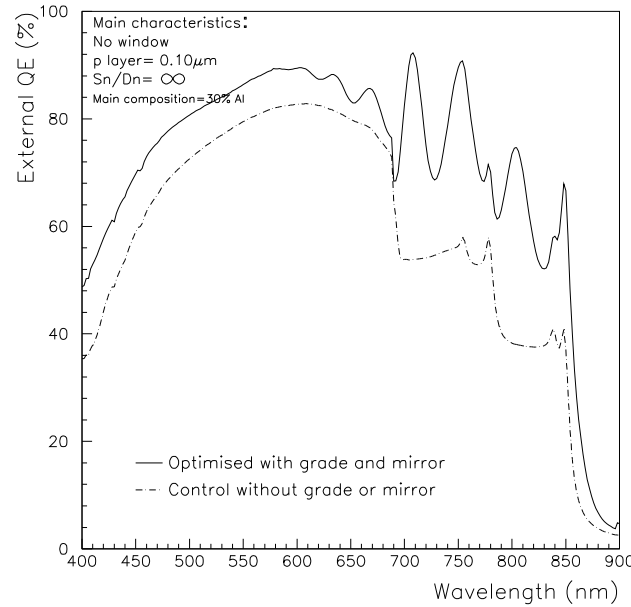


Figure 8.45: Theoretical prediction for optimised sample B combining the Eindhoven reflectivity, a thin $0.10\mu\text{m}$ grade with $X_{b1} = 67\%$ and $X_{b2} = 30\%$, no window, a negligible surface recombination and a back surface mirror.

Material with More Efficient Transport

Further efficiency enhancements are possible in material with improved minority transport parameters. We saw in section 5.2.4 that a graded p layer may reduce the efficiency of samples with good material quality. Section 8.1.5 further showed that the QE of graded structures in particular is sensitive to the position dependence of the diffusivity. Without a systematic study of the compositional dependence of the minority carrier transport in such material, therefore, we cannot reliably make predictions of the QE and J_{sc} enhancements expected in this system.

We therefore limit ourselves to short circuit current predictions of the best possible ungraded $\text{Al}_x\text{Ga}_{1-x}\text{As}$ QWSC cell, using the highest reported literature values for the transport parameters. We will compare these projected efficiencies with the results of the previous optimisation section.

The paper by Ludowise [27] mentioned in section 3.1.1 reports very high diffusion lengths in a series of solar cell samples grown by MOVPE. These values were derived from internal QE spectra, using a method similar to the one described

in this thesis.

An optimisation based on the Ludowise diffusion length of $L_n \sim 1.4\mu m$ at 30% aluminium composition yields a value of $J_{sc} = 25.6 \text{mAcm}^{-2}$. This corresponds to an efficiency between 21% and 24% for low and high values of FF and V_{oc} in AM1.5. These results apply to a 50 well sample with a back surface mirror, a $0.02\mu m$ window of composition 90% aluminium, no compositional grade and an optimum p layer thickness of $0.15\mu m$.

The Ludowise diffusion lengths, however, were estimated from a set of n-p algaas samples. The structure of the samples is not given in detail. The front n layer, however, is very thin. This indicates that the diffusion lengths are estimated from the QE near the $\text{Al}_x\text{Ga}_{1-x}\text{As}$ band-edge. The paper does not make clear how the n and p contributions to the QE in this regime were separated, since the methods we have used in this work do not apply to the Ludowise n-p structure. Loo [28] however has reported hole diffusion lengths of $2\mu m$ at an aluminium composition of 30% and a minority carrier lifetime of 13ns, which is close to GaAs. The Loo paper combined with data from Ludowise indicates that high minority carrier transport parameters are achievable in $\text{Al}_x\text{Ga}_{1-x}\text{As}$.

More readily achievable minority carrier lifetimes are reviewed in the review by Ahrenkiel [45]. These qualitatively agree with the values we have derived for the Eindhoven samples studied in section 8.2, and reproduce the functional form of the Hamaker parametrisation. Using a value of $L_n \sim 0.4\mu m$ and a structure similar to that described in the previous paragraph, we find an optimum short circuit current of the order of $J_{sc} = 24.2 \text{mAcm}^{-2}$. This corresponds to lower and higher limits to the estimated final efficiency of 20% to 23%.

The second optimisation is more likely to be achievable, since it is based on reproducible material quality. It should be noted that the final efficiency estimates are subject to large errors because of the lack of a reliable model for the V_{oc} and the FF .

We note that the estimated efficiencies for optimised QWSC structures without grades but with a back surface mirror are only about 5% to 10% greater than those of the optimised graded structures presented in the previous section for

the $\text{Al}_x\text{Ga}_{1-x}\text{As}$ material with significantly poorer minority transport efficiency studied in this thesis.

8.8 Conclusions to chapter 8

This chapter has demonstrated the accuracy of the theoretical model for the QE of mirrored and compositionally graded QWSCs by comparison with experiment for a wide range of $\text{Al}_x\text{Ga}_{1-x}\text{As}$ samples.

Results from a set of samples grown and processed in Eindhoven University of Technology showed that the theoretical model is capable of reproducing experimental data for QWSC and p - i - n structures with graded i layers. These samples further demonstrated accurate fits in samples with good material.

MOVPE and MBE structures with and without quantum wells and with ungraded neutral layers were characterised. These are used to establish the dependence of the minority carrier diffusion length L_n on aluminium fraction. These samples have been successfully modelled, and values of L_n for both growth systems extracted. MOVPE values are more variable than MBE ones but remain only fractionally different to MBE ones. The fitting is most accurate for intermediate aluminium fractions of $X_{b2} \simeq 30\%$. The model has some difficulty reproducing experimental QE data near the band edge E_{b2} for material with low aluminium fractions. At higher aluminium fractions, the well QE could not be modelled in one MBE sample. This is ascribed to a loss mechanism in the quantum wells.

Very high values of the surface recombination parameter \mathcal{S} were required to fit some samples. The origin of this problem has not been established. It is suggested that it may be due to shortcomings in the way the surface recombination is modelled. The presence of a damaged layer near the surface of the cell may explain this behaviour. Another candidate is dopant diffusion in MBE $\text{Al}_x\text{Ga}_{1-x}\text{As}$, since this effect would extend the width of the p layer, thereby reducing the QE at short wavelengths. More information is required to resolve this issue.

A wide range of QWSC and p - i - n designs with graded p layers was then in-

vestigated. Samples grown by MOVPE have demonstrated the QE enhancement but have shown significant materials problems. One optimised sample in particular cannot be modelled despite extensive characterisation. This is ascribed to the poor material quality indicated by high background doping levels and a very low p layer QE .

Graded structures grown by MBE have shown a clearer picture. Good fits are obtained overall with values of the diffusivity field \mathcal{D}_χ which are between 0 and the Hamaker value. Samples requiring $\mathcal{D}_\chi \simeq 0$ are interpreted as departing from the assumptions we have made regarding the variation of L_n with aluminium fraction, and, in some instances, to the reproducibility of the SiN reflectivity.

An optimised sample which did not initially perform as expected has been successfully modelled after supplementary information was provided by SIMS and TEM measurements carried out by collaborators. This information allowed us to correct the device specifications to allow for dopant diffusion in MBE material. This has cast some doubt over the p layer thicknesses used in modelling MBE samples from the same growth system. It was concluded however that the influence on the modelled transport parameters is less critical for other samples, because they have thicker p layers. This however is reminiscent of the conclusions we reached when discussing the surface recombination parameter.

The optimised MBE sample was repeated on the MOVPE reactor. Experimental data from this sample cannot be modelled despite similar characterisation. The SIMS together with MIV measurements, however, indicate poor material quality. This indicates that the samples may be too highly contaminated by impurities to operate successfully as solar cells.

Mirrored samples have been modelled accurately. One sample has confirmed that the phase change upon reflection at the back mirror is a variable parameter. A significant and variable broadening mechanism has been demonstrated by comparison of different devices processed from the same wafer. In the case of a QT468a device, this can be explained by an accidentally roughened back surface mirror and consequent randomising of the relative phase of the incident light.

The spacing of Fabry-Perot peaks on the wavelength axis has been accurately

reproduced. This indicates that QE characterisation of mirror backed samples may be of use in establishing the optical thickness of samples. Finally, mirror backed samples are also useful in determining the precise aluminium composition X_{b2} of QWSC samples, since the onset of Fabry-Perot oscillations is a sensitive function of the former.

We have demonstrated that both grades and mirrors are effective in increasing the QE and hence the short circuit current of QWSC structures in $Al_xGa_{1-x}As$ with poor minority transport characteristics.

This information gives us sufficient confidence in the diagnostic and predictive capabilities of the model to suggest further optimisations.

Optimisations using the model together with information from the experimental data were presented. The projected efficiency for the first of these optimisations is based on separate successful design changes which were verified experimentally. This produces a projected J_{sc} which is significantly greater than published good conventional $Al_xGa_{1-x}As$ solar cells with comparable aluminium fractions.

The second optimisation makes design changes which are an extrapolation of experimentally measured samples, but only exceeds the conservatively optimised sample of the previous paragraph slightly. A rough estimate of the efficiencies of these projections suggests a value of the order of 19% in AM1.5

Finally, these optimisations apply to available material. Further optimisations of growth conditions are required for the QWSC application in order to produce material with the minority carrier transport efficiencies which have been observed in Eindhoven material for example. We have mentioned the work by Amano [73] which started with fairly poor material but produced efficient minority carrier transport after a detailed growth optimisation study.

A set of calculations based on good material quality has predicted efficiencies of between 20% and 24% in optimised QWSC structures without grades but with back surface mirrors. This study shows that the material quality is the prime problem. A grade can compensate for poor material quality to a certain extent, but is not expected to improve good quality material.

We conclude however that the combination of a grade and a back surface mirror can bring the J_{sc} of QWSCs fabricated from poor material quality to within a few percent of that achievable with the best material.

Chapter 9

Conclusions

This thesis has addressed the problem of increasing the quantum efficiency (QE) of QWSC and p - i - n solar cells in the GaAs/ Al_xGa_{1-x} As materials system. The approach to the problem consisted of joint theoretical and experimental investigations.

Chapter 3 reviewed previous models dealing with compositionally graded structures. These do not attempt to reproduce data. We have developed a theory based on previous work which is capable of modelling a wide range of cells with position dependent bandgaps in all regions of the solar cell. In addition, the model is designed to model solar cells with back surface mirrors. The internal reflections from quantum well-barrier interfaces however was not treated.

We discussed properties of the analytical and numerical solutions for the QE . We concluded that the wavelength dependence of the QE enables us to estimate the minority electron diffusion length in certain samples. We further concluded that the recombination velocity in the p layer is less significant in graded p layers.

Consequences of the modelling were discussed in chapter 5, together with an analysis of the ideas underlying the optimisation program. The effect of compositional grades in the p type emitter layer, and the effect of adding a back mirror were investigated and illustrated for a range of significant cell parameters. Theoretical predictions of the QE enhancement were presented separately for the compositional grading technique and the mirror design.

After an introduction to the experimental techniques used in the project, the preliminary characterisation of our samples was presented. These results suggest a background doping problem in multiple quantum well material. The problem is more severe in MOVPE material. It was suggested that this problem is due to a loss of compensation between carbon and oxygen background impurities in the MOVPE QWSC structures.

The effect of the anti reflection coat on solar cell MIV characteristics was considered. Parallels were drawn with hydrogen passivated samples examined in the course of a collaboration with Eindhoven University of Technology.

A set of samples with a range of i region compositional profiles including quantum wells and grades was characterised and modelled. The high minority carrier efficiency predicted in these samples indicated good material quality. These samples have confirmed the capacity of the model to reproduce the QE of a range of complex graded i layers. They also demonstrate successful modelling of the QE of p and n layers with efficient minority carrier transport.

We then examined a set of QWSC and p - i - n MBE samples with different aluminium fractions. A tabulation of minority electron diffusion lengths L_n in the p layer was estimated from the modelling. The MOVPE samples grown for this project were also considered and showed values of L_n which are similar to the MBE material. These values are significantly lower than those estimated for Eindhoven material at a similar composition. Furthermore, the values of L_n are lower than the majority of the published data for low aluminium fractions, and are weakly dependent on composition overall. We concluded that the minority carrier transport parameters can be improved in both materials systems.

QWSC and p - i - n samples with compositionally graded p emitter layers were designed and characterised. Experimental enhancements were observed in all these structures, except one MOVPE sample. The QE measurements were modelled subject to the following assumptions. We assumed that the variation of L_n with aluminium composition in grades was similar to that estimated from QE measurements of ungraded samples. We also assumed that the diffusivity decreases exponentially with increasing aluminium fraction. This allowed us to

model the solar cells with a limited number of parameters.

The experimental QE data were successfully modelled for a range of samples grown by MOVPE and MBE. One device which could not be modelled initially was characterised extensively by SIMS and TEM. This additional information allowed accurate modelling of the experimental QE with corrected sample specifications. Diffusion of the beryllium p type dopant into the i region was identified as a problem. With this increased knowledge of the sample structure, a good fit was obtained. The companion MOVPE sample proved to suffer from poor material quality. Despite similar extensive characterisation, this sample could not be modelled.

The study of ungraded samples has shown that the material used in this work suffers from relatively poor minority carrier transport efficiency.

The QE data for graded structures concluded that significant QE enhancements can be achieved by compositional grading of the p type emitter.

A series of mirror backed QWSC samples was examined. Significant enhancements were seen in all devices. The front reflectivity was used as a fitting parameter to adjust the amplitude of the Fabry-Perot peaks observed in the data. One sample which shows no Fabry-Perot peaks supports the suggestion that this decreased amplitude is due to imperfectly smooth back surface mirrors.

Two devices from a 50 quantum well sample showed evidence of phase changes upon reflection from the back surface which differ by approximately π . This variation supported the use of the back surface phase change as a fitting parameter to model the wavelength position of the Fabry-Perot peaks.

We then showed that the QE model for mirrored samples is capable of accurately verifying both the optical thickness of the sample and the aluminium composition of the quantum well barriers. The origin of the overestimation of the Fabry-Perot peak amplitude by the model should, however, be verified. A calculation of the effect of light reflection at the quantum well-barrier interfaces would contribute to better understanding of this point. One sample matched the efficiency (about 14.2% in AM1.5) of our previous best $\text{Al}_x\text{Ga}_{1-x}\text{As}$ solar cell with benefitted from significantly better minority carrier transport.

The final part of this work presented two optimised designs incorporating these two design features. The first is based on optimisations observed separately in samples characterised during the course of the work. This predicted a theoretical short circuit current of $22.3\text{mA}/\text{cm}^2$. This represents an enhancement of 31% over a control without grade or back surface mirror. The projected lower limit to the efficiency in this case is 18.6% for AM1.5.

The second optimised device extrapolated from the previous design by thinning the p layer and removing the window layer. In this design, the theoretical short circuit current prediction was $23.6\text{mA}/\text{cm}^2$. This represents an enhancement of 20% over a control, and a final projected efficiency of about 19.7%. These calculations demonstrate enhancements possible relatively poor material. These efficiencies assume an unchanging V_{oc} and FF , and therefore represent only a lower limit.

Preliminary calculations in section 8.7 compared the highest projected short circuit current obtainable from graded QWSCs made from available material, and ungraded QWSCs made from the best reported $\text{Al}_x\text{Ga}_{1-x}\text{As}$. Both designs were coated with a back surface mirror. The QWSC structures made from the best reported material have projected short circuit current densities between $24.2\text{mA}/\text{cm}^2$ for the most commonly reported higher limits to minority carrier transport, and $25.6\text{mA}/\text{cm}^2$ for the highest reported values. The projected efficiencies ranged from 21% to 24% for the most efficient material, and from 20% to 23% for the standard, high quality material. These calculations suggest that the compositional grading and back surface mirror techniques can enhance the short circuit current density and efficiencies of solar cells made from poor material to within a few percent of cells made from the best material. All these projections are significantly greater than the efficient, independently verified 14.6% achieved by Amano *et al.* [73] and mentioned in chapter 8.7.

We conclude that both optimisation techniques have been successfully demonstrated, and that significant enhancements in short circuit current are possible.

Future work will investigate the optimised designs presented in chapter 8. The light intensity calculation should be generalised to include internal reflec-

tions at interfaces other than the front and back surfaces. The optimisation and modelling techniques can furthermore be generalised to other materials systems where material quality is an issue, and where compositional grades are attractive, such as CdHgTe or CuInGaSe.

Appendix A

Analytical Solutions

The analytical solutions for the quantum efficiency of the neutral regions were described in section 3. This appendix discusses exact and approximate analytical solutions to the differential equation for the minority carrier concentration 3.23 of chapter 3, and uses the same definitions.

The solutions to equation 3.23 are dependent on three materials and device dependent transport parameters, which are the diffusion length L_n , the recombination velocity S_n and the diffusivity D_n . The number of free parameters must be reduced to one before experimental data can be modelled with confidence and optimised structures designed.

This appendix examines these analytical solutions in a number of limiting cases in order to determine conditions in which the number of free parameters may be reduced in order to allow single parameter fits.

The discussion quotes the results given in section 3, and is similarly restricted to the case of a p type layer for brevity. Where illustrative examples are given, the calculations apply to a p type layer with an aluminium fraction of 30%, which is the design most commonly found in our structures.

The first section briefly restates the solutions obtained in section 3 and states the exact general solution subject to the usual boundary conditions.

The second section deals with an ungraded cell without fields in the neutral regions. We examine the behaviour of the analytical solution for the QE in a

number of limiting cases.

We then consider a cell with constant electric field in the neutral regions, but again with constant minority carrier transport parameters, and compare these results with the results for the cell without fields.

A.1 General Form of the Analytical Solution

The general solution to equation 3.23 can be written

$$n(x) = a_1 U_1 + a_2 U_2 + U_3 \quad (\text{A.1})$$

where functions U_1 , U_2 and U_3 are described in the general case in section 3.4. We saw in section 3.7.2 that the effective field experienced by the minority electrons in the conduction band can be expressed in per metre as

$$\mathcal{E}_f = \frac{qE}{2k_B T} \quad (\text{A.2})$$

In order to further simplify the final expression for the photocurrent, we introduce a surface boundary condition parameter \mathcal{S} which includes both the recombination velocity and electric field at the front of the layer

$$\mathcal{S} = 2\mathcal{E}_f - \frac{S_n}{D_n} \quad (\text{A.3})$$

The surface boundary condition is then of the form

$$\mathcal{S}n(0) + n'(0) = 0 \quad (\text{A.4})$$

The boundary condition at the interface between the neutral region and the space charge region in the depletion approximation is that the excess minority carrier concentration is zero

$$n(z) = 0 \quad (\text{A.5})$$

where z is the position of the depletion region, measured from the front of the p

layer.

Substituting for the expression for n and n' into these two boundary conditions allows us to express the general form of the constants a_1 and a_2 , which are

$$a_1 = \frac{-U_3(z)(U_2'(0) + \mathcal{S}U_2(0)) + U_2(z)(U_3'(0) + \mathcal{S}U_3(0))}{U_1(z)(U_2'(0) + \mathcal{S}U_2(0)) - U_2(z)(U_1'(0) + \mathcal{S}U_1(0))} \quad (\text{A.6})$$

$$a_2 = \frac{U_3(z)(U_1'(0) + \mathcal{S}U_1(0)) - U_1(z)(U_3'(0) + \mathcal{S}U_3(0))}{U_1(z)(U_2'(0) + \mathcal{S}U_2(0)) - U_2(z)(U_1'(0) + \mathcal{S}U_1(0))} \quad (\text{A.7})$$

These expressions define the general solution to equation 3.23. It proves difficult however to find an analytical expression for functions U_1 and U_2 in most cases. We now consider the two simplest cases where this is possible.

A.2 Ungraded p Layers

For an ungraded layer, the transport parameters are constant and the pseudo-field is zero. We have seen in section 3.7 that the functions U_1 and U_2 for an ungraded p layer are

$$\begin{aligned} U_1 &= e^{+kx} \\ U_2 &= e^{-kx} \end{aligned} \quad (\text{A.8})$$

where k is

$$k = 1/L_n \quad (\text{A.9})$$

The generation function g defined in section 3.6.2 takes the form

$$g(x, \lambda) = \frac{\alpha e^{-\alpha x}}{D_n} \quad (\text{A.10})$$

Function U_3 and its differential U_3' are then found from equation 3.29 and take the form

$$\begin{aligned} U_3 &= \frac{-\alpha e^{-\alpha x}}{D_n(\alpha^2 - k^2)} \\ U_3' &= \frac{\alpha^2 e^{-\alpha x}}{D_n(\alpha^2 - k^2)} \end{aligned} \quad (\text{A.11})$$

We note that both U_3 and U_3' are inversely proportional to the diffusivity D_n .

Equations A.6 and A.7 for this case yield the following forms for a_1 and a_2 :

$$a_1 = \frac{\alpha e^{-\alpha z}(\mathcal{S} - k) + e^{-kz}(\alpha^2 - \alpha \mathcal{S})}{D_n(\alpha^2 - k^2)[e^{+kz}(\mathcal{S} - k) - e^{-kz}(\mathcal{S} + k)]} \quad (\text{A.12})$$

$$a_2 = \frac{-\alpha e^{-\alpha z}(\mathcal{S} + k) - e^{+kz}(\alpha^2 - \alpha \mathcal{S})}{D_n(\alpha^2 - k^2)[e^{+kz}(\mathcal{S} - k) - e^{-kz}(\mathcal{S} + k)]} \quad (\text{A.13})$$

Equations A.8 to A.13 define the excess minority carrier concentration n . We can then write down the quantum efficiency using equations 3.1 and 3.20 from chapter 3. We choose to express the QE for a unit incident light flux in terms of the three following functions

$$f_1 = \frac{\alpha k e^{+kz}}{k^2 - \alpha^2} \left[\frac{e^{-\alpha z}(\mathcal{S} - k) + e^{-kz}(\alpha - \mathcal{S})}{e^{+kz}(\mathcal{S} - k) - e^{-kz}(\mathcal{S} + k)} \right] \quad (\text{A.14})$$

$$f_2 = \frac{\alpha k e^{-kz}}{k^2 - \alpha^2} \left[\frac{e^{-\alpha z}(\mathcal{S} + k) + e^{+kz}(\alpha - \mathcal{S})}{e^{+kz}(\mathcal{S} - k) - e^{-kz}(\mathcal{S} + k)} \right] \quad (\text{A.15})$$

$$f_3 = \frac{\alpha^2 e^{-\alpha z}}{\alpha^2 - k^2} \quad (\text{A.16})$$

such that the fractional quantum efficiency is

$$QE(\lambda) = f_1 + f_2 + f_3 \quad (\text{A.17})$$

We note that all three functions go through a singularity at $k = \alpha$. It can be shown that f_1 is continuous. Although functions f_2 and f_3 are both discontinuous, a numerical study shows that the sum $f_2 + f_3$ is small compared to f_1 and continuous. This is illustrated in figures A.1 and A.2 for high and low values of the diffusion length and high recombination velocity.

The figures show that f_1 dominates the general form the QE , whereas the sum $f_2 + f_3$ constitutes a correction which has a varying significance in different physical limits.

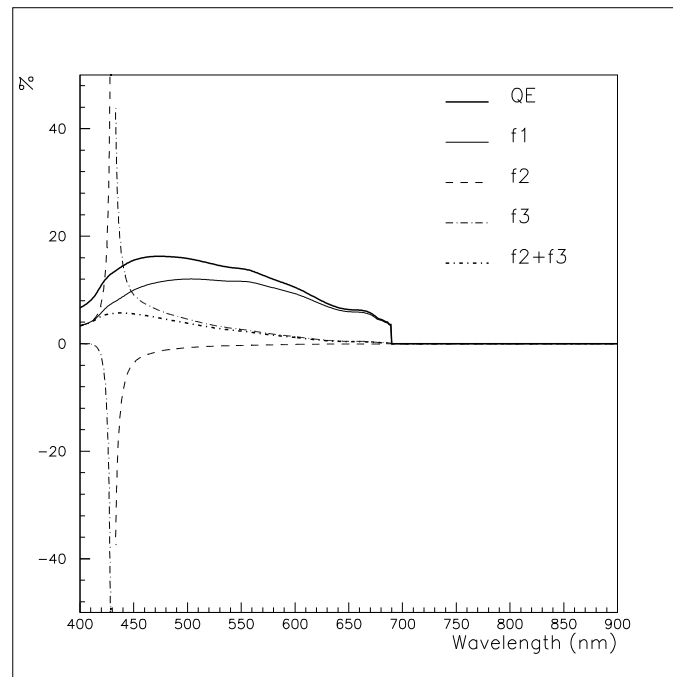


Figure A.1: Components of the quantum efficiency for small diffusion length

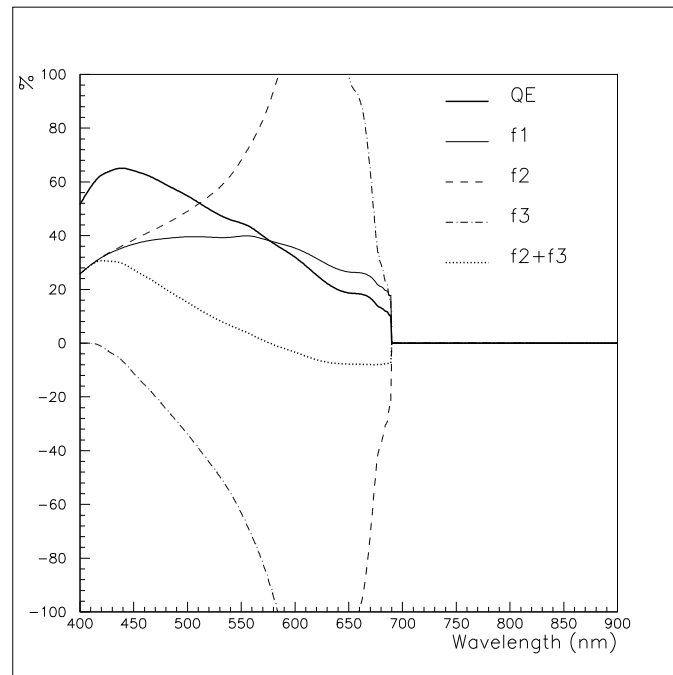


Figure A.2: Components of the quantum efficiency for large diffusion length

A.2.1 Case of Dominant Bulk Recombination

An examination of equations A.14 to A.15 shows that the surface boundary condition parameter \mathcal{S} occurs in terms $\mathcal{S} \pm k$ and in the term $\alpha^2 - \alpha\mathcal{S}$. For absorption coefficients greater than $\sim 10^6$, the latter is dominated by α^2 . This is true in particular of the absorption coefficient from $400nm$ to approximately $600nm$ in the typical 30% $Al_xGa_{1-x}As$ layer we are considering as an example.

We will see in the next section that for longer wavelengths and lower absorption coefficients, the effect of the recombination velocity is small if the diffusion length is small compared with z .

We find that the QE will be insensitive to both the recombination velocity and the diffusivity if $|\mathcal{S} \pm k| \simeq k$. Expressed in terms of the materials parameters, this gives the condition

$$\frac{1}{L_n} \gg \frac{S_n}{D_n} \quad (A.18)$$

This is trivially true if the recombination velocity is very low in which case the only free parameter is L_n .

More significantly, this condition will hold if the diffusion length is very small. In this case, the number of minority carriers lost at the surface is dwarfed by recombination in the bulk, and L_n is the main parameter determining the QE . Further discussion of the balance between these parameters is given in chapter 8.

For \mathcal{S} much greater than k and α , functions f_1 and f_2 both tend to limits which are independent of \mathcal{S} . This is equivalent to a vanishingly small minority carrier concentration at the front of the p layer. We conclude that the QE is again independent of the magnitude of S_n and D_n for \mathcal{S} much larger than k and α .

A.2.2 QE Near the Band Edge

This section investigates simple limits for the behaviour of the quantum efficiency near the band edge. In this regime, the absorption coefficient is small compared to z and the generation rate is approximately constant. Generation rates in this regime are illustrated in chapter 5.

Small Diffusion Length

If the diffusion length is small compared to the p layer thickness z , the product kz becomes large. Function U_1 is much greater than U_2 :

$$e^{-kz} \ll e^{+kz} \quad (\text{A.19})$$

This condition is usually true in the QWSC designs we consider, function U_1 being typically one or two orders of magnitude greater than U_2 .

Of the three functions contributing to the QE , functions f_1 and f_2 have prefactors e^{kz} and e^{-kz} respectively. Neglecting the contribution from function f_2 and terms in e^{-kz} in function f_1 gives the following expression for the QE near the band edge

$$QE \simeq \frac{\alpha^2 e^{-\alpha z} + k\alpha^2 e^{-\alpha z}}{k^2 - \alpha^2} \quad (\text{A.20})$$

Cancelling by $\alpha + k$ and assuming $\alpha \ll k$ in the resulting denominator gives the following result, expressed in terms of the diffusion length:

$$QE \simeq L_n \alpha e^{-\alpha z} \quad (\text{A.21})$$

The QE in this regime is independent of the surface boundary condition and hence of the diffusivity. We are left with only one fitting parameter, which is the diffusion length.

An identical result is reached if we assume that all carriers generated within a diffusion length of the depletion region are collected. The quantum efficiency in this picture is determined by the number of carriers generated in a region of thickness L_n adjacent to the depletion layer. For low absorption and a constant generation rate, this is simply the product of the generation rate and the diffusion length, which is the result we obtain in equation A.21.

Figure A.3 illustrates the agreement between this approximation and the exact result for our standard 30% Al p layer of thickness $0.15\mu m$ for a standard diffusion length of $0.08\mu m$ and a high surface recombination velocity of $500ms^{-1}$.

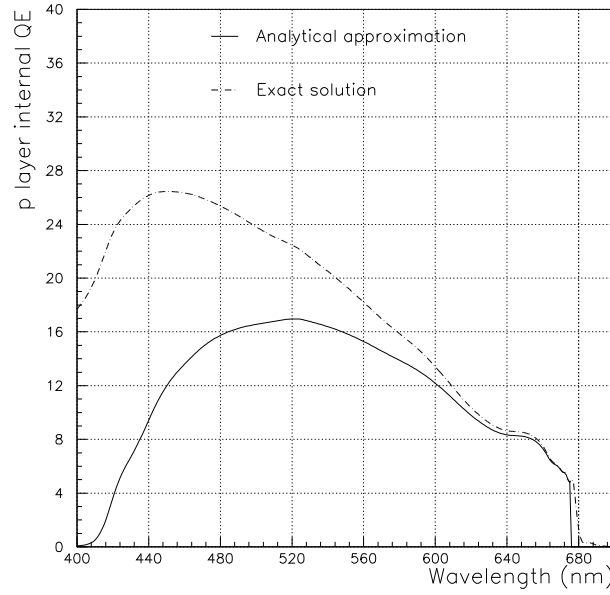


Figure A.3: Comparison of exact and approximate solutions to the QE for low absorption and low diffusion length $L_n = 0.07\mu m$ for $x_{wp} = 0.148\mu m$

The approximation is remarkably accurate for wavelength within a few tens of nanometers of the band-edge.

For samples obeying this limit, modelling can indicate values of the diffusion length from the magnitude of the QE near the band-edge, since the absorption coefficient is well known. The QE near the surface can then be modelled in terms of the surface recombination velocity. This is a useful diagnostic tool, which has already been proposed by Hovel [69] and used by Ludowise [27].

At higher energies the generation rate becomes strongly position dependent and the expression overestimates the minority carrier concentration at the edge of the depletion region, leading to overestimated values for the QE .

If the diffusion length is not small compared to z , minority carriers can diffuse to the surface and recombine. The QE across the whole wavelength range becomes sensitive to the surface recombination.

A.2.3 High Absorption

Figures A.1 and A.2 show that function f_3 tends to zero at short wavelengths. This is because the term $e^{-\alpha z}$ becomes small. To a good approximation, the QE in this wavelength range is approximately given by

$$QE \simeq f_1 + f_2 \quad (\text{A.22})$$

Neglecting terms in $e^{-\alpha z}$ in functions f_1 and f_2 then yields

$$QE \simeq \frac{\alpha k(\alpha - \mathcal{S})}{(k^2 - \alpha^2)(\mathcal{S} \sinh(kz) - k \cosh(kz))} \quad (\text{A.23})$$

Low Diffusion Length

For low diffusion length, $\sinh(kz) \sim \cosh(kz) \sim e^{kz}/2$. Equation A.23 becomes

$$QE \simeq \frac{2\alpha k(\alpha - \mathcal{S})e^{-kz}}{(k^2 - \alpha^2)(\mathcal{S} - k)} \quad (\text{A.24})$$

The short wavelength QE is sensitive to both the surface recombination velocity and the diffusion length

Since, however, section A.2.2 has shown that a low L_n can be estimated by modelling experimental data in the long wavelength, low absorption regime, parameter \mathcal{S} can be estimated separately by modelling the short wavelength response.

High Diffusion Length

If the diffusion length is large compared with z , $\sinh(kz) \sim kz$ and $\cosh(kz) \sim 1$. Furthermore, k is small, and $\alpha \gg k$. Equation A.23 takes the simple form

$$QE \simeq \frac{\alpha - \mathcal{S}}{\alpha^2(\mathcal{S}z - 1)} \quad (\text{A.25})$$

This expression is accurate to within about 5% of the QE for a range of about 10nm below 400nm, for typical structures.

The QE in this case largely determined by the surface recombination parameter. This means it is sensitive to a combination of recombination velocity and minority carrier diffusivity. Recombination losses in the bulk become negligible compared to surface losses, and the QE reaches a maximum which is limited by surface recombination.

A.3 Homogeneous Cells with Electric Fields

We now examine the hypothetical case of a cell with a non-zero effective field in the doped regions but with constant transport parameters. Models of this type are frequently used in theoretical investigations of compositionally varying structures (see section 3.1.1).

The parameters of equation for this type of structure are $b = 2\mathcal{E}_f$ and $c = -1/L_n$, where definitions and solutions are as given in section 3.7.2, but are repeated here for convenience and take the form

$$k_1 = +\sqrt{\mathcal{E}_f^2 + L^{-2}} - \mathcal{E}_f \quad (\text{A.26})$$

$$k_2 = -\sqrt{\mathcal{E}_f^2 + L^{-2}} - \mathcal{E}_f \quad (\text{A.27})$$

The two functions making up the restricted solution to the minority carrier equation were shown to be

$$U_1 = e^{k_1 x} \quad (\text{A.28})$$

$$U_2 = e^{k_2 x} \quad (\text{A.29})$$

Although the boundary condition at the edge of the depletion region remains unchanged, a field term appears in the surface recombination boundary condition, as explained in 3.6. The surface recombination parameter \mathcal{S} of equation A.6 is replaced with

$$\mathcal{S} = 2\mathcal{E}_f - S_n/D_n \quad (\text{A.30})$$

In a well designed cell, the field is negative, causing carriers to drift towards the

space charge region. This study deals with fields $E \sim -10^6 \text{Vm}^{-1}$, such that $\mathcal{E}_f \sim -10^7 \text{m}^{-1}$ at room temperatures. This corresponds to a moderate grade from 40% Al at the front surface of the layer to 30% at the top interface of the depletion layer.

The presence of a field removes some of the symmetry we found in the solutions for an ungraded layer. Function U_2 is no longer the inverse of U_1 . It becomes necessary to consider the relative magnitudes of \mathcal{E}_f , L_n and S_n/D_n .

The presence of a field term in the surface boundary condition increases the magnitude of the surface boundary parameter \mathcal{S} . This indicates a higher gradient in the minority carrier concentration $n'(0)$ (subject to the magnitude of $n(0)$). This seemingly contradictory increase in the value of \mathcal{S} is due to the fact that minority carriers are removed away from the surface by the effective field and swept towards the depletion layer. The minority carrier profile as a whole is shifted in a positive direction, increasing the gradient and hence the QE at the edge of the depletion layer. This is illustrated in chapter 5.

The solution for the QE in this case is of a similar form to that for an ungraded cell, but with the new expressions 3.42 to A.30 substituted. Accordingly, we rewrite equations A.14 to A.16 in terms of three new functions:

$$e_1 = \frac{\alpha}{(\alpha + k_1)(\alpha + k_2)} \left[\frac{k_1 e^{k_1 z} (e^{-\alpha z} (\mathcal{S} + k_2) + e^{k_2 z} (\alpha - \mathcal{S}))}{e^{k_1 z} (\mathcal{S} + k_2) - e^{k_2 z} (\mathcal{S} + k_1)} \right] \quad (\text{A.31})$$

$$e_2 = \frac{\alpha}{(\alpha + k_1)(\alpha + k_2)} \left[\frac{-k_2 e^{k_2 z} (e^{-\alpha z} (\mathcal{S} + k_1) + e^{k_1 z} (\alpha - \mathcal{S}))}{e^{k_1 z} (\mathcal{S} + k_2) - e^{k_2 z} (\mathcal{S} + k_1)} \right] \quad (\text{A.32})$$

$$e_3 = \frac{\alpha^2 e^{-\alpha z}}{(\alpha + k_1)(\alpha + k_2)} \quad (\text{A.33})$$

such that the fractional quantum efficiency is

$$QE(\lambda) = e_1 + e_2 + e_3 \quad (\text{A.34})$$

A.3.1 Surface Recombination Effect with Field

In this section we consider analogue to the balance between bulk and surface recombination which was discussed in section A.2.1. The discussion of this case is more restricted than for an ungraded cell because the spatial variation of materials parameters forbids many of the simplifications we were able to make in the previous section. We restrict the discussion principally to the effect of the surface recombination.

In section A.2.1 we saw that the relative magnitudes of k and \mathcal{S} determine the dominant recombination effect. Equations A.31 and A.32 show that the QE in this case is insensitive to the surface recombination velocity if $k_1 + \mathcal{S}$ and $k_2 + \mathcal{S}$ are both weakly dependent on S_n/D_n

If the diffusion length is very small such that $\mathcal{E}_f \ll L_n^{-2}$, we return to the situation described in section A.2.1. A calculation shows that this limit applies only for diffusion lengths below $0.01\mu m$ for the field strengths mentioned above.

More significantly, functions e_1 and e_2 will be insensitive to the surface recombination velocity if \mathcal{S} is dominated by $2\mathcal{E}_f$, that is, if

$$|\mathcal{E}_f| \gg \frac{S_n}{2D_n} \quad (\text{A.35})$$

This condition is less stringent than equation A.18 of section A.2.1 and is fulfilled even the moderate values of \mathcal{E}_f of $\sim -10^7 m^{-1}$.

A.3.2 QE Near the Band Edge for Small Diffusion Length with Field

Because \mathcal{E}_f is negative, we see that the positive k_1 is greater than k whereas the magnitude of k_2 is smaller than k . The condition of section A.2.1 is more readily fulfilled. That is,

$$e^{k_1 z} \gg e^{k_2 z} \quad (\text{A.36})$$

This remains true even for very large diffusion lengths, for which $k_1 \simeq +|\mathcal{E}_f|$ and $k_2 \simeq -|\mathcal{E}_f|$.

We follow a similar argument to that given in section A.2.2. Neglecting terms in $e^{k_2 z}$ and assuming $\alpha \ll |k_2|$ gives

$$QE \simeq \frac{\alpha e^{-\alpha z}}{\sqrt{\mathcal{E}_f^2 + L_n^{-2}} + \mathcal{E}_f} \quad (\text{A.37})$$

This expression is in fact a restatement of equation A.21 in the presence of a field.

A.4 Conclusions

A.4.1 Ungraded Solar Cells

In section A.2 we established that the analytical expression for the QE of a p layer can be reduced to simple analytical expressions in a number of limiting cases.

For high absorption coefficient at short wavelengths, the QE is in general sensitive to both surface recombination and diffusion length, and tends to a constant value.

For low absorption within a few tens of nm of the bandedge, the QE is independent of the surface recombination for the structures we are studying, because the diffusion length is smaller than the width of the p layer. The only free parameter in this regime is the diffusion length.

Values of the diffusion length can therefore be estimated from the QE at long wavelengths. The short wavelength response is then modelled independently in terms of the recombination velocity.

Cases where very large values of \mathcal{S} are required indicate a poor surface and the existence of a dead layer and a zero minority carrier concentration at the front of the p layer. We have seen however that the QE in the low absorption regime remains principally determined by the diffusion length.

A.4.2 Solar Cells With Fields but Constant Materials Parameters

A first approximation to the QE for a compositionally graded cell is the example of an ungraded cell where an effective field is present in the doped regions. Fewer conclusions can be drawn from this case than for an ungraded cell because the spatial variation of materials parameters is not negligible.

The main conclusion we reach is that even moderate grades generate fields of sufficient magnitude to reduce the effect of the recombination velocity to negligible levels.

This model however overestimates the QE for a graded structure for two reasons. The constant absorption coefficient overestimates the amount of light absorbed, particularly at long wavelengths. Secondly, comparison between numerical and analytical calculations shows that the gradient in the transport parameters is important. The gradient in D_n , and hence the minority carrier mobility, contributes a field-like term which is opposite to the band gap gradient field.

The QE in a real cell therefore remains insensitive to the magnitude of the recombination velocity for realistic values of the latter, but is significantly lower than the predictions of the simplified analytical model.

References

- [1] Markvart T (Ed.), *Solar Electricity*, Wiley, New York, (1994)
- [2] de Francieu R, *Multicrystalline Modules: Improvement of Industrialization and Product Reliability*, Proc. ISES Solar World Congress Harare (1995)
- [3] O'Regan B, Grätzel M, *A Low-Cost, High-Efficiency Solar Cell Based on Sensitized Colloidal TiO₂ Films*, Nature **53** (353), pp 737 – 740 (1991)
- [4] Sze, SM, *Physics of Semiconductor Devices*, Wiley, New York (1981)
- [5] Sah CT *et al.*, *Carrier Generation and Recombination in $p - n$ Junctions and $p - n$ Junction Characteristics*, Proc. IRE, **45**, pp 1045 (1957)
- [6] Pankove JI, *Optical Processes in Semiconductors*, Prentice Hall, New Jersey, pp 35–38 (1971)
- [7] Shockley W *et al.*, *Electrons and Holes in Semiconductors*, Van Nostrand, Princeton, 1950.
- [8] Paxman M, PhD thesis, Physics Department, Imperial College of Science, Technology and Medicine (1992)
- [9] Henry CH, *Limiting efficiencies of ideal single and multiple energy gap terrestrial solar cells*, J. Appl. Phys. **51**(8), pp 4494–4500 (1980)
- [10] Bertness KA *et al.*, *29.5-percent Efficient GaInP/GaAs Tandem Solar Cells*, Appl. Phys Lett., **65**(8), pp 989 – 991 (1994)

- [11] Green MA *et al.*, *Solar Cell Efficiency Tables*, (version 7), in: Progress in Photovoltaics, Wiley, **4**(59) (1996)
- [12] Barnham KWJ and Duggan G, *A new approach to high-efficiency multi-band-gap solar cells*, J. Appl. Phys. **67**(7) 1990
- [13] Nelson J *et al.*, *Steady-state carrier escape from single quantum wells*, IEEE J. Quantum Elect., **29**(6), pp1460–1467 (1993)
- [14] Barnham KWJ *et al.*, *Voltage enhancement in quantum well solar cells*, J. Appl. Phys. **80**(2) (1996) pp 1201–1206
- [15] Nelson J, *Quantum-well structures for photovoltaic energy conversion* in: Thin Films, volume **21**, pp 311–368, 1996
- [16] Adachi S, *GaAs, AlAs and $Al_xGa_{1-x}As$: Materials Parameters for use in Research and Device Applications*, J. Appl. Phys **58**(3), (1985)
- [17] Rosenberg HM, *The Solid State* (2nd edition), Clarendon Press (1978) p 168
- [18] Walukiewicz W, *Low-Field Mobilities in $Al_xGa_{1-x}As$ alloys*, in: Adachi S (Ed) Properties of Aluminium Gallium Arsenide, EMIS Datareviews Series No. 7, INSPEC, London (1992), pp. 221 – 224.
- [19] Fonash SJ, *Solar Cell Device Physics*, Academic Press, New York (1981)
- [20] Konagai M and Takahashi K, *Theoretical Analysis of Graded-Band-Gap Gallium-Aluminium Arsenide/Gallium Arsenide $p-Ga_{1-x}Al_x/p-GaAs/n-GaAs$ Solar Cells*, Solid State Electronics vol. 19, (1976) pp 259–264
- [21] Hutchby JA, *Theoretical Analysis of $Al_xGa_{1-x}As$ Graded Bandgap Solar Cell*, J. Appl. Phys. **47** (7),pp 3140–3151 (1976)
- [22] Sutherland JE and Hauser JR, *A Computer Model of Heterojunction and Graded Composition Solar Cells*, IEEE Transactions on Electr. Devices, **ED-24**(4), pp 363 – 372 (1976)

- [23] Sassi G, *Theoretical Analysis of Solar Cells Based on Graded Band-Gap structures*, J. Appl. Phys., **54**(9), pp 5421 – 5427
- [24] Hamaker H C (1985), *Computer modelling of the effects of inhomogeneous doping and/or composition in GaAs solar – cell devices*, J. Appl. Phys. **58**(6):2344 – 2351.
- [25] Connolly JP *et al.*, *Optimisation of High Efficiency $\text{Al}_x\text{Ga}_{1-x}\text{As}$ MQW Solar Cells*, Proc. ISES Solar World Congress (1995)
- [26] Boas M, *Mathematical Methods in the Physical Sciences*, Wiley, New York, 2nd edition (1982)
- [27] Ludowise MJ and Dietze WT, *High Spectral response and Photoluminescence of $\text{Al}_x\text{Ga}_{1-x}\text{As}$ Solar Cell Structures grown by Metalorganic Chemical Vapour Phase Deposition ($0.28 \leq x \leq 0.53$)*, J. Appl. Phys **55**(12), pp 4318 – 4321 (1984)
- [28] Loo RY and Kamath GS, *High Efficiency $\text{Al}_{0.38}\text{Ga}_{0.62}\text{As}$ Solar Cells*, 20th IEEE PVSC, pp 635 – 639 (1988)
- [29] Press WH, Flannery B, Teukolsky SA and Vetterling WT, *Numerical Recipes*, Cambridge University Press, Cambridge (1986)
- [30] Potter D, *Computational Physics*, Wiley, New York, p. 23 (1979)
- [31] Connolly JP, MSc thesis, Physics Department, Imperial College of Science, Technology and Medicine (1991)
- [32] Aspnes DE, *Table of Optical Functions of GaAs: Refractive index and Absorption Coefficient vs Energy (0–155 eV)*, In: Properties of Gallium Arsenide, EMIS Datareviews Series 2, 2nd edition, INSPEC, London, pp. 157 – 160 (1989)
- [33] Aspnes DE *et al.*, *Optical Properties of $\text{Al}_x\text{Ga}_{1-x}\text{As}$* J.Apl. Phys, **60**(2),pp 754 – 767 (1986)

- [34] Hass G, *Filmed Surfaces for Reflecting Optics*, J. Opt. Soc. of America **45**(11), pp 945 – 952 (1955)
- [35] Macleod HA, *Thin-Film Optical Filters*, Adam Hilger, London (1969)
- [36] Whitehead M *et al.*, *Multiple Quantum Well Asymmetric Fabry-Perot Etalons for High Contrast, Low Insertion Loss Optical Modulation*, Electronics Letters, **26**(19), pp 1588 – 1590 (1990)
- [37] Whitehead M, private communication 1993
- [38] Foxon CT, Joyce BA, *Growth of Thin Films and Heterostructures of III-V Compounds by Molecular Beam Epitaxy*, In: Growth and Characterisation of Semiconductors, IOP Publishing, London, pp 35 – 64 (1990)
- [39] Pollack FH, *Energy Gaps of AlGaAs*, In: Properties of Gallium Arsenide, EMIS Datareviews Series 2, 2nd edition, INSPEC, London, pp. 53 – 224 (1992)
- [40] Timmons ML, *Surface and Interface Recombination Velocities in AlGaAs*, In: Properties of Gallium Arsenide, EMIS Datareviews Series 2, 2nd edition, INSPEC, London, pp. 235 – 237 (1992)
- [41] Ahrenkiel RK *et al.*, *Minority Carrier Lifetime in $\text{Al}_x\text{Ga}_{1-x}\text{As}$ grown by Molecular Beam Epitaxy*, Appl. Phys. Lett., **69**(5), pp 3094 – 3096 (1991)
- [42] Zarem HA *et al.*, *Effect of Al Mole Fraction on Carrier Diffusion Lengths and Lifetimes in $\text{Al}_x\text{Ga}_{1-x}\text{As}$* , Appl. Phys. Lett., **55**(25), pp 2622 – 2624 (1989)
- [43] Bachrach RZ, Rev. Sci. Instrum. (USA), **43**, pp 734 (1972)
- [44] Casey HC, Panish B, *Heterostructure Lasers*, part B. Academic Press, New York (1978)

- [45] Ahrenkiel R K, *Minority – Carrier Lifetime and Diffusion Length in AlGaAs*, In: Adachi S (Ed) Properties of Aluminium Gallium Arsenide, EMIS Datareviews Series No. 7, INSPEC, London, pp. 221 – 224 (1982)
- [46] Grünbaum E *et al.*, *Evaluation of the Minority Carrier Diffusion Length by Means of Electron Beam induced Current and Monte Carlo Simulation in AlGaAs and GaAs p-i-n Solar Cells*, Semicond. Sci. Technol **10**, pp 627 – 633 (1985)
- [47] 'tHooft GW, van Opdorp C, *Determination of Bulk Minority Carrier Lifetime and Surface-interface Recombination velocity from Photoluminescence Decay of a Semi-infinite Semiconductor Slab*, J. Appl. Phys. **60**(3), pp 1065 – 1070 (1986)
- [48] Barun B, MSc thesis, Physics Department, Imperial College of Science, Technology and Medicine (1990)
- [49] Paxman M *et al.*, *Modelling the Spectral Response of the Quantum Well Solar Cell*, J. Appl. Phys **74**(1), pp 614–621 (1993)
- [50] Barnham K *et al.* (1994), Quantum well Solar Cells, Optoelectronics – Devices and technologies 9(4), Mita Press, Tokyo (1994), pp. 483 – 498
- [51] Murray R (1990), Passivation of Defects in GaAs by Hydrogenation, In: Properties of Gallium Arsenide, EMIS Datareviews Series 2, 2nd edition, INSPEC, London, pp. 298 – 303
- [52] Pavesi L (1992), Hydrogen Passivation of impurity States and Defects in AlGaAs, In: Adachi S (Ed) Properties of Aluminium Gallium Arsenide, EMIS Datareviews Series No. 7, INSPEC, London, pp. 303 – 316
- [53] Ragay FW, High Efficiency Solar Cells Based on III-V Semiconductors, grown by MBE, internal report, Applied Physics Group, Eindhoven University of Technology, 1993

- [54] Chatterjee B and Ringel SA, *Hydrogen Passivation of $n+$ p and $p+$ n Heteroepitaxial InP Solar Cell Structures*, In: Progress in Photovoltaics **4**, pp 91 – 100 (1996)
- [55] Roberts, C, Private Communication
- [56] Roberts, J S, Private Communications, 1993-1994
- [57] Caccavale, F., Private Communication 1996.
- [58] Illegems M, *Beryllium Doping and Diffusion in Molecular-Beam Epitaxy of GaAs and $\text{Al}_x\text{Ga}_{1-x}\text{As}$* , J. Appl. Phys **48** (3), pp 1278 – 1287 (1977)
- [59] Lee CC *et al.*, *Diffusion of Implanted Be in $\text{Al}_x\text{Ga}_{1-x}\text{As}$ as a Function of Al Concentration and Anneal Temperature*, Appl. Phys. Letts., **66** (3), pp 355 – 357 (1985)
- [60] Nelson J. A., Private Communication 1996
- [61] Pate M. A., Private Communications 1991-1996
- [62] Zachariou A, PhD thesis, Physics Department ,Imperial College of Science, Technology and Medicine, 1996
- [63] Holt DB, *Scanning Electron Microscopy (SEM) Microcharacterisation of Semiconducting Materials and Devices*, In: Growth and Characterisation of Semiconductors, IOP Publishing, London, pp 65 – 86 (1990)
- [64] Hutchinson JL, *High resolution electron Microscopy of Semiconductors*, In: Growth and Characterisation of Semiconductors, IOP Publishing, London, pp 225 – 234 (1990)
- [65] Clegg JB, *Depth Profiling of Semiconductor Materials by Secondary Ion Mass Spectrometry*, In: Growth and Characterisation of Semiconductors, IOP Publishing, London, pp 65 – 86 (1990)
- [66] Haarpaintner G. PhD thesis, Physics Department, Imperial College of Science, Technology and Medicine, 1995

- [67] Barnes J M, PhD thesis, Physics Department, Imperial College of Science, Technology and Medicine, 1994
- [68] Haarpaintner G (1994) *et al*, *Voltage Performance of Quantum Well Solar Cells in the $\text{Al}_x\text{Ga}_{1-x}\text{As}/\text{GaAs}$ and the $\text{GaAs}/\text{In}_y\text{Ga}_{1-y}\text{As}$ Material Systems*, Proc. 1st World Photovoltaic Energy Conference, 5-9 December 1994 Hawaii, pp 1783 – 1786
- [69] Hovel HJ, *Solar Cells*, In: Willardson R K, Beer A C (Eds), *Semiconductors and Semimetals*, Vol. 11, Academic Press New York (1975)
- [70] Roberts J S *et al.* (1994), *High Purity AlGaAs from methyl based precursors using in situ gettering of alkoxides*, Journal of Crystal Growth 143:135 – 140
- [71] Singh J (1993), *Physics of Semiconductors and their Heterostructures*, first edition. McGraw-Hill International Edition
- [72] Tsui E T *et al.* (1995), *Determination of the Quasi Fermi level separation in single quantum well p-i-n diodes*, J. Appl. Phys., **80**(8), pp 4599 – 4603 (1996).
- [73] Amano C *et al.*, *High Efficiency $\text{Al}_{0.3}\text{Ga}_{0.7}\text{As}$ Solar Cells Grown by Molecular Beam Epitaxy*, Appl. Phys. Lett., **51**(14), pp. 1075–1077 (1987)